FLUID MECHANICS IN A MAGNETOPLASMADYNAMIC THRUSTER

by

Daniel John Heimerdinger

B.S.E., Princeton University, 1981
S.M., Massachusetts Institute of Technology, 1984

SUBMITTED TO THE DEPARTMENT OF AERONAUTICS AND ASTRONAUTICS
IN PARTIAL FULFILLMENT OF THE REQUIREMENTS FOR
THE DEGREE OF

DOCTOR OF PHILOSOPHY

at the

MASSACHUSETTS INSTITUTE OF TECHNOLOGY

January 8, 1988

Signature of Author _____
Department of Aeronautics and Astronautics
January 8, 1988

Certified by _____
Professor Manuel Martinez-Sanchez
Thesis Supervisor

Certified by _____
Professor Jean Louis
Thesis Supervisor

Certified by _____
Dr. Peter Turchi, Director R&D Associates,
Washington Research Laboratory
Thesis Supervisor

Accepted by _____
Professor Harold Wachman
Chairman, Departmental Graduate Committee

FLUID MECHANICS IN A MAGNETOPLASMADYNAMIC THRUSTER

by

Daniel John Heimerdinger

Submitted to the Department of Aeronautics and Astronautics
on January 8, 1988 in partial fulfillment of the
requirements for the Degree of Doctor of Philosophy in
Aeronautics and Astronautics

ABSTRACT

A theoretical and experimental study was conducted on the fluid mechanics of a quasi-steady magnetoplasmadynamic (MPD) accelerator. Two mechanisms for performance limiting operation were noted from purely electrofluid-dynamic considerations. Both limitations are ultimately manifested by strong current concentrations that cause severe electrode and insulator erosion. One mechanism is attributed to arcjet geometry and the other to the inherent two-dimensionality of the Hall effect in the plasma discharge.

The approximate two-dimensional theory shows that the current density distribution along the arcjet channel may be controlled by a proper selection of a converging-diverging interelectrode separation. The lack of back emf at the arcjet entrance and exit, due to the low entrance velocity and the low exit magnetic field, requires the entire arcjet voltage to be resistively dissipated by the plasma. Increasing the interelectrode separation lowers the local electric field and reduces the local current density.

The theory also demonstrates that the accelerating magnetic force has a component that tends to deplete the anode region of plasma. As the anode region loses charge carriers, large anode drops develop in order to attract electrons. Eventually a limit is reached where the discharge cannot support such large electrode drops and the discharge coalesces into concentrated arcs.

An experiment was conducted to test the predictions from the two-dimensional model. Three annular MPD geometries were tested to examine the effect of interelectrode separation on the arcjets' performance. The arcjets were operated to 60 kA with an argon mass flow rate of 4 g/s and the experiment verified that the current concentrations were partially mitigated in the geometries with the flared channels. The experiment also verified the existence of the previously described anode depletion mechanism in all of the experimental geometries.

Significant anode drops were noted to begin at about 30 kA at an argon mass flow rate of 4 g/s and accounted for almost 50% of the total discharge voltage at 60 kA. At 60 kA, the anode drop appeared to decrease and the magnitude of high frequency voltage oscillations increased dramatically. The frequency of these oscillations appear to correspond to the plasma residence time in the channel and are hypothesized to be concentrated anode arcs that are convected with the plasma flow. At this current level, severe thruster erosion was also noted. This phenomenon appears to have the same characteristics as the "onset" limitation which has been used to characterize anomalous thruster operation for the past decade.

Thesis Supervisor: Dr. Manuel Martinez-Sanchez
Title: Associate Professor of Aeronautics and Astronautics

Thesis Supervisor: Dr. Jean Louis
Title: Professor of Aeronautics and Astronautics

Thesis Supervisor: Dr. Peter Turchi
Title: Director, R&D Associates Washington Research Laboratory in Alexandria, Virginia

ACKNOWLEDGMENTS

Over the past six and a half years, there have been many people who have helped me in a variety of MIT matters, all of which, in one way or another, have led to this small document which will soon be filed away in an expansive library basement. I often ask the question, has it been worth it? This dissertation represents a great deal of sweat, hard work, lost income, and lost relationships. But it also represents a piece of work that I am proud of, and it is partially a testament to the help and friendship of three people here at The Institute.

I owe a huge debt of gratitude to Professor Manuel Martinez-Sanchez who started me on this contract from day one and made me into a scientist. His expertise, patience, and friendship not only kept me here at MIT, but he made me feel good about my work, which was more often than not, very frustrating. The second person that really helped me through it all, is my good friend Bob Bourret. When I was down, he was always there. When I needed another hand in Washington, he was on the next plane. What more can you say about someone like that? These two people have been true and dear friends.

I cannot think of going through this whole process again without the companionship of my girlfriend, Evie Vance. Over the past three years she has helped keep me sane through the worst of it. I might have gotten through it without her, but my life certainly would not have been as complete and enjoyable as it has been.

In addition to the three people previously mentioned, I must also thank Dr. Peter Turchi and the staff of R&D Associates, Washington Research Laboratory for allowing us to use their facilities for this experiment. They treated me more like a regular employee and a friend than as a graduate student and a guest, and I really appreciated that.

Even with the support here at MIT, I cannot imagine getting this work done without my parents' encouragement. They not only have had the patience and pocketbook to put up with all these years of gainful unemployment, but they really helped me through some very rough times.

This past year has put this whole experience into perspective. Although times were tough both here at MIT and at RDA, I still remember taking the Metro from work in Alexandria to the National Institutes of Health and seeing my poor mother fight the toughest battle of her life. She lost that battle, but I remember vividly what she went through, recalling her courage and dignity, at the same time thinking what we as a family did for her, and I realize that MIT was not really so tough after all. To my parents and family I dedicate this dissertation. My only regret is that my mother never lived to see it.

This work was supported by the Air Force Office of Scientific Research under contract number AFOSR-86-0119.

Table of Contents

List of Figures

Nomenclature

A channel area (V.23)
$\underline{A}$ matrix (A5.6)
A_n n^{th} intermediate coefficient (A4.66)
A_n n^{th} series coefficient (A4.41)
a constant (A4.32)
a magnetoacoustic speed (II.19)
a nondimensional area (A2.10)
a_{MA} magnetoacoustic speed (A2.37)
a_0 entrance area (A2.21)
B magnetic induction field (I.4)
$\underline{B}$ matrix (A5.6)
B_n n^{th} intermediate coefficient (A4.67)
B_0 entrance magnetic field (V.11)
b constant (A4.32)
b nondimensional magnetic field (A2.10)
C capacitance (Figure III.3, A5.1)
$\underline{C}$ matrix (A5.8)
$C_{-1,-2}$ modified Fourier coefficients for the -1, -2 eigenvalues (A4.54)
C_n n^{th} modified Fourier coefficients (A4.54)
c Hall parameter constant (II.8)
$\langle c \rangle$ mean thermal speed of the electrons (A8.19)
c_i mean collision speed for ionic species (A10.8)
$\langle c_{in} \rangle$ mean ion-neutral collision speed (A10.33)
c_n mean collision speed for neutral species (A10.8)
c_p specific heat at constant pressure (V.17)
E electric field (II.4)
E_r radial component of the electric field (V.7, A8.9)
E_x axial electric field (A8.9)
E_y transverse electric field (V.27)
e fundamental charge (II.4)
e nondimensional electric field (A2.10)
e_i internal energy (A10.20)
F thrust (A9.18)
F_{em} electromagnetic force (A9.1)
$F_{x,cathode}$ total axial force on the cathode (A9.8)
f friction factor (A10.6)
f function (A4.63)
f parameter (A9.10)
f_{em} electromagnetic thrust density (I.4)
G momentum integral (A2.21)
G total stream function (A4.35)
G_{ffc} correction term for the fully flared channel (A9.10)
G_{pfc} correction term for the partially flared channel (A9.18)
g parameter (A9.10)
g weighting function (A4.62)
H channel height (A10.31)

h enthalpy (V.27)
h channel height (A8.51)
h thruster interelectrode separation (Figure II.2)
h_p Planck's constant (V.29)
h^* throat area (V.10)
I loop current (A5.3)
i $(-1)^{1/2}$ (A4.47)
J total current (I.2)
J^* onset current (A4.100)
j current density (I.4)
j_e electron current density (A10.27)
j_{ey} transverse electron current density (A10.28)
j_r radial component of the current density (V.7, A8.11)
j_x axial component of the current density (V.7)
j_y transverse current density (A4.31)
K_n n^{th} series coefficient (A4.49)
k Boltzmann's constant (V.4)
L channel length (V.19, A8.9)
L conductor length (A5.16)
L inductance (Figure III.3, A5.1)
L_p parasitic inductance (A5.3)
L_T terminating (or final) inductance (Figure II.3, A5.5)
M_A Magnetoacoustic (Mach-Alfven) number (Figure A3.1)
M atomic mass of the gas (A4.100)
m parameter (A4.72)
$\dot{m}$ mass flow rate (I.1)
m_e electron rest mass (II.7)
m_i ion rest mass (II.9)
n index (A4.48)
n number of inductor-capacity stages (A5.1)
$\vec{n}$ outward pointing normal (A9.2)
n_e electron density (II.4)
n_e^* equilibrium electron number density (A10.25)
n_i ion number density (A10.8)
n_n neutral number density (A10.8)
n_n^* equilibrium neutral number density (A10.25)
$\dot{n}_e$ net production rate of electrons (A10.25)
p thermodynamic pressure (II.1)
p_e electron pressure (II.4)
p_{mag} magnetic pressure (V.11)
p_{therm} thermodynamic pressure (IV.10)
Q_{ii} ion-ion collision cross section (A10.9)
Q_{in} ion-neutral collision cross section (V.29)
$Q_{i,int}$ ion internal partition function (A10.35)
$Q_{n,int}$ neutral internal partition function (A10.35)
Q_{nn} neutral-neutral collision cross section (A10.9)
q strength of the viscous source (V.24)
R gas constant (II.3)
R internal resistance of the inductor (A5.3)
R_B ballast resistance (Figure III.4)
$R_{Ballast}$ ballast resistance (Figure III.3)

R_L load resistance (A5.5)
R_{MPD} MPD arcjet resistance (Figure III.3)
R_m magnetic Reynolds' number (A2.10)
R_T termination resistance (A5.5)
R universal gas constant (A4.100)
Re_x Reynolds' number with respect to the axial direction (V.22)
r constant (A4.35)
r radial coordinate (A1.17)
r_a anode radius (I.2)
r_c cathode radius (I.2)
r_{co} initial cathode radius (A9.7)
r_m mean channel radius (A2.16)
r_n n^{th} series variable (A4.42)
s constant (A4.35)
s_F relative error in the floating potential measurement (A7.2)
s_T relative error in the terminal voltage measurement (A7.2)
T temperature (II.3)
T thrust (I.1)
T_e electron temperature (A10.26)
t constant (A4.35)
t time (II.1)
u axial velocity component (II.11)
$\vec{u}$ velocity vector (II.1)
u_e exhaust velocity (I.1)
u_r radial component of the plasma velocity (A8.10)
u_x axial component of the plasma velocity (A8.10)
V thruster voltage (I.3)
V volume (A9.1)
%V nondimensional voltage relative to the cathode (A7.1)
$\%V_{error}$ propagated measurement error in %V (A7.2)
$V_{aerodynamic}$ back emf voltage contribution from the thrust provided by the thermodynamic pressure on the thruster (figure V.4)
V_{Bulk} bulk plasma voltage (IV.17)
$V_{em,calc}$ calculated electromagnetic voltage component (Figure V.4)
V_F floating potential (A7.1)
V_H terminal voltage hash (VI.4)
$V_{Hall,\nabla Pe}$ voltage contributions due to the Hall parameter and plasma pressure gradient (Figure V.4)
V_i ionization potential (V.28)
V_{Ohmic} Ohmic voltage contribution (Figure V.4)
V_T MPD terminal voltage (A7.1)
$V_{Terminal}$ MPD terminal voltage (Figure V.5)
v nondimensional voltage (A2.10)
v transverse velocity component (II.11)
v_e electron velocity (A10.27)
w channel depth (V.23)
X separation function (A4.37)
x axial coordinate (II.11)
$\underline{x}$ state vector (A5.7)
Y separation function (A4.37)

Y_m m^{th} eigenfunction (A4.59)
Y_n n^{th} eigenfunction (A4.56)
y transverse coordinate (II.11)
Z impedance (A5.2)
Z degree of ionization (A10.14)
z depth coordinate (Figure II.1)

α ionization fraction (V.2)
β Hall parameter (II.4)
Γ nondimensional momentum (A4.22e)
γ function (A4.84)
ΔV_a measured potential drop in anode region (Figure IV.15)
ΔV_c measured potential drop in cathode region (Figure V.4)
ΔV_p measured bulk plasma voltage (Figure II.2)
δ boundary layer thickness (V.22)
δ Dirac delta function (A4.61)
δ skin depth (A5.15)
ϵ small parameter (A8.26)
ϵ_0 permittivity of free space (A10.14)
Λ quantity in the Spitzer logarithm (A10.15)
η nondimensional density perturbation (A4.28)
η thruster efficiency (I.3)
$\eta_{em,calc}$ calculated electromagnetic efficiency (Figure V.6)
$\eta_{Thruster}$ thruster efficiency (Figure V.6)
λ_i ion mean free path (A10.8)
λ_m m^{th} eigenvalue (A4.59)
λ_n mean free path for neutrals (A10.8)
λ_n n^{th} eigenvalue (A4.38)
μ plasma viscosity (V.24)
μ_i ion mobility (A10.29)
μ_i plasma viscosity for singly ionized species (V.26)
μ_{in} ion-neutral reduced mass (A10.32)
μ_n viscosity of the neutral gas (V.26)
μ_0 permeability of free space (I.2)
ν collision frequency (A4.20)
ν_{ei} electron-ion collision frequency (II.7)
ξ dummy parameter (A9.10)
ξ nondimensional momentum perturbation (A4.78)
Π total pressure (II.17)
π pi (I.2)
ρ plasma density (II.1)
σ conductivity (A5.15)
σ plasma conductivity (II.4)
τ characteristic pulse time (A5.1)
τ interaction parameter (A2.10)
τ_{flow} plasma residence time (V.19)
τ_{rec} plasma recombination time (V.20)
τ_w viscous wall stress (V.25)
Ψ stream function (A4.11)
Ω Bate's recombination coefficient (V.19)

ω angular frequency (A5.15)
ω arbitrary function (A4.12)

Subscripts:

$_e$ pertaining to the electron (II.7)
$_H$ homogenious solution (A4.32)
$_i$ pertaining to the ion (II.7)
$_n$ index subscript (A4.38)
$_n$ pertaining to the neutral species (V.29)
$_{-1,-2}$ indices pertaining to the -1 and -2 eigenvalues (A4.52)
$_p$ particular solution (A4.85)
$_r$ pertaining to the r (radial) direction (V.6)
$_{ref}$ reference quantity (A10.44)
$_s$ isentropic (II.19)
$_w$ evaluated at electrode surface (V.25)
$_0$ evaluated at channel entrance (V.28)

Superscripts:

$^{+,-}$ pertaining to the sign in equation A4.42
* nondimensional notation (A2.10)
$^'$ perturbation quantity (A4.22a)
* throat condition (A2.10)
^{0} zeroth order quantity (A4.22a)

Miscellaneous:

$\dot{}$ first derivative with respect to time (A5.3)
$\ddot{}$ second derivative with respect to time (A5.3)
$\langle\ \rangle$ axial mean (A4.33)
$\langle\ \rangle$ transverse average (A8.35)
$\underline{\ }$ matrix quantity (A5.6)
$\vec{\ }$ vector quantity (II.1)

Chapter I: Introduction

I.1: Introduction

The magnetoplasmadynamic (MPD) arcjet is one member of a group of rocket thrusters that are classified as electric propulsion devices. Electric propulsion differs from chemical propulsion in that the energy source is electric and external to the moving fluid rather than an exothermic combustion process.

Chemical engines have an ultimate limit on the amount of thrust delivered for a unit mass of fuel. This is determined strictly through the stoichiometry of the combustion reaction. In electric thrusters, the energy used to accelerate the working fluid comes from a powerplant so that the ultimate ceiling on the thrust per unit mass of fuel is limited by other restrictions such as the powerplant size and thruster material properties.

There are three classifications of electric thrusters. A thruster is either an electrothermal, electrostatic, or electromagnetic accelerator. In electrothermal arcjets, heating is accomplished either with an electric heater or a columnated arc; in an electrostatic device (e.g. an ion engine), a rarefied plasma is electrostatically accelerated through an applied voltage; in an electromagnetic thruster (typically an MPD accelerator), a voltage is applied across a plasma and thrust is developed from the interaction of the current flowing through the plasma and the associated self magnetic field created by the current flow. In these electric devices, the "fuel" is simply the vehicle through which momentum

transfer occurs.

Of the three types of electric thrusters, both electrothermal arcjets and electrostatic thrusters have met with limited developmental success. Their modest power requirements make them desirable and more readily integrable into existing or near term space projects. Their major drawbacks are that the electrothermal devices have low specific impulses and the electrostatic thrusters have very low thrust densities and require a large amount of power conditioning. Electromagnetic accelerators operate at higher thrust densities than electrostatic devices and operate at higher specific impulses than electrothermal arcjets. Their primary drawback is their lower efficiency, except at high power levels, which require very large and massive power supplies.

Although electric thrusters appear to be more versatile than chemical engines, there are certain missions for which chemical propulsion is required, or at least, more desirable. This stems from the inherent low thrust of electric thrusters in comparison with their chemical counterparts. The thrust of a rocket engine can be approximated by the following equation

$$T = \dot{m}\, u_e \qquad \text{I.1}$$

where $\dot{m}$ is the mass flow rate of the fuel and u_e is the average exhaust velocity. For a typical cylindrical MPD geometry, the exhaust velocity scales as

$$u_e = \frac{\mu_0 J^2}{4\pi\dot{m}} \left(\ln\left(\frac{r_a}{r_c}\right) + \frac{3}{4} \right) \qquad \text{I.2}$$

where r_a and r_c are, respectively, the anode and cathode radii.[1] The bracketed terms arise from the geometry of the channel. This relation

shows that the exhaust velocity is strongly related to the total current, inversely proportional to the mass flow rate, and weakly dependent on thruster geometry. Its efficiency can be defined as the exhaust kinetic power divided by the input power or

$$\eta = \frac{1}{2}\frac{\dot{m}u_e^2}{JV} \qquad \text{I.3}$$

where V is the thruster voltage. Given a 1.0 megawatt power supply and assuming an efficiency of 0.4, an anode to cathode radius ratio of 5, and a mass flow rate of 0.004 kg/s, these equations provide for a thrust of 56.6 N, an exhaust velocity of 14,142 m/s, and an operating current of 15,484 A at 64.6 V. The thrust levels achievable with an MPD arcjet preclude its use for ground launchers, but its higher specific impulse provides a greater momentum change per fuel increment, so a given velocity change can be achieved with a smaller quantity of fuel. This makes electric thrusters attractive for orbital transfer and stationkeeping where the requisite thrust levels are not as large.

From these relations, it is apparent that the thrust and the efficiency of the MPD arcjet rapidly increase with current. This is what makes the MPD arcjet such a promising candidate for future missions.

I.2: MPD Arcjet Operation

A typical coaxial MPD arcjet geometry is shown in figure I.1.[2] A central cathode surrounded by a concentric anode are separated by an insulating material through which gas is injected. A voltage across the electrodes causes dielectric breakdown to occur, initiating the flow of current. In this geometry, a self magnetic field is created in the $-\theta$

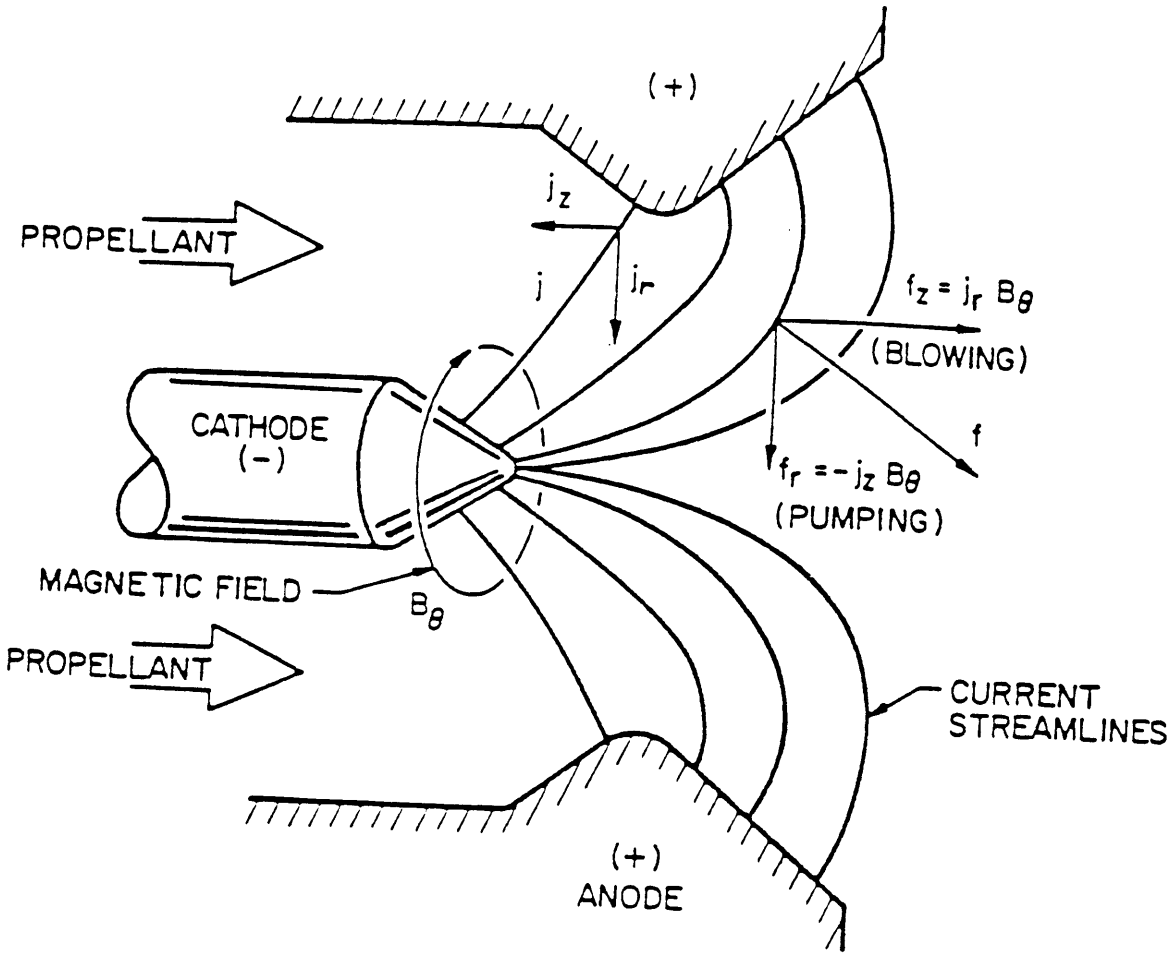

f = force

j = current density

B = magnetic field

Figure I.1: The Magnetoplasmadynamic (MPD) Thruster

direction. Hall currents, which occur in the presence of a magnetic field, imply tensor conductivity, and the current has both axial and radial components.

The arcjet's thrust comes from two sources. Gas expansion from Ohmic heating of the plasma accounts for one source; the other is the Lorentz, or ponderomotive, force caused by the interaction of the current density and the magnetic field. The electromagnetic force density is expressed as

$$\vec{f}_{em} = \vec{J} \times \vec{B} \qquad \text{I.4}$$

where $\vec{f}_{em}$ is mutually orthogonal to both the current density and the magnetic field vectors. The relative magnitude of the electrothermal and electromagnetic thrust contributions varies as the arcjet transitions from primarily electrothermal (low current) to primarily electromagnetic (high current) acceleration. The electrothermal thrust component in an electromagnetic thruster accounts for about 15% of the total thrust.

The electromagnetic force has two components--an axial "blowing force" and a radial "pumping force". The blowing force is sensible thrust, and the pumping force directs mass towards the cathode region where it pressurizes the cathode and depletes the anode. This both improves and limits arcjet operation. As the plasma is driven towards the cathode, it moves into a region of higher magnetic field (due to the cylindrical geometry) where it undergoes stronger Lorentz acceleration. However, this motion also causes a local depletion of charge carriers at the anode which can lead to a condition where the anode is no longer able to attract enough electrons for diffuse current conduction. If more current is demanded of the device, a diffuse current discharge cannot be

supported by the anode and concentrated arcs must form. When this occurs, local erosion increases and thruster performance is reduced.

I.3: MPD Research History

One would expect a successful research program to have a strong experimental aspect balanced by an equally strong theoretical and mathematical foundation. However, substantial theoretical modeling has been almost nonexistant in an overly experimental program for a quarter of a century. This is primarily due to the complex nature of the equations governing the MPD arcjet. The electromagnetic body force, which drives the arcjet, is a cross term and complicates modeling efforts by its inherent two-dimensionality. The MPD arcjet is also a device which, in the steady-state, has both a strong transition from a cold nonconducting gas to a high speed ionized plasma in addition to a complex two-dimensional plasma structure.[3,4] This structure, as well as the plasma sheaths near the electrodes, further complicates the mathematics of the discharge. The system of equations and the fundamental physics are so exasperatingly complex that even with a large number of simplifying assumptions and the computational power available today, the numerical simulation of MPD flow is exceedingly difficult, time consuming, and costly. For these reasons three decades ago, the small group of scientists conducting MPD arcjet research decided to follow an empirical program aimed at discovering the physical processes inherent to arcjet operation. The result has been the accumulation of a fairly large body of scattered data with very little hard and supporting theory.

Over the course of this period, some very interesting and puzzling phenomena have been discovered. Scientists have noted varied arcjet behavior with only subtle variations in mass injection and other geometrical changes.[5-7] Some scientists have operated thrusters with the additional inclusion of external magnetic fields, but no comprehensive theories have been presented to clarify its effect. Probably the most important problem noted by all groups investigating the operation of the MPD arcjet is the poor lifetime associated with operation at high power levels. For this reason, the physics associated with lifetime limiting processes are considered to be among the more immediate studies required for the development of a successful MPD propulsion system. The occurrence of this limitation has been termed "onset" due to the onset of increased thruster erosion and unsteady oscillations in the overall thruster voltage. This terminology is somewhat vague and deceptive due to the poor understanding of the phenomenology of this limitation. The next section will deal with the various studies of the onset phenomenon, and it will detail, in summary, their limitations. Section I.5 will detail the focus of this dissertation with respect to the study of the various erosion processes and their connections to the onset phenomenon as outlined in section I.4.

I.4: The Onset Phenomenon

Onset occurs with a natural progression of the current level to that point where thruster performance is first seen to degrade. Increased levels of thruster erosion have been associated with onset.[8] Serious

pitting of the electrodes as well as damage caused by moving arcs scar their surfaces. The insulating material also becomes subject to severe localized erosion.[3,9] Another feature associated with onset is a sharp increase in the thruster voltage and an appearance of large amplitude high frequency voltage oscillations.[3,7,10,11] In some thruster geometries, a luminous cylindrical layer, concentric with the cathode, appears. This "barrel" region appears to be a layer of high dissipation and Hall parameter.[3]

The consequences of onset are quite detrimental to arcjet operation. Because of the associated ablation, protracted operation at or above onset could lead to premature failure of the arcjet due to electrode or insulator destruction. With ablation, mass flow rates, and therefore thrust levels, cannot be accurately predicted.

Several theories have been advanced that attempt to forward reasons for the onset limit. Barnett has collated and categorized the major onset theories and their limitations.[12] These theories are concerned with the physics of onset initiation. Some theories describe a process related to anode onset, others a cathode related onset, and still others a plasma bulk related onset.

Promising theoretical models have been developed that describe onset and its relation to anode starvation.[13-15] As previously explained, it is hypothesized that this phenomenon is due to local anode starvation which causes a large voltage drop to develop as the anode tries to attract electrons. As the anode layer becomes unable to support a diffuse discharge, the discharge breaks down into a series of concentrated arcs.

This possibly explains the large voltage increase associated with onset; however, this theory does not provide any real insight into the mechanisms behind the high frequency voltage oscillations seen to appear with onset.

Baksht presented a very simple yet elegant work that described a mathematical model of the anode starvation process.[13] It shows the anticipated drop in electron density near the anode, as well as the approximate scaling of onset with $J^2/\dot{m}$ previously seen in experiment.[16-18] Heimerdinger and Martinez-Sanchez amplified Baksht's model to account for nonequilibrium processes and a nonconstant sheath potential.[14,15]

Perhaps the most persuasive experimental results that substantiate the anode starvation theories comes from the work of Vainberg and Hugel.[10-11] Several graphs are presented in figure I.2 that detail Vainberg's experimental work. His data clearly shows the depletion of density at the anode as current is increased towards onset. He also shows that the corrected potential drop at the anode changes sign near onset. This is predicted by Martinez-Sanchez who shows that the random flux of electrons is more than sufficient to conduct current below onset, and the anode is actually electron repelling.[15] As onset is approached, the anode changes to electron attracting in order to ensure that the current is conducted. Hugel also shows the rise of anode voltage as $J^2/\dot{m}$ is increased towards the onset value (figure I.3). Unfortunately, none of this data explains the full onset phenomenon since there is no reasonable connection to the high frequency voltage oscillations.

Several experimentalists and theoreticians have ascribed onset to a cathode related phenomena. Boyle linked the onset phenomenon to the

Potential Probe

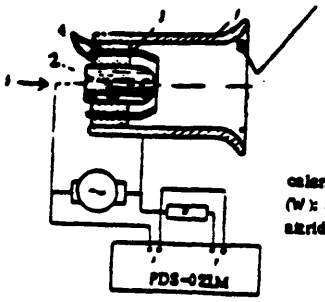

Diagram of the end-fire accelerator. 1) Anode (W); 2) cathode (W); 3) insert (W); 4) insulators (boron nitride); 5) working medium.

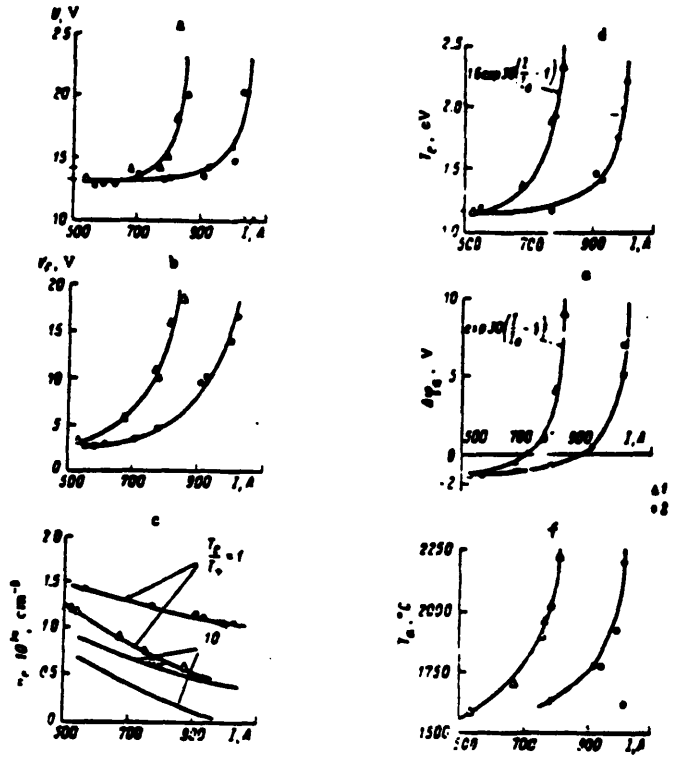

a) Voltage-current characteristics

b) Floating potential a few mm from anode

c) electron and ion number densities

d) electron temperature

e) anode potential drop (same as b), corrected to plasma potential)

f) Temperature at the inner anode surface

Figure I.2: The Experimental Results of Vainberg[10]

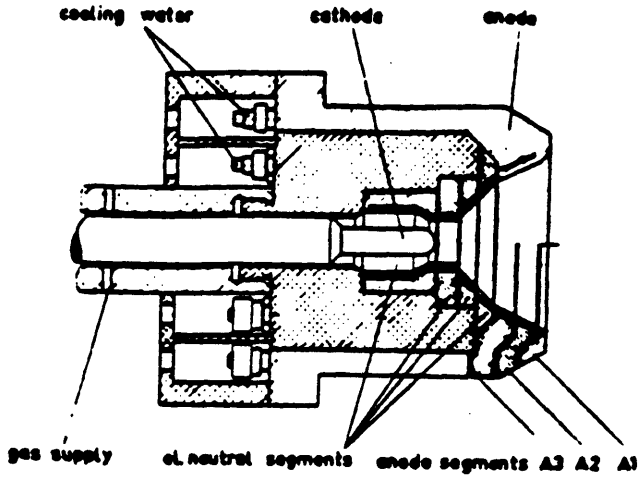

Schematic of apparatus.

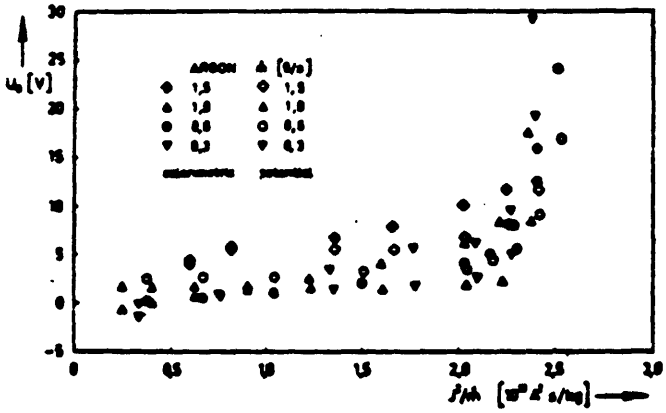

Experimentally determined anode fall in Argon as a function of $\bar{J}^2/\dot{m}$. The open symbols are results of potential measurements whereas the full symbols represent results of the calorimetrical measurements.

Figure I.3: The Experimental Results of Hugel[11]

cathode when he saw a large voltage increase in the electric field data near the cathode.[19,20] This electric field data also showed the characteristic high frequency oscillation associated with onset. He also noted increased luminous activity in this region which he attributed to onset. Other more rigorous works point to a cathode related onset. Work at Stuttgart by Schrade claims that the motion of microarcs is strongly affected in the presence of significant magnetic fields.[21] The magnetic fields cause the microarcs to bend and stream axially causing an increase in the near cathode voltage and in the local ablation rate due to increased localized cathode heating. These results also seem to correlate well with experimental data.

Ho showed that one could affect the luminosity distribution, the local potential drops, and the location of onset appearance through varied mass injection.[7] His important contribution to the field is that cathode processes in addition to anode processes appear to contribute to the overall onset phenomenon. At the present time, there is no apparent understanding how both the anode and cathode simultaneously know about onset. This linkage is most clearly shown in the Japanese work by Kuriki and Onishi who showed that both ablation rates at the anode and cathode increase dramatically at onset.[8]

Other scientists have looked towards bulk plasma phenomena to describe onset. Plasma turbulence, anomalous conductivity, and various instability mechanisms have been proposed, but these have yet to be demonstrated with any significant or conclusive data.[22-24] One might expect a wave structure to be responsible for the voltage oscillations,

but the results from a preliminary spectral analysis of the voltage shows that the characteristic frequencies were not clearly related to any known plasma instabilities.[25] Furthermore, Poon and Martinez-Sanchez showed that one of the more promising mechanisms for instability, the ionization instability, is most probably not present in the arcjet.[26] Heat conduction, and other diffusive effects, plus the small size of the region with above-critical Hall parameter, damp out any initiated wave.

These studies all have neglected to mention the importance of the overall fluid-dynamics of the arcjet to the erosion processes in the channel. Local analysis, such as the anode starvation models and experiments have shown compelling evidence to the existence of anode starvation and a link to electrode erosion. However, one would expect that in a given channel, the anode would initially become starved at a specific location on the anode resulting in the breakdown of the discharge into concentrated arcs so that a fully starved electrode may never result. In fact, the results from Vainberg and Hugel suggest that such starvation is indeed a local phenomenon. Given these considerations, it is difficult to understand how such a phenomenon could explain the widespread ablation throughout the arcjet at elevated current levels, not only at the anode, but at the cathode and the insulator. Ho's work shows that the erosion associated with high current operation occurs throughout the channel and is not restricted to local arcing at the anode. For this reason, other mechanisms appear to be partially responsible for arcjet erosion at elevated current levels. This dissertation forwards the thesis that geometrical considerations manifested by the interelectrode separation in

the channel become important in the determination of the distribution of current density throughout the channel at high current levels below those associated with electrode erosion from the formation of concentrated anode arcs.

I.5: The Dissertation Focus

This dissertation will focus on fluid-dynamic considerations that attribute electrode erosion to thruster geometry in addition to the anode starvation processes inherent to the two-dimensionality of the MPD channel flow. Previous research on MPD thrusters have concerned themselves with diagnoses of channels that were convenient to machine. In many of these cases, geometries with a constant interelectrode separation were chosen. For these geometries, strong inlet and exit current concentrations are to be expected, due to the local lack of back emf attributable to the low plasma velocity at the channel entrance and the low magnetic field at the channel exit. This dearth of back emf requires the local plasma to translate all of the electric field into current density. If one were to increase the interelectrode separation in these regions of low back emf, the local electric field would be diminished, and the current concentration lowered. This implies that it may be possible to reduce local current concentrations through a judicious variation of the interelectrode separation. In fact, it is conceivable that one might be able to specify a maximum allowable current density, defined by material limits, and design a thruster geometry so that the current density never exceeds this value.

This dissertation will forward a model and an experiment that considers both channel geometry and anode starvation mechanisms in the study of the performance of an MPD channel. It will be divided into numerous sections to improve clarity and to separate the various important subjects from the more peripheral, but still important, topics.

The format of this dissertation is presented as a series of chapters and appendices. The chapters will detail the primary contributions of the theory and experiment, and the appendices will provide additional information in the form of more detailed analysis, data, or supporting theory.

The theory is outlined in the second chapter after which the arcjet experiment is introduced in Chapter III. Chapters IV through VI discuss the results from the experiment and are broken down in the following manner. The first part of Chapter IV details the results pertaining to the data on the effect of interelectrode separation on the current density distributions in the experimental channels. The second part of Chapter IV outlines the data detailing the anode starvation processes in the channels under diagnosis. Chapter V discusses the effect of the variation of interelectrode separation and anode starvation on the overall performance of the arcjet. Chapter VI discusses a new theory of the phenomenology of onset and its relation to the general operation of the MPD thruster. Chapter VII concludes the dissertation with a discussion on the theses and results presented in this dissertation, in addition to their implications for MPD thruster design and future directions for MPD thruster research.

There are eleven appendices all of which contain important, but

peripheral information. As a result they are not incorporated into the body of this dissertation. Appendix 1 contains a detailed derivation of the general MHD formulation of the multidimensional MPD induction equation. Appendices 2 and 3 provide interesting theories which detail the flow of ideal MHD flows first at infinite and then at finite magnetic Reynolds' numbers. Appendix 4 continues by taking the results of the first appendix and deriving the complete two-dimensional model outlined in Chapter II. Appendix 5 details the design of the power supply for the experiment and includes analysis of the pulse forming network and the design of other peripheral power supply elements. The arcjet schematics are found in Appendix 6 and the determination of the steady-state operation of these devices is outlined in Appendix 7. Further arcjet models are found in Appendices 8 through 10 with Appendix 8 deriving a Baksht-like analysis of a channel with a cylindrical geometry and a constant electrode separation, Appendix 9 providing derivations for the integrated thrust of three different arcjet geometries, and Appendix 10 detailing real gas effects in the MPD channels. The final appendix, Appendix 11 lists the various computer codes utilized throughout this dissertation.

Chapter II: MPD Arcjet Modeling

II.1 Introduction

Detailed numerical simulations of arcjet operation represent a significant investment of time and money. Although solutions may be possible, it is not clear that they will elucidate the basic arcjet physics and the interplay between the various operational parameters. Since Baksht, few significant advances have been made in the analysis of the arcjet. To date, the most complete model is by Martinez-Sanchez and offers the first approximate asymptotically matched one-dimensional analysis of the MPD channel satisfying realistic boundary conditions from inlet to vacuum.[27] This chapter will be devoted to the derivation of a simplified two-dimensional model of arcjet operation. These models are more properly called local analyses for their region of validity is limited by a variety of strong assumptions.

These local analyses are undoubtably numerically approximate due to their inherent simplifications. However, they demonstrate trends that are seen in experiment, and they indicate trends that should be seen in experiments. The behavior and interrelation of the various operational parameters should be the ultimate measure of the strengths or weaknesses of these theories. With this in mind, the following fluid-dynamic analysis is presented. Particle kinetics appear through three parameters, all of which depend on the collisionality of the plasma. These three parameters are the plasma conductivity, σ, the Hall parameter, β, which is

the ratio of the electron gyro frequency to its collision frequency, and the plasma viscosity, μ. Various references can be consulted for the calculation of the particular kinetic parameter.[28-33]

II.2: Derivation of the Two-Dimensional Model for MPD Channel Flow

Before tackling the generalized system of equations for MHD fluid flow, it is necessary to determine the characteristics of MPD plasma flows. Five nondimensional parameters help justify the ultimate formulation of the model. These parameters include the Knudsen number which is used to determine the plasma collisionality, the Reynolds' number used to determine the level of turbulence in the flow, the Hartmann number used to indicate the relative importance of magnetic forces to viscous forces, the Prandtl number used to relate the importance of momentum and thermal transport, and the magnetic Reynolds' number which is used to compare the relative importance between convection and diffusion in a magnetized plasma.

In order to use an MHD formulation, it is important to justify that the plasma is acting as a continuum flow. The Knudsen number helps determine this because it relates the characteristic mean free path with the appropriate scale distance in the medium. In the MPD the largest cross section for momentum transport is that for the electron-ion Coulomb collisions, and the smallest channel dimension maximizes the Knudsen number. For a one electron volt plasma in a channel with a smallest characteristic dimension of two centimeters, the largest Knudsen number is approximately 0.0005 implying that a continuum formulation is appropriate

except for any region where the collisional cross section gets larger than the characteristic flow dimension. This could occur in several regions such as in the anode sheath and in the plasma plume, defined as the region of the discharge downstream of the channel exit. However, these regions will be neglected in this analysis.

The Reynolds' number is another important parameter because it helps to characterize the level of flow turbulence and therefore the significance of the flow parameters. The Reynolds' number requires a knowledge of the plasma viscosity which can be found in references 30 and 32. For a mass flow rate of 4 g/s of Argon in a channel 0.1 m long, the Reynold's number is somewhere between 800 and 2000 depending on the magnitude of the plasma viscosity. This indicates that the plasma can be treated as a laminar flow throughout most of the channel. In the plume, this assumption may break down, but since this region is not analyzed, no problems arise.

The Hartmann number is the ratio of the magnetic stresses to the viscous stresses in the plasma. If it is large, then the viscous stresses may be neglected from the fluid formulation. In the bulk of the MPD flow, the Hartmann number falls in the range of 100 to 400. This may break down in the sheath regions which are also neglected in this analysis.

These parameters indicate that the plasma flow can be portrayed as a continuum model of a laminar flow. Another parameter, the Prandtl number relates the plasma's ability to transport momentum versus thermal energy. For a cold gas, this parameter has a value near unity. As the plasma becomes ionized, the viscosity decreases and the thermal conductivity

increases implying that the Prandtl number drops to a value significantly less than one. In this case, the thermal layer is quite thin so the flow can be assumed to be approximately constant in the transverse direction. Theory and experiment have shown that the temperature in the plasma does not vary strongly except in the thin entrance layer where the initial plasma thermalization occurs.[14,34] As a result, this flow is also modeled as an isothermal plasma eliminating the need for an energy balance.

The magnetic Reynolds' number is a nondimensional parameter that appears in the nondimensional MHD formulation of Ohms' law. It is used to characterize the flow as one that is dominated by magnetic diffusion or convection. For low magnetic Reynolds' numbers, the magnetic field distribution is primarily determined through diffusive means, and magnetic convection can be considered of secondary importance. At high magnetic Reynolds' numbers, the plasma flow is primarily reactive, that is the back emf caused by magnetic field convection is the primary factor for magnetic field distribution and diffusive effects are secondary. In the MPD, the magnetic Reynolds' number appears to fall between 4 and 12. This implies that the discharge is strongly but not predominantly reactive in nature.

From these considerations, the generalized MHD formulation for an inviscid plasma flow can be completely expressed in six equations representing the conservation of mass (equation II.1), conservation of momentum (equation II.2), state (equation II.3), Ohm's law (equation II.4), Faraday's equation (equation II.4), and Ampere's Law (equation II.6) as shown below

$$\frac{\partial \rho}{\partial t} + \nabla\cdot(\rho\vec{u}) = 0 \qquad \text{II.1}$$

$$\rho \frac{\partial \vec{u}}{\partial t} + \rho (\vec{u} \cdot \nabla) \vec{u} = -\nabla p + \vec{J} \times \vec{B} \qquad \text{II.2}$$

$$p = \rho R T \qquad \text{II.3}$$

$$\vec{J} + \vec{J} \times \vec{\beta} = \sigma \left(\vec{E} + \vec{u} \times \vec{B} + \frac{\nabla p_e}{e n_e} \right) \qquad \text{II.4}$$

$$\nabla \times \vec{E} = - \frac{\partial \vec{B}}{\partial t} \qquad \text{II.5}$$

$$\nabla \times \vec{B} = \mu_0 \vec{J} \qquad \text{II.6}$$

Here ion slip has been neglected since the ion Hall parameter is normally much less than the electron Hall parameter, which, as will be shown, is of order unity.

The scalar Hall parameter and conductivity are defined as

$$\beta = \frac{eB}{m_e \nu_{ei}} \qquad \text{and} \qquad \sigma = \frac{e^2 n_e}{m_e \nu_{ei}} \qquad \text{II.7}$$

and are based on the Coulomb cross section. The Hall parameter may be rewritten in terms of the density so that

$$\beta = c \frac{B}{\rho} \qquad \text{II.8}$$

where

$$c = \frac{\sigma e}{m_i} \qquad \text{II.9}$$

This system of equations can be woven into a single induction equation which balances the convection of the magnetic field with its diffusion and Hall processes. A complete derivation of this induction equation can be found in Appendix 1. The results for a steady state, two-dimensional geometry is found in equation II.10 below:

$$\mu_0 \sigma \rho \left(\vec{u} \cdot \nabla \right) \frac{\vec{B}}{\rho} = \nabla^2 \vec{B} + c \nabla \left(\frac{1}{\rho} \right) \times \nabla \left(\frac{B^2}{2} \right) \qquad \text{II.10}$$

This assumes that both σ and c are constants throughout the discharge. This equation can be written in its expanded form as

$$\frac{\partial^2 B}{\partial x^2} + \frac{\partial^2 B}{\partial y^2} + \frac{cB}{\rho^2} \left[\frac{\partial B}{\partial x} \frac{\partial \rho}{\partial y} - \frac{\partial B}{\partial y} \frac{\partial \rho}{\partial x} \right] = \mu_0 \sigma \rho \left(u \frac{\partial}{\partial x}\left(\frac{B}{\rho}\right) + v \frac{\partial}{\partial y}\left(\frac{B}{\rho}\right) \right) \qquad \text{II.11}$$

where B is the z-component of $\vec{B}$, which is the only one assumed present.

Strong two-dimensional effects can be simplified by the use of the "thin channel" assumption widely used in boundary layer theory. In a thin channel, such as the one shown in figure II.1, the characteristic axial dimension is much larger than the transverse dimension. This allows several terms containing derivatives to be neglected. Under this assumption, the transverse magnetic diffusion term is of higher order than its axial counterpart except in thin transition regions commensurate with the distance associated with a magnetic Reynolds' number of unity. In this geometry, the narrow channel prevents significant transverse velocity from accumulating, which allows tranverse convection of the magnetized plasma to be neglected in comparison to axial convection. This leaves the two-dimensional induction equation in the form

$$\frac{\partial^2 B}{\partial y^2} + \frac{cB}{\rho^2}\left[\frac{\partial B}{\partial x}\frac{\partial \rho}{\partial y} - \frac{\partial B}{\partial y}\frac{\partial \rho}{\partial x}\right] = \mu_0 \sigma \rho u \frac{\partial}{\partial x}\left(\frac{B}{\rho}\right) \qquad \text{II.12}$$

which will be further simplified by use of the momentum equation.

The steady state inviscid MHD momentum equation can be written in component form as

$$x: \quad \rho\left(u\frac{\partial u}{\partial x} + v\frac{\partial u}{\partial y}\right) = -\frac{\partial}{\partial x}\left(p + \frac{B^2}{2\mu_0}\right) \qquad \text{II.13}$$

$$y: \quad \rho\left(u\frac{\partial v}{\partial x} + v\frac{\partial v}{\partial y}\right) = -\frac{\partial}{\partial y}\left(p + \frac{B^2}{2\mu_0}\right) \qquad \text{II.14}$$

where Ampere's law has been used to transform the Lorentz force into the magnetic stress tensor form. In the context of the thin channel assumption, these equations can be simplified to

$$x: \quad \rho u \frac{\partial u}{\partial x} = -\frac{\partial}{\partial x}\left(p + \frac{B^2}{2\mu_0}\right) \qquad \text{II.15}$$

$$y: \quad 0 = -\frac{\partial}{\partial y}\left(p + \frac{B^2}{2\mu_0}\right) \qquad \text{II.16}$$

The transverse momentum equation, equation II.16, implies that hydrostatic equilibrium between the magnetic and thermodynamic pressures is reached,

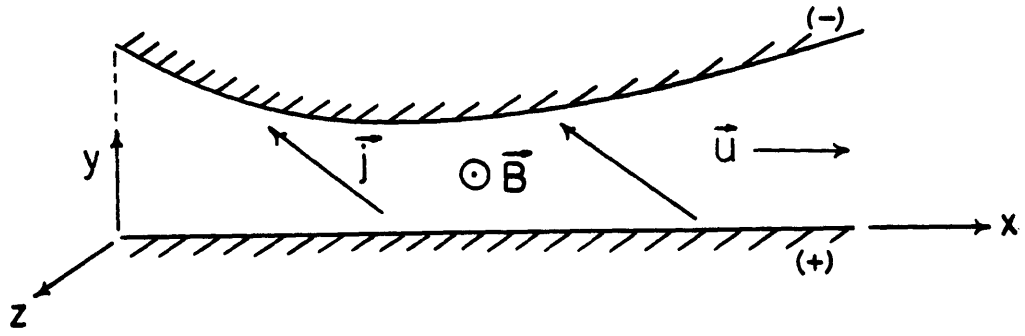

Figure II.1: Two-Dimensional MPD Arcjet Geometry

and, that the total pressure, defined by

$$\Pi(x) = p + \frac{B^2}{2\mu_0} \qquad \text{II.17}$$

is a function only of the axial coordinate. This relation allows the Hall term in equation II.12 to be rewritten directly in terms of the transverse partial derivative of the magnetic field and the ordinary derivative of the total pressure. With this additional simplification, the induction equation can be written as

$$\frac{\partial^2 B}{\partial y^2} + \frac{\mu_0 c}{\rho^2} \frac{d\Pi}{dx} \frac{\partial \rho}{\partial y} = \mu_0 \sigma \rho u \frac{\partial}{\partial x}\left(\frac{B}{\rho}\right) \qquad \text{II.18}$$

The implications of II.17 and II.18 are far reaching. It is possible to derive a characteristic speed based on the isentropic partial derivative of the total pressure with respect to the plasma density. This is analogous to the definition of the speed of sound in an ordinary compressible gas. This quantity,

$$\left(\frac{\partial \Pi}{\partial \rho}\right)_s = a^2 = \left(\frac{\partial p}{\partial \rho}\right)_s + \left(\frac{B}{\mu_0} \frac{\partial B}{\partial \rho}\right)_s \qquad \text{II.19}$$

the magnetoacoustic speed, is a combination of the local thermodynamic speed of sound and and a quantity that represents the propogation speed of a pressure wave through a magnetized medium in the absence of thermodynamic considerations. The existence of this magnetoacoustic speed is interesting because it implies that at infinite conductivity and finite Hall parameter, the throat section should always be "choked" at this speed, not at the local speed of sound. At finite values of the conductivity, where the dissipative terms may be substantial, this "choking condition" is only approximate. This is still important and illustrates the role of the magnetic pressure in determining the overall flow characteristics of an MPD discharge at varying current levels.

Equation II.18 can be solved approximately using perturbation techniques. This derivation is quite complex and tedious, so only some highlights are presented here. For a complete derivation, refer to Appendix 4.

This technique is based on a zeroth order channel which as no axial flow of current. For this condition, there is no possibility for transverse variation in the zeroth order density. This is also true for the zeroth order magnetic field. The solution to the zeroth order equation becomes

$$\frac{B}{\rho} = \text{constant} \qquad \text{II.20}$$

which is identical to the solution for a high interaction (infinite magnetic Reynolds' number) flow presented in Appendix 2 of this dissertation. For this case, the magnetoacoustic velocity simplifies to

$$\left(\frac{\partial \Pi}{\partial \rho} \right)_s = a^2 = RT + \frac{B^2}{\mu_0 \rho} \qquad \text{II.21}$$

which is a combination of the isothermal speed of sound and the Alfven speed.

In order to construct such a zeroth order solution, there is an implicit requirement for a nonzero axial component of the electric field to cancel the Hall current. The complete solution imposes that this axial field is cancelled by a perturbation axial electric field. This connection leads to a system of differential equations for perturbation quantities based on the zeroth order parameters. Solution of this system is quite complicated but the resulting trends described by the model show the anticipated behavior of area variation and anode starvation.

For solution, it is necessary to specify both an axial variation of

the total pressure along the channel as well as the initial conditions for the model. The entrance conditions for the model reflect the state of the accelerated plasma following passage through a layer where the cold gas is initially ionized and diffusion mechanisms are responsible for the motion of the plasma. For this reason, the entrance conditions for the model do not translate into the cold flow inlet conditions. Specification of the initial conditions for the model and specification for the transverse variation of the total pressure, $\Pi(x)$, are somewhat arbitrary. One can imagine that the plasma state at the edge of the initial ionization region can be controlled by varying the mass injection scheme and the interelectrode separation. Assuming this, it is then possible to select convenient initial conditions which are reasonable and come about from some initial thruster geometry and mass flow injection. And, the arcjet designer, in specifying a desirable current density distribution along the electrodes is almost specifying the total pressure distribution since the magnetic pressure is usually larger than the thermodynamic pressure. Therefore any general specification for $\Pi(x)$ is primarily a specification of the magnetic field variation (or the current density axial distribution) and results in a general specification for the interelectrode separation.

In order to proceed with the model's calculations, it is necessary to specify an axial variation of the total pressure, initial variations of the density and momentum perturbations, stream function, and conductivity. The theory produces the resultant channel dimensions based on the perturbation solution in addition to the variation in fluid and

electrodynamic variables. From this, the resulting mass flow rate and total current may be calculated. The model is then iterated for a desired thruster geometry, total thruster current, and mass flow rate. In this dissertation, a quadratic form of $\Pi(x)$ was selected to provide an approximately constant zeroth order current density distribution. Also the initial density perturbation is chosen to be linear, the initial momentum perturbation to be zero, and the remaining specifications are selected as detailed in Appendix 4. For these specifications a thruster about 9 cm long, operating at a mass flow rate of 3.95 g/s at approximately 43,365 A is found. The interelectrode separation has a converging-diverging profile as shown in figure II.2 and a spatial density variation as shown in figure II.3. The graph of the density shows the effect of the pumping force on the distribution of plasma. Figure II.3 clearly shows the appearance of a stressed layer at a point on the anode where the plasma density goes to zero at a point upstream of the channel's throat Figure II.4 shows the variation in the magnetic field along the channel. It is seen to decrease to the exit in a fairly linear manner as initially specified, and increase slightly toward the anode. This increase reflects the nonzero Hall contribution which requires for axial deflection of current. The nonzero Hall parameter is seen in figure II.5 and gets very large at the anode where the density goes to zero. This is expected since the Hall parameter is inversely proportional to the plasma density.

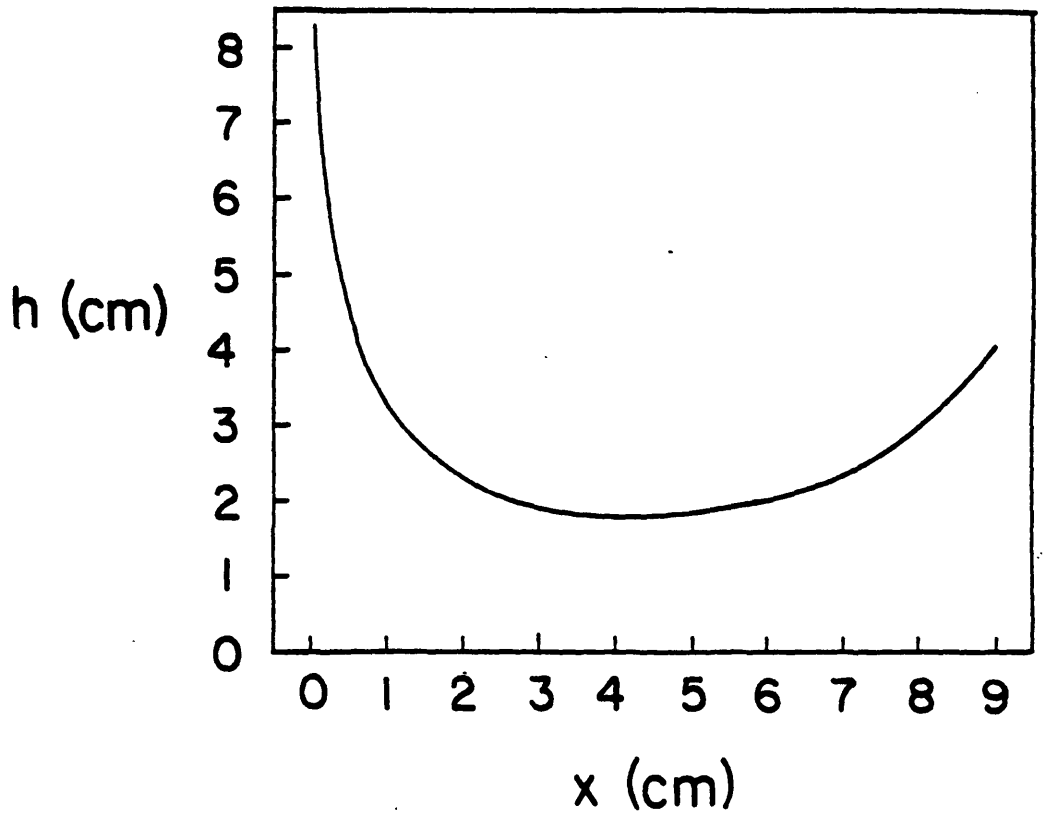

Figure II.2: Calculated Variation of the Interelectrode Separation

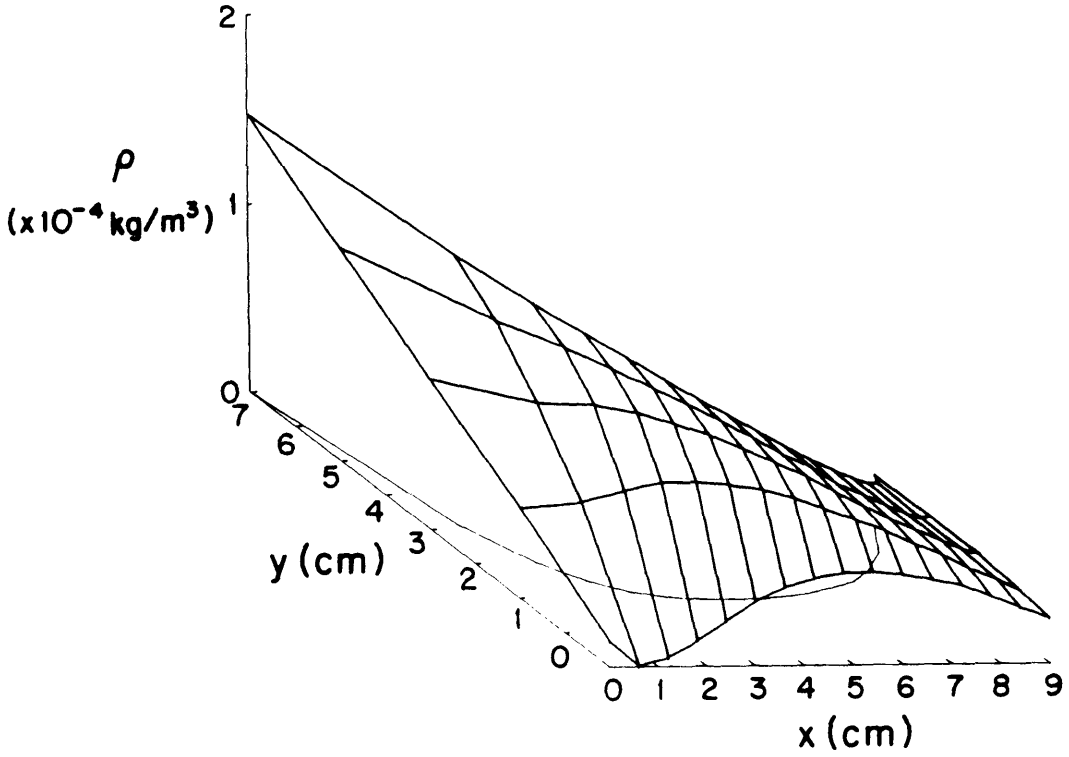

Figure II.3: Calculated Variation of the Plasma Density Throughout the Arcjet Channel

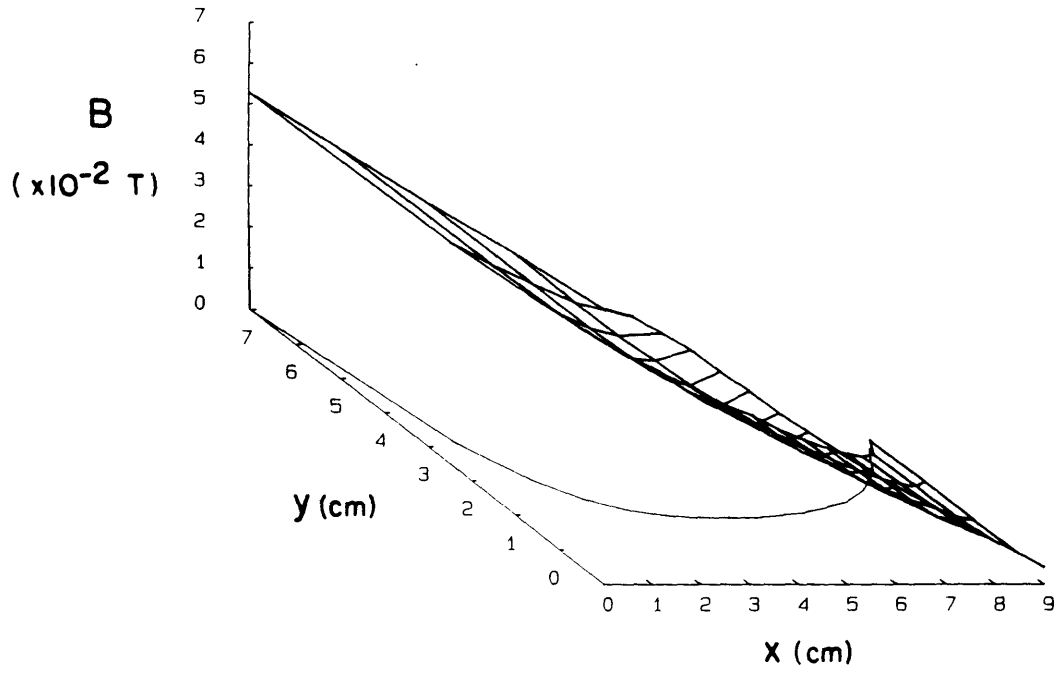

Figure II.4: Calculated Variation of the Magnetic Field Throughout the Channel at 43 kA and an Argon Mass Flow Rate of 4 g/s

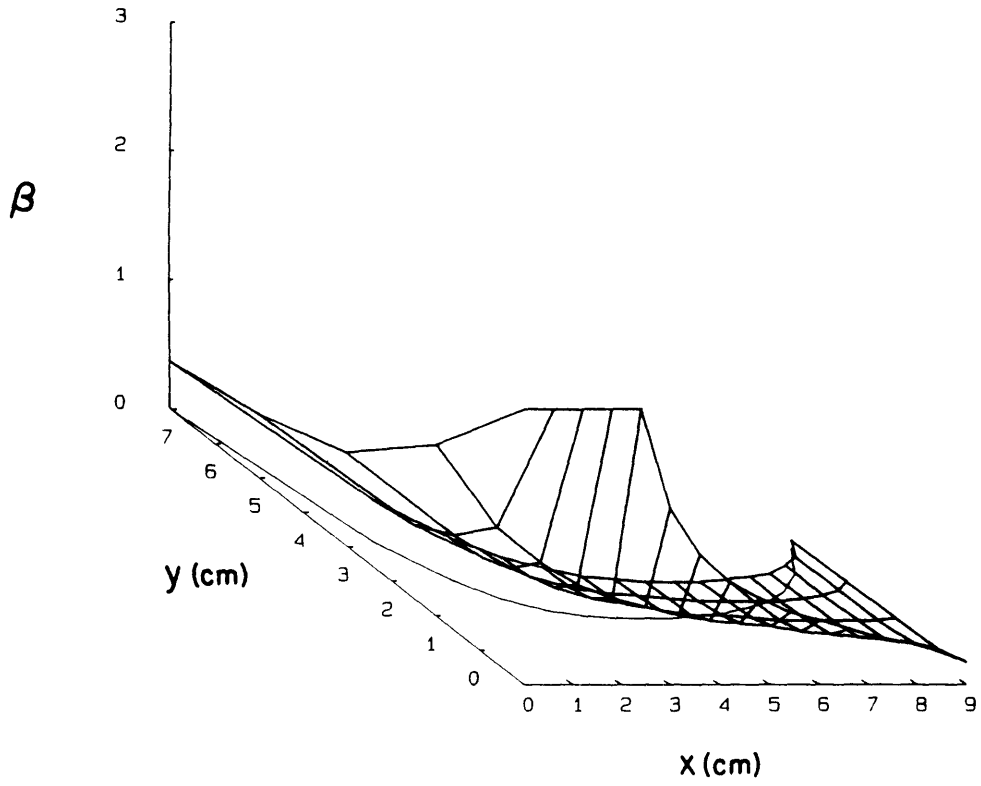

Figure II.5: Calculated Variation of the Hall Parameter Throughout the Channel at 43 kA and an Argon Mass Flow Rate of 4 g/s

II.3: Conclusions

An approximate model has been presented that clearly exhibits the anticipated connection between the interelectrode separation and current density distribution, and the connection between the radial pumping force and anode depletion. In order to test the theory and the validity of the two-dimensional geometry, an experiment will be conducted and presented. The next chapter details the design of the experimental apparatus and some of the problems and considerations necessary in the construction of a MPD thruster.

Chapter III: The Experimental Apparatus and Diagnostic Technique

III.1: Introduction

Without experimental verification, theoretical models of the MPD arcjet remain just theories. To conduct an experiment, it is necessary to design, construct, and operate an MPD arcjet system. Such a system requires a large amount of space, time, finances, and engineering to make it operate inexpensively and safely. These requirements could not be supported by facilities at MIT, so a joint agreement was drafted between MIT and R&D Associates' Washington Research Laboratory (RDA) in Alexandria, Virginia. An experiment was built on their premises, with common funds, to be used for the establishment of an MPD arcjet facility which could be readily modified for other experiments. This enabled MIT to conduct an experiment at a reasonable expenditure without any committment of facilities.

There are basic system requirements necessary for MPD arcjet operation. The arcjet must operate in a vacuum and have a sufficient power supply to operate as an electromagnetic thruster. It must have systems to deliver the proper mass flow, sequence events, and acquire data. Figure III.1 shows a block diagram of the total MIT/RDA MPD arcjet system. In addition to the actual thruster, there are many important subassemblies necessary for thruster operation and diagnosis. The design of each subassembly was based on an iterative process dependent on expedience, experimental necessity, and the availability of resources.

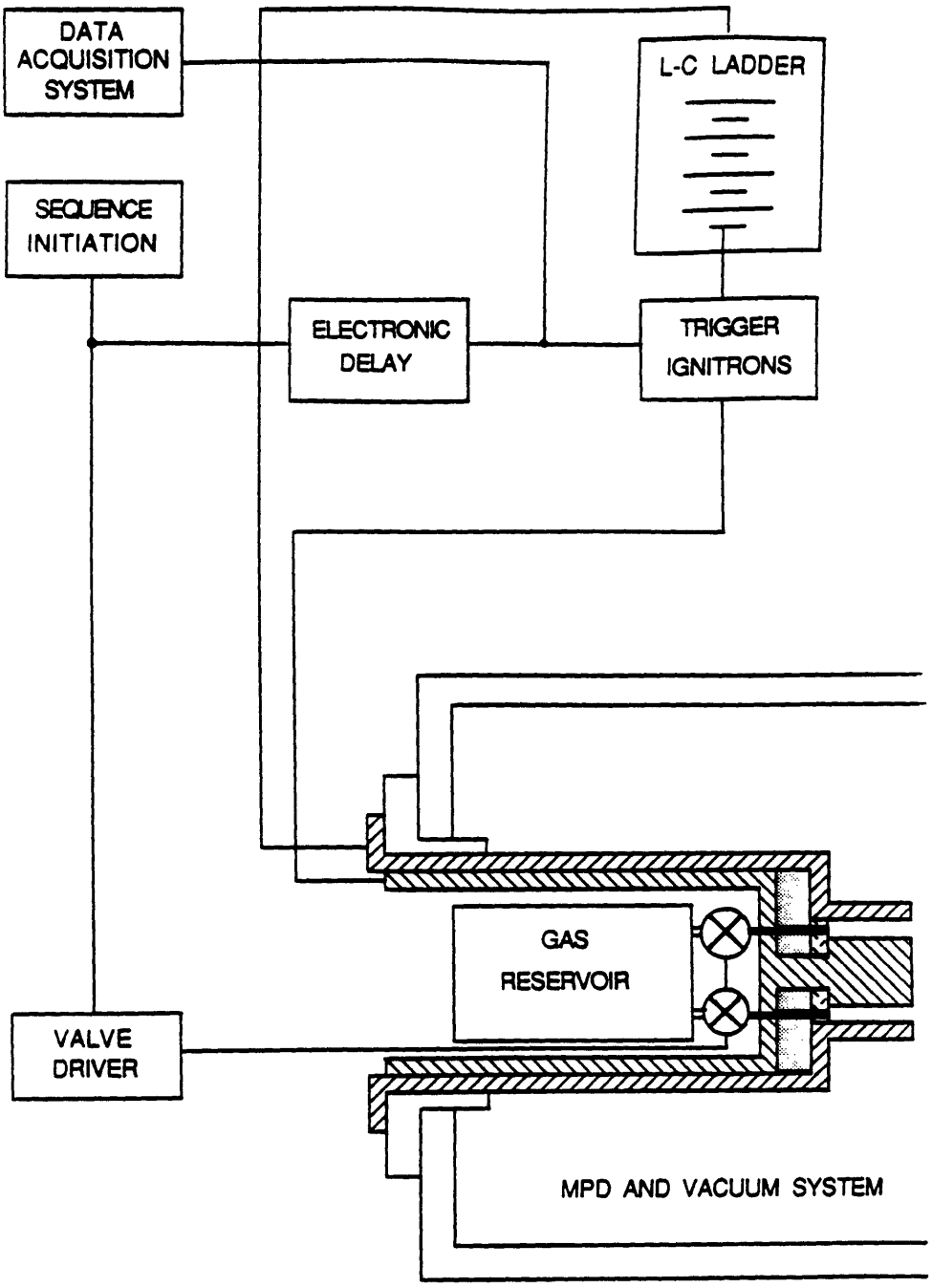

Figure III.1: Block Diagram of the MPD Arcjet System

III.2: The Design Criteria

The design tradeoffs began by determining the minimal requirements for a successful arcjet experiment. Ideally, an arcjet should be a multimegawatt, steady-state system operating at a dynamic vacuum of $< 10^{-5}$ torr so as to attempt to simulate the local vacuum near a spacecraft and to minimize any dynamic entrainment of the ambient plasma by the discharge. This is an unrealistic goal for a low budget system. The existing facilities at RDA dictated that the system utilize an existing vacuum tank, pumping system, and capacitors for a power supply. Other requirements dictated that all construction should be completed in less than six months for under $15,000. These restrictions were quite severe. In comparison to the ideal operating point, the requirements an MPD arcjet are that it operate at a vacuum of $\leq 10^{-4}$ torr for a pulse duration of no less than 400 μs at a quasi-steady level up to 70 kA. These requirements are seen to be the minimum necessary for the elimination of transients to arcjet operation in a quasi-steady mode and also guarantee operation above critical current levels.[12] The power supply had to be designed so that it could be configured for use on other experiments eventually conducted at RDA. These constraints dictated that vaccum system must be able to handle a pulsed discharge of at least 0.01 kg/s of argon without any significant flow and electrodynamic interactions with the vacuum tank. And finally, the data acquisition system had to be able to diagnose the arcjet while being isolated from the system so that discharge transients would not affect the results, nor harm the instrumentation. For these reasons, the subsystems were designed and

placed in the locations shown in the floor plan presented in figure III.2.

The arcjet resides in a long vacuum tank directly adjoining with the mass delivery system. An optical bench is adjacent to the vacuum system so that optical access to the arcjet is facilitated. Arcjet power is supplied by a capacitor bank located as far from the arcjet as possible. This facilitates access to both the vacuum and power systems. The data acquisition system is located reasonably far away from both the vacuum system and the power supply. It is placed inside a large copper Faraday cage which prevents any electromagnetic noise from pretriggering or possibly destroying the sensitive equipment. It would be best to locate the Faraday cage as far away from the high power as possible to protect both the instrumentation and operators, but this was not very practical. It is difficult to maintain a ground reference between the data acquisition system and the arcjet when the experiment is a very fast event. The more distant the data acquisition system, the more difficult this becomes. It is also more difficult to electrically transmit and receive data between the probes and diagnostic equipment. Hence the need for a sufficient ground plane reference and adequate protection for the experiment's operators.

The remainder of this chapter will focus on the subsystems of the MPD arcjet--the power supply, the vacuum system, the data acquisition system, and the arcjet itself.

III.3: The Power Supply

Design of the power supply centered around a large preexisting

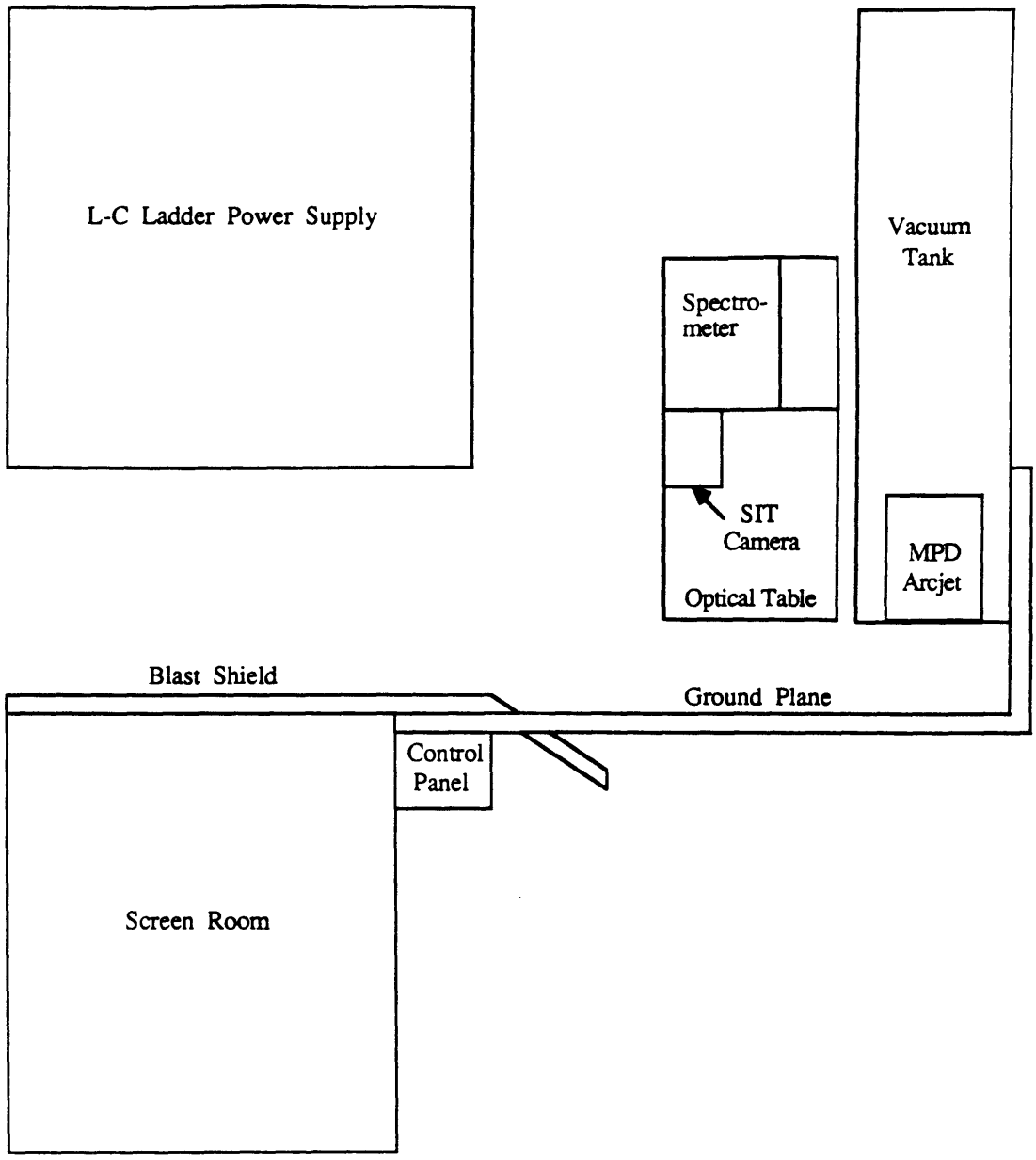

Figure III.2: Orientation of the RDA/MIT Arcjet Facility

capacitor comprised of eight independently triggerable stations (or stages). Each station consists of sixteen capacitors connected in parallel. Each is rated at approximately 15.6 μF and 20,000 V for a total energy capacity of 400 kJ. The total stage capacitance is approximately 250 μF. Each capacitor is connected to a central conductor via a wire fuse which provides a total parasitic stage inductance of 1 μH. Each station is connected to the main conductor by a General Electric mercury Ignitron Switch. The Ignitrons are independently triggerable by a voltage pulse, which, when all eight Ignitrons are triggered simultaneously, supply a discharge from a bank with a 2.0 mF capacitance. The magnitude of the pulse from this capacitor is very large, however its duration is quite short. This cannot be considered steady, since its shape is basically the discharge of an LCR circuit. An approximately square pulse can be achieved by creating an inductor–capacitor (L–C) ladder network. Inductors allow the single large capacitor to be segmented into stations which can be made to behave as a L–C Ladder network through selective Ignitron triggering (figure III.3). If all eight Ignitrons are simultaneously triggered, the presence of the inductors would not affect the output of the 2 mF capacitor bank since, over the time duration of the event, little or no current would pass through each inductor. If only the final Ignitron (Ignitron #8) is triggered, the capacitor bank looks like an eight stage L–C ladder and if Ignitrons #1 and #8 are triggered, the eight stage ladder feeds the arcjet from both sides as if two four stage ladders were in parallel. As more Ignitrons are triggered, the discharge time is decreased, but the current to the arcjet is increased. Based on

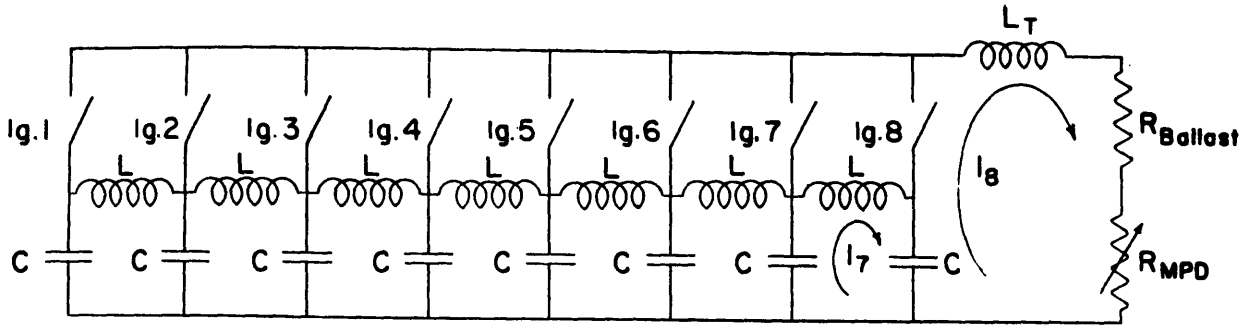

Figure III.3: Schematic of the MPD Arcjet Power Supply

the minimum requirements for arcjet operation, an inductor value of 10 μF was selected. This value allows for a sufficient pulse length and magnitude without charging the capacitors to a dangerously high voltage. This inductor value also allows the system to provide two reasonable pulses via the two previously described ladder configurations. The network triggered by a single Ignitron provides a pulse of about 35 kA for 800 μs while the network triggered by two Ignitrons supplies about 60 kA for about 400 μs at a safe charging voltage. Both configurations are shown in figure III.4.

The flat waveform is achieved by a phased blending of the capacitive discharges from each stage. When the Ignitron(s) is(are) triggered, the first stage voltage drops as current flows to the arcjet. As the first stage's voltage drops, the voltage difference between stages causes current to flow from the next stage, preventing the arcjet current from dropping. As the second stage's voltage drops, current begins to flow from the next stage, and so on, until there are no more stages left and the discharge ends. A longer and more square waveform is achieved by adding more stages. But in the previously described geometries, the singly triggered Ignitron configuration has a lower amplitude current level at a given voltage due to a higher network impedance. Herein lies one significant tradeoff. Additional considerations must be made in the network design. Because of the capacitors' ratings, the geometric restrictions placed on the power supply by RDA, and the pulse length requirements for thruster diagnoses, the network impedance is rigidly fixed at about 0.1 to 0.2 Ω. The arcjet's impedance is also fixed at a

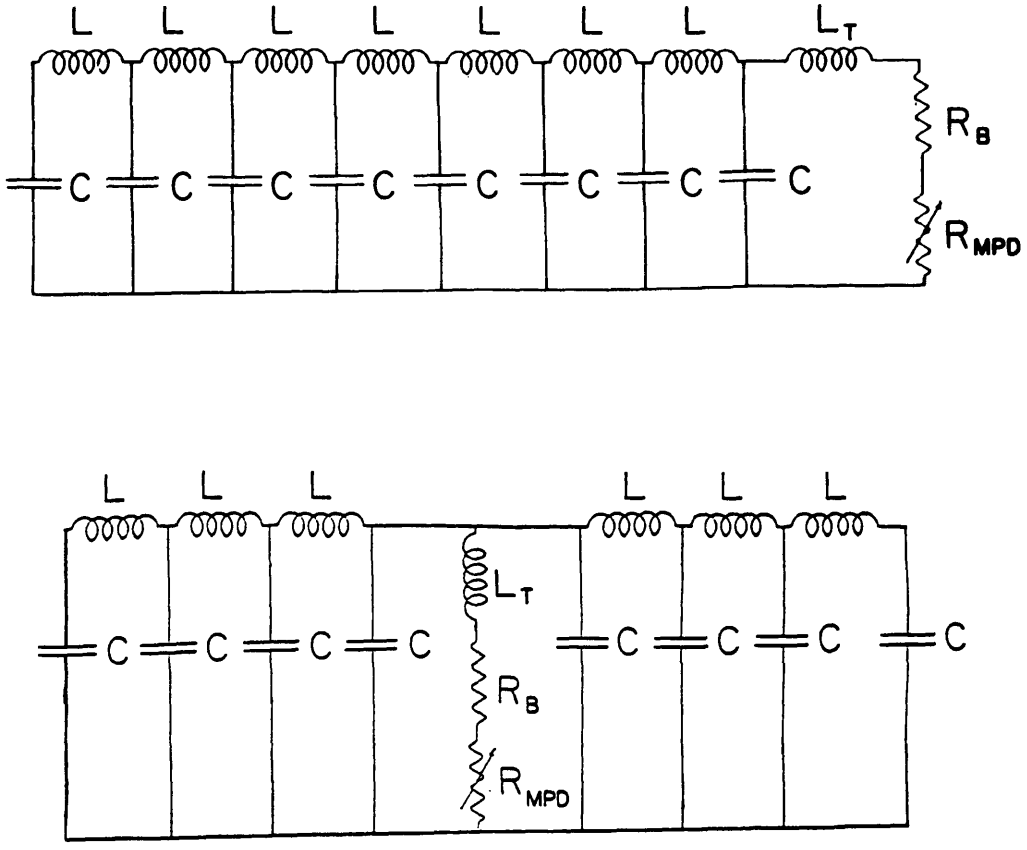

Figure III.4: Two Different L-C Ladder Configurations

value of only a few milliohms. Therefore, a ballast resistor must be included to match the network with the arcjet and significant power is dissipated in the resistor. The resistor must be designed to handle repeated discharges without a corresponding change in resistance due to Ohmic heating. This requirement, along with its inherent simplicity, adjustability, and cost led to the construction of a copper sulfate "garbage pail" resistor.

Appendix 5 presents the derivation of the circuit equations for the various L-C networks. It also contains a description of the design process involved for both the 10 μH helical inductors and the copper sulfate ballast resistor. The results of the calculation for the current from a 12 kV charge using the two-Ignitron geometry is presented in figure III.5 and predicts the real waveform quite accurately.

III.4: The Vacuum System

As stated previously, the vacuum system must be able to sustain discharge into an ambient vacuum of 10^{-4} torr at high argon mass flow rates. However, the vacuum system's capabilities have already been determined by the preexisting vaccum tank and diffusion pumps. This system consists of a 0.6 m diameter stainless steel tube that can be either five, six, or seven meters long depending on the number of tank extensions used. The vacuum is maintained at a static pressure level of $< 10^{-5}$ torr by two six inch oil diffusion pumps. The low static pressure and the long discharge chamber allow the arcjet to discharge into a very low pressure background. Since the discharge duration is shorter than the

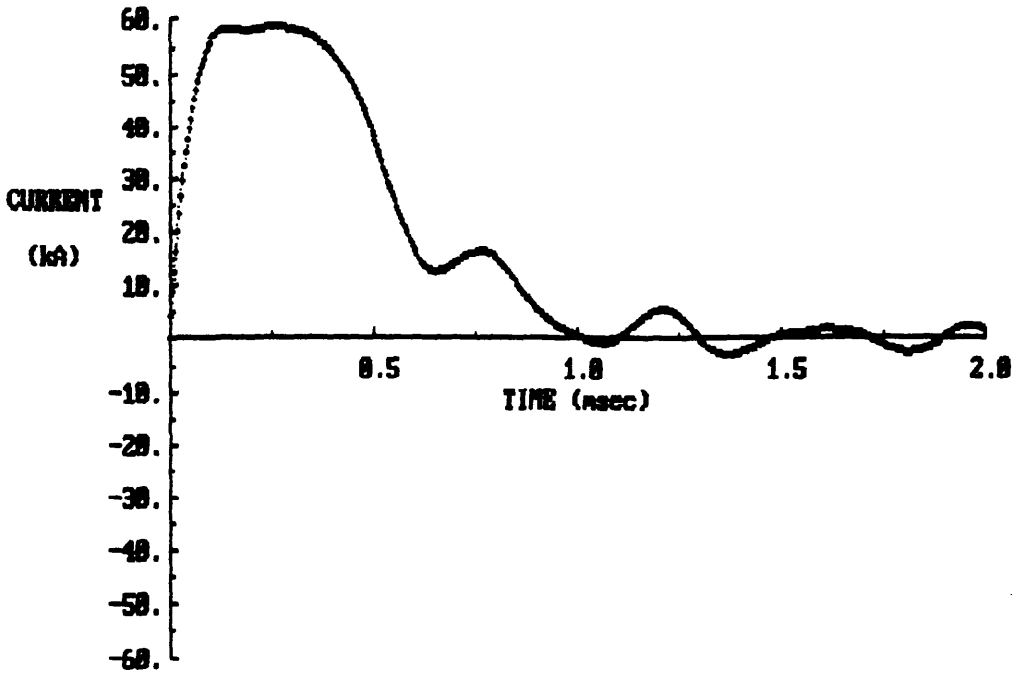

Figure III.5: Theoretical Current Pulse from the Arcjet Power Supply for a 12 kV Charge Fired with the Two Ignitrons

time necessary for pressure reflections to provide for gas equilibration, the background pressure remains low throughout the discharge.

The tank has a sufficient number of Plexiglas (or quartz) windows which allow for easy optical access for thruster diagnosis. It also has fittings which allow for probes to be placed at virtually any position in the plasma stream. This is a necessity since the use of probes is an unavoidable plasma diagnostic technique.

Since the tank is stainless steel and the pumps are constantly on, it is important to make sure that there is no possibility for the discharge to find an alternative current path through the tank, pumps, or building. This would affect arcjet operation and bias any measurement requiring knowledge of an accurate ground reference. In addition to diagnostic difficulties, such a problem could be dangerous to personnel and equipment by placing large voltages where they do not belong. Therefore the tank and associated pumps are kept electrically floating to prevent spurious alternate current paths for the pulse forming network (PFN) - arcjet circuit.

III.5: The Data Acquisition System

The diagnostics used in this experiment characterize the overall operating parameters, such as thruster voltage and current, and the internal spatially varying parameters such as magnetic and electric fields, particle densities, electron and ion temperatures, as well as the plasma velocity. These diagnostics utilize both optical and electronic systems. Included in the repertoire of diagnostic tools are a variety of

probes and cameras. Langmuir, voltage, and Rogowski probes are used to determine the internal distribution of the electric and magnetic fields as well as the overall voltage and current, and two classes of cameras are used to diagnose the plasma discharge.

An open shutter, or integrating camera, takes an open shutter photograph of the discharge and is used primarily to discern discharge structure and symmetry. Other more specialized cameras can be gated and take photographs over a small period anywhere in the discharge event. These photographs are used to study either transient phenomena without the contribution of steady-state light or vice versa.

When diagnosing a high power transient discharge, it is important to fully know where the electrical ground is. Ground loops must be avoided at all costs; an unanticipated overvoltage could cause serious damage to delicate instruments as well as bias measurements. To protect against these loops, several steps are taken. The power supply--MPD channel loop is kept at a floating potential so as to isolate the high power. This isolates the MPD and power supply from the tank and the Faraday cage housing the data acquisition system and operating personnel.

One characteristic of high power transient discharges is the variability of the ground reference at various times and locations throughout the system. It is important to maintain a stiff ground reference, otherwise significant measurement biases may occur. In order to account for the transient nature of the discharge, a large ground reference was constructed. Such a ground reference must have a small enough resistance so that any voltage difference from one part of the

system to another is small. A large ground plane is required since the resistance of the plane is inversely proportional to the conducting cross sectional area which is small since current is conducted through a skin depth consistent with the diffusion properties of a wave through the conducting medium over the discharge time. This ground plane is shown in the photograph in figure III.6. The channels on the ground plane act both as stiffeners and as trays for probe and data cables. Further ground loop protection is achieved either by powering all electrical equipment from the screen room (which is kept floating from the line voltage by isolation transformers) or by disconnecting the equipment before the discharge.

The optical equipment is primarily located on a stainless steel optical table. This table is in the proximity of building outlets, the vacuum chamber, the power cables, and some equipment powered from 120 VAC. For safety, the optical bench is also completely isolated from all equipment and all electrical connections in case it were somehow brought to voltage.

The heart of the data acquisition system is a Tektronix computer. It controls all of the oscilloscopes and post-processing all of the data. All of the electrical parameters of the discharge are recorded on these oscilloscopes. These parameters include the total current and voltage in addition to the signals from the probes measuring the internal distributions of electric and magnetic field.

III.5.1: The Electrical Probes

Measurements of voltages and currents are done with simple probes

Figure III.6: Photographs of the Ground Plane

described in detail in Huddlestone and Leonard.[35] Current is measured with a Rogowski loop, which is a simple coil of wire that measures magnetic field flux. A transient magnetic field induces a voltage across this closed loop. This voltage is dependent on the rate of change of the magnetic field, the loop area, and the number of turns in the loop (see figure III.7). Since magnetic field and current are related through Ampere's law, integration of the coil voltage provides a value for the enclosed current based on a known correlation constant. This type of coil is used to measure both the total current to the arcjet, and the enclosed current in the arcjet. A small open coil is used to measure the internal distribution of current from inside the plasma discharge, and a toroidal geometry is used externally to measure the total thruster current. The signals from both of these coils must be integrated to give the appropriate current. The two Rogowski loops are quite different. The small ten turn coil (figure III.8), approximately 1/16 of an inch in diameter is enclosed in a quartz tube and is placed inside the plasma discharge. The large toroidal Rogowski loop, shown in figure III.9, has approximately 1200 turns and a very large cross sectional area. The signals from the two probes are quite different. The toroidal geometry, with a large cross section and number of turns has a much larger output than the small ten turn coil. Active integrators with integration time constants commensurate with the signal magnitude were used to integrate the probe voltages. The toroidal Rogowski uses an integrator with a time constant of 377 μs. This integrator has a long characteristic "droop" time constant equal to approximately 70 ms, so the integrator operates

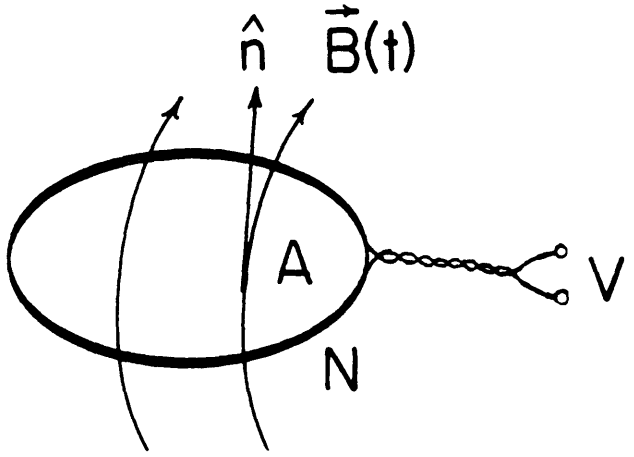

$$\left(\frac{d\vec{B}}{dt} \cdot \hat{n} \right) AN \sim V$$

N ≡ Number of turns in the coil
A ≡ Area of the coil
$\hat{n}$ ≡ Unit normal vector to the coil face
V ≡ Induced voltage
$\vec{B}$ ≡ Magnetic field

Figure III.7: Rogowski Coil for Measuring Time Varying Magnetic Fields

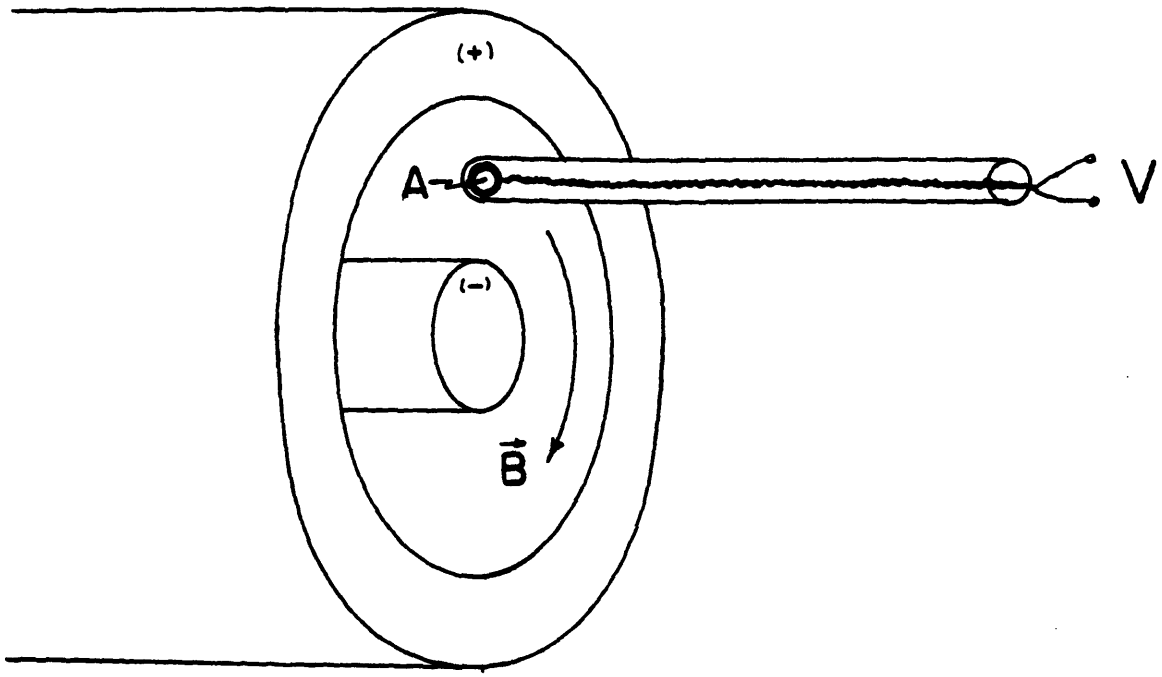

Figure III.8: Magnetic Field Probe Configuration for Internal Arcjet Diagnosis

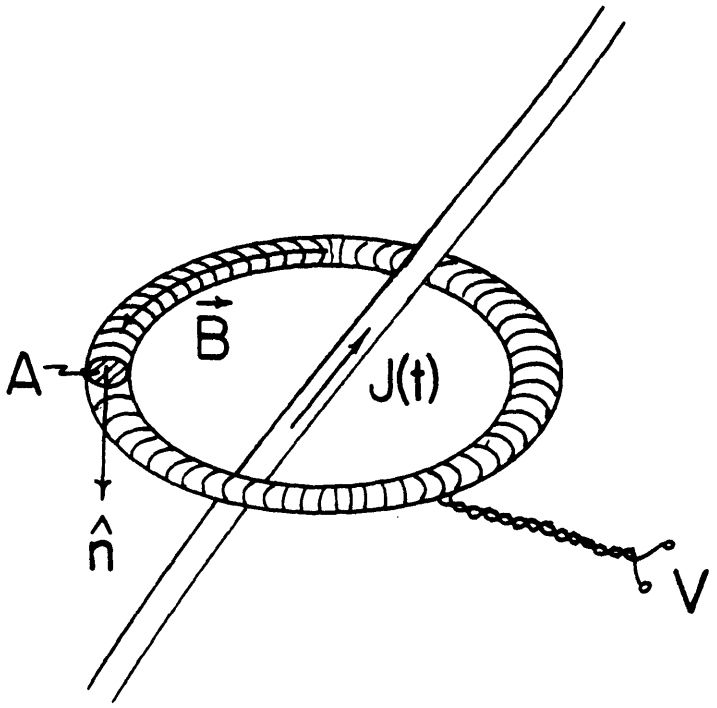

J(t) ≡ Current through the wire

Figure III.9: Toroidal Rogowski Loop for Measurement of the Total Arcjet Current

linearly over the millisecond discharge. The small Rogowski loop that is enclosed in a quartz tube for plasma isolation, uses an active integrator with a 3.49 μs integration time constant. This integrator also has a 70 ms droop time constant, which, in addition to its small integration time constant makes it a very temperamental and sensitive device. These integrators were designed and patiently rebuilt by Dr. Steve Seiler of RDA. The probes are connected by shielded two connector Twinax cables connected directly into the integrators which are then connected to the oscilloscopes. The oscilloscopes are in no danger of an overvoltage or a current surge, since the integrators act as a fuse preventing the surge from reaching the oscilloscopes.

Terminal voltage is measured from a Tektronix 1000:1 high voltage probe. The output of this device goes to a LeCroy fiberoptic transformer which is used to prevent high voltage from passing directly to the oscilloscopes. A LeCroy fiberoptic receiver converts the optical signal back into a voltage which is readable by the oscilloscope. Any overvoltage would saturate the datalinks and thereby protect the oscilloscopes.

The spatial distribution of electric potential is measured from a single 0.3 mil piece of Tungsten wire exposed directly to the plasma through a quartz tube. It draws negligible current and measures the floating potential of the plasma. The signal is attenuated by a 202:1 probe designed at RDA and is measured relative to the anode. Like the total voltage, the floating potential is optically isolated from the data acquition system to protect the oscilloscopes.

III.5.2: Optical Diagnostics

Optical diagnostics are very useful for characterizing the plasma discharge. They are nonintrusive means to determine discharge symmetry, overall shape, general distribution of intensity, and distribution of species and temperature.

In this experiment, a variety of cameras are used for thruster diagnoses. Open shutter, or integrated photographs, are taken with a large Polaroid bellows camera and a 35 mm Nikon Single Lens Reflex camera. Time resolved photographs are taken with a gated microchannel plate (MCP) camera invented at RDA. This camera uses a gated image intensifier to take a fast, low light Polaroid photograph. Another camera, called a Princeton Applied Research Silicon Intensified Target (SIT) camera also uses an intensifier to amplify the transient image. The input of the SIT camera is attached to the output of a SPEX 1.26 m spectrometer and is used to photograph a portion of the observed spectrum. The SIT camera is interfaced to an IBM Series 9000 computer which displays and analyzes the digitized output.

The simplest optical diagnostic uses the integrating camera. This camera is used primarily for discharge symmetry diagnosis and determination of overall discharge shape and intensity. It can also be used to measure, to a limited degree, the distribution of species when used in conjunction with color film or narrow bandpass filters. The main drawback of these cameras is that they cannot be gated and cannot be used to discern transient thruster behavior. For this task, the MCP channel is quite useful.

The MCP camera is an electronic device that uses photon excitation and electron amplification to intensify an initial signal. When a photon strikes the surface of the plate, an electron is excited and accelerates through a high voltage onto a phosphorescent surface which then displays the amplified image. The image is many times more intense than the original discharge and can be recorded on ordinary high speed Polaroid film. A five volt trigger signal is sent to the camera which triggers the MCP camera providing image amplification. These devices can be gated down to a five nanosecond exposure, so, depending on the light level, very accurate time resolution can be achieved.

Optical analysis can also be used to determine electron density, electron temperature, and ion temperature. Griem outlines a procedure for measuring hydrogen lines to determine the spatial distribution of electron density in a cylindrical discharge.[38] This technique uses the Abel Inversion for transforming the light into a radial intensity distribution. To isolate the specific hydrogen lines, a spectrometer with good resolving power is required. A Spex model 1269 1.26 Czerny-Turner spectrometer is utilized for just this purpose. A 1200 groove per millimeter grating allows for a resolving power approaching 300,000 for third order spectral lines. This translates into a theoretical resolution of better than 0.02 Angstroms at a wavelength of 4000 Angstroms. To facilitate this procedure, the SIT camera is affixed to the output of the spectrometer, and the spectral lines are recorded onto the image intensifier. The IBM series 9000 computer records the discretized image with software written by Kevin Rhoades of the High Voltage Research Laboratory at MIT. This

software enables the image to be used from the SIT camera to be viewed directly on the computer monitor. The user can then view, for example, a plot of the line intensity versus wavelength at a specific spatial location, or view the line intensity versus location at a specific wavelength. Another graduate student in the electric propulsion program at MIT, Dan Kilfoyle, modified this program to do a full Abel inversion of the data in a single keystroke. Thus deconvoluted, a spatial distribution of intensity versus wavelength is known, enabling calculation of electron density and other parameters. This device, when working, is a sophisticated tool that can be used for rapid characterization of the fluid-dynamic flow field in the MPD arcjet.

III.5.3: Coordination of the Data Acquisition System

The data acquisition system is triggered at a very specific point in the trigger sequence. A delay circuit, also designed by Steve Seiler at RDA, coordinates the discharge. Upon user command, the delay box fires the valves which provide mass flow to the arcjet. After equilibration of the mass flow rate, the bank and oscilloscopes are triggered. If the MCP camera is used, another delay is preset, and the camera is gated at the appropriate time in the arc discharge. The integrated cameras are open shutter and are not electronically triggered.

III.6: The MPD Arcjet

The purpose of the MPD arcjet experiment is to investigate real arcjet behavior in comparison to the behavior implied by the theory. The

major premises presented in the approximate theories are that the magnetic field distribution can be specified along the electrodes via judicious variation of interelectrode separation and that the onset phenomenon is related to an anode starvation mechanism. To test these hypotheses, three channels were designed. The first channel is a benchmark thruster and has a constant interelectrode separation. The second channel is flared downstream of a constant area section. This channel, the partially flared channel, was used to see if any variation in magnetic field distribution and thruster performance is accomplished from partial electrode flaring. The third channel was completely flared, both upstream and downstream of the throat. This channel is called the fully flared channel.

Several factors must be considered in the design of the arcjet. The interelectrode separation should conform to theory as closely as possible. It must also be easily diagnosed, machined, and assembled. The thruster must provide a discharge that does not interact strongly with the vacuum chamber, and it must be inexpensive. The most important requirement is that the thruster correlate with the theoretical design so that the anticipated trends can be verified. Since the theory is two-dimensional, a two-dimensional channel would be desirable. Such a geometry was considered, but discarded. It was believed that a two-dimensional channel comprised of continuous electrodes would have considerable three-dimensional structure due to surface imperfections, end effects, and other real gas effects. Therefore a cylindrical geometry with a large diameter anode and cathode was chosen to minimize the cylindrical contributions. A channel with an area variation similar to the geometry

derived in Chapter II was selected. This channel has a minimum interelectrode separation of about 1.9 cm and an exit interelectrode separation of about 4.0 cm. Because of the low entrance speed, the initial interelectrode separation predicted by the theory is very large—too large for any reasonable MPD channel used in this experiment. This mean radius of the channel is also important because, for a fixed operating current, a larger cathode radius will decrease the local current density making discharge initiation tenuous, thus leaving (as it turned out) an asymmetric discharge. Therefore, care must be taken so as not to get too obsessed with two-dimensionality.

A rudimentary analysis was done to check the interaction of the channel's plume with the vacuum tank. This analysis was a simple two-dimensional geometrical wave construction based on a $\gamma=2$ gas. The analysis showed that a thruster with an inner anode radius of about 7.25 cm has no significantly strong wall interactions. This is a conservative estimate since three-dimensional effects also tend to dissipate the pressure waves more rapidly at large radii. Therefore, the inner radius of the anode is kept less than 7.25 cm.

Experience has shown that copper and aluminum make good anode conductors. Aluminum was selected because of its greater availability, machinability, weight, and cost. The cathode, being approximately 5.5 cm. in radius, is quite large. Aluminum is the lightest material but is a very poor emmitter and therefore not a good selection. Therefore copper, stainless steel, and thoriated tungsten are the current materials of choice. Both stainless steel and tungsten are very difficult to machine,

and thoriated tungsten is prohibitively expensive, so copper is the material of choice for the cathode.

The electrode separation is controlled by varying the cathode radius in the flared geometries. The internal compound curves, that would be required on a flared anode, are too difficult to machine accurately. Therefore a cylindrical anode greatly simplifies the machining process and reduces the total cost of the arcjet. A single cylindrical anode may now be used for all these thrusters while three separate cathodes must be machined.

For reference, an assembly drawing of the arcjet is presented in figure III.10 as well as detailed blueprints which are found in Appendix 6.

The thruster is constructed in two main assemblies. It is based on a coaxial geometry, selected for its low inductance and ease in assembly. The anode assembly is comprised of the anode, an anode connector, an anode sleeve, and an anode flange. This assembly is completely constructed of aluminum. It is sealed to the vacuum tank by an O-ring to a Plexiglas insulator flange which is ultimately sealed to the vacuum tank end plate with another O-ring. The exterior of the anode assembly is exposed to vacuum and is anodized with a black 2 mil layer of Hardcote. Anodization is used to inhibit current conduction outside of the actual channel. The cathode assembly also contains the mass injection system and is fully removable for thruster servicing. The cathode assembly is constructed on an aluminum cathode sleeve. The cathode sleeve is connected to an aluminum cathode base which connects to the cathode. The cathode is

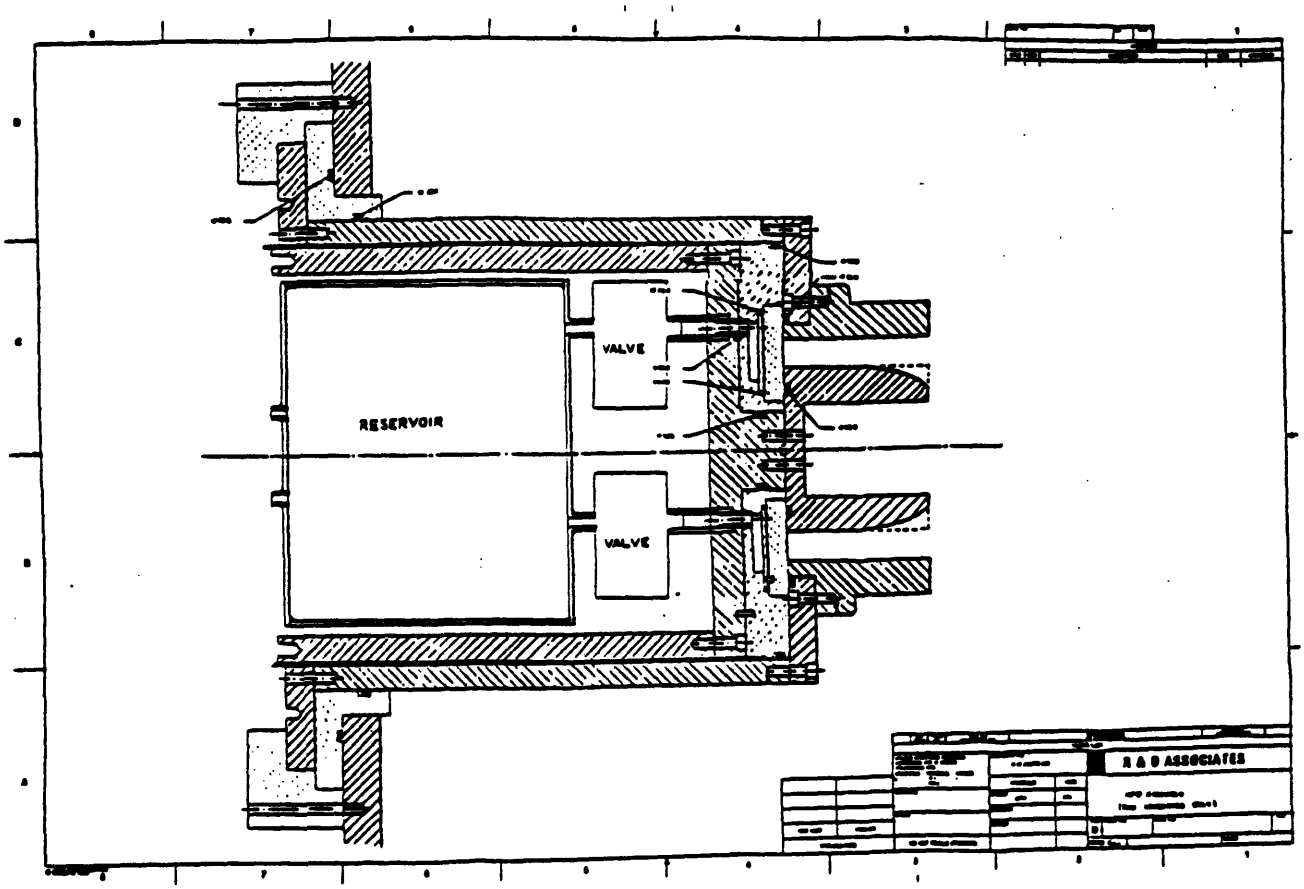

Figure III.10: MPD Arcjet Assembly Drawing

hollow in order to minimize its weight. Still, the cathodes weigh over twenty pounds, and the cathode-anode assembly almost sixty. An insulating cover is placed in the cathode bore to prevent current and plasma from flowing into the interior of the cathode. Proper alignment is accomplished by the snug fit and the forces of the vacuum.

Sandwiched between the cathode and cathode base is an insulator/mass injection subsystem. This subsystem centers around a Plexiglas injector plate into which the mass flows. The flow is metered by a Plexiglas choking plate which abutts a boron nitride insulator. This insulator is used both as insulation between the anode and cathode at the channel entrance and as a plate through which mass is injected into the channel. Boron nitride, although very expensive, is selected for its dielectric strength, thermal resistance, and machinability. To complete the electrical insulation, the anode and cathode assemblies are electrically isolated by a mylar plastic wrap taped to the exterior of the cathode assembly.

The entire system is kept vacuum tight by an O-ring located on the Plexiglas injector plate. The O-rings that press against the boron nitride insulator are not for sealing purposes; they are used to retain the insulator and choking plate.

Mass injection is accomplished by another subassembly located within the cathode assembly. A gas reservoir, located inside the cathode sleeve, is supplied by a large gas bottle. Six solenoid valves join the reservoir to the cathode assembly. Six nozzles make a vacuum seal and provide a path for the gas to a pre-expansion plenum, located upstream of the boron

nitride insulator and Plexiglas choking plate, in the Plexiglas injector plate. Six valves provide for a fast gas pulse transient enabling steady-state cold gas flow to be established in about 10 ms prior to arc ignition. The valves are opened in less than 100 μs by a 3000 V pulse from a valve drive circuit designed by Dr. Steve Seiler at RDA. This entire subassembly is kept floating with respect to the arcjet and the vacuum system. The valve driver is optically triggered to further isolate the valve drive system.

The power is connected to the arcjet via a "squirrel cage" assembly. This structure relies on coaxial cables to connect the anode and cathode to the L-C ladder network. The external braid is connected to the anode assembly through a cage-like construction, while the center conductor goes directly to the cathode assembly. Swagelock fittings are used to allow for repeated disassembly and reassembly.

Chapter IV: The Experimental Results

IV.1: Introduction

The results from the diagnoses of the three MPD arcjet channels will be presented along with an accompanying analysis detailing the physics of internal electrodynamic and fluid-dynamic interactions. Arcjet behavior, as experimentally demonstrated, will be compared to the behavior predicted by the simplified model presented in Chapter II. The implications of the analysis and experiment will be discussed as well the relative merit of the overall work.

For the coaxial geometries with the characteristic dimensions found in this experiment, discharge symmetry did not occur reproducibly until the thruster was operated above 40 kA for an argon flow rate of 4 g/s. Photographic analysis of the constant area channel shows that at the lower current levels, the discharge tends to concentrate in a sector of the channel. Unlike an instability, the discharge just tends to sit at a specific region of the channel. As the current is increased, that discharge grows until it fills the channel and symmetry is established. This seems to indicate that there is a minimum current density required for arc discharge symmetry. This phenomenon is most probably associated with cathode emission processes rather than anode processes since the anode can passively absorb electrons at these current levels relatively easily. It may also be the result of the inability of thermal conduction to heat the entire plasma so that it could conduct the current uniformly.

Assuming the discharge becomes symmetrical at 40 kA, this implies (in the case of the constant area cathode) that the minimum current density for a symmetrical discharge is about 450 A/cm^2 at the cathode surface.

Probing the discharge made it more difficult to achieve a symmetric discharge. The presence of a probe locally stagnates the flow and causes a reduction in the local back emf. The local plasma becomes primarily resistive and current flows more readily in this region. This problem is exacerbated when the probes are placed near the electrodes, especially near the anode. This phenomenon never disappeared when the probes were placed adjacent to the anode. Anode erosion was noted whenever the probes were placed adjacent to the anode. At high current levels (> 50 kA) the presence of a probe near the anode did not seem to disturb the distribution of current throughout the channel. This was tested by placing a magnetic field test probe in the middle of the constant area channel at various axial and radial locations. The test probe data showed that above 50 kA there was almost no discernable difference in the probe signal when an additional probe was placed adjacent to the anode. It was believed that these results might be higher in the flared channel because of the larger plasma volume. Therefore the three channels were operated at 60 kA with an approximate argon flow rate of 4 g/s. This is 14 kA above the design current level. Unfortunately it was required in order to guarantee a symmetrical discharge.

The large radius coaxial geometry, selected to minimize cylindrical effects and approach two-dimensionality, was assumed to have azimuthal discharge symmetry. For verification, photographs were taken to visually

inspect the discharge, and further probe measurements were used to verify electrodynamic symmetry. Both open shutter and microchannel plate photographs were used to observe both the time integrated and transient discharge behavior.

Initially, asymmetric operation was noted, but after several shots, the electrodes became sufficiently conditioned so that the discharge appears to be symmetrical at the 60 kA operating point. This is visually evidenced in the integrated photograph (figure IV.1) and in the microchannel plate photograph taken with a fifty nanosecond exposure at 300 μs into the discharge (figure IV.2). Magnetic field and floating potential measurements further indicate discharge symmetry at the 60 kA operating point.

Once symmetry is established, and the discharge voltage has settled to a repeatable value for a given input current and mass flow rate, thruster diagnosis can begin. This process involves measuring both the terminal characteristics and the internal distributions of current and floating potential in the arcjet at a predetermined quasi-steady portion of the discharge. The determination of quasi-steady operation is outlined in Appendix 7 along with a detailed discussion of the measurement technique used in evaluating the oscillogram data.

Comparison of the thrusters can be done on the basis of overall performance measurments and on the basis of differences in the internal distributions of the various parameters. Overall performance is most easily measured via thrust data and calculations of specific impulse and efficiency. In this experiment, thrust is not measured and can only be

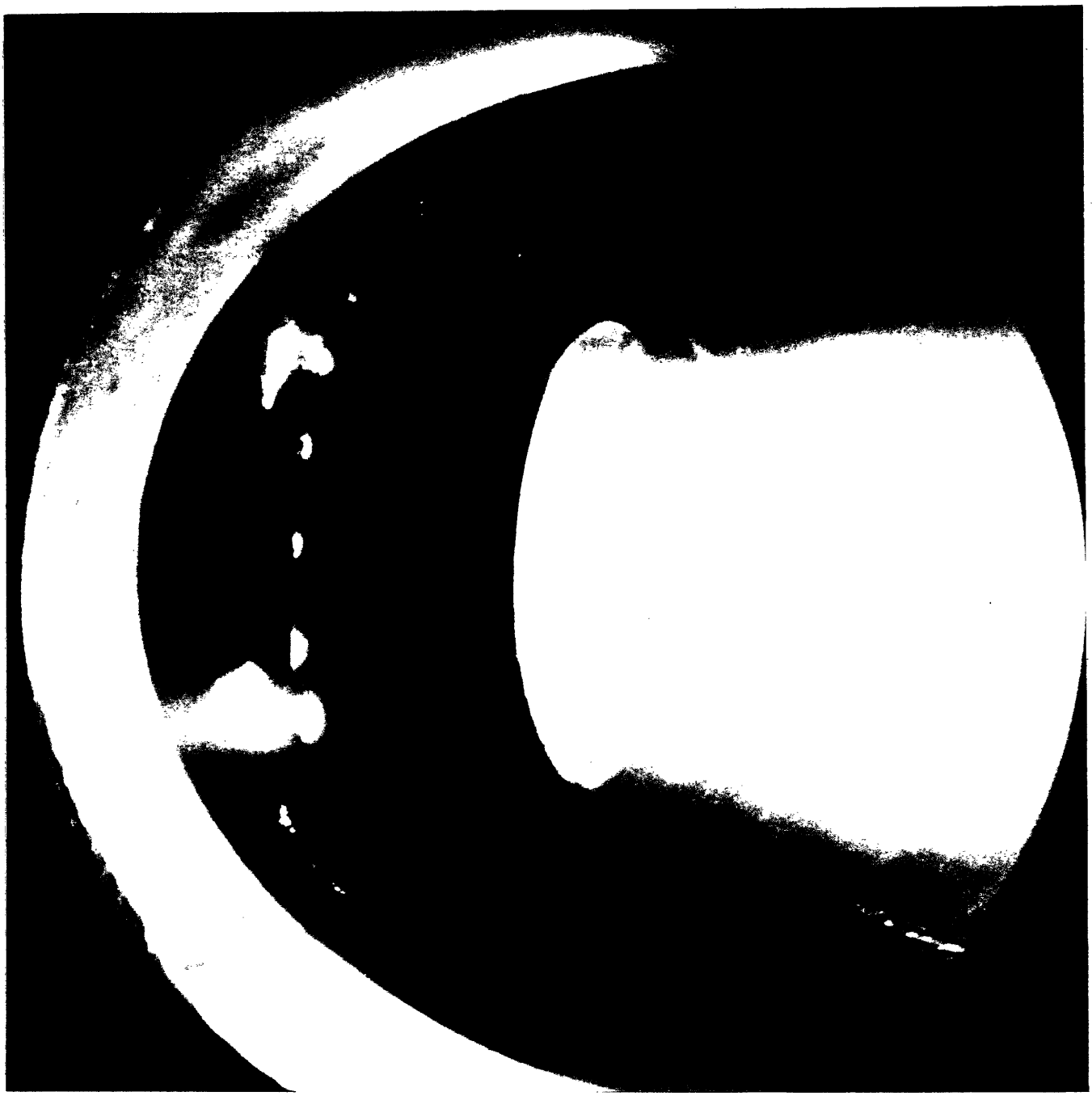

Figure IV.1: Open Shutter Photograph of the MPD Arcjet

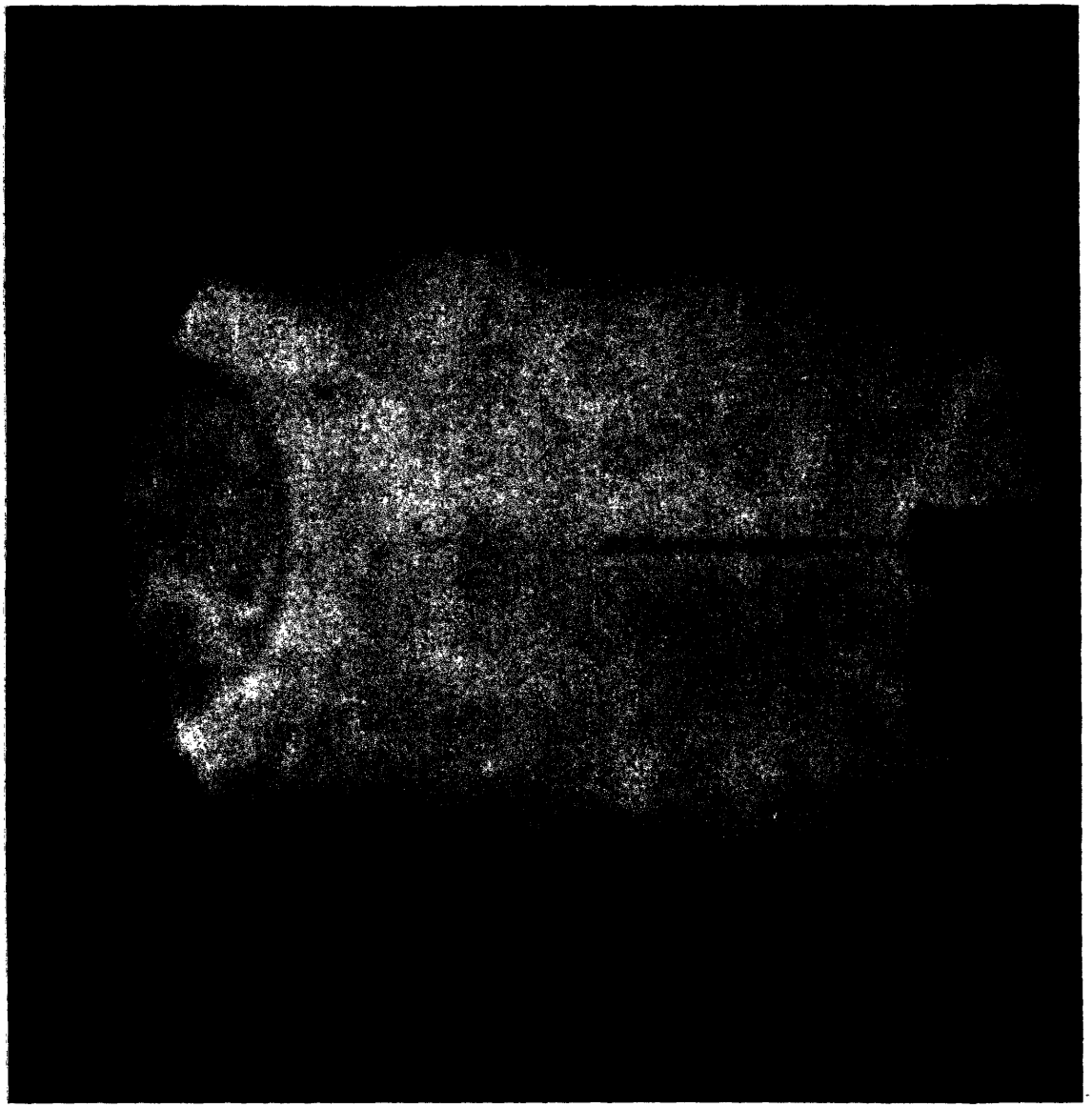

Figure IV.2: Microchannel Plate Photograph of the MPD Discharge

inferred from detailed analyis of the few parameters under examination. Therefore discussion will focus primarily on the analysis of the internal distributions of field and floating potential, terminal voltage, photographic data, and a-posteriori thruster examination. From this pool of data, several topics will be addressed. These topics include the effect of interelectrode separation on the discharge physics, operation of the MPD arcjet relative to onset, the origin of the terminal voltage in the MPD arcjet, and a discussion of the phenomenology of the onset condition.

IV.2: Presentation of Data

The voltage-current relationship characterizes the "load line" which directly reflects the MPD arcjet's impedance. The three channels were operated through a wide current range to determine each thruster's load line. The combined results for the three channels at an argon mass flow rate of 4 g/s are presented in figure IV.3. Cursory inspection shows that the voltage has a monotonically increasing variation which gets steeper with current, and that the channels all operate at similar voltage levels. The two flared channels are, within experimental error, identical, while the channel with the constant electrode separation consistently operates a lower voltage except for very low currents. The similarity between the two flared channels is to be expected since there is only a small geometric difference between the two devices.

Internal measurements of current and field were also taken during the quasi-steady portion of the discharge. The plots of the current density

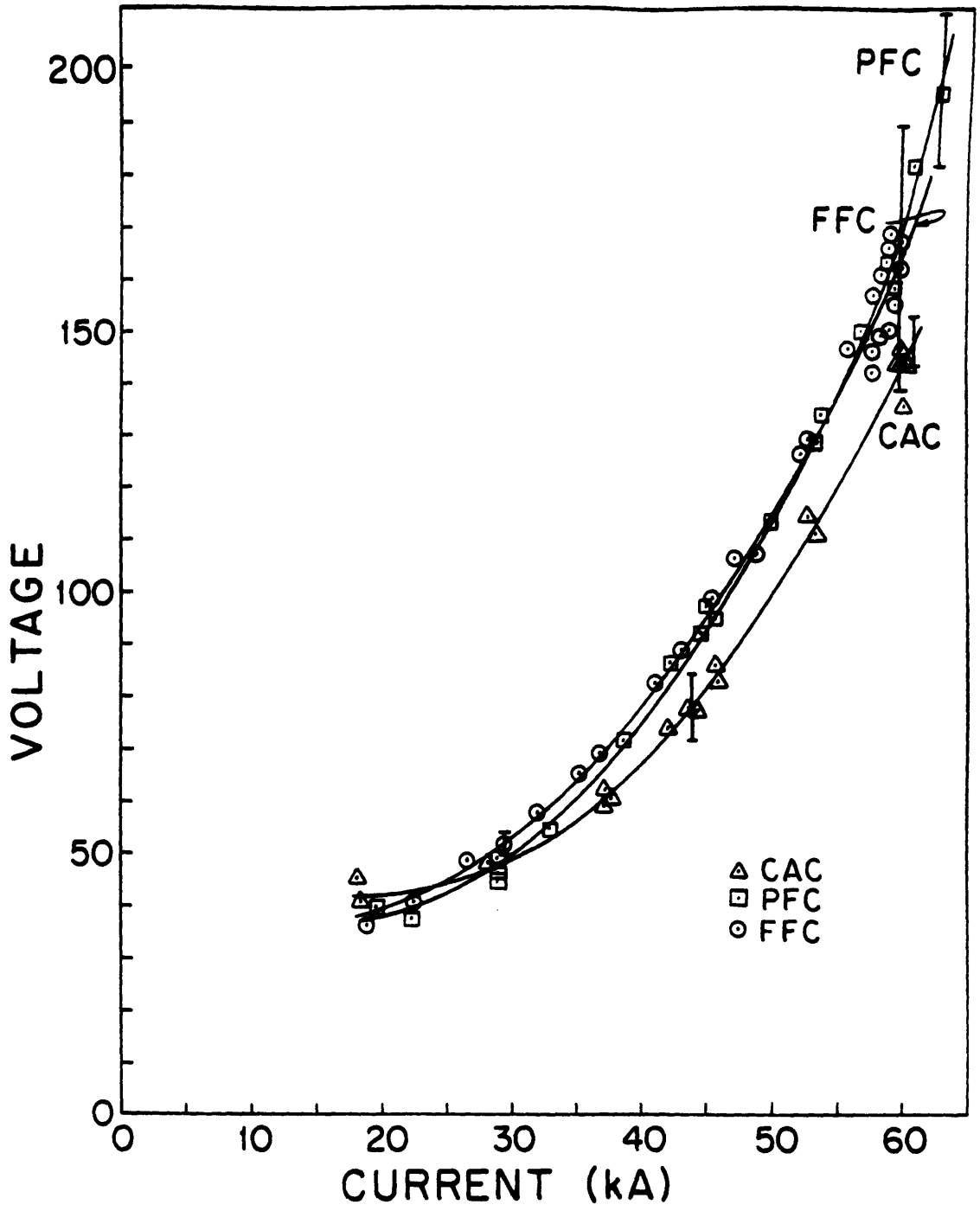

Figure IV.3: Thruster Voltage Versus Total Current for an Argon Mass Flow Rate of 4 g/s

and floating potential contours at an operating point of 60 kA for each channel are found in figures IV.4 through IV.6.

IV.3: The Effects of Variation of Interelectrode Separation

Axial variation of the thruster electrodes produces many expected and unexpected effects. One of the more interesting and puzzling phenomena associated with geometric channel variation is its effect on the transient voltage pulse. In the channel with a constant interelectrode separation, the discharge begins with a high voltage transient causing the plasma to break down to a voltage about half the quasi-steady value. The fully flared channel starts with the high voltage spike, but its voltage drops to a very low value, and its rise to the quasi-steady value follows the current pulse. The partially flared channel behaves in a manner somewhat in between the two other extremes. This behavior is illustrated in figure IV.7 which contains examples of the voltage traces from the three channels. The voltage trace for the fully flared channel is quite different from the other two in that it exhibits large amplitude voltage spikes, or oscillations. These oscillations are discussed in Chapter VI and are theorized to be caused by the development of concentrated anode arcs.

The approximate model introduced in Chapter II predicts that variation of the interelectrode separation should provide control of the axial current density concentrations throughout the arcjet channel. This is desirable due to the bifurcated (presence of a point of inflection) current distributions associated with constant area high magnetic

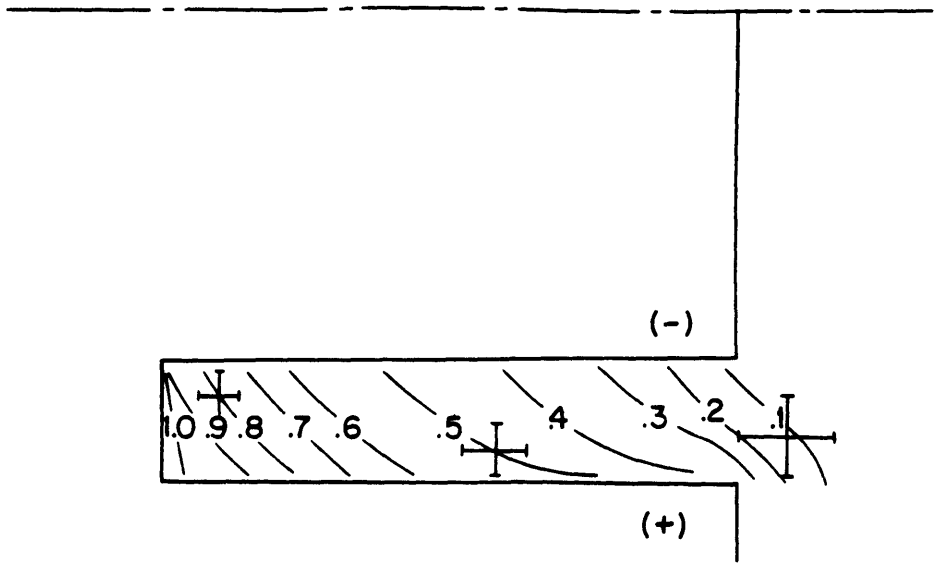

a) Enclosed current

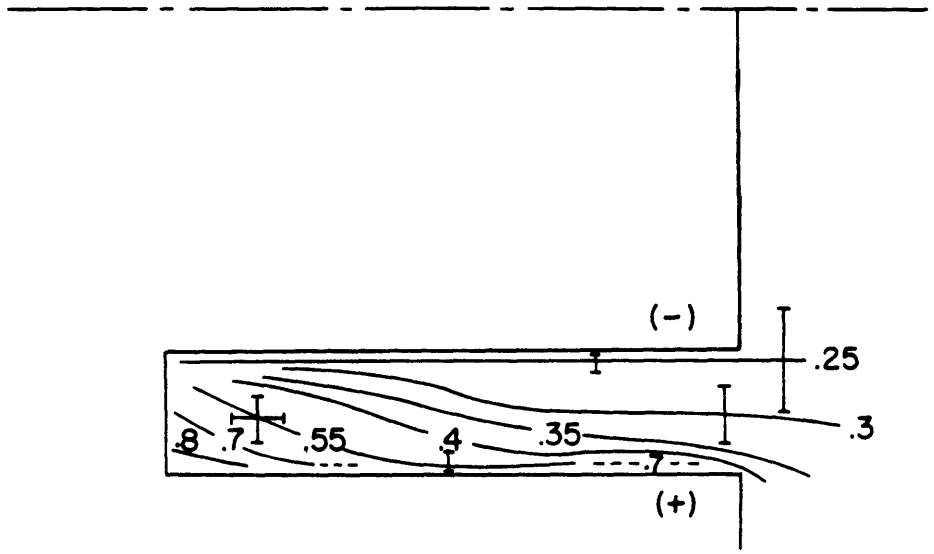

b) Floating potential

Figure IV.4: Enclosed Current and Floating Potential in the Constant Area Channel at 60 kA for an Argon Mass Flow Rate of 4 g/s

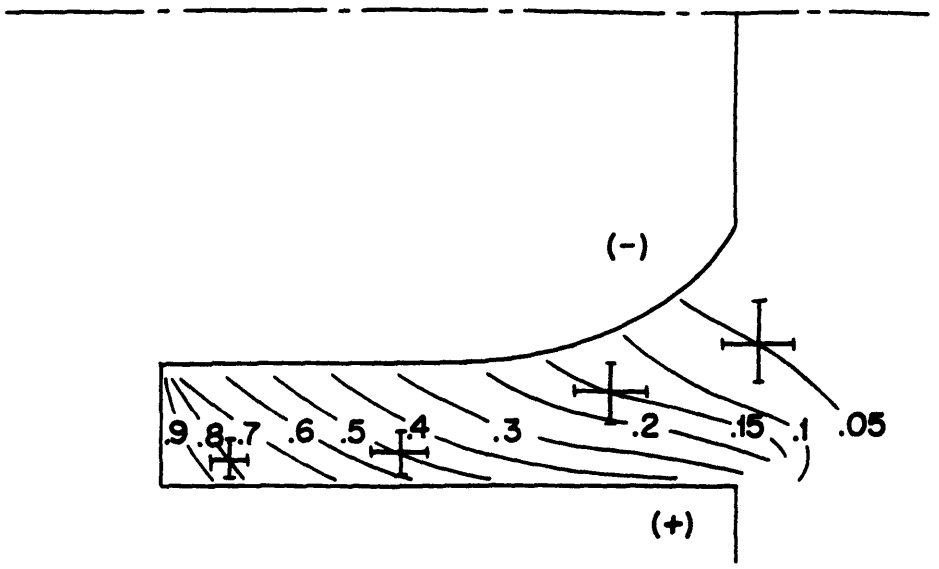

a) Enclosed current

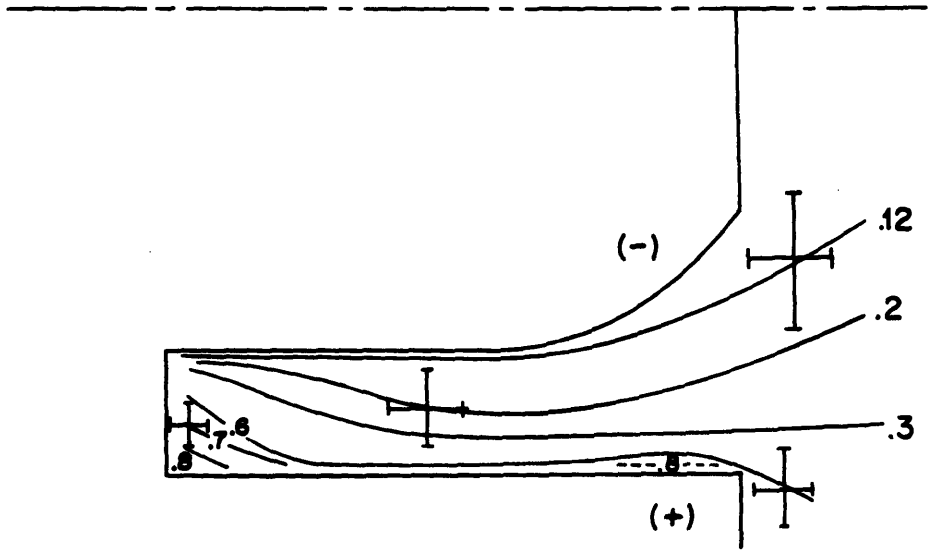

b) Floating potential

Figure IV.5: Enclosed Current and Floating Potential in the Partially Flared Channel at 60 kA for an Argon Mass Flow Rate of 4 g/s

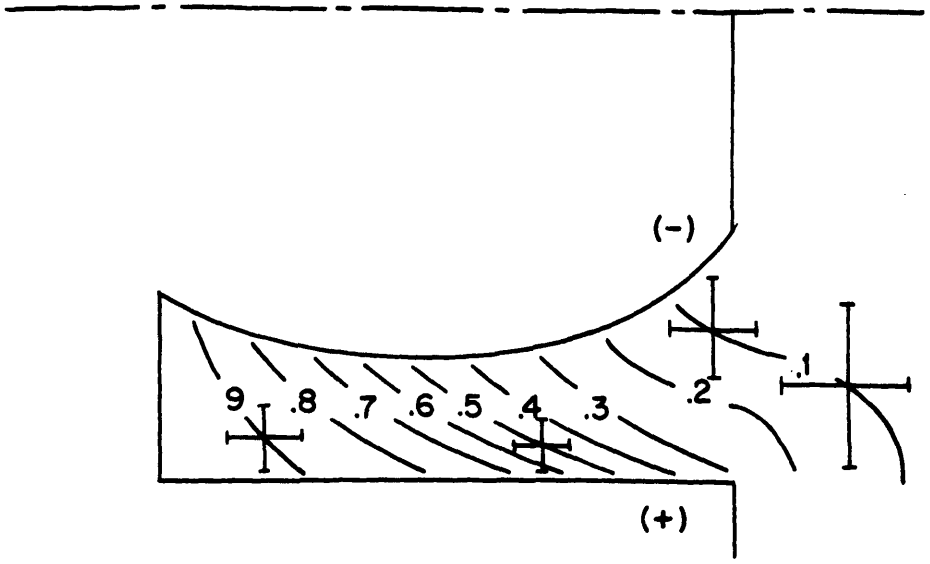

a) Enclosed current

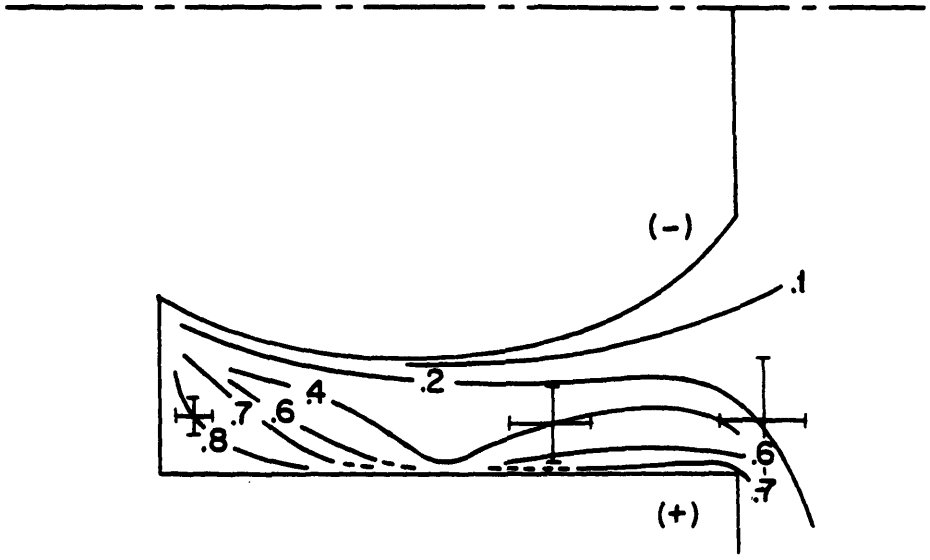

b) Floating potential

Figure IV.6: Enclosed Current and Floating Potential in the Fully Flared Channel at 60 kA for an Argon Mass Flow Rate of 4 g/s

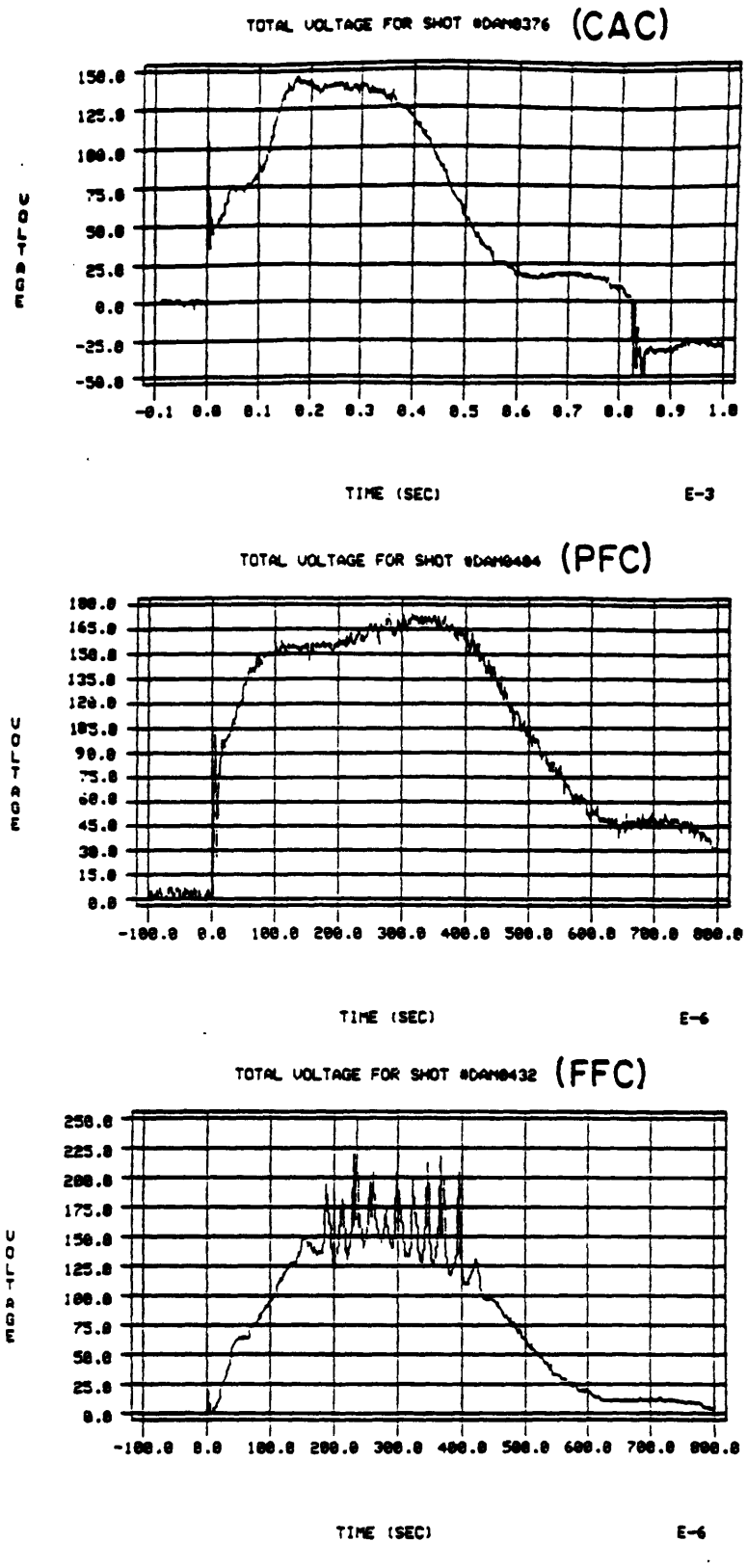

Figure IV.7: **Voltage Characteristics for the Three Different Geometries for an Argon Mass Flow Rate of 4 g/s** and a Current Level of 60 kA

Reynolds' number flows which exhibit current concentrations at both the inlet and exit. The higher the magnetic Reynolds' number, the stronger the concentrations. These regions have thicknesses, and therefore strengths, commensurate with a distance that makes the local magnetic Reynolds' number unity.[37] Higher magnetic Reynolds' number flows should have a higher incidence of erosion due to the increased local dissipation. These regions of high local dissipation, which get thinner at high current levels, decrease the efficiency of the channel by adding excess electrothermal energy into the exhaust which is never fully recovered.[27] It is therefore highly desirable to decrease these concentrations in the current density distribution. Figures IV.4 to IV.6 show that there is some difference in the current distribution due to increased interelectrode separation, however more detailed analysis is necessary to determine the magnitude of the change and its correspondence to theory.

The difference in current density distributions is more clearly noted in figure IV.8 in a plot of the local current density along the projected surface of each cathode. This data was calculated by dividing the fraction of the total current entering a portion of the cathode and dividing that amount by the area of that portion. The abscissa in this figure represents the cathode surface position only in the case of the cylindrical cathode. For the flared cathodes, it reflects the position along the centerline of the thruster, or the projection of a point on the cathode surface onto the thruster's centerline.

Several interesting features can be noted in this figure. The most notable detail is the lack of concentrated current at the exits of the

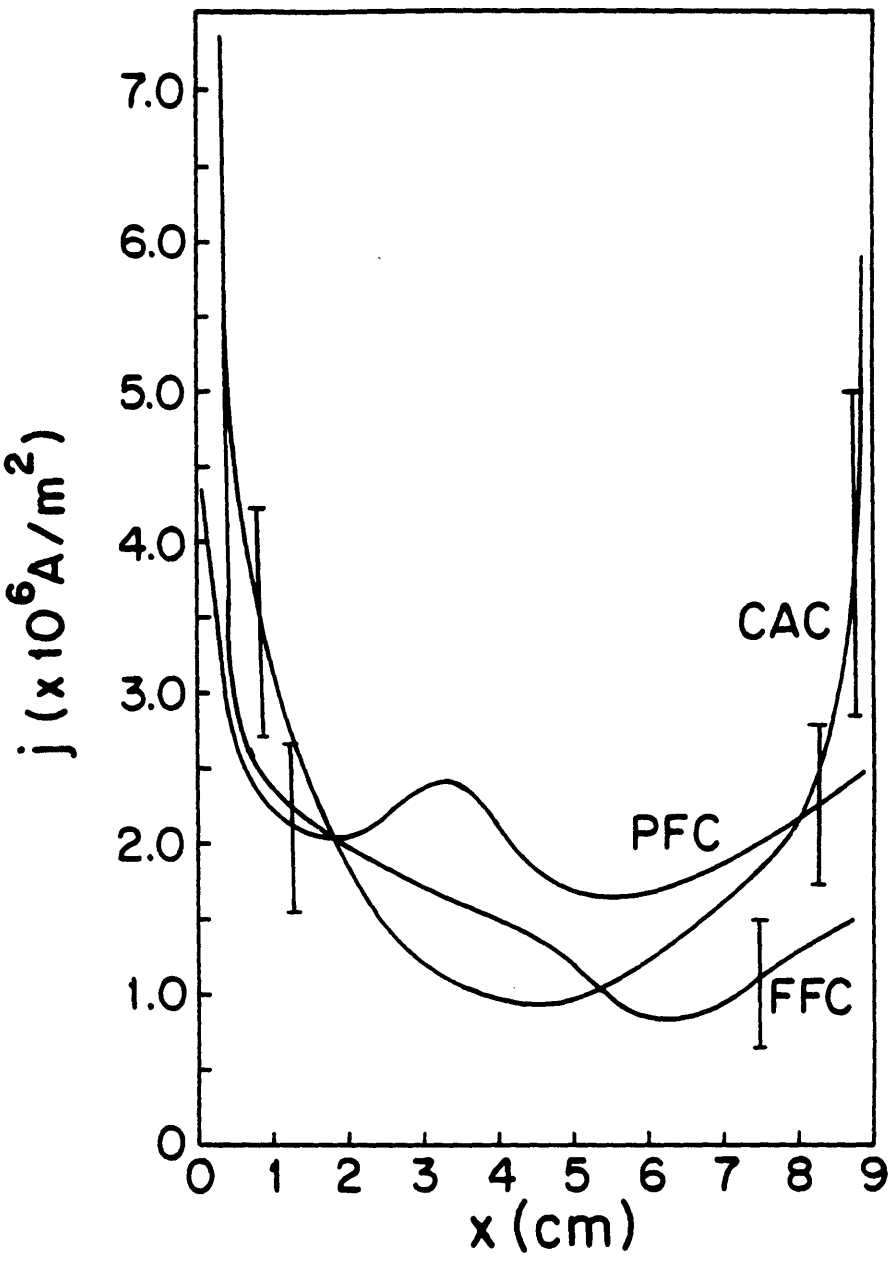

Figure IV.8: Current Density Distribution on Each Cathode at 60 kA for an Argon Mass Flow Rate of 4 g/s

flared geometries in comparison to the constant channel geometry. In this channel, the current increase is due to the anticipated drop in back emf without any commensurate increase in electrode separation, so that the local electric field is maintained at a high value. The current density distributions for the flared geometries also increase towards the exits. These increases are due partially to the cylindrical effects which provide for increased magnetic field and decreased cathode surface area with decreasing radius. If the nozzle is also underexpanded, excess current is expected to attach at the exits. In the two-dimensional theories presented in Chapter II and Appendix 2, cylindrical effects were neglected. In a real channel these effects are present and may be strong, especially where there are large radial variations due to electrode separation.

In the partially flared channel, only the downstream portion of the cathode is flared. The flared portion takes less total current than in the constant area channel, so the remaining cathode must have an elevated current density distribution in order to pass the same specified current. The entrance, effectively a constant area channel, also has an initial current concentration due to the low back emf. This initial current concentration is partially mitigated by increasing the interelectrode separation at the entrance in the fully flared channel. The reduction of the cathode radius at the entrance acts to increase the local current density by increasing the local magnetic field and decreasing the cathode surface area. The cylindrical effects thus tend to oppose the effects of the decrease in the local electric field on the current density. However,

the local electric field, as opposed to cylindrical effects, more strongly affects the current density distribution in this coaxial geometry. In the fully flared channel, both the entrance and exit concentrations have been decreased so there is a required coincident increase in the concentration of current near the central portion of the channel in order to pass the specified current.

The strong entrance and exit current concentrations are also evidenced by the erosion patterns on the cathodes' surfaces shown in the photographs presented in figures IV.9 through IV.11. Examination of the cathodes shows erosion, primarily in the entrance region of each channel. In fact, after less than 100 discharges, copper from the cathode is seen to be deposited onto the boron nitride injector plate.

On the constant area cathode, eroded bands of clean copper, about a half a centimeter wide, are seen at both the entrance and the exit. The band at the entrance looks like freshly machined copper, indicative of strong and even erosion, while the band at the exit is well defined but not quite as shiny, possibly indicating a weaker current concentration. The entrance band is composed largely of semicircular clean regions directly downstream from the mass injection ports on the backplate. Additional clean spots are noted about one half to one centimeter further downstream, directly in line with other mass injection holes in the boron nitride insulator. The remaining cathode shows strong evidence of fine line arc structures extending from the cathode downstream end almost to the cathode root. These fine structures are branch-like and appear to branch in an upstream direction, implying retrograde motion or multiple

Figure IV.9: Photograph of the Constant Area Cathode

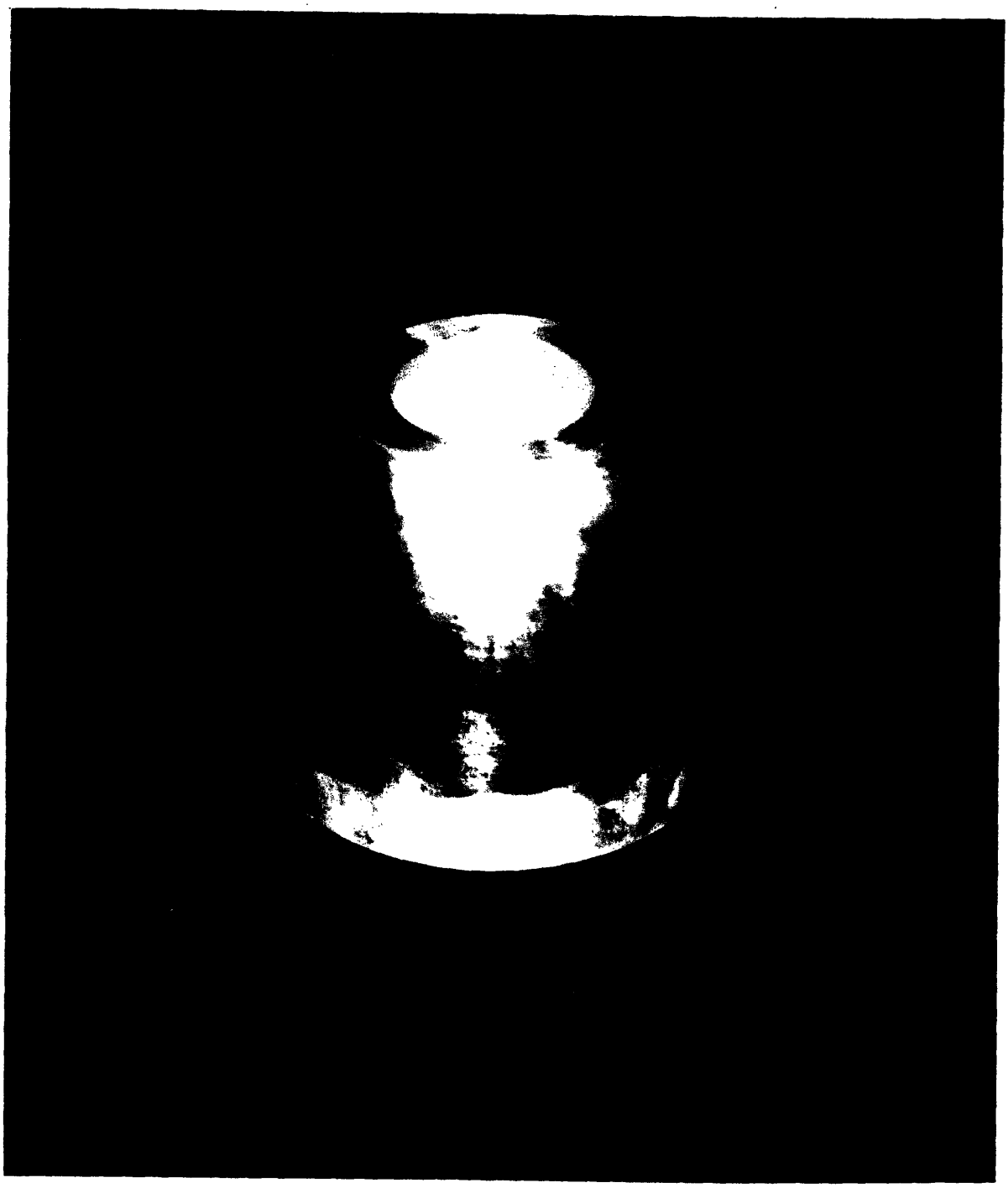

Figure IV.10: Photograph of the Partially Flared Cathode

Figure IV.11: Photograph of the Fully Flared Cathode

spots gathering into a single arc spot. This evidence is, at best, circumstantial. All of it is based on electrode examination after the tests were completed, so there is no way to determine whether these arcs are phenomena associated with transient or steady-state operation.

In the partially flared channel, the clean band at the exit is absent, but there is a wide clean band at the cathode base at least 0.75 cm to 1.3 cm in extent. Unlike that found on the constant diameter cathode, this band has a very poorly defined downstream edge. This may be due to the increased total current in the constant area section due to the decreased amount of current on the flared section from the lowered local electric field. The fine line structures previously found on the cylindrical cathode are now completely absent.

The erosion pattern on the fully flared channel shows only a small amount of wear at the entrance region. On this cathode, a small clean band less than two millimeters in width is evidenced. The remaining cathode shows the same arc-like structures seen on the constant radius cathode.

An interesting observation is that these eroded bands have a thickness of the same order as the strong entrance current concentrations shown in figure IV.8. In these channels, the magnetic probe data have a significant associated error so that the contours that appear in figures IV.4 through IV.6 are also subject to significant error, especially in the region near the insulator where probe resolution is only about two to four millimeters, and near the exit where the signal to noise ratio is drastically reduced. Regardless of this, it is clear that the areas of

intense erosion correspond to the regions of high current concentration, and by decreasing the local electric field, such concentrations can be controlled.

The increase in the current density in the upstream portion of the partially flared channel coupled with the larger axial component of current probably leads to a higher local ionization fraction than in the fully flared channel. The approximate Ohmic dissipation based on the square of the local current density, is shown in figure IV.12 for various regions of the upstream portions of each channel. This quantity was calculated based on an assumed value for the conductivity. This approximation neglects convection and voltage drop contributions to the local dissipation, hence the downstream portion, where convection is strongest and anode voltage drops become large, is not shown If more dissipation is present in a given channel, its temperature is most probably elevated and the conductivity and ionization fraction are probably increased. This would result in a decrease in the local dissipation so the actual comparison shown in figure IV.12 is somewhat exaggerated.

The thickness of this dissipation layer in the constant area channel appears to be about two centimeters-commensurate with the thickness of the clean band noted on the partially flared cathode's surface. Evidence of the higher dissipation may be seen in figures IV.13 which shows the transverse variation of electron temperature at the exit plane of each channel.

Figure IV.13 represents preliminary data taken and analyzed by Daniel

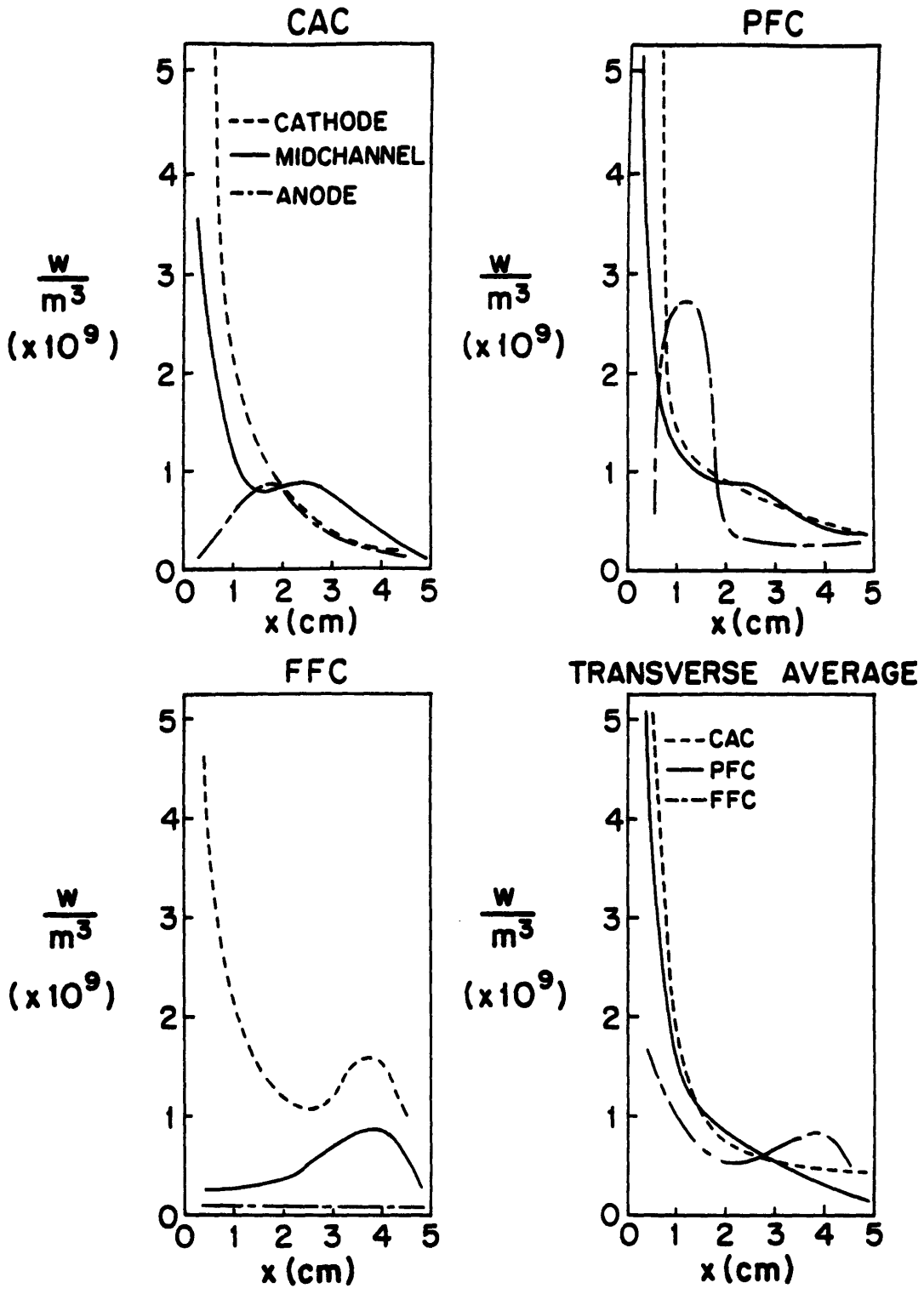

Figure IV.12: Approximate Dissipation in the Upstream Section of Each Channel at 60 kA for an Argon Mass Flow Rate of 4 g/s

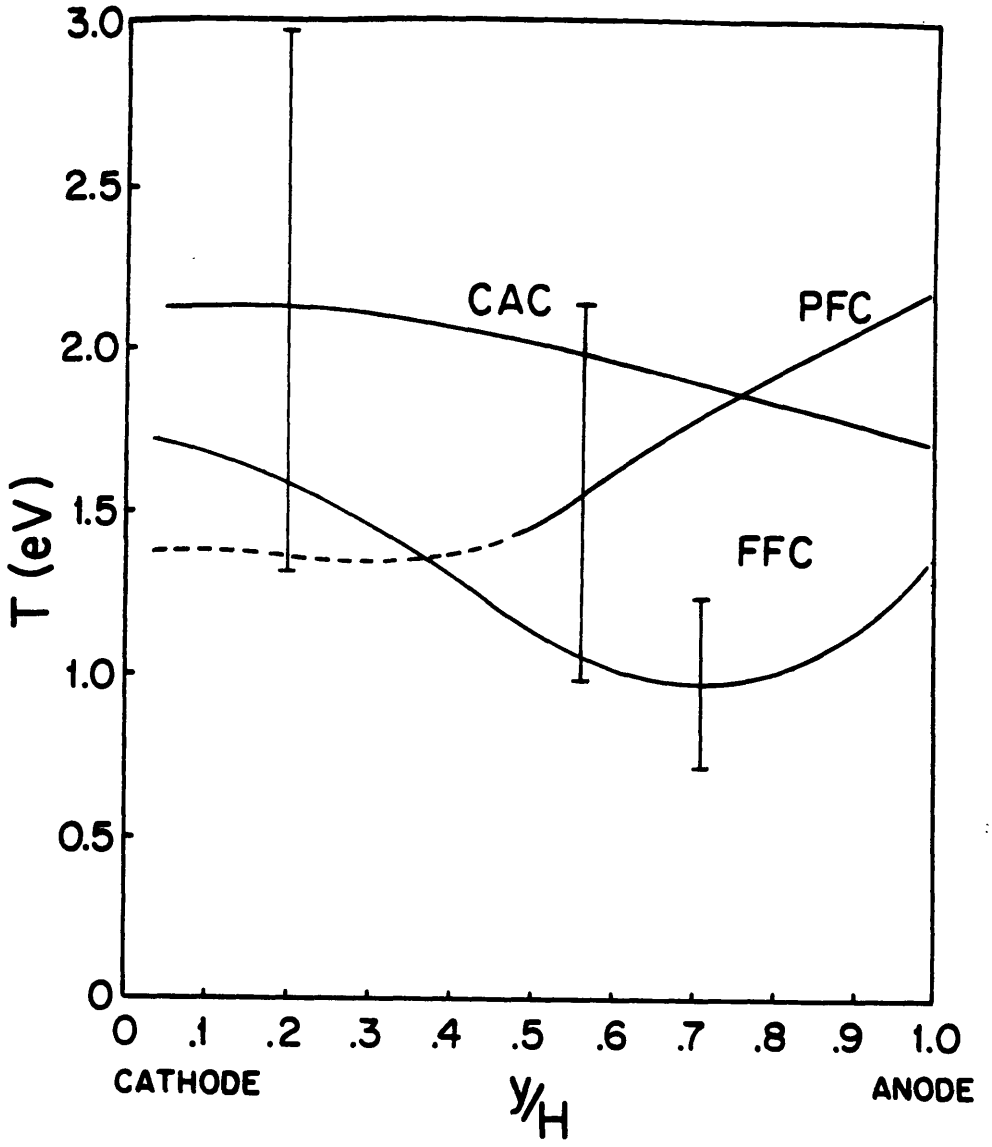

Figure IV.13: Transverse Variation of Electron Temperature at the Thruster Exit Plane at 60 kA for an Argon Mass Flow Rate of 4 g/s

Kilfoyle, a Masters degree candidate here at M.I.T. He used the SIT camera to photograph the lineshapes of three argon lines, each of which represents an electron transition at a high level in the argon ion. By selecting the proper lines (with upper levels within a few electron volts of the continuum), the bound electrons may be assumed to be equilibrated with the free electrons allowing a Boltzmann plot to be utilized in the calculation of the electron temperature. In the Boltzmann plot, the relative intensities of the lines are related to the electron temperature in a plasma in local thermodynamic equilibrium. For the exact technique, refer to Kilfoyle's upcoming Masters thesis. The data presented in figure IV.13 are preliminary, but suggest that the exhaust electron temperature is highest in the constant area channel. Some other interesting results are also suggested by these data.

In the constant area channel, the electron temperature appears to be approximately constant at about two electron volts. The slight increase at the cathode may be partially due to the increased dissipation from cylindrical effects, as well as by the contribution from the large cathode fall. The partially flared geometry shows a marked increase in temperature toward the cathode. This requires further explanation. The electron temperature near the cathode for the partially flared channel is represented by a dotted line because the raw data indicates a significant departure from equilibrium which causes elevated electron temperatures near the cathode. Without further analysis of the discharge, this behavior cannot be explained.

It is difficult to justify the application of these results taken at

the thrusters' exits to describe global arcjet behavior since the local temperature and ionization fraction arise through local nonequilibrium processes including ionization, recombination, thermal and radiative transport, etc... Until more precise local data is available, they can only be used as indicators rather than as global discharge parameters.

In conclusion, it has been shown that the variation of interelectrode separation does lead to a redistribution of current in the channel. Large current concentrations, noted in the constant area channels, have been reduced by increasing the local electrode separation. The experimental results have also shown that the variation of the interelectrode separation also modifies the distribution of dissipation and the discharge temperature. The experiment has also shown that cylindrical effects are not insignificant and act to oppose (in this coaxial geometry) the decrease in current density attributed to the increase in electrode separation.

The data from this experiment also show that anode starvation mechanisms are also present. This result is discussed in the following section.

IV.4: Anode Depletion in the Experimental MPD Channels

Figures IV.4 to IV.6 imply that all of the channels are operating in a mode where the anode is being depleted of charge carriers. The large anode region voltage drops coupled with the large axial deflection of current (implying a significant Hall parameter) suggest the presence of a strong starvation mechanism. This conclusion is supported by two

additional figures.

Figure IV.14 is a plot of the transverse variation of the electron density at the exit plane of the fully flared channel. This data was also taken by Dan Kilfoyle, a Masters degree candidate at MIT, and is calculated from the analysis of the cylindrical variation of the broadened $H\alpha$ line. This line, which is predominantly Stark broadened, is particularly sensitive to the variation in electron density. Figure IV.14 shows that the electron density decreases dramatically towards the anode region. The measured magnitude of the electron density should be considered as an upper limit because the line width is actually broadened by Stark and Doppler mechanisms, and the calculation of the electron density is based on a convolution considering only Stark broadening.

The growth of potential in the anode region is further evidenced in figure IV.15 which shows the variation of this voltage at an axial distance of 4.3 cm. downstream in the fully flared channel. This graph clearly shows the increasing nature of the voltage as current is increased. This axial location was chosen since it appears to be the region where the anode voltage drop is at a maximum in the fully flared channel. From this figure, significant voltage growth is seen to occur in the neighborhood of 30 to 40 kA, stabilizing, and even decreasing at about 60 kA. The large error bars at 60 kA show that, depending on the time, the anode fall is either very large, or very small. This voltage stabilization may be indicative of electrode saturation (the inability to continue to attract electrons in a diffuse arc) and the initiation of concentrated arcing required to conduct the specified current. Evidence

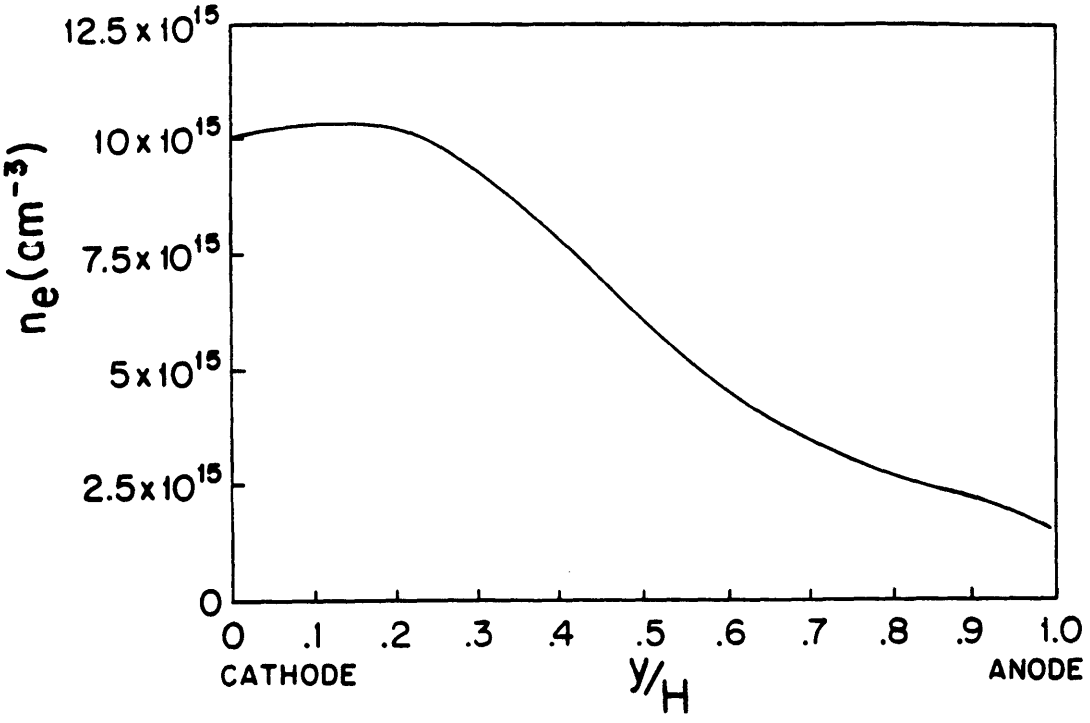

Figure IV.14: Transverse Variation of the Electron Density at the Exit of the Fully Flared Channel at 60 kA for an Argon Mass Flow Rate of 4 g/s

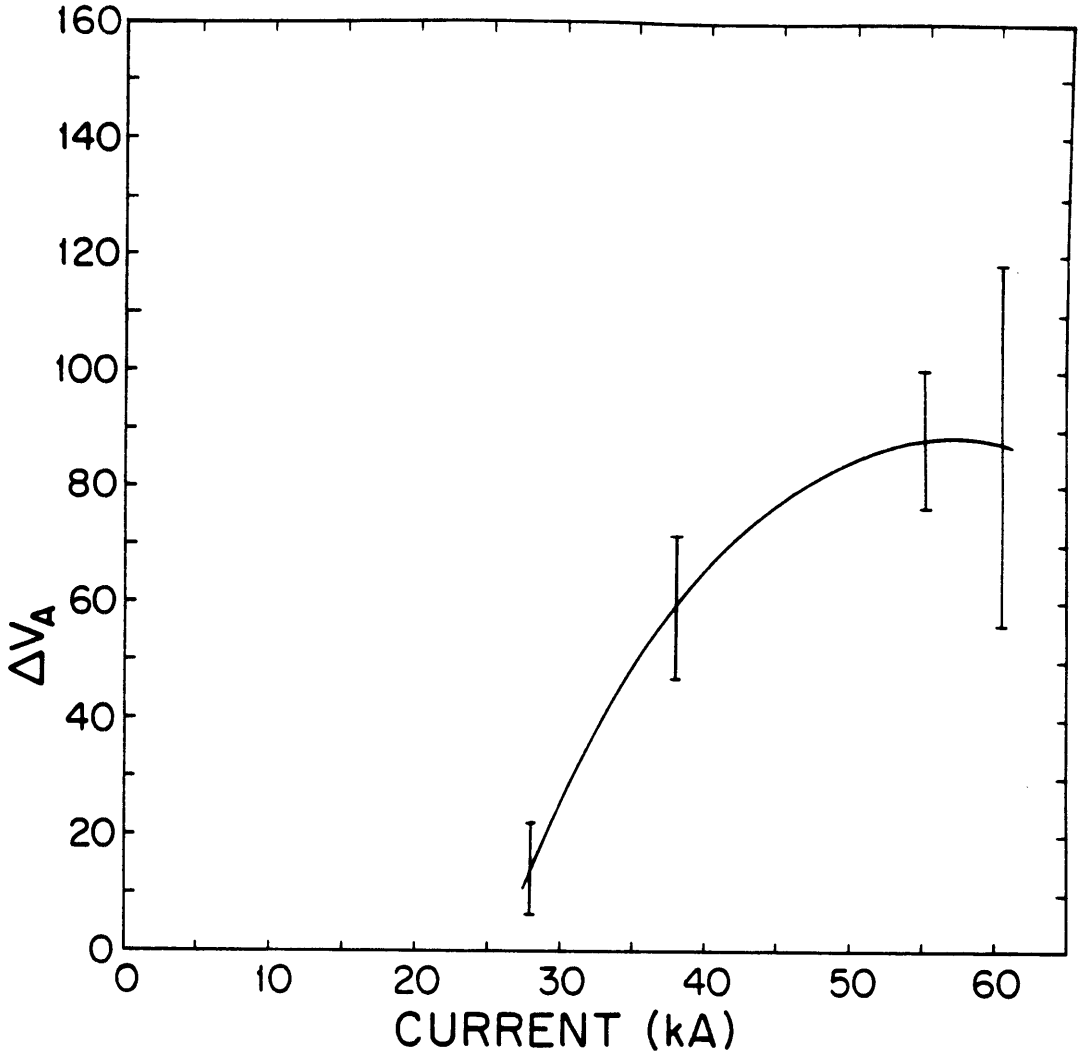

Figure IV.15: Variation of the Voltage Drop from the Anode to a Point Two Millimeters from the Anode as a Function of Thruster Current in the Fully Flared Channel for an Argon Mass Flow Rate of 4 g/s

of severe anode arcing is seen in a physical inspection of the arcjet anode and is shown in a photograph after about sixty discharges (figure IV.16). Of course, there is no temporal resolution in this photograph, so it is possible that these arcs are manifestations of some other phenomenon associated with MPD arcjet operation, although such arc damage is not seen until high current operation.

Based on figures IV.14 to IV.16 it is probably safe to say that all three channels are operating beyond anode onset in the sense of a depleted anode. For the fully flared channel, depletion appears to occur at about 30 to 40 kA for an argon mass flow rate of 4 g/s, and arcing appears to occur at about 59 kA under the same mass flow conditions.

IV.5: Comparison of the Experimental to the Theoretical Results

It would be a useful exercise to compare the measured results with those predicted from the theory. This is not easily done in this experiment. It has been shown that the arcjets are operating in a severely starved mode. Figure IV.14 shows that the density in the anode region is only a small fraction of the average density. For the perturbation model (such as presented in Chapter II) to demonstrate such behavior, the perturbations have to be of the same order as the unperturbed values thus bringing model validity into question. To put it differently, the value of the Hall parameter needs to be small; but in the experiment, Hall parameters of one to three are readily found. In fact the model was pushed to this limit and predicted that anode onset was initiated at about 43 kA. The experiment appears to corroborate this

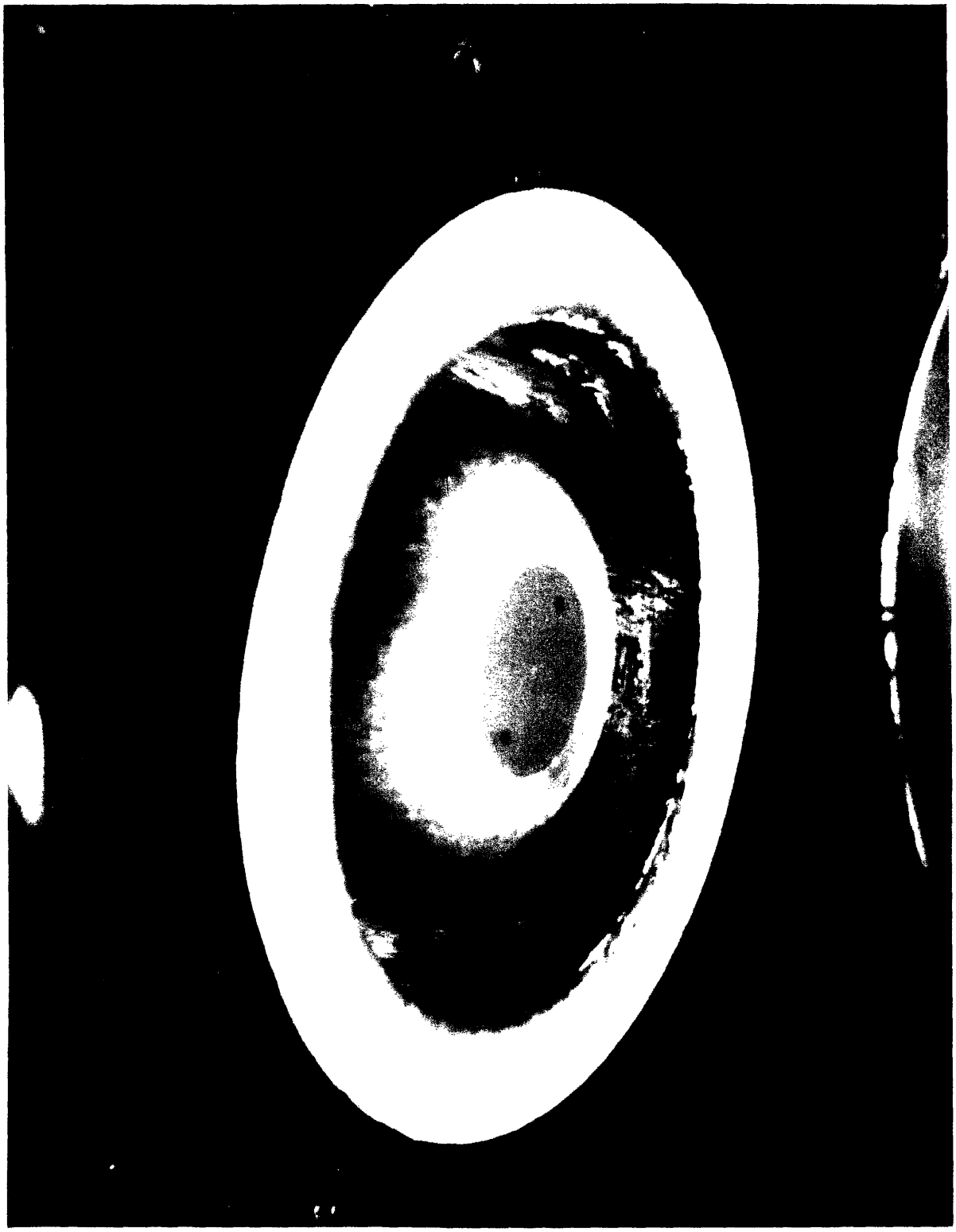

Figure IV.16: Photograph of the MPD Arcjet After Many Discharges

estimate, however the channels will not allow the discharges to be diagnosed accurately with probes below about 45 kA in a very reproducible manner.

At lower currents, many shots can be required to get meaningful data representative of symmetrical behavior. The addition of a probe into the discharge further enhances the asymmetric behavior of the discharge. Because of this, it was necessary to operate the channel at higher current levels in order to probe each channel successfully.

Figure IV.17 compares the predicted distribution of current throughout the fully flared channel at 43 kA along with the experimentally determined variation at 60 kA. Note that the theoretical contours are not continued near the cathode in the channel entrance since the experimental flaring deviates significantly from the interelectrode separation predicted by the theory in this region of the channel. As one might expect, the contours in the theoretical channel at 43 kA demonstrate less severe behavior due to the lower current which would make the local Hall parameter less than in the experimental channel. If one were to take the experimental mean magnetic field found in the fully flared channel, and input it into the theory as the prescribed variation in magnetic field, a new "design channel" is predicted for operation at 60 kA. This new channel is shown in figure IV.18 and compared with the channel predicted by the linear variation in total pressure at 43 kA. The resulting channel is a little different in that the channel seems to be axially compressed. This is a result of the faster drop in the magnetic field which controls the axial distribution of the interelectrode separation. The

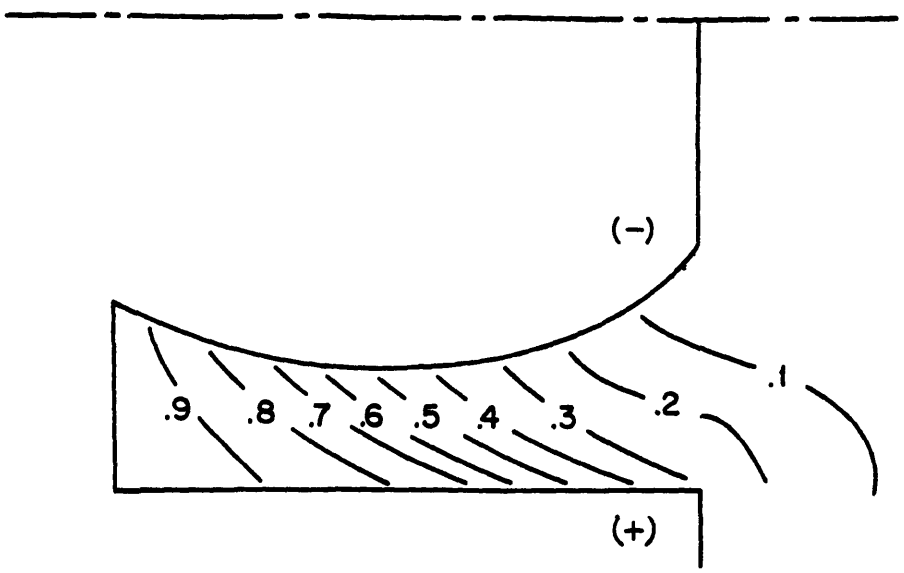

Experimental channel
J = 60 kA

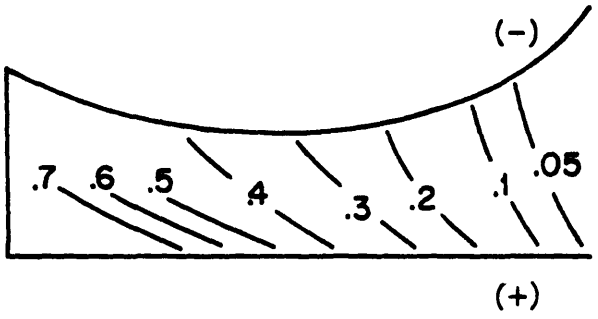

Theoretical channel (2-D)
J = 43 kA

Figure IV.17: Experimental and Theoretical Enclosed Current Contours in the Fully Flared Channel Geometry for an Argon Mass Flow Rate of 4 g/s

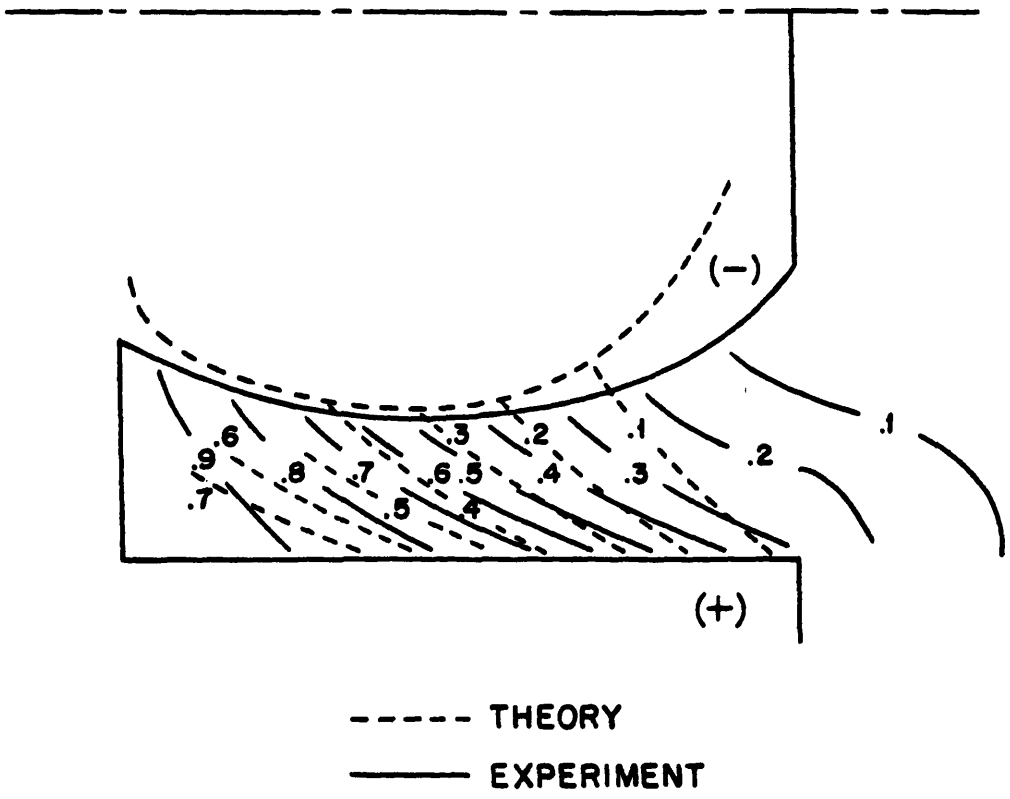

Figure IV.18: Experimental and Theoretical Enclosed Current Contours in the Fully Flared Channel Based on Experimental Data at 60 kA and an Argon Mass Flow Rate of 4 g/s

theoretically and experimentally determined enclosed current profiles match well in the contour shapes although their magnitudes are off. This is due to the theoretical limitations and experimental error, but it is interesting to note that both theory and experiment show that anode starvation seems to occur near the throat of the channel. The theory also predicts that a thruster based on the experimentally determined magnetic field distribution (figure IV.13) has a large portion of the anode operating in a starved mode. The previous figure representing the theoretical model at 43 kA, has been taken just to the limit of starvation where the density has gone to zero at a single point on the anode.

Unfortunately, the experimental discharge and the theory presented in Chapter II are not really comparable due to the limitations of the perturbation technique. Further discussion of this problem is included in the next chapter.

Chapter V: Terminal Voltage and the MPD Arcjet Performance

The terminal voltage in the MPD arcjet reflects the demands placed on the thruster. For a given geometry and operating point, the thruster must adjust its overall operation (i.e. its electrode falls and its partition between thermal and electromagnetic acceleration processes) to define a consistent operating voltage.

The terminal voltage characteristics, shown in figure IV.3, at first glance look representative of the transition from electrothermal to electromagnetic thrusters, but closer analysis shows that the terminal voltage measurement is not necessarily a good gauge of arcjet performance. If the data from figure IV.6 is replotted onto log-log scales, as in figure V.1, the transition from a linear voltage dependence to a cubic one is clearly not seen. The theory predicting this anticipated transition fails to include such effects as discharge symmetry, electrode falls (which in the case of a starved anode increase exponentially rather than in a cubic manner), pressure gradient, and Hall contributions. Instead, the theory is based on a symmetrical and uniform plasma flow with no electrode falls with the hopes that any resulting falls are small in comparison to the generated back emf. Cursory examination of figures IV.4 to IV.6 shows that the anode and cathode regions account for about half of the total voltage for operation at 60 kA with an argon flow rate of 4 g/s. Therefore almost half of the total voltage does not contribute significantly to directed momentum transfer thereby decreasing thruster

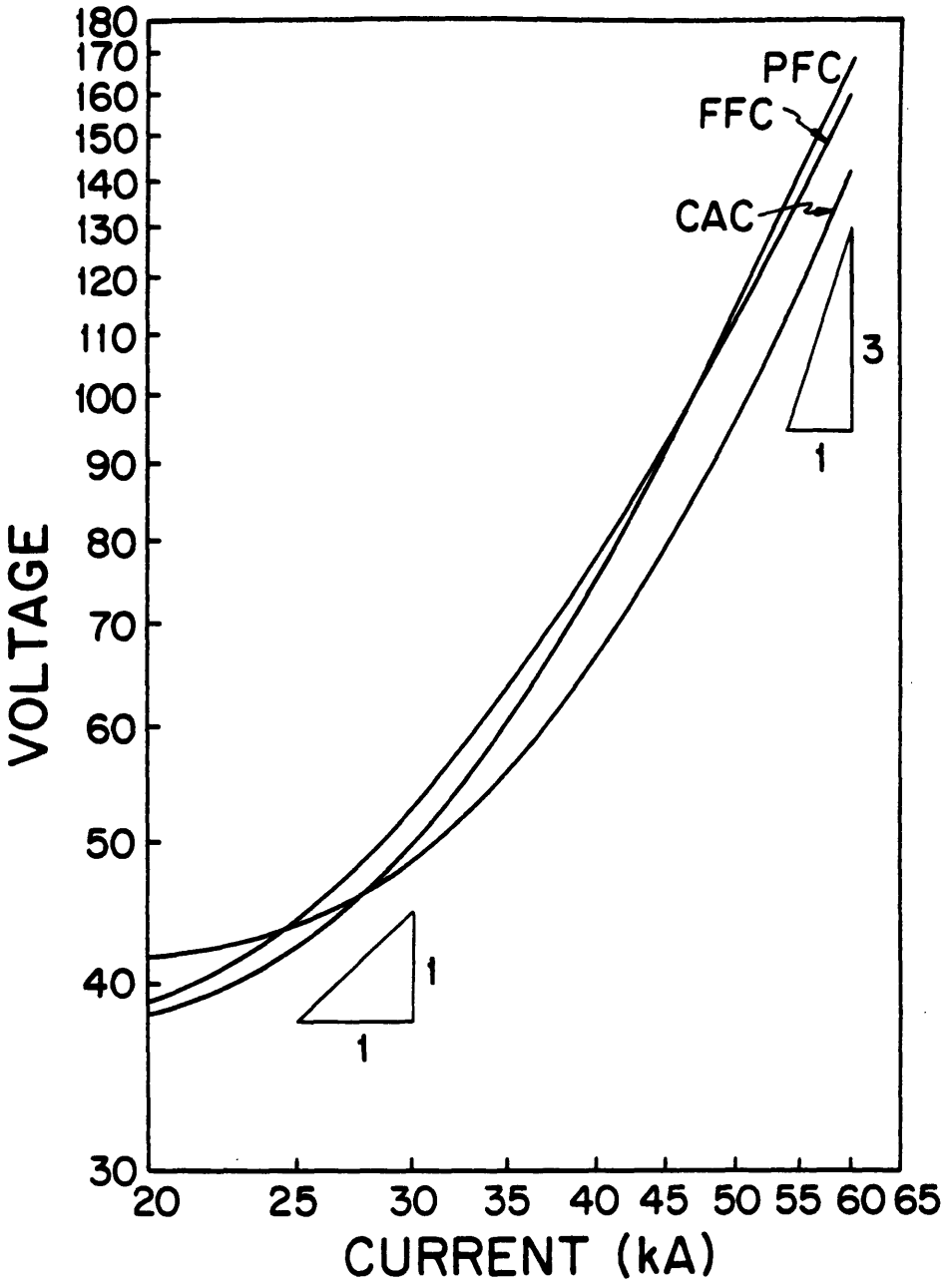

Figure V.1: Logarithmic Plot of the Thruster Voltage Versus Total Current for an Argon Mass Flow Rate of 4 g/s

efficiency. So, it is important to understand every contribution to overall thruster voltage as well as the accuracy of the theory in its ability to predict the actual bulk plasma voltage.

V.1: Composition of the Thruster Voltage

One simplified version of Ohm's law states that there are four major components comprising the local electric field for a steady-state plasma flow

$$\vec{E} = \frac{\vec{j}}{\sigma} + \frac{\vec{j} \times \vec{B}}{\sigma} - \frac{\nabla p_e}{en_e} - \vec{u} \times \vec{B} \qquad V.1$$

The first term is the Ohmic contribution, the second is due to the Hall effect, the third comes from the resulting electron pressure gradient, and the fourth is the back emf. It is important to try to account for the contribution of each term to the total voltage. It is possible to estimate each contribution from existing theory and data except for the pressure gradient term. However, even without knowledge of the density field, explicit calculation of the pressure gradient term is still possible. The Hall and the pressure gradient terms can be combined through simple algebraic manipulations. From the inviscid momentum equation

$$(\rho\vec{u} \cdot \nabla)\vec{u} = -\nabla p + \vec{j} \times \vec{B} \qquad V.2$$

This equation can be rewritten in terms of the Hall parameter and the electron density by using the definition of the Hall parameter

$$\vec{\beta} = \frac{\sigma}{en_e} \vec{B} \qquad V.3$$

and the perfect gas law for a fully ionized gas

$$p = 2n_e kT \qquad V.4$$

giving

$$\frac{m_a}{e}(\vec{u}\cdot\nabla)\vec{u} + \frac{2kT}{e}\frac{1}{n_e}\nabla n_e = \frac{\vec{J}\times\vec{\beta}}{\sigma} \qquad V.5$$

In a transverse momentum balance for this channel geometry, the plasma momentum is neglected, giving

$$\frac{(\nabla p_a)_r}{en_e} = \frac{1}{2\sigma}(\vec{J}\times\vec{\beta})_r \qquad V.6$$

Substitution into equation V.1 shows that the transverse field can be rewritten as

$$E_r = \frac{j_r}{\sigma} + \frac{j_x\beta}{2\sigma} + uB \qquad V.7$$

This relation shows that the pressure gradient term, in the absence of significant transverse flow velocity, reduces the Hall contribution by a factor of 1/2. In Appendix 8, the components of the current density are shown to be simply related as

$$j_x = -\beta\, j_r \qquad V.8$$

assuming small axial gradients of density and potential, so that

$$E_r = \frac{j_r}{\sigma}\left(1 + \frac{\beta^2}{2}\right) + uB \qquad V.9$$

The terms comprising equation V.9 account for the appropriate voltage contributions to the plasma bulk. Several theories and models are available for computational analysis of the various pieces of equation V.8. In addition to the one-dimensional models presented in Appendices 2 and 3, a Baksht-type model for a cylindrical geometry is presented in Appendix 8 and integral thrust equations for various cylindrical geometries are presented in Appendix 9.

V.2: Partition of Voltage in the Constant Area Channel

Based on the probe measurements resulting in the enclosed current and

floating potential contours in figures IV.4 to IV.6, the three channels have the mid-channel voltage breakdown distribution shown in figure V.2 for operation at 60 kA and an argon flow rate of 4 g/s.

For each channel, several tools exist to determine the voltage contribution of the plasma bulk. For the constant area channel, the one-dimensional model presented in Appendix 3 can be used to approximate the bulk voltage. The lack of two-dimensionality excludes the contributions from both the Hall effect and the electron pressure gradient. Furthermore, the model does not include the additional voltage caused by the thrust increment from the thermodynamic pressure acting on the thruster surfaces. This contribution acts to increase the back emf of the channel and can contribute significantly to the overall thruster voltage.

For an inviscid discharge at 60 kA, an argon mass flow rate of 4 g/s, at a constant electrical conductivity of 8900 mho/m for a 2 eV plasma, a voltage, comprised of the back emf and Ohmic contributions, of about 46 V is predicted. The $\vec{j}x\vec{\beta}$ and ∇p_e contribution can be estimated from figure IV.7 by noting that the Hall parameter (approximated by the angle between the current density vector and the electric field in the plasma reference frame) is approximately unity, and from figure IV.8, the local current density is seen to be about 1.0×10^6 A/m^2. If the plasma bulk has a measured thickness of about 1.6 cm (due to electric probe physical limitation), then the Hall and pressure gradient contribution approximately totals

$$\frac{j_r \beta^2}{2\sigma} h^* \cong 1 \text{ V} \qquad \text{V.10}$$

Region	Constant Channel (Volts)	Partially Flared Channel (Volts)	Fully Flared Channel (Volts)
Cathode	36 ± 15	25 ± 20	16 ± 55
Plasma	43 ± 30	67 ± 40	62 ± 85
Anode	64 ± 15	75 ± 20	82 ± 30
Total	143 ± 5	168 ± 9	160 ± 25

Figure V.2: Experimental Midchannel Potential Variation For Each Channel By Region

One can estimate the contribution to the back emf from the thrust attributed to the thermodynamic expansion of the plasma. In the constant area channel, this force acts on the thruster backplate. It is possible to estimate the additional back emf contribution to the total voltage by comparing the ratio of the magnetic and thermodynamic pressures at the backplate

$$\frac{P_{mag}}{P_{therm}} = \frac{B_0^2}{2\mu_0 \rho RT} \simeq \frac{B_0^2}{4\mu_0 n_e kT} \qquad V.11$$

Using an electron density of about $4x10^{21}$ m^{-3}, an electron temperature of two electon volts, and an input current of 60,000 A (providing a value of 0.194 T for B_0) this pressure ratio is approximately

$$\frac{P_{mag}}{P_{therm}} \simeq 5.8 \qquad V.12$$

Therefore the thermodynamic pressure is about 17% of the magnetic pressure and adds this amount to the total back emf of the thruster.

The 46 V predicted by the model includes the contributions from the back emf and from the resistive (Ohmic) contribution. This latter contribution can be estimated from the parameters in relation V.10 to be about two volts. This implies that the calculated back emf contribution from the model is 44 volts. Therefore, the aerothermodynamic thrust acting on the backplate, contributes an additional eight volts (17% of 44 volts) to the discharge voltage. This gives an estimated bulk voltage for the constant area channel as

$$V_{Bulk} \cong 46 + 1 + 8 = 55 \text{ V} \qquad V.13$$

which is about twelve volts too high.

The bulk voltage can also be estimated from the integral thrust equation derived in section 1 of Appendix 9. This formulation only

accounts for the contribution from the back emf, so the other components must also be added. From equation A9.19, the electromagnetic voltage component can calculated to be 25 V. For completeness, the Hall and electron pressure gradient, Ohmic, and aerothermodynamic contributions must be included. In this case, the aerothermodynamic contribution is about 4 volts (17% of 25 volts). This provides an approximate voltage of

$$V_{Bulk} \cong 25 + 1 + 2 + 4 = 32 \text{ V} \qquad \text{V.14}$$

This estimation is low. These results have been based on the temperature and density measurements by Kilfoyle which are then used to characterize the conductivity. If the electron temperature estimate was high by a factor of two, then the conductivity would be three times less. The aerothermodynamic term would decrease by half, but the Hall, pressure gradient, and Ohmic contributions would increase by three. The net result would be an increase in total voltage by 7 volts. The bulk voltage predicted by the model in Appendix 3 would change as well. The 46 V prediction is still valid, however the Ohmic portion of this is now six volts. The aerothermodynamic contribution from equation V.10 is now about 8% of the total back emf (or about 3 V), and the Hall-pressure gradient contribution is also about 3 V. Therefore the total voltage would become about 52 V and the bulk voltage based on the calculation from the integral thrust equation would become about 40 V. The latter is still low but within experimental error. This illustrates the importance of an accurate knowledge of the electron temperature.

The cylindrical Baksht-like model presented in Appendix 8 is not useful for predicting the bulk plasma potential for conditions aside from

anode related onset, but it does show axial variation of plasma potential remarkably consistent with patterns exhibited in the real arcjet. The axial potential variation for a thin, cylindrical, concentric electrode geometry is prescribed by equation A8.49. This equation represents a potential based on transversely averaged quantities comprised of Ohmic, Hall, back emf, and pressure gradient terms and is, therefore, quite complete. This model shows, in figure V.3, that the total plasma potential at the entrance and exit (where the back emf is small) is considerably larger than in the midchannel region where the back emf is dominant due to the reduced local current density. In a real channel, the electrode falls would have to make up for the voltage deficit in the midchannel region. The anode voltage drop is therefore larger in the middle of the channel than at the entrance and exit. This requirement that the electrode voltage drops be large to maintain a consistent terminal voltage adds to thruster inefficiency and therefore decreases its performance. It also implies that anode starvation first occurs in the middle of the channel where the anode voltage drop is at a maximum. This problem may be aided by electrode flaring which reduces the local electric fields by lowering the local Ohmic voltage contribution at the entrance and exit so that the anode drops do not have to be so large so as to match the overall thruster voltage.

V.3: Partition of Voltage in the Partially Flared Channel

A similar analysis can be done for the partially flared channel. In figure V.2, the midchannel voltage breakdown can be seen. A total of 67 V

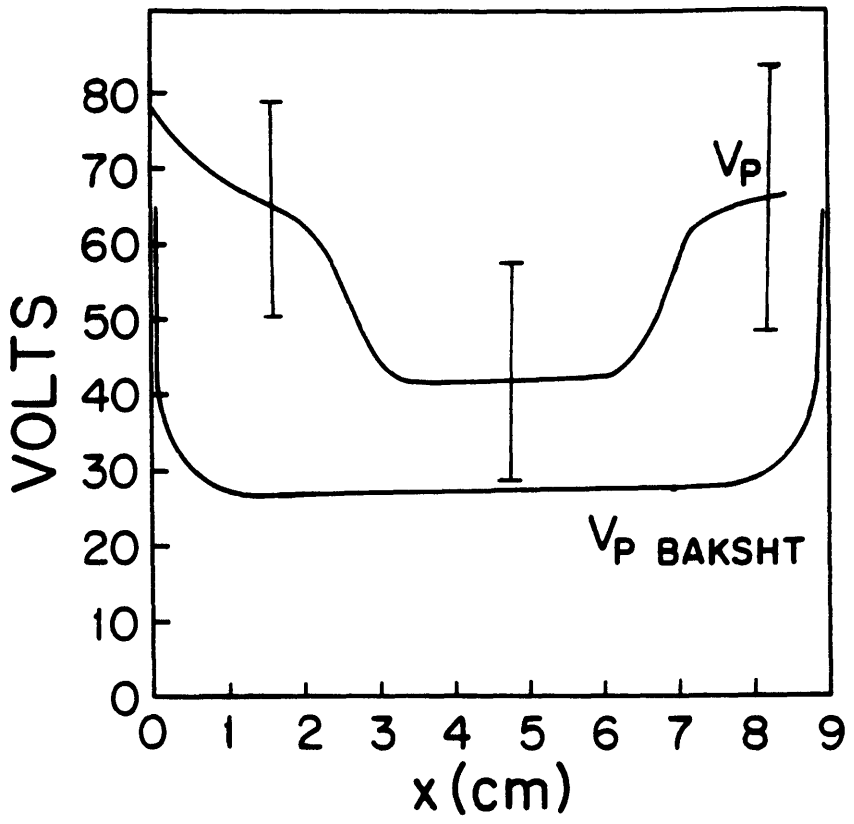

Figure V.3: Predicted and Experimental Axial Variation in Plasma Potential for the Constant Area Channel at 60 kA for an Argon Mass Flow Rate of 4 g/s

must be accounted for. Unfortunately, no simulation in Appendix 3 can be forced to describe a partially, or for that matter, fully flared geometry. Regardless of magnetic field specification, including those based on measured data from figures IV.5 and IV.6, no geometries could be constructed that remotely resemble the experimental geometries. The inviscid simulation also provided unreasonably high voltages due to the rapid increase in velocity at high magnetic Reynolds' number causing a large voltage contribution from the back emf. As the flow accelerates at a high magnetic Reynolds' number, the field and density get very small simultaneously, and the electrode separation gets very large. Although this numerical method was not too fruitful, the plasma voltage can be adequately estimated from an integral thrust equation derived for the partially flared channel in Appendix 9.

Substitution of the appropriate values in equation A9.20 provides for an electromagnetic contribution of about 38 V. A deficit of 29 V is seen; however, this calculated voltage, as in the previous section, does not include the contribution of the Hall effect, pressure gradient, Ohmic contribution, and the aerodynamic thrust due to the effect of the plasma pressure on the electrode surface.

In the flared channels, the aerodynamic thrust component is not only due to the ordinary expansion of the plasma. The pumping force contributes to the aerodynamic thrust by forcing the plasma against the cathode. This pressurization, which is electromagnetic in origin, is realized as thrust since the flared channels have a projected area orthogonal to the flow direction. This effect is not felt at the

backplate since there is no radial pumping force immediately adjacent to this wall. This aerodynamic force can be estimated by taking the pressure contribution at the backplate and adding it to the net contribution at the surface of the cathode. This latter contribution can be approximated from a cylindrical transverse momentum balance by neglecting the transverse convection which then provides for a condition of hydrostatic equilibrium. If the thermodynamic pressure in neglected near the anode, the pressure distribution on the cathode surface can be estimated and the net thrust contribution can be approximated. This contribution is then added to the electromagnetic thrust and a corresponding voltage is calculated. The voltage is calculated by assuming that the total power delivered as back emf ($IV_{Back\ emf}$) goes into the kinetic power of the plasma (refer to equation A9.18).

In the partially flared geometry, the mean current density is about 1.5×10^6 A/m^2 and the Hall parameter can be estimated at about two. Assuming an electric conductivity of about 7500 mhos/m (based on an electron temperature of about 1.8 eV from figure IV.13), the Ohmic contribution is approximately 4 V and the Hall and pressure gradient contribution is about 6 V. The aerothermodynamic contribution by the gas expansion is different than in the constant area channel. At the backplate, the pressure acts on almost twice the area (due to the divergent nozzle) but the density is also lower. The temperature is also lower, so the net contribution by the gas expansion at the backplate is about 15% of the total magnetic pressure at the backplate (or about 5 V). The thrust contribution due to the cathode pressurization can be estimated

to contribute about 7 V to the total back emf giving a net contribution from the aerodynamic thrust at about 12 V. Therefore

$$V_{Bulk} \cong 38 + 4 + 6 + 12 = 60 \text{ V} \qquad \text{V.15}$$

about 7 V shy of the experimentally determined voltage but well within experimental error.

It appears that it is not too difficult to reasonably account for the plasma voltage components, however further modeling and experimental measurements for operation below the point of anode starvation would be desirable for a more accurate characterization of the partition of voltage in the plasma bulk for the partially flared channel.

V.4: Partition of Voltage in the Fully Flared Channel

The exact same procedure followed in the analysis of the partially flared channel is done for the fully flared channel. The only difference is that the integral thrust equation is derived for a geometry with a converging-diverging profile. This is also presented in Appendix 9. From figure V.2, the bulk plasma voltage is experimentally seen to be about 62 V. Calculation of the electromagnetic contribution from equation A9.21 gives an electromagnetic contribution of approximately 39 V. In the flared geometry, the average current density at the midchannel is about 2×10^6 A/m^2 and the Hall parameter can be estimated at about 1.5. For a plasma with an electrical conductivity of 5200 mho/m (based on an electron temperature of about 1.4 eV) and a thickness of about 1.6 cm, the Ohmic contribution is about 6 V while the Hall and electron pressure gradient contribution is approximately 7 V. The aerodynamic contribution can be

estimated once again. The contribution at the backplate can be estimated to be about 12% of the magnetic pressure at the backplate, so it will contribute about 5 V to the back emf. The other component due to the cathode pressurization can be estimated to add another 4 V to the total back emf for a total aerodynamic contribution of 9 V. In this channel, the converging section upstream of the channel throat actually gives a negative contribution to the thrust. This may be one reason that the aerodynamic thrust contribution is less for the fully flared channel than the partially flared channel. The estimated voltage for the plasma bulk in the fully flared channel is

$$V_{Bulk} \cong 39 + 6 + 7 + 9 = 61 \text{ V} \qquad \text{V.16}$$

which is one volt less than the measured voltage and certainly within experimental error.

The results of this section with the previous sections are summarized in figure V.4.

Utilization of the data from figures IV.15 (anode fall vs total current) and IV.3 (the terminal voltage characteristics) allows further analysis of the terminal voltage contributions for the fully flared channel. For increments in current, the terminal voltage and the electrode falls are experimentally known. At 60 kA, the complete transverse voltage breakdown has also been experimentally determined. The electromagnetic thrust components can be estimated once again from equation A9.21. Estimates of the Ohmic, Hall, and pressure gradient contributions can also be estimated by scaling the current density and Hall parameter to the values at 60 kA since the total current, along with

Voltage Component	Constant Channel (Volts)	Partially Flared Channel (Volts)	Fully Flared Channel (Volts)
ΔV_a	64 ± 15	75 ± 20	82 ± 30
ΔV_c	36 ± 20	25 ± 30	16 ± 60
ΔV_p	43 ± 35	67 ± 50	62 ± 30
$\Sigma\ \Delta V$	143 ± 5	168 ± 9	160 ± 25
$V_{em,calc}$	25	38	39
$V_{Hall,VPe}$	1 ± 1	6 ± 6	7 ± 7
V_{Ohmic}	2 ± 2	4 ± 4	6 ± 6
$V_{aerodynamic}$	4 ± 4	12 ± 12	9 ± 9
$\Sigma\ V$	32 ± 7	60 ± 22	61 ± 22
$\Delta V_p - \Sigma\ V$	11 ± 42	7 ± 77	1 ± 52

Figure V.4: Breakdown of Thruster Voltage at Midchannel for Each Geometry

the current density and Hall parameter scale with the magnetic field. For example, 40 kA is 2/3 of 60 kA so the average midchannel current density is 1.3×10^6 A/m^2 (2/3 of 2×10^6 A/m^2) and the average midchannel Hall parameter is about 2/3. If the temperature is also scaled by approximating the local dissipation with the enthalpy change then

$$\frac{j^2}{\sigma} \sim c_p T \qquad \text{V.17}$$

or

$$j^{4/5} \sim T \quad ; \quad j^{6/5} \sim \sigma \qquad \text{V.18}$$

allowing the voltage contribution due to the Hall and electron pressure gradient, Ohmic, and aerodynamic contributions to be estimated and tabulated in figure V.5. From this figure it can be seen that the experimental data does not correlate too well with the estimated voltage contributions. There are many possible reasons for these discrepancies. One strong possibility is the asymmetric discharge at lower currents. It is possible that introduction of a probe, especially near an electrode, may make the discharge more difficult to make symmetrical. This is possible since the presence of a probe locally decreases the back emf and enhances current conduction to that area. Another discrepancy may arise from the simplistic variation of the conductivity and temperature with current. The variation in electrical conductivity may be quite large and should be estimated from measured values of temperature. This could change the results by several volts. So, the voltage contributions from the Ohmic and Hall terms are probably somewhat off at the lower current levels. Similarly, the aerothermodynamic pressure contributions are probably different since accurate knowledge of the temperature is not

I		20	30	40	50	60
$V_{Terminal}$	(exp)	40 ± 3	50 ± 4	75 ± 5	114 ± 7	160 ± 25
ΔV_a	(exp)	5 ± 10	25 ± 10	58 ± 10	77 ± 15	82 ± 30
ΔV_c	(exp)	11 ± 10	12 ± 10	14 ± 10	15 ± 15	16 ± 55
$V_{em,calc}$	(th)	1	5	11	22	39
V_{Ohmic}	(est)	7 ± 7	7 ± 7	6 ± 6	6 ± 6	6 ± 6
$V_{Hall,ope}$	(est)	2 ± 2	4 ± 4	4 ± 4	5 ± 5	7 ± 7
$V_{aerodynamic}$	(est)	4 ± 4	6 ± 6	7 ± 7	8 ± 8	9 ± 9
$\Sigma(\Delta V+V_{em,calc})$		30 ± 33	59 ± 37	100 ± 37	133 ± 49	159 ± 107
$V_{Terminal}-\Sigma(\Delta V+V_{em})$		10 ± 36	- 9 ± 41	-25 ± 42	-19 ± 56	1 ± 132

Figure V.5: Extrapolated Breakdown of the Thruster Voltage at Midchannel for Various Current Levels in the Fully Flared Channel

available.

Further measurement of the potential in the cathode region is necessary to isolate the various voltage contributions and special care must be taken since there can be large measurement errors associated with floating potential measurements. At onset current levels, the back emf is not large and anode starvation is rapidly increasing the local anode potential. The cathode potential then becomes the difference between two signals of the same magnitude, and if these signals are noisy, the measurement is not very accurate.

V.5: Estimation of Thruster Efficiencies

Two significant contributors to the arcjet voltage, for a fixed geometry and mass flow, come from the electrode falls and from the plasma bulk regions where the back emf is maximum. The back emf is a representative measure of how well the arcjet accelerates the fluid, and the anode potential drop is a strong indicator of the voltage lost due to the thruster's proximity to onset as defined by anode starvation. As operation is pushed towards this onset level, potential is either removed from accelerating the plasma flow, or is increased to achieve a given thrust level; both act to lower thruster efficiency.

All of the voltage data presented in these past few sections can be used to estimate the electromagnetic efficiency of the arcjet. For each channel, the thruster efficiency may be estimated as the ratio of the experimentally determined bulk voltage to the total voltage. These efficiencies, shown in figure V.6, reflect the voltage applied to the

Efficiency	Constant Channel (%)	Partially Flared Channel (%)	Fully Flared Channel (%)
$\eta_{Thruster}$	30	40	39
$\eta_{eff,calc}$	17	23	24

Figure V.6: Experimental and Calculated Efficiencies Based on the Ratio of the Plasma Bulk Voltage to the Total Thruster Voltage for the Three Geometries

kinetic stream of the plasma rather than the electrode falls. As expected, the flared channels are more efficient due to the controlled plasma expansion and possible reduced viscous losses.

The previous efficiency can be rewritten in terms of the calculated electromagnetic thrust from Appendix 9 rather than on the experimentally determined bulk voltage. This calculated efficiency is low due to the lack of information on the net contributions from the various aerodynamic thrust mechanisms which act to increase the local back emf. These efficiencies can be calculated for increasing current levels in each channel. The results of these calculations for all three channels are presented in figure V.7. The flared channels operate at higher efficiencies due to the decreased inner radius of the cathode, which leads to higher inlet magnetic pressures, as well the divergent section in the flared channels which increases the thrust by the greater magnetic field at the reduced radii. Increasing efficiency is expected for increasing current since the electromagnetic thrust starts to dominate over the Ohmic contributions. One would expect the efficiencies to drop as the anode fall mounts near onset. This does not appear to happen and is probably due to the arcing that occurs once the anode fall grows too large.

V.5.1: Estimation of Frozen Flow Losses

It is interesting to note that one can discuss the relative efficiencies of each channel with regards to frozen flow losses. Figure IV.12 and IV.13 show the relative magnitudes of the dissipation and electron temperature for each channel. As expected, flaring decreases

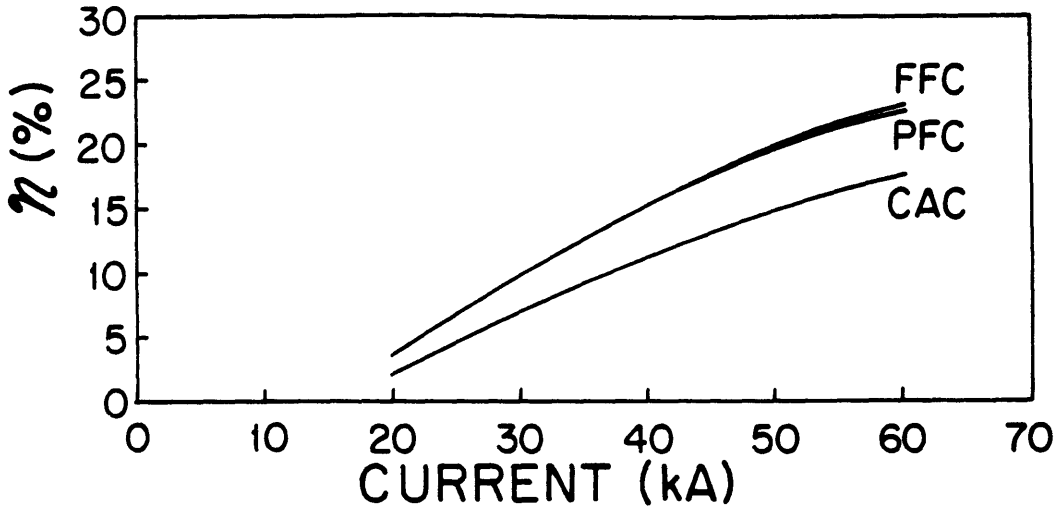

Figure V.7: Variation of the Calculated Electromagnetic Efficiencies as a Function of Thruster Current for an Argon Mass Flow Rate of 4 g/s

this dissipation and temperature by decreasing the local electric field. Some of the excess dissipation may result in additional ionization of the plasma which may result in increased frozen losses. It is possible to rank the channels in the order which probably has the highest frozen flow losses. This can be approximated by comparing the plasma residence time with the time constant for recombination. The plasma residence time is defined as

$$\tau_{flow} = \frac{L}{u_e} \qquad \text{V.19}$$

is approximately 5 μs for a 9 cm channel. The recombination time constant

$$\tau_{rec} = \frac{1}{\Omega(T) n_e^2} \qquad \text{V.20}$$

where $\Omega(T)$ is the constant defined by Bates' law[29]

$$\Omega(T) = \frac{1.09 \times 10^{-20}}{T^{9/2}} \qquad \text{V.21}$$

From the electron temperature measured by Kilfoyle in figure IV.13, recombination time constants can be approximated based on an electron density of about 5×10^{21} m^{-3}. In the constant area channel, the recombination time constant is about 162 μs; in the partially flared channel, 101 μs; and in the fully flared channel, 33 μs. All of the recombination times are significantly longer than the residence time implying that the plasma has significant frozen flow losses and that assumptions of equilibrium are not really valid since recombination is more dependent on diffusion rather than collisional processes. Therefore, since the constant area channel has more dissipation for the same current and also a larger recombination time, it is most probably the channel with the highest degree of frozen flow losses.

V.6: The Role of Viscosity in MPD Arcjet Performance

Viscous effects have never been quantified in the MPD arcjet. Insufficient understanding of the physics and the local Knudsen number have, so far, prevented any derivation of any meaningful models detailing boundary layer development in the MPD arcjet. This lack of any model prevents any basis for realistic estimates of performance degradation. Until recently, viscosity has been ignored because the geometries have had sufficiently large dimensions and flow rates so that viscous dissipation was, most probably, a second order effect. Even if this were not the case, the MPD arcjet community still cannot readily measure thrust accurately.

There are some indications from experiment that drag could be important in certain geometries. This was experimentally inferred by Wolff for a thruster with a very high aspect ratio.[38] He made preliminary and inconclusive thrust measurements that showed a significantly lower thrust than implied by previously derived thrust equations.[1,3,38] He attributed this deficit to the effects of viscous drag.

Viscosity and other real gas effects tend to complicate the understanding of the discharge physics. A viscous channel would have the effect of decreasing the overall back emf, which would then modify the distribution of the current in the channel. This would then redistribute the local dissipation which could change the local temperature and ionization fraction, which would also change the local viscosity.

Some understanding of the viscous behavior is important because the viscosity of a plasma varies drastically over a very small temperature

range in an equilibrium plasma. This is illustrated in figure V.8[30]. Based on this data, the boundary layer thickness can be estimated. Using an equation for the boundary thickness for a laminar boundary layer from White,[48]

$$\delta \simeq 5x(Re_x)^{1/2} \qquad V.22$$

where x is the axial distance and Re_x is the Reynolds' number based on the axial distance. For an argon mass flow rate of 4 g/s, a channel cross sectional area of 7.46×10^{-3} m^2, an axial distance of 0.09 m, and a viscosity of 5×10^{-5} kg/ms, a value of 1.4 cm is calculated--more than half of the distance from the anode to the cathode. As a result, the channel can be approximated as a fully developed viscous flow. To get some understanding of the contribution of viscosity in the MPD arcjet, some analysis can be done to determine viscosity's overall contributions to the thruster operation. In the following model an approximate analysis of a steady-state, one-dimensional, flow of a plasma with real gas effects is developed. A more complete derivation is presented in Appendix 10 and is only outlined below.

Viscosity's strong ionization fraction and temperature dependence does not enable one, in the spirit of an approximate one-dimensional analysis, to neglect an energy equation. Previous data and analysis show that the temperature in a typical arcjet is approximately constant, except in the initial ionization layer, and this temperature corresponds to the region where viscosity varies rapidly.[14,34] Therefore, depending on the local dissipation, the channel will either be mostly viscous, mixed, or inviscid. This complicates the system of equations by requiring

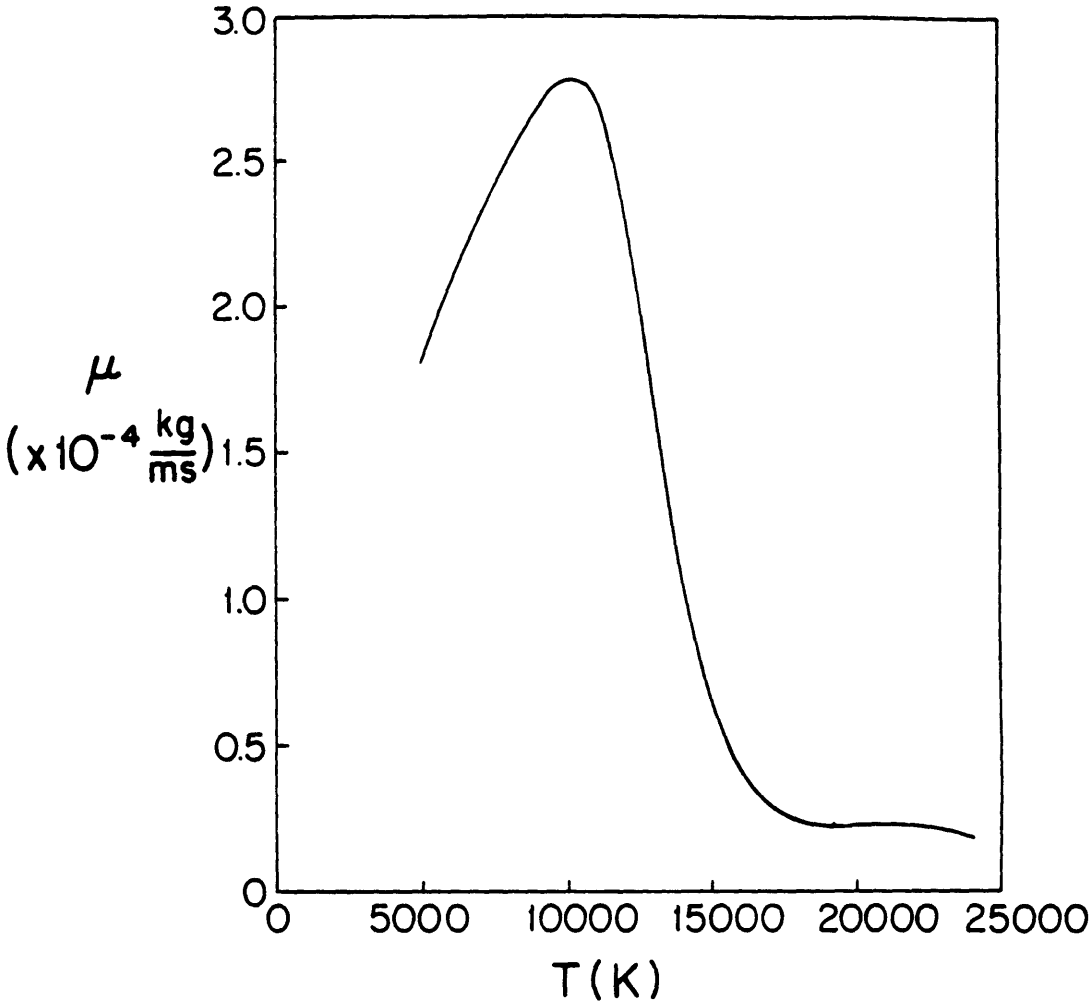

Figure V.8: Viscosity of an Equilibrium Argon Plasma at Atmospheric Pressure

calculation of the ionization fraction and temperature for a nonequilibrium plasma. Because of the rapid variations in plasma temperature and viscosity, care must be taken to accurately calculate the plasma state or significant error may result. Fortunately, the variation of μ with enthalpy is nearly linear in the ionization range so that one can keep track of its development reasonably well. This is important since the inherent simplifications in this one-dimensional analysis only allow for an approximation of arcjet behavior. To model the device with an approximate energy equation in order to capture the rapid decrease in viscosity is a great simplification, but is a first step.

Viscous effects modify only the momentum equation, which can be rewritten in a one-dimensional form as

$$\rho u A \frac{du}{dx} + A \frac{d}{dx} \left(p + \frac{B^2}{2\mu_0} \right) = - 2 w \tau_w \qquad V.23$$

Here the viscous effects are modeled as losses to the wall via a wall shear stress, τ_w. The coefficient of 2 in front of the wall shear stress accounts for the frictional loss at both electrodes while w accounts for the depth of the channel. This equation assumes that the anode and cathode boundary layers are fluid-dynamically equivalent. The skin friction at the wall can be estimated by assuming a constant transverse distribution of viscous sources (viscous force per unit volume) so that

$$q = \frac{d}{dy} \left(\mu \frac{du}{dy} \right) \qquad V.24$$

where u, in this equation is the axial velocity at a given transverse position and q is the strength of the viscous sources. The shear stress coefficient, τ_w, can be calculated to be

$$\tau_w = \mu \left(\frac{du}{dy} \right)_w = \frac{6\mu u}{H} \qquad V.25$$

This relation shows the dependence of the viscous term on the thruster dimensions, flow velocity, and viscosity. For the calculation of this parameter, the variation in viscosity must be detailed.

In a gas allowing for single ionization, the viscosity of a plasma can be written as

$$\mu = \mu_n \left\{ (1 - \alpha) + \frac{\alpha}{(1-\alpha) + \alpha \frac{\mu_n}{\mu_i}} \right\} \qquad \text{V.26}$$

where μ_n is the viscosity of the neutral species and μ_i is the viscosity of the ionized atom. In reality, multiple ionization can occur. Similar equations based on the single and double ion viscosities, as well as the ionization fraction for multiple species, can be derived with the result that the viscosity of the multiply ionized species moderates the total viscosity and begins to dominate at significant ionization fractions.

In order to characterize the plasma state and calculate the viscosity, a simple energy equation and a nonequilibrium electron conservation equation can be derived. These two equations allow for the plasma temperature and ionization fraction to be determined without the restrictions of the Saha equation. An equation of the overall one-dimensional conservation of energy can be written in terms of the enthalpy

$$h + \frac{u^2}{2} + \frac{E_z A}{\mu_0 \dot{m}} B = \left(h + \frac{u^2}{2} + \frac{E_z A}{\mu_0 \dot{m}} B \right)_0 \qquad \text{V.27}$$

where the enthalpy is expressed as

$$h = \left(\alpha + \frac{5}{2} \right) \frac{kT}{m_i} + \frac{\alpha e V_i}{m_i} \qquad \text{V.28}$$

This equation now relies on the specific nonequilibrium model detailing the relationship between the ionization fraction and temperature.

A balance between electron ionization, ambipolar diffusion, and three body recombination can be created to get an approximate idea of the variation of temperature and ionization fraction in the arcjet. This knowledge will enable the viscosity to be determined so that the viscous effects may be estimated. From this nonequilibrium model, an electron conservation equation can be found to relate the plasma temperature, ionization fraction and density

$$\frac{12\ w^2}{A^2 Q_{i\,n}} \left(\frac{\pi k}{m_i}\right)^{1/2} = \frac{1.09\times10^{-20}\rho^3}{m_i^{\,3} T^6} (1-\alpha) \left\{(1-\alpha)\left(\frac{2\pi m_a kT}{h_p^{\,2}}\right)^{3/2} \frac{m_i}{\rho} \exp\left(-\frac{eV_i}{kT}\right) - \alpha^2\right\} \qquad V.29$$

This equation has a very interesting behavior described more completely in Appendix 10.

The results from this simplified analysis are shown in Appendix 10 in great detail. In summary, the results indicate that viscous effects are not important in channels with significant magnetic interaction. In cooler channels with low ionization (lower current discharges), viscous effects could decrease performance significantly. However in channels with appreciable ionization and plasma temperatures in excess of one electron volt, the plasma viscosity is negligible. In fact, the data taken by Kilfoyle indicates that the MPD temperatures are probably sufficient to guarantee little viscous influence. If viscosity were to be important, one would expect it to be important near the cathode where the plasma is forced to flow along a wall.

This model can only be used as a guideline to estimate the importance of friction in the operation of various geometries. Greater fidelity

requires a more substantial model of the arcjet--not only more independent dimensions, but a more accurate description of the plasma boundary layers and plasma state, and a more careful treatment of the thruster thermodynamics.

V.7: Summary

In this chapter it was shown that the composition of the terminal voltage on the MPD arcjet can be broken down into components relating to the electrode regions and the plasma bulk. It was indicated that at low current levels, the discharge was noted to be asymmetric so that the terminal voltage was approximately constant until the discharge utilized the entire channel, after which it began to increase. This increase was shown to be composed of various voltage components which grew at different rates. As the current increased, the anode region began to contribute a disproportionate amount to the overall voltage thus decreasing the thruster efficiency since this voltage was used to attract electrons rather than accelerate the plasma. This mechanism was shown to be the one that tended to decrease thruster performance. It was shown that large losses are attributable to the large anode falls that tend to appear in the middle of the channel. It has been implied that these falls may be reduced by increasing the interelectrode separation at the entrance and exit thus reducing the large contribution to the total voltage from the initial Ohmic voltage component.

Other phenomena, such as plasma viscosity, were estimated to be noncontributory in comparison to the anode voltage contribution.

The performance limitation due to the growing anode potential does not appear to improve with current. In the next chapter, it will be shown that arcjet performance rapidly degrades to a point where thruster erosion becomes unacceptable.

Chapter VI: Arcjet Operation in the Vicinity of Onset

VI.1: Phenomenology of Onset

In previous works, onset has been defined to occur when the magnitude of high frequency voltage oscillations reach 10% of the terminal value.[3] Onset has also been linked to the increased rates of thruster erosion and therefore decreased lifetime. According to anode starvation theories, onset is defined as the point at which depletion of charge carriers in the anode vicinity, due to the Hall effect, prevents the prescribed current from conducting in a diffuse manner. At this point, large deflection of current in the axial direction occurs and large positive potential drops develop in the anode region.

With regards to the onset phenomenon, the important questions are, what exactly is onset, and what is its phenomenology. These questions will not be answered fully, however the data from this experiment tends to support the various anode starvation theories.

In the Princeton arcjets, the high frequency voltage oscillations (also referred to as voltage hash) appear at high current levels signaling decreased arcjet performance. In this experiment, the appearance of oscillatory terminal voltage, if present at all, was preceded by a sudden rise in local anode potential. In this experiment, voltage hash is only seen in the flared channels. But unlike the voltage hash found in the terminal measurements at Princeton, these oscillations have a very characteristic and regular signature with large amplitude oscillations

occurring at a rate near 50,000 Hz. As shown in figure VI.1, the hash observed on the Princeton voltage oscillogram has higher frequency components than in the arcjets examined in this experiment. Regardless of the origins of the hash (which will be discussed later), these oscillations increase in amplitude only in the cases of the flared channels. This is demonstrated in figure VI.2 which shows a dramatic rise in voltage hash for the fully flared channel at about 58 kA and for the partially flared channel, a moderate rise near 61 kA.

It is interesting to note that magnetic field probe signals downstream from the minimum area section in the flared channels exhibit similar oscillatory behavior which appear at the same time in the discharge as the voltage oscillations, except that they have a characteristic frequency of about 17,000 Hz. This is seen in figure VI.3 which is a trace of the signal from a magnetic field probe placed at a position 5.3 cm from the backplate and 0.3 cm from the cathode surface. Barnett also noted that these oscillations tended to originate in the plume region near or just beyond the exit plane of the arcjet at a current level corresponding to the appearance of the voltage oscillations[12].

Another interesting discharge feature appears in figures IV.4 through IV.6. In the constant area channel, a slightly lower anode voltage drop is seen at about 4.3 cm downstream from the backplate where the anode voltage drop always appears to be maximum. The constant area channel operates at a voltage of about 143 V at 60 kA which is about 25 V less than the partially flared channel and about 17 V less than the fully flared channel. Its anode drop is approximately 64 V versus 75 V for the

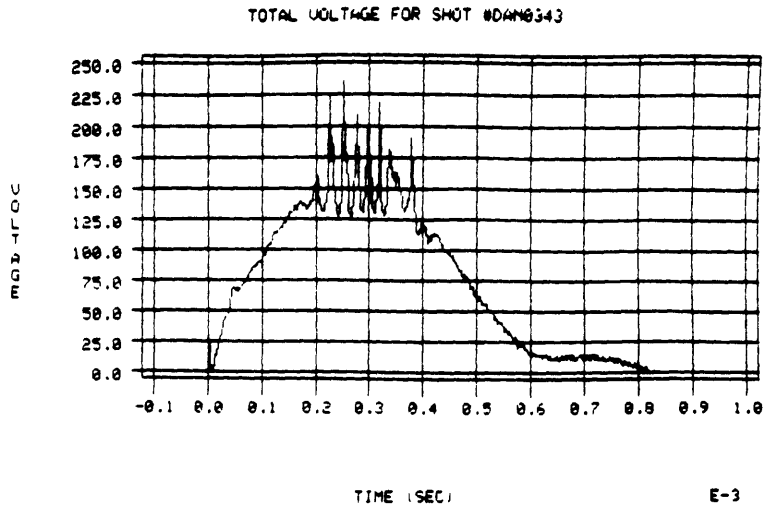

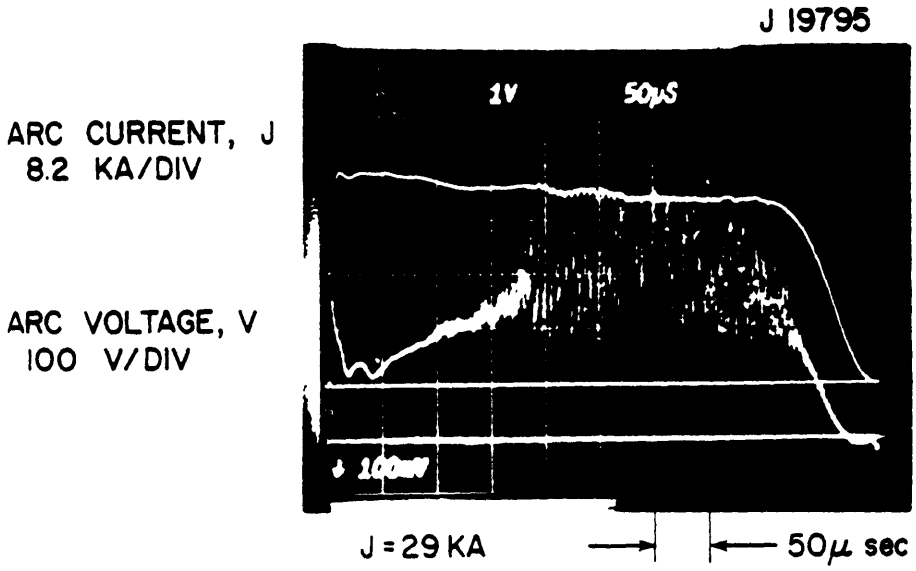

Figure VI.1: Oscillatory Voltage Traces
Top: MIT/RDA Fully Flared Channel
Bottom: Princeton Benchmark[7]

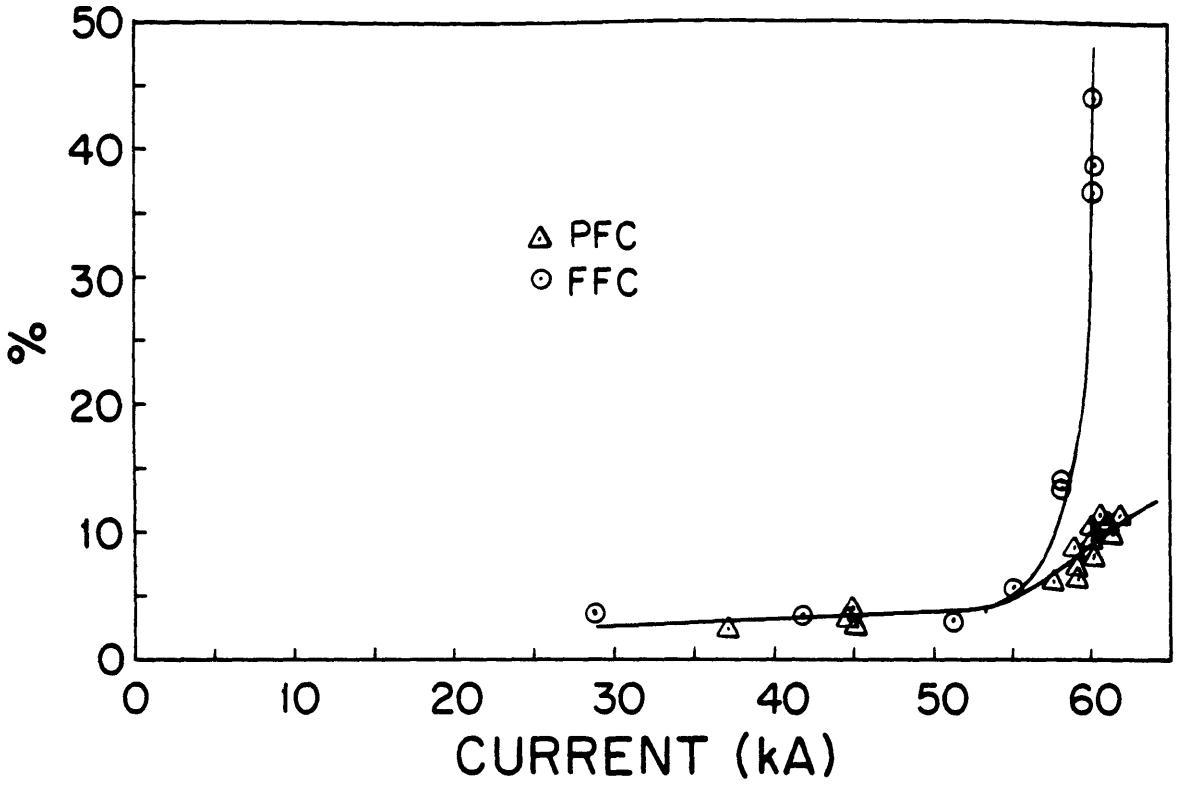

Figure VI.2: Variation of the Voltage Hash as a Function of Thruster Current in the Partially and Fully Flared Channels at 60 kA for an Argon Mass Flow Rate of 4 g/s

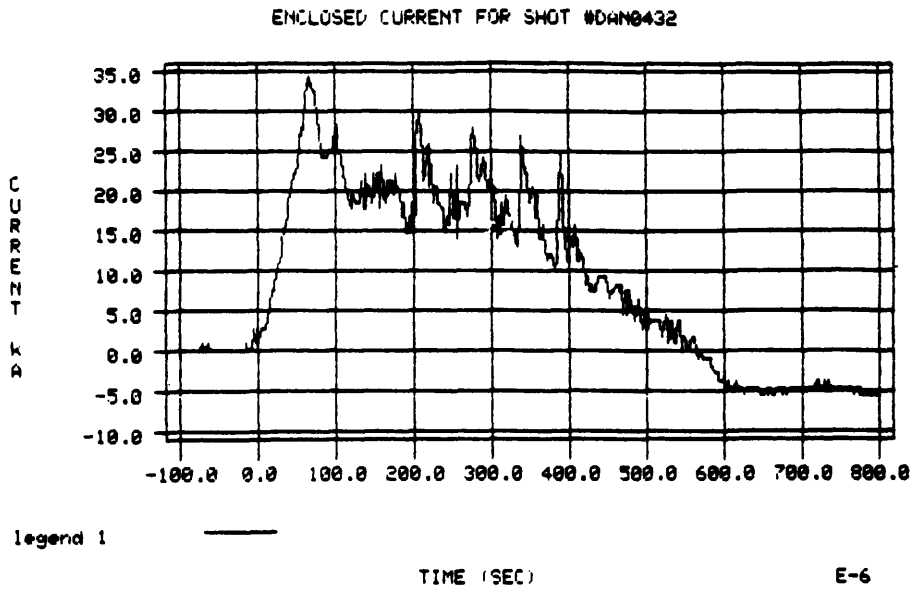

Figure VI.3: Oscillatory Signal from the Magnetic Field Probe

partially flared channel and 85 V for the fully flared channel.

VI.2: A Mechanism for Onset

The data presented show a compelling picture for an onset initiated by a depleted anode. A calculation based on a cylindrical variant of the Baksht model (presented in Appendix 8) shows that for a channel with the same characteristic dimensions, flow rate, and temperature of about one electron volt, anode starvation occurs at about 31 kA. This is remarkably close to the value noted in figure IV.15. The appearance of the anode potential rise is compared to the rise in terminal voltage hash in figure VI.4, a combination of figure IV.15 and VI.2 which show that the voltage hash increases only after the anode potential has reached a plateau. One possible explanation for this is that upon initiation of starvation, the anode rises in potential until the initiation of arcing. The arc formation prevents further growth in the anode potential. As the arc is convected downstream, it becomes more tenuous and eventually detaches, forming again as the anode potential increases. This may explain the very regular oscillatory voltage associated with this operational regime. If this is the proper physics of this phenomenon, then the periodic behavior in the voltage trace should have a representative frequency commensurate with convected disturbances in the channel. For the arcjets in this experiment, a typical convective frequency for a plasma flowing at a speed of 10^4 m/s through a channel 0.1 m long is about 100 kHz. This frequency is of the same order as the 50 Hz frequency noted in the oscillogram of the terminal voltage in figure

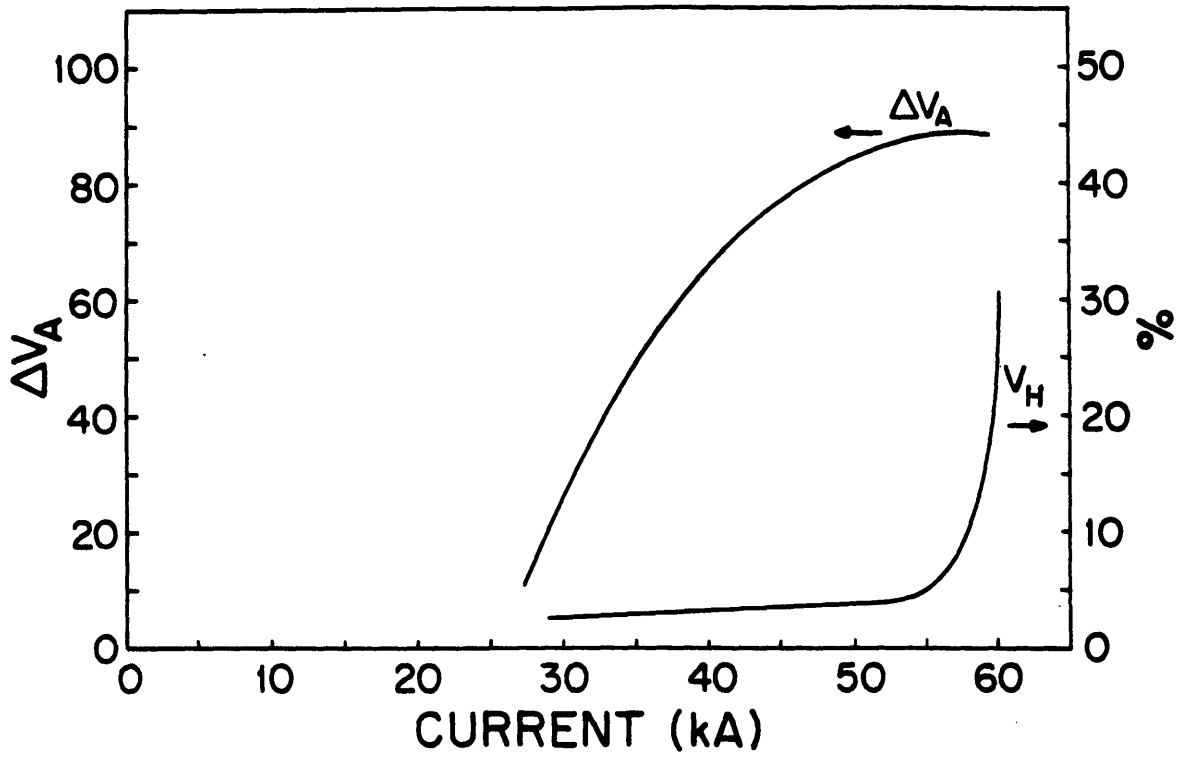

Figure VI.4: Variation of the Anode Voltage Drop and the Voltage Hash as a Function of the Thruster Current in the Fully Flared Channel at 60 kA for an Argon Mass Flow Rate of 4 g/s

VI.1a. But, it does not correspond to the higher frequencies associated with the operation of the Princeton devices. This may be due to the geometric differences between the MIT and Princeton arcjet channels. The Princeton benchmark channel has an anode lip that has an attachment surface about one to two centimeters in length rather than ten centimeters. These convective oscillations would have a characteristic frequency between 500 kHz and 1 MHz which is consistent with the oscillations found in the oscillogram from Princeton shown in figure VI.1b.

The typical convective frequencies for the channels in this experiment are a factor of six greater than the characteristic frequencies noted in the signal from the magnetic field probe in figure VI.3. This is possibly due to the localized measurement characteristics of an intrusive probe. The terminal measurement shown in figure VI.1a reacts to the dynamics of the entire discharge whereas the probe measures the local properties of the discharge. So, the magnetic field probe may only see a portion of the arcs in the arcjet. This implies that the anode breakdown may occur at regular intervals but in different perhaps random regions of the channel.

In summary, the onset mechanism may be characterized by local anode depletion which may lead to regular concentrated arcing initiated at the anode.

The constant area channel exhibits some of the characteristics of the starved channels except that the voltage and magnetic field oscillations are absent. This can also be explained from an anode starvation

standpoint. It has been assumed that the only mechanism for anode starvation arises from the radial pumping force. In the constant area channel, this force is partially balanced by a pressure gradient supported by the cylindrical cathode. The flared channels, unlike the constant area channel, allow the plasma to expand aerodynamically in a diverging nozzle so that there are no mechanical means to restrain the plasma from leaving the anode region. This expansion tends to aid the starvation process and may act to drive the anode into conditions requiring concentrated arcs at a lower current level, thus reducing the apparent onset limit. The fully flared channel, in addition to the divergent section has an initial convergent section which allows for a weaker initial pressure gradient due to the larger interelectrode separation. This further enhances the anode depletion mechanisms thus reducing the current level at which arcing first appears. These trends have been indicated by the lack of oscillations in the constant area channel, their appearance in the partially flared channel at 61 kA, and their appearance in the fully flared channel at about 58 kA.

It may be possible for the pumping force, separately or in concert with the plasma expansion, to induce electrofluiddynamic separation. Such a separation has not been explicitly observed in the arcjet channel, and it is unclear as to whether such a separation would occur before the anode voltage fall would normally reach the level where it would break down under attached flow conditions. Furthermore, flow separation is difficult to initiate in accelerating flows; therefore, more analysis is necessary to determine whether such a phenomenon is possible in this type of

channel. But ordinary fluid-dynamic separation has been noted at the anode exit. The inability of the plasma to make an abrupt right angle turn causes the plasma to separate from the anode surface. Such results have also been noted by Barnett.[12]

The relationship of voltage hash with the onset phenomenon is not fully understood, but from this data, it is clear that the onset of anode starvation precedes the appearance of the large amplitude voltage oscillations. These oscillations are theorized as due to concentrated anode arcs which form in the presence of high anode voltage drops and are convected at a frequency characteristic of the plasma residence time in the channel.

Chapter VII: Conclusions and Recommendations for Future Research

VII.1: General Summary

This dissertation attempted to advance the understanding of the fluid-dynamics in an MPD arcjet with an additional emphasis on the phenomenology associated with onset. Physical understanding of the interaction of the flow and electromagnetic parameters is important and has been aided by some simplified theory. Subsequently, an experiment was designed to investigate some of the claims advanced by the theory.

The theory demonstrated the strong coupling of the electrodynamic fields with the fluid-dynamics of the arcjet. The high magnetic Reynolds' numbers characterizing the operation of these devices was shown to strongly influence the distribution of current throughout the channel. This work shows the importance of a converging-diverging geometry and its effect on flow acceleration and current distribution. The theory also detailed the thruster's inherent starvation mechanism brought about by the inherent two-dimensionality caused by a nonzero Hall parameter. But the approximate nature of all of these models necessitated the construction of an experiment to verify the anticipated trends in the arcjet's operation.

The primary successes of this dissertation were threefold. Firstly, theory was derived that helped gain intuition into the operation of the MPD arcjet. Secondly, the experiment verified the premise that current concentrations and thruster efficiency can be controlled through variation in interelectrode separation. And thirdly, the onset phenomena was

examined in detail and a new phenomenology was forwarded with experimental evidence persuasively demonstrating cause and effect.

This experiment also illustrated the unfortunate pitfalls inherent to simplified theory. The theory, although limited and not accurately predictive of discharge structure, showed important trends for arcjet design. Unfortunately, the inherent simplifications enabling solution do not allow for the appearance of many of the phenomena observed in the experiment. The overall anticipated trends briefly detailed in the previous chapters and in the appendices were noted, however the experiment demonstrated that the theories were very incomplete.

This experiment was designed to emulate a two-dimensional geometry and simulate the theory advanced in Chapter II. The large cathode radius and narrow channel was designed to minimize the overall 1/r effects of the actual cylindrical geometry. Unfortunately, the quest for two-dimensionality and discharge symmetry was not possible because of the antagonistic behavior of these requirements with the selected geometry. By selecting a geometry with a large cathode radius, high current levels were necessary to guarantee discharge uniformity. These levels corresponded to arcjet operation in an anode starvation mode for the selected geometries. It is undesirable to operate with a depleted anode due to the losses associated with the associated anode potential drop, but this geometry disallowed operation in an unstarved mode due to the unavoidable discharge asymmetry found at lower current levels.

This asymmetric behavior prevented arcjet operation before significant anode starvation occured. Because of this, the channel was

operating in a regime outside the range of validity of the theory derived in Chapter II. As a perturbation theory, any simulation where the value of the perturbation is of the same magnitude as the unperturbed quantity must be considered questionable. It would have been desirable to conduct an experiment and compare the results directly with the theoretical results. Unfortunately, this could not be accomplished in this experiment.

VII.1: MPD Arcjet Design Considerations

It is important to maxmize both MPD arcjet thrust and efficiency in order to provide a viable propulsion technology. In order to meet this goal, the designer must be aware of the various mechanisms associated with inefficiency and lifetime. The designer must understand that although thrust is monotonically increasing with current, high current operation can decrease thruster lifetime and efficiency if the thruster geometry is not selected to prevent current concentrations from eroding the electrodes and if the thruster is not operated prior to anode starvation.

This work does not point towards the ultimate design solution. It does show that a controllable, more uniform current distribution can be accomplished with a converging-diverging geometry. It also shows that there exists a limitation related to a depletion of mass in the anode region inhibiting efficient operation at desirable current levels. Since the latter phenomenon is associated with low plasma density in the region near the arcjet anode, the arcjet designer must be careful not to allow ordinary plasma expansion through a divergent section from lowering the

local plasma density to a starvation level. And, the designer must also be aware of the tradeoff noted between thruster size, discharge symmetry, and the operation in the vicinity of a depleted anode.

At the time being, the complete story is too poorly understood to stop doing research and build a flight ready device. In addition to the previously mentioned phenomena, very little is understood about a whole host of practical matters and their effects on the overall operation on the MPD arcjet. For example, it has been hinted in this work that the cylindricity of the arcjet is very important in the overall operation of the MPD arcjet. Other works have also discussed the importance of mass injection on the operation of the thruster.[5,6,7] Before real hardware is developed arcjet, more research must be undertaken with continued emphasis in theoretical, computational, and experimental development.

VII.2: Directions for Future Research

If electromagnetic propulsion is to become viable, it is necessary to continue with local analyses of the arcjet in order to get a fundamental understanding of the thruster operation, while at the same time advancing the numerical simulations to include cylindrical geometries, real gas and electrode effects, and other transient phenomena. Verification of the theory and numerical simuluations cannot be accomplished without strong experimental support. Cylindricity and real gas effects are important so as to understand the ultimate steady-state flow structure, and transient simulations including real electrode effects are of interest due to the complex performance limiting behavior associated with increased current

levels. The question of onset, or of the various onset mechanisms is still not fully understood, although strong evidence indicates the existence of a starvation mechanism. It is also important to elucidate from a fluid-dynamic and kinetic stance whether or not there exist unstable or poorly damped features of the discharge which are ignored by the theoretical formulations in this dissertation, and under what circumstances they can be made to disappear. Unfortunately, kinetic models and simulations are much more difficult to implement and understand.

Computational methods hold the ultimate key to thruster modeling and simulation. With them, parametric variations in thruster geometry and operating conditions can be done before any committment to experiment. Care must be taken with this approach because the approximate analyses, although imprecise, enlighten the scientists and engineers to the fundamental physics of the MPD discharge. In the large numerical simulations, the physics is often hidden by the code so that cause and effect can be hidden.

Verification of the localized theories and the numerical simulations is also necessary and experimentation can provide the only solution. The current lack of suitable facilities hampers this effort, and without clear cut direction, experiments often become misdirected and veer from a central path. The course of experimentation is also, by nature, expensive, slow, and subject to the vagaries of the experimental apparatus.

MPD arcjet experimentation and the associated diagnostic capabilities

have remained in the stone age when compared to our fusion counterparts. Large power supplies and vacuum systems capable of providing high power for steady-state operation are standard in most fusion operations, but because of size and cost are not available for the electric propulsion community. Apart from facilities, reliance on intrusive probing techniques is awkward, time consuming, and inaccurate. Placement of a probe in a plasma locally stagnates the flow reducing the local back emf. If the probe is near an electrode, arc initiation becomes a strong possibility since the local voltage is decreased. Once this occurs, the operational characteristics of the arcjet have been altered. Optical diagnosis must be utilized more completely. The Japanese have begun to experiment with geometries that facilitate such optical diagnosis. They have also developed innovative techniques for studying the magnetic field distribution with the use of a magnetic field sensitive film.[39]

Many interesting theories and data have been presented in this dissertation. Unfortunately the experimental geometry did not allow accurate emulation of the theory.

The central question is what experimental path should be undertaken in order to most efficiently understand the physics of the MPD arcjet. Data from this experiment indicated that the electrode falls account for a large fraction of the total voltage at all power levels below onset. Reduction of these losses is mandatory if efficient arcjet operation is to occur. Concurrently, the voltage attributed to the back emf should be maximized with respect to the minimum possible electrode falls in order to improve the arcjet efficiency to an acceptable value. Theory and

experiments should be designed to study the whole plasma structure instead of just a portion of it.

A two-dimensional geometry, such as used by the Japanese, would enable one to easily apply an external electric field to cancel the Hall effect and essentially provide one-dimensional MPD arcjet.[39] This would allow for analysis of the device and allow comparison to simple theories which study the plasma acceleration processes, ionization processes, boundary layer development, and high power operation in the absence of significant $\vec{j}x\vec{B}$ induced voltage falls. Photographic and spectrographic analysis of the configurations with or without an external electric field would be greatly facilitated and could be compared to analyze the pumping force's contribution to arcjet performance. Analysis of species distribution, densities, and temperatures would provide useful information regarding the state of nonequilibrium, the $\vec{j}x\vec{B}$ contribution to viscous losses, as well as other processes governing ionization and recombination in a fully two-dimensional geometry as compared with a one-dimensional channel. Once the differences between one- and two-dimensional geometries are more completely understood, more complex geometries, such as the cylindrical device or the Princeton benchmark channel could be diagnosed.

This type of program is less complicated for both physicists and computational fluid dynamicists. One- and two-dimensional geometries are much easier to model than axisymmetric or three-dimensional geometries. This allows for more detailed physics to be incorporated more readily into the various models, allowing for more complete and accurate arcjet simulations.

If MPD arcjets are to fly, then the performance question must be answered. This dissertation has focused on several aspects of the performance limiting features in arcjet operation, and has showed limited success in identifying and advancing solution to some of the effects previously, and in some cases wrongly, associated with the onset limitation. Many important questions still remain, and the path to solution is hazy, but it is there.

Appendix 1: Derivation of the Overall Induction Equation

The overall vector induction equation in cylindrical coordinates can be derived from the application of five equations. Ohm's law, Ampere's Law, Faraday's equation, the continuity equation, and an equation of state are written as follows

Ohm's Law:

$$\vec{J} + \vec{J} \times \vec{\beta} = \sigma \left(\vec{E} + \vec{u} \times \vec{B} + \frac{\nabla p_e}{e n_e} \right) \qquad \text{A1.1}$$

Ampere's Law:

$$\nabla \times \vec{B} = \mu_0 \vec{J} \qquad \text{A1.2}$$

Faraday's Law:

$$\nabla \times \vec{E} = - \frac{\partial \vec{B}}{\partial t} \qquad \text{A1.3}$$

Continuity:

$$\frac{\partial \rho}{\partial t} + \nabla \cdot (\rho \vec{u}) = 0 \qquad \text{A1.4}$$

State:

$$p = \rho R T \qquad \text{A1.5}$$

By assuming full ionization and constant temperature, an energy equation can be neglected, further simplifying the formulation. Under these assumptions, the equation of state can be rewritten as

$$p = 2 \, n_e \, k T \qquad \text{A1.7}$$

The curl of Ohm's law, combined with equation A1.7, results in

$$\nabla \times \vec{J} + \nabla \times \vec{J} \times \vec{\beta} = \sigma \left(\nabla \times \vec{E} + \nabla \times \vec{u} \times \vec{B} + \frac{2kT}{e} \nabla \times \nabla \ln n_e \right) \qquad \text{A1.8}$$

Equation A1.8 can be simplified to

$$\nabla \times \vec{J} + \nabla \times \vec{J} \times \vec{\beta} = \sigma \left(- \frac{\partial \vec{B}}{\partial t} + \nabla \times \vec{u} \times \vec{B} \right) \qquad \text{A1.9}$$

The first term, the curl of the current density, can be expressed in terms of the magnetic field by using equation A1.2 and various vector identities leaving

$$\nabla \times \vec{J} = \nabla \times \nabla \times \frac{\vec{B}}{\mu_0} = \frac{1}{\mu_0} [\nabla (\nabla \cdot \vec{B}) - \nabla^2 \vec{B}] \qquad \text{A1.10}$$

Since the magnetic field is solenoidal, equation A1.10 becomes

$$\nabla \times \vec{J} = - \frac{1}{\mu_0} \nabla^2 \vec{B} \qquad \text{A1.11}$$

The next term, the curl of $\vec{J} \times \vec{\beta}$, is

$$\nabla \times \vec{J} \times \vec{\beta} = \frac{1}{\mu_0} \nabla \times (\nabla \times \vec{B} \times c \frac{\vec{B}}{\rho}) \qquad \text{A1.12}$$

where

$$c = \frac{\sigma e}{m_i} \qquad \text{A1.13}$$

With some vector algebra, equation A1.12 expands to

$$\nabla \times \vec{J} \times \vec{\beta} = \frac{c}{\mu_0} \nabla \times (\frac{\vec{B}}{\rho} \cdot \nabla) \vec{B} - \frac{c}{\mu_0} \nabla (\frac{1}{\rho}) \times \nabla (\frac{B^2}{2}) \qquad \text{A1.14}$$

The final term in equation A1.9, the curl of the back emf, expands to

$$\nabla \times \vec{u} \times \vec{B} = (\vec{B} \cdot \nabla) \vec{u} - (\vec{u} \cdot \nabla) \vec{B} + \vec{u} (\nabla \cdot \vec{B}) - \vec{B} (\nabla \cdot \vec{u}) \qquad \text{A1.15}$$

The first term disappears, because the derivative of the velocity along the magnetic field (which only has an azimuthal component) is zero. As in equation A1.10, the third term also disappears, leaving equation A1.15 (when combined with the continuity equation, equation A1.4) as

$$\nabla \times \vec{u} \times \vec{B} = - \rho (\vec{u} \cdot \nabla) \frac{\vec{B}}{\rho} \qquad \text{A1.15}$$

Combining equations A1.11, A1.14, and A1.16 gives the vector induction equation for MPD flows under assumptions of a fully and singly ionized plasma at a constant temperature

$$\mu_0 \sigma \rho (\vec{u} \cdot \nabla) \frac{\vec{B}}{\rho} = - \mu_0 \sigma \frac{\partial \vec{B}}{\partial t} + \nabla^2 \vec{B} + c \nabla (\frac{1}{\rho}) \times \nabla (\frac{B^2}{2}) - c \nabla \times (\frac{\vec{B}}{\rho} \cdot \nabla) \vec{B} \qquad \text{A1.16}$$

The first term in equation A1.16 is the convection of the magnetic field

and the fluid density with the fluid, the second is the temporal variation of the magnetic induction, the third is the magnetic diffusion, the fourth is the Hall term, and the last is akin to a magnetic field "centripetal" term--that is, the change of the magnetic field along the magnetic field.

In cylindrical coordinates, this last term can be written as

$$\nabla \times \left(\frac{\vec{B}}{\rho} \cdot \nabla \right) \vec{B} = \left[0 , - \frac{B}{\rho r} \frac{\partial B}{\partial z} , - \frac{B}{\rho r} \frac{\partial (rB)}{\partial r} \right] \qquad \text{A1.17}$$

In a two-dimensional geometry, the variation of the magnetic field in its direction is exactly zero, and the two-dimensional induction equation becomes

$$\mu_0 \sigma \rho \left(\vec{u} \cdot \nabla \right) \frac{\vec{B}}{\rho} = - \mu_0 \sigma \frac{\partial \vec{B}}{\partial t} + \nabla^2 \vec{B} + c \nabla \left(\frac{1}{\rho} \right) \times \nabla \left(\frac{B^2}{2} \right) \qquad \text{A1.18}$$

Appendix 2: Analysis of the Equations of Motion for MPD Flows With Special Attention to Flows in the Limit of Infinite Magnetic Reynolds' Number

A2.1: Introduction

This appendix will focus on the analysis of the flows in an MPD channel extended to the limit of infinite magnetic Reynolds' number. The appendix will begin with a derivation of the one-dimensional MHD equations for MPD flows. A nondimensionalization scheme will be presented and the limit of infinite magnetic Reynolds' number will be analyzed. The infinite magnetic Reynold's number will then be extended to two-dimensional flows and an analogy to ordinary compressible gas dynamics will be established.

A2.2: One-Dimensional MPD Fluid Flow With Large Magnetic Reynolds' Number and Area Variation

In this model, the one-dimensional equations of motion for a constant temperature steady-state plasma can be written for both a truly one-dimensional channel and a one-dimensional channel with area variation of the form shown in figure A2.1. In this geometry, the y, or transverse axis, goes from the anode to the cathode; the x, or axial axis, is in the direction of the plasma flow; and the z axis, is in the direction of the magnetic field vector $\vec{B}$. This set of equations includes both conservation

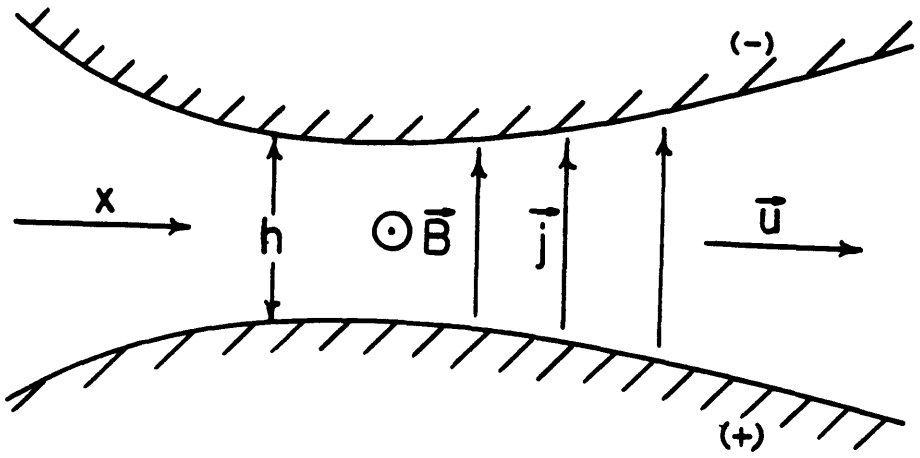

Figure A2.1: One-Dimensional Channel With Area Variation

of mass and momentum as well as a state equation written as

$$\rho u A = \dot{m} \qquad \text{A2.1}$$

$$\rho u \frac{du}{dx} = - \frac{d}{dx}\left(p + \frac{B^2}{2\mu_0} \right) \qquad \text{A2.2}$$

$$p = \rho R T \qquad \text{A2.3}$$

where Ampere's law

$$\nabla \times \vec{B} = \mu_0 \vec{j} \qquad \text{A2.4}$$

in one-dimension, has been substituted for the Lorentz force in equation A2.2. Two more equations, Ohm's law and Faraday's equation, are necessary to close the system. Ohm's law in two dimensions has the form

$$\vec{j} + \vec{j} \times \vec{\beta} = \sigma \left(\vec{E} + \vec{u} \times \vec{B} \right) \qquad \text{A2.5}$$

which, in one dimension, becomes

$$\frac{dB}{dx} = - \mu_0 \sigma \left(E - uB \right) \qquad \text{A2.6}$$

Neglecting two-dimensionality implies that mechanisms leading to two-dimensional structure cannot exist. This requires that there be no axial current in the MPD channel since it would produce a lateral component of the $\vec{j} \times \vec{B}$ force. This condition implies the need for an axial drop in electrode potential, perhaps accomplished through electrode segmentation. Faraday's equation

$$\nabla \times \vec{E} = - \frac{\partial \vec{B}}{\partial t} \qquad \text{A2.7}$$

for steady, one-dimensional flow is simply

$$EA = \text{constant} \qquad \text{A2.8}$$

It is useful to nondimensionalize these equations. One can postulate, from the structure of the continuity equation, the possible existence of a "throat" where the interelectrode separation is minimized.

By taking the logarithmic derivative of the continuity equation,

$$\frac{d\rho}{\rho} + \frac{du}{u} + \frac{dA}{A} = 0 \qquad \text{A2.9}$$

the differential, dA, may go to zero while the other two may not. This implies a throat in the channel. This would be an appropriate place for nondimensionalization because all the parameters will have magnitudes of order one throughout most of the channel. But, only the throat area is a known quantity. The unknown location of the throat as well as the unknown throat conditions make this nondimensionalization difficult to implement. And, for a constant area channel where there is no throat, this nondimensionalization is ambiguous. For this reason a more appropriate basis for nondimensionalization is at the channel entrance where all of the parameters may be specified, augmented with the channel area at the throat. These entrance values will be denoted by the subscript, $_0$, and the throat condition by the superscript, *, providing the following nondimensional forms

$$a = \frac{A}{A^*}\ , \quad b = \frac{B}{B_0}\ , \quad \rho' = \frac{\rho}{\frac{\mu_0 \dot{m}^2}{B_0^{\,2} A^{*2}}}\ , \quad u' = \frac{u}{\frac{B_0^{\,2} A^*}{\mu_0 \dot{m}}}\ , \quad e = \frac{E}{\frac{B_0^{\,3} A^*}{\mu_0 \dot{m}}}\ , \quad x' = \frac{x}{L}\ ,$$

$$\tau = \left(\frac{\dot{m}\,\mu_0}{A^* B_0^{\,2}}\right)^2 RT\ , \quad R_n = \sigma L \frac{B_0^{\,2} A^*}{\dot{m}}\ , \quad v = \frac{Vw}{\frac{B_0^{\,3} A^{*2}}{\mu_0 \dot{m}}} \qquad \text{A2.10}$$

where w is a mean channel depth. With these nondimensionalizations, equations A2.1 through A2.9 become

$$\rho' u' a = 1 \qquad \text{A2.11}$$

$$\rho' u' \frac{du'}{dx'} = -\frac{d}{dx'}\left(\tau\rho' + \frac{b^2}{2}\right) \qquad \text{A2.12}$$

$$\frac{db}{dx'} = -R_n\,(e - u'b) \qquad \text{A2.13}$$

$$ea = v \qquad \text{A2.14}$$

$$\frac{d\rho'}{\rho'} + \frac{du'}{u'} + \frac{da}{a} = 0 \qquad \text{A2.15}$$

where the two parameters, τ and R_m, appear. The interaction parameter, τ, as defined in equation A2.10, is the ratio of the square of the isothermal speed of sound to the square of the Alfven speed at the entrance. This gives an indication of the relative magnitudes of the two propagation speeds, as well as the importance of the two pressures on the plasma—the thermodynamic pressure, and the magnetic pressure. The second parameter, R_m, also defined in equation A2.10, is the magnetic Reynolds' number which relates the relative importance between the convection and diffusion of magnetic field in the magnetized plasma. The magnitudes of these parameters can be estimated with the help of Ampere's law written as

$$B_0 = \frac{\mu_0 J}{2\pi r_m} \qquad \text{A2.16}$$

where r_m is the mean radius at the channel entrance. For an anode radius of 7.5 cm, cathode radius of 5.0 cm, and total current of 30,000 A, the initial mean magnetic field, B_0 is approximately 0.096 T. For an argon mass flow rate of 4 g/s, and for a fully ionized argon plasma at 12,000 K, a plasma conductivity of 3300 mho/m, and a thruster 9 cm long, the values for these nondimensional parameters are calculated to be

$$\tau = 0.015 \text{ and } R_m = 6.7 \qquad \text{A2.17}$$

At these conditions, the small value for τ implies that the magnetic pressure is much more important than the thermodynamic pressure. It also implies that the characteristic isothermal speed of sound is about a tenth of the characteristic Alfven speed.

In the limit of infinite, or very high magnetic Reynolds' number, the body of the plasma is acting as if the flow is purely reactive, i.e. the electric field is determined by the back emf. Except in regions of

large magnetic field gradients (very high local current density), the plasma operates at a voltage just above the value of the back emf. Therefore

$$ea = v \simeq u'ba \qquad \text{A2.18}$$

With equations A2.11 and A2.14, this condition shows that the quantity

$$\frac{b}{\rho'} = v \qquad \text{A2.19}$$

is constant throughout the channel except near the inlet and exit where strong gradients are present. This condition is similar to the adiabatic invariants derived from simple charged particle motion in the presence of a spatially varying magnetic field. In this fluid-dynamic formulation, equation A2.19 implies that, in the limit of very high magnetic Reynolds' number, the magnetic field is convected with the flow. This condition will be refered to as the convective, or reactive limit. This relation greatly simplifies equation A2.12 by making it immediately integrable if the plasma temperature is assumed to be spatially constant

$$\frac{u'^2}{2} + vb + \tau \ln b = \text{constant} = G \qquad \text{A2.20}$$

The value for G, the momentum integral can be calculated from equation A2.18 evaluated at the origin where $a=a_0$ and $b=b_0$. Equation A2.20 does not apply all the way to the inlet plane in general, due to the existence of a singular current layer there. So while one can put $a=a_0$, one should not set $b_0=1$, but rather $b=b_0<1$, the difference $1-b_0$ becoming small as a_0 increases. In the limit where a_0 gets large, this value of G can be related to the nondimensional voltage as

$$G = v + \frac{v^2}{2a_0} \qquad \text{A2.21}$$

To solve for the nondimensional voltage, the continuity equation in the

form of equation A2.15, is solved for the derivative of ln(a) with respect to b in terms of b. This gives a minimum channel area at the value of the magnetic field where the derivative vanishes, which is, by definition of the nondimensionalization, where $b = b^*$. This condition helps determine v as

$$v = \left(\frac{3b^* - 2}{2}\right) a_0^2 + \left(\left(\frac{3b^* - 2}{2}\right)^2 a_0^4 + \tau a_0^2 (1 + 2 \ln b^*)\right)^{1/2} \qquad \text{A2.22}$$

In the limit of $\tau=0$,

$$\lim_{\tau \to 0} v = (3b^* - 2) a_0^2 \qquad \text{A2.23}$$

$$\lim_{\tau \to 0} G = \frac{(3b^* - 2)^2}{2a_0^2} + 3b^* - 2 \qquad \text{A2.24}$$

From these relations, the velocity and density at the throat can be calculated but are not done so due to their complexity.

For solution, it is easiest to make a specification for the magnetic field and then iterate to determine a voltage that will provide for the desired minimum channel area of unity.

This formulation for the high magnetic Reynolds' number flow is useful since it can be directly modified for a channel with a constant electrode separation. It was previously mentioned that another nondimensionalization based on the throat conditions is possible, but not convenient from an implementation standpoint. The convenience of this formulation is that the relationships between certain parameters can be demonstrated more cleanly and compactly. This approach will be demonstrated in the following section.

A2.2.1: Nondimensionalization of the One-Dimensional High Magnetic Reynolds' Number Model to the Throat Conditions

Nondimensionalization to the conditions at the throat of the channel makes the quantity b unity at the channel throat. Under this formulation, the quantity b(0) is not known and, along with v, must be found in order to satisfy the conditions of $b^* = a^* = 1$. But, under this nondimensionalization, the relationships for all of the other quantities become simpler. Once again, the momentum integral can be solved for at the throat instead of at the entrance, arriving at a similar result

$$G = v + \frac{v^2}{2} \qquad \text{A2.25}$$

The momentum integral can also be found by minimizing the area from the continuity equation A2.15 leaving

$$G = \frac{\tau + 3v}{2} \qquad \text{A2.26}$$

These two equations can be solved for v

$$v = \frac{1}{2} + \left(\frac{1}{4} + \tau \right)^{1/2} \qquad \text{A2.27}$$

This relation shows that the voltage and the interaction parameter are not independent. Substituting equation A2.27 into equation A2.26 shows that G and τ are also not independent

$$G = \frac{\tau + 1.5 \left(1 + (1 + 4\tau)^{1/2}\right)}{2} \qquad \text{A2.28}$$

In the limit of $\tau=0$, $G \to 1.5$ and $v \to 1$. In the additional limit of u(0)=0, the limiting values for b(0) and $\rho(0)$ can be found as

$$\lim_{\substack{\tau \to 0 \\ u(0) \to 0}} b(0) = \lim_{\substack{\tau \to 0 \\ u(0) \to 0}} \rho(0) \to \frac{3}{2} \qquad \text{A2.29}$$

This result is somewhat misleading. The range of validity of this model does not allow for one simultaneously to neglect sonic passage (by neglecting τ) and go to u'(0)=0. Martinez-Sanchez has shown that the

correct procedure is to match as $x \to 0^+$ the solution to an "inner" solution which gives a nonzero value for $u'(0)$. The only condition where the previous limit may approach validity is if the initial area is so large that $u'(0^+) \to 0$.[27]

Back substituting equations A2.19 into A2.18 with equation A2.27 gives the velocity and density at the throat as

$$u'^* = \left(\tau + \frac{1 + (1+4\tau)^{1/2}}{2}\right)^{1/2} \quad \text{and} \quad \rho'^* = \frac{2}{1 + (1+4\tau)^{1/2}} \qquad \text{A2.30}$$

In dimensional terms, the first relation in A2.30, states that the speed at the channel throat is the local isothermal magnetoacoustic speed, defined as the speed of propagation of a pressure wave in a compressible magnetized medium. In the limit of $\tau=0$, the flow is limited by the local Alfven speed, $B^2/\mu_0\rho$. The channel, in this limit, also behaves like an ordinary isentropic gas with a specific heat ratio of two. This analysis implies that the one-dimensional infinite magnetic Reynolds' number MPD arcjet, to zeroth order, is mathematically analogous to an ordinary compressible gas.

Several other important features can be observed in this simplified model of the MPD discharge. The theory implies that inviscid flow of a plasma at high magnetic Reynolds' number in a channel with a constant electrode separation is everywhere magnetosonic. For this to occur, there must exist an initial layer to accelerate the plasma. In this layer, the convective limit of b/ρ'=constant breaks down and requires further local analysis. Here, many different phenomena occur including ionization, the initial rise in conductivity, and the initial plasma acceleration. This dissipative layer has a thickness on the order of $1/R_m$ since the

transition to convective domination begins at a local magnetic Reynolds' number of unity. So as the magnetic Reynolds' number is increased, the initial dissipation layer is reduced in depth. The exit of the arcjet has some similar characteristics of this thin entrance layer.

At the exit, the plasma further expands to match the ambient conditions of zero field and pressure. This expansion occurs in a finite distance, but in the limits of this model, the magnetic field must go to zero at the exit. This is somewhat severe as it implies a significant current concentration at the exit (see figure A2.2). In reality, both of these trends appear, and are attributed to the low back emf at the entrance and exit due to the low initial velocity and the low exit magnetic field. If the channel is given an interelectrode converging-diverging variation, magnetosonic speed is reached at the throat, and the corresponding axial variation in magnetic field is controlled by the axial variation in interelectrode separation.

In ordinary inviscid nozzle flow of a compressible gas, the axial area variation is solely of function of pressure ratio. The nozzle is designed to produce a pressure drop to maximize thrust at a specific altitude and to minimize boundary layer development, separation, etc..., the latter being primarily second order considerations. In the MPD arcjet, this analysis shows that specification of a smoothly decreasing magnetic pressure along the channel implies a converging-diverging electrode separation. Any specification can be chosen, with the result that each will lead to a different resultant geometry. This is an important consideration, for if one controls the magnetic field variation

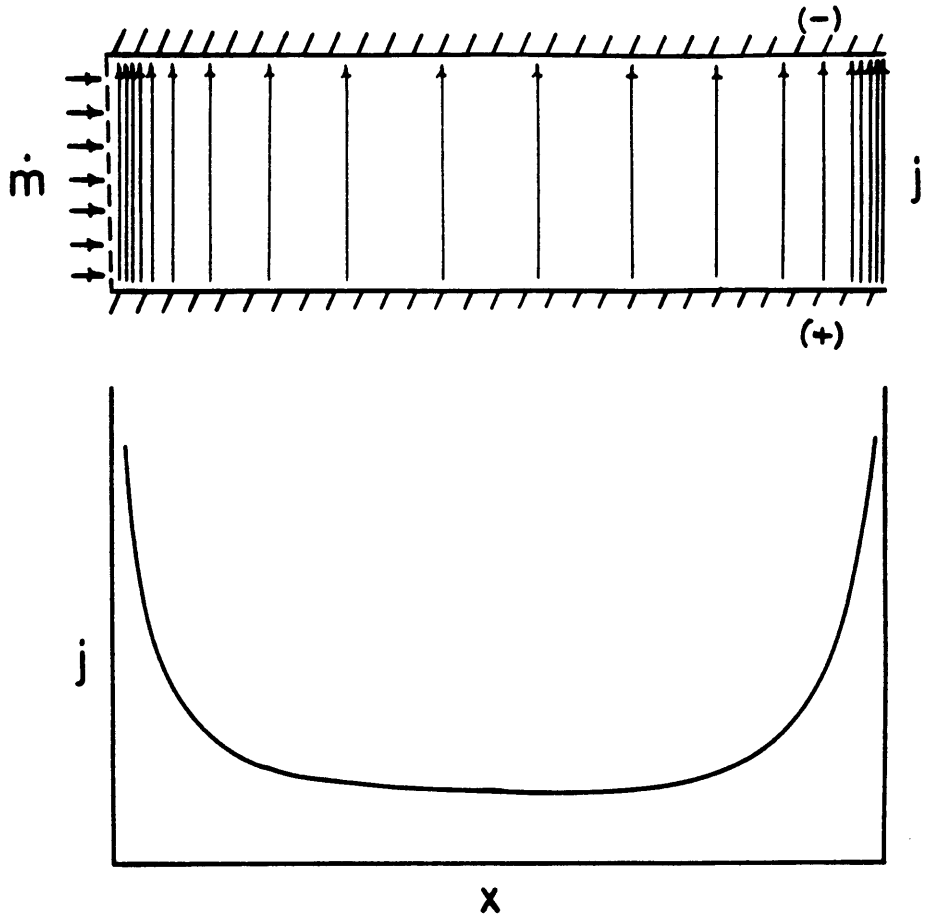

Figure A2.2: Constant Area MPD Channel at High Magnetic Reynolds' Number

along a channel, the current density becomes specified along the electrodes. It may then be possible to minimize the local current concentrations which have been associated with significant thruster erosion. Physically, variation of the interelectrode separation changes the local electric field, which, in the absence of dissipation and electrode sheath effects, drives the current density. Figure A2.3 shows the qualitativie comparison between a constant gap channel and a flared channel. In this figure, the separation of the constant area channel is the same as the throat separation on the flared channel. The effect of electrode flaring on actual current density concentrations can be seen in the works by Yoshikawa, Kuriki, and Uematsu.[40-42]

In the limit of this model, it is assumed that the conductivity of the plasma is sufficient to support the assertion that the electric field is determined by the back emf. At the entrance, the local magnetic Reynolds' number is finite and small. Here diffusive effects are important. At the exit, convective effects prevent the magnetic field from dropping to zero so drastically. For these reasons, this model is by no means a complete and accurate picture of MPD arcjet physics; however, it does elucidate some interesting behavior of the zeroth order fluid-dynamics in MPD arcjet flows. This limit can also be used to extend the analysis to two-dimensional flows. This will be accomplished in the following section.

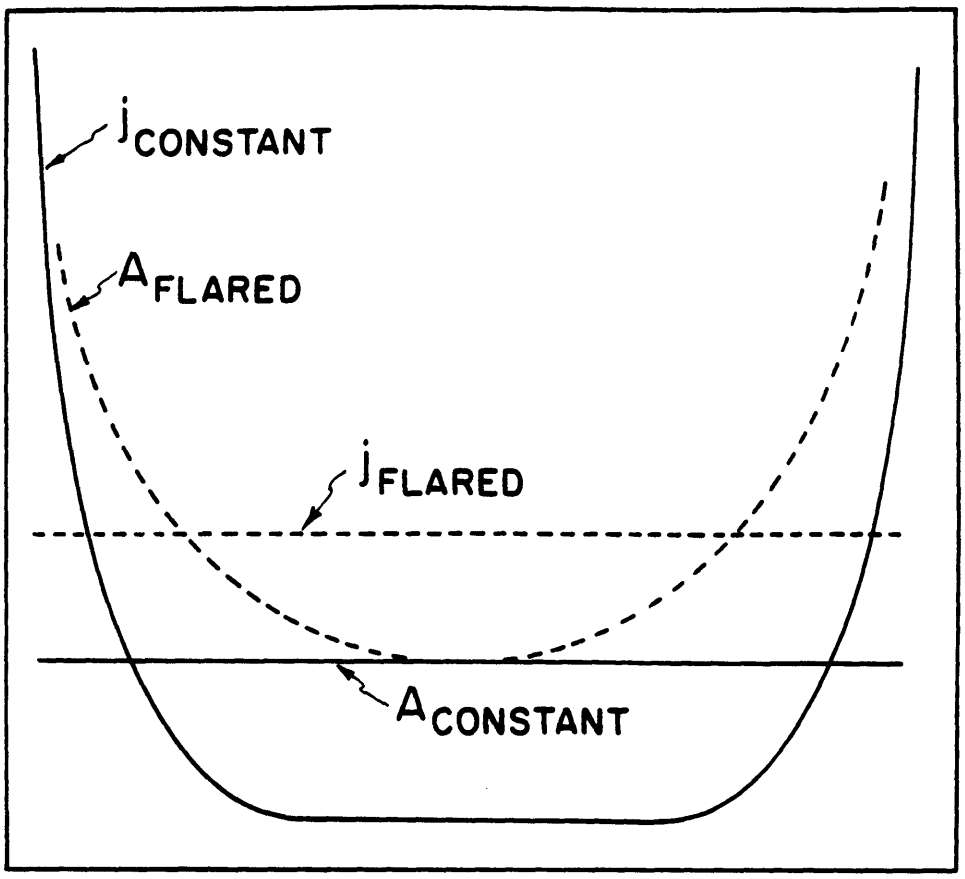

Figure A2.3: Qualitative Comparison of the Current Density and Interelectrode Separation Between the Constant Area and Flared MPD Geometries

A2.2.2: The Limit of Infinite Magnetic Reynolds' Number on Two-Dimensional Flows

In this brief section, the infinite magnetic Reynolds' number limit will be extended to discern some general fluid-dynamic trends in two-dimensional MPD arcjet flows. A starting point for this analysis is the general induction equation derived in Appendix 1, equation A1.18

$$\mu_0 \sigma \rho \left(\vec{u} \cdot \nabla \right) \frac{\vec{B}}{\rho} = - \mu_0 \sigma \frac{\partial \vec{B}}{\partial t} + \nabla^2 \vec{B} + c \nabla \left(\frac{1}{\rho} \right) \times \nabla \left(\frac{B^2}{2} \right) \qquad \text{A2.31}$$

This equation can be rewritten in a nondimensional form containing the magnetic Reynolds' number. For a steady-state flow at infinite magnetic Reynolds' number and finite Hall parameter, this equation reduces to

$$\left(\vec{u}' \cdot \nabla \right) \frac{\vec{B}}{\rho'} \simeq 0 \qquad \text{A2.32}$$

showing that the quantity $\vec{B}/\rho'$ is still a convective quantity. This implies that streamlines become equipotentials in the convective limit.

The nondimensional, inviscid, steady state, two-dimensional momentum equation

$$\rho' \left(\vec{u}' \cdot \nabla \right) \vec{u}' = - \nabla \left(\tau \rho' + \frac{b^2}{2} \right) \qquad \text{A2.33}$$

is written in this form by rewriting the Lorentz force density in terms of the magnetic stress tensor for a two-dimensional geometry. In a slender geometry, the transverse component of the momentum equation shows that the total pressure, Π, is solely a function of axial coordinate,

$$\Pi(x) = \tau \rho' + \frac{b^2}{2} \qquad \text{A2.34}$$

and with equation A2.32 shows that the total pressure is only a function of density (barotropic) and on a streamline,

$$\Pi(x) = \tau \rho' + \frac{1}{2} \left(\frac{b}{\rho'} \right)^2 \rho'^2 \qquad \text{A2.35}$$

The axial momentum equation can be written as a Bernoulli-like

conservation equation, on a streamline, under conditions of high magnetic Reynolds' numbers

$$\vec{u}' \cdot \nabla \left(\frac{u'^2}{2} + \tau \ln \rho' + \left(\frac{b}{\rho'}\right)^2 \rho'^2 \right) = 0 \qquad \text{A2.36}$$

For a slender channel in the limit as $\tau \to 0$, the quantity b/ρ' is transversally constant and therefore is the same on all streamlines.

In the limit as $\tau \to 0$, the total pressure is proportional to the square of the density, or that the plasma, once again, behaves as an isentropic gas with a specific heat ratio, τ, of two. For this flow, the magnetosonic velocity can be defined as

$$a_{ma}^2 = \left(\frac{\partial \Pi}{\partial \rho}\right)_s = \tau + \frac{b^2}{\rho'} \qquad \text{A2.37}$$

From this analysis, it is possible to make additional comparisons to ordinary compressible gasdynamics. The existence of a magnetoacoustic velocity implies the existence of shocks and expansion waves of the Prandtl-Meyer family. But because of the convection of the magnetic field with the flow, these Prandtl-Meyerlike expansions, being isodensity lines, are also lines of constant magnetic field and therefore lines of electric current. This implies that an underexpanded MPD channel will have an expansion fan whose strength is commensurate with the degree of underexpansion. If it is strong, the point where the expansion waves coalesce will have large current concentration and local dissipation. This would act to increase local thruster erosion.

The analogy of infinite magnetic Reynolds' number MPD flows with ordinary compressible gasdynamics is useful. Although plasma flows at such high magnetic Reynolds' numbers are not ordinarily seen in MPD arcjets, the basic principles of ordinary gasdynamics are applicable to

MPD flows and allow for some remarkable comparisons and simplifications useful for building intuition into the arcjet behavior.

Appendix 3: Numerical Simulation of One-Dimensional MPD Flows at Finite Magnetic Reynolds' Numbers

For finite magnetic Reynolds' number, equations A2.11-A2.14 can be solved numerically. The problem, in theory, is a simple boundary value "shooting problem". For a given axial specification of magnetic field, the exit boundary condition of b(1)=0 is matched by varying the nondimensional voltage. This, in practice, is very difficult due a need for sonic passage. A nonzero value for τ requires passage through the sonic point singularity (located very near the inlet), as well as satisfaction of b=0 at the exit. The throat is exactly magnetosonic only when the magnetic Reynolds' number goes to infinity, but it is nearly magnetosonic for values of the magnetic Reynolds' number of interest (>2). Martinez-Sanchez has shown that the overall voltage is determined by the magnetoacoustic choking phenomenon in the body of the discharge, and that sonic passage, which occurs near the channel entrance is related to the voltage, but its role is to set the inlet conditions.[27] He also shows that for constant area channels, the effects of the thermodynamic pressure can strongly affect the arcjet characteristics. From a numerical standpoint, it would be desirable to neglect the thermal effects inside the arcjet by setting the interaction parameter, τ, to zero. But for lower magnetic Reynolds' numbers, he shows that there are two local phenomena which occur that affect the overall arcjet operation. In the

constant area channel, where the magnetic field is forced to zero at the exit, the arcjet becomes thermally choked. Because of this, the strength of the exit layer (dependent on the magnetic Reynolds' number) controls the local dissipation and determines the exit temperature and the local sonic condition. The strong dissipation causes the thermodynamic pressure to rise which, in the absence of a strong $\vec{j}x\vec{B}$ pumping force, acts to decelerate the plasma flow. This exit requirement can force the existence of a shock condition inside the channel since the magnetic field must be continuous and the thruster length and exit conditions are physically specified. Such conditions show the strong role of the thermodynamic pressure in the physics of the constant area arcjet. These phenomena tend to increase thruster dissipation and slow the plasma thereby decreasing the back emf and with it, the overall voltage of the arcjet. In the flared geometries, the strong aerothermodynamic effects are mitigated to some extent by the expansion in the diverging section and the lowered dissipation in both the converging and diverging sections. So, although it may be possible to neglect τ in the flared geometries, it is not really valid to neglect the interaction parameter in the nonflared thrusters.

For very small values of τ, it is easy to find a numerical solution, but for larger values, the solution search becomes very difficult. Martinez-Sanchez saw that this region is characterized by very steep gradients in density, velocity, and area, thus making solution tedious. When real gas effects, such as viscosity and variable electrical conductivity, are included (as in the next section) nonzero values of τ make solution very difficult. So, in this analysis, the thermodynamics of

the discharge will be neglected for simplicity (by setting τ=0) with the understanding that this assumption can strongly alter the numerical results for the finite magnetic Reynolds' number operation of a constant area channel, especially at lower magnetic Reynolds' numbers (< 5).

Neglecting τ makes numerical solution almost trivial. Results for both constant and a variable area channels, with τ=0, at magnetic Reynolds' numbers of 1, 5, and 10 are found in figures A3.1 through A3.6. The variable area channels are calculated based on a linear axial distribution of magnetic field while the constant area channels have a fixed area and the magnetic field variation is whatever it has to be.

Several interesting features are noted in these graphs. In figure A3.7, the thruster voltage is shown versus the magnetic Reynolds' number for an inviscid, constant conductivity, constant length channel. The voltage is monotonically decreasing, with the flared channel voltage being slightly higher for a given magnetic Reynolds' number. In this graph, increased magnetic Reynolds' number implies a more reactive flow. In other words, the contribution to the voltage by Ohmic dissipation is less than that due to the back emf. This is further evidenced by the reduced difference between the total voltage and the back emf as the magnetic Reynolds' number is increased. This trend is seen in figures A3.1 to A3.6 where the quantity $(e-ub)_{MAX}$ is found to decrease monotonically with increasing magnetic Reynolds' number.

Another feature shown in figures A3.1 to A3.6 is that the magnetoacoustic number at the throat is not quite unity. This is due to the fact that the magnetic Reynolds' number in these channels is not

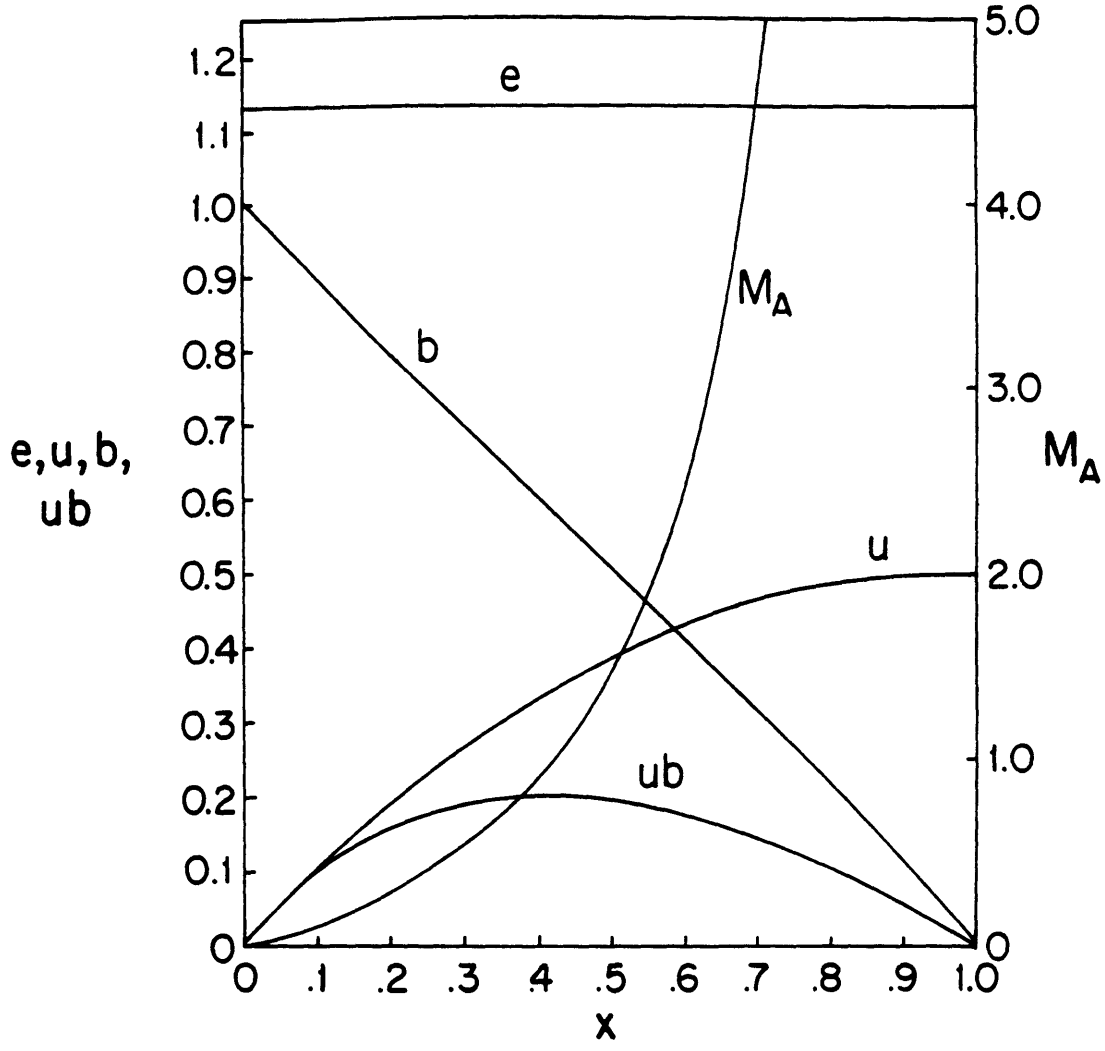

Figure A3.1: Distribution of Arcjet Parameters for the Inviscid Constant Area Channel at a Magnetic Reynolds' Number of One and an Argon Mass Flow Rate of 4 g/s

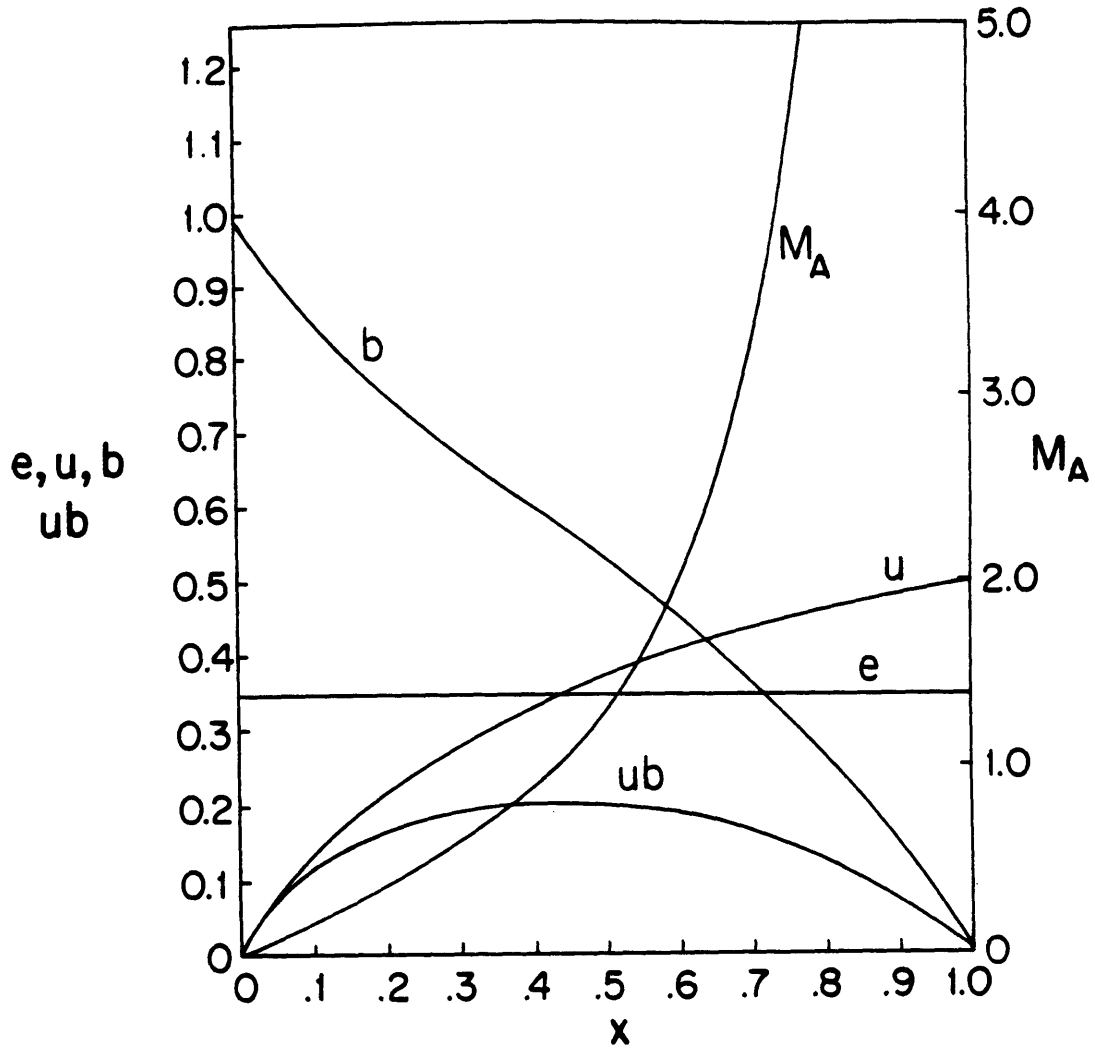

Figure A3.2: Distribution of Arcjet Parameters for the Inviscid Constant Area Channel at a Magnetic Reynolds' Number of Five and an Argon Mass Flow Rate of 4 g/s

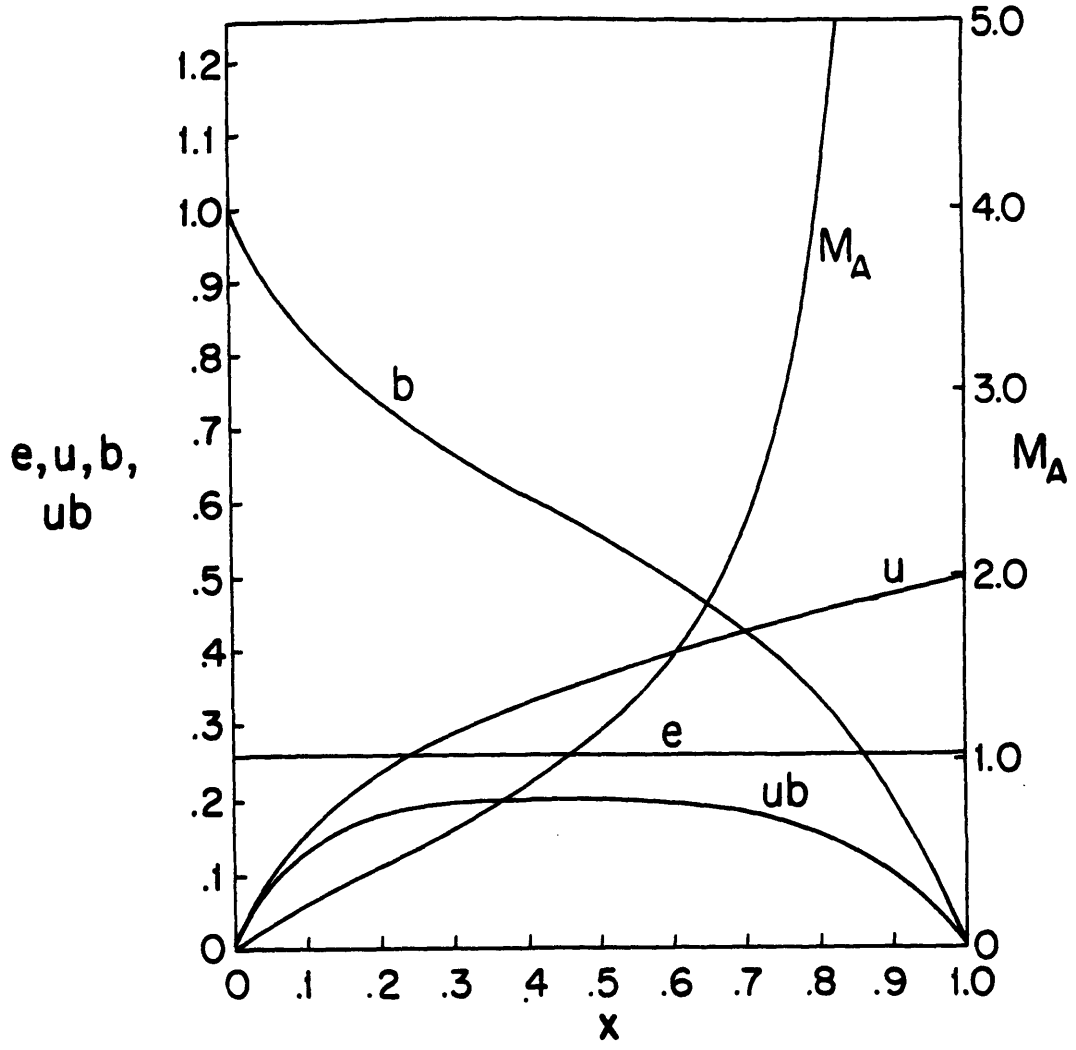

Figure A3.3: Distribution of Arcjet Parameters for the Inviscid Constant Area Channel at a Magnetic Reynolds' Number of Ten and an Argon Mass Flow Rate of 4 g/s

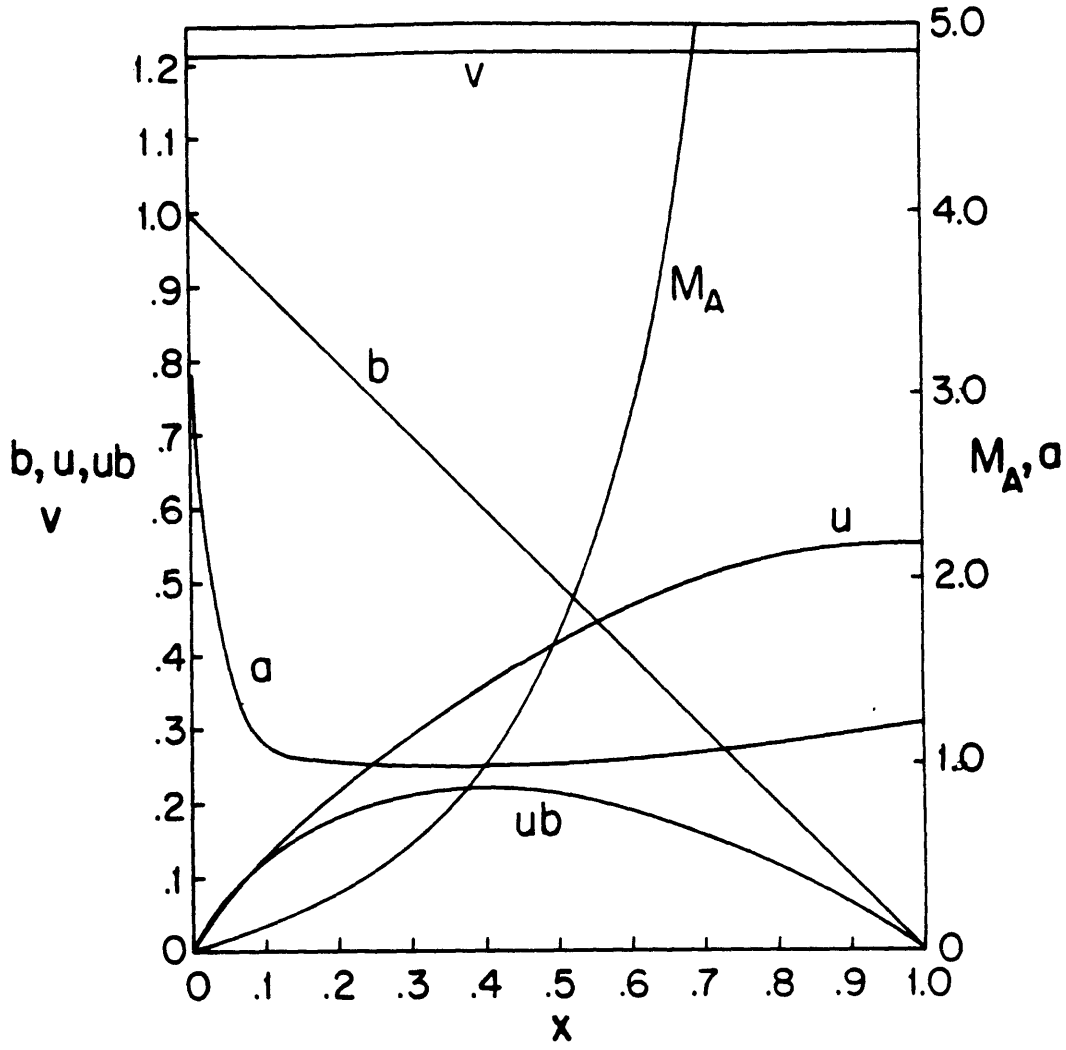

Figure A3.4: Distribution of Arcjet Parameters for the Inviscid Flared Channel at a Magnetic Reynolds' Number of One and an Argon Mass Flow Rate of 4 g/s

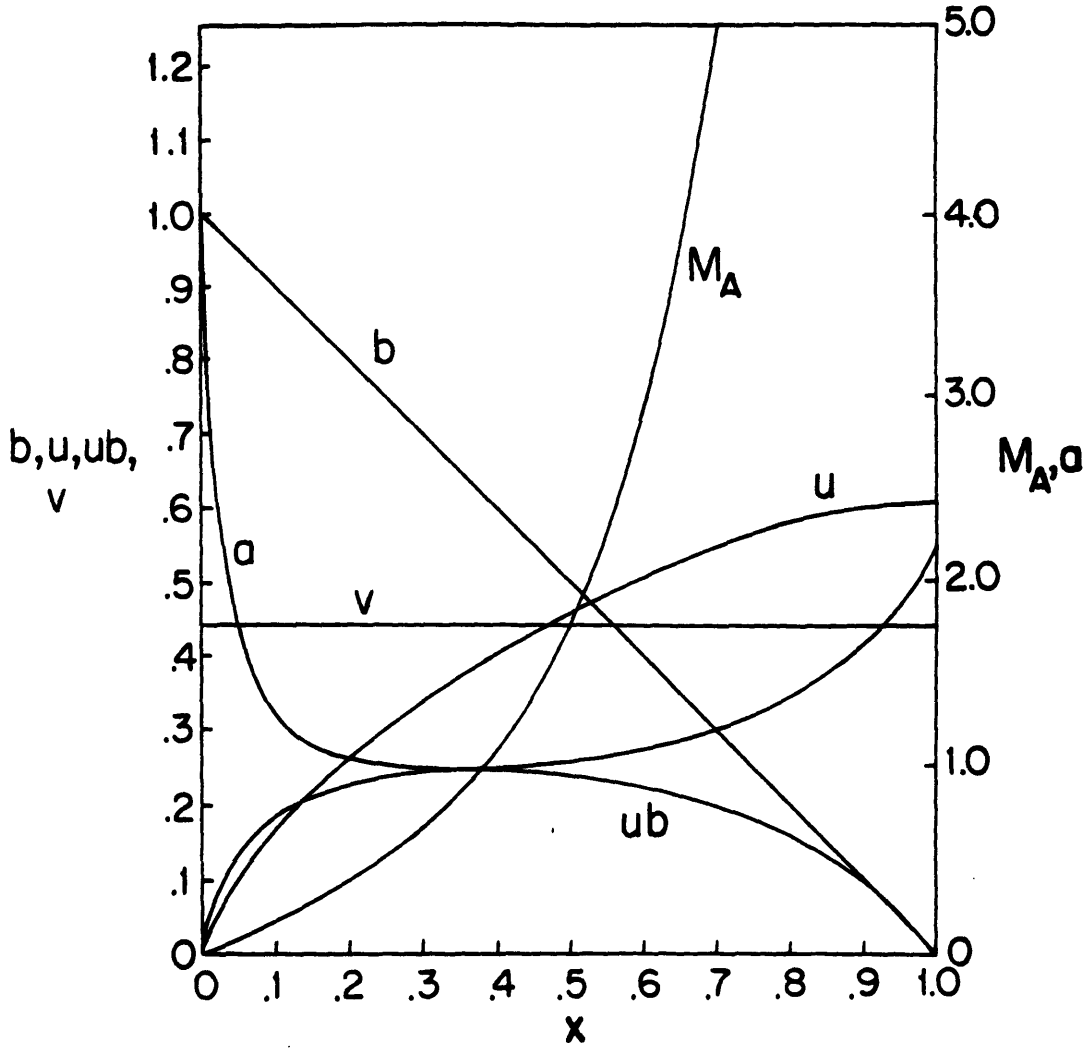

Figure A3.5: Distribution of Arcjet Parameters for the Inviscid Flared Channel at a Magnetic Reynolds' Number of Five and an Argon Mass Flow Rate of 4 g/s

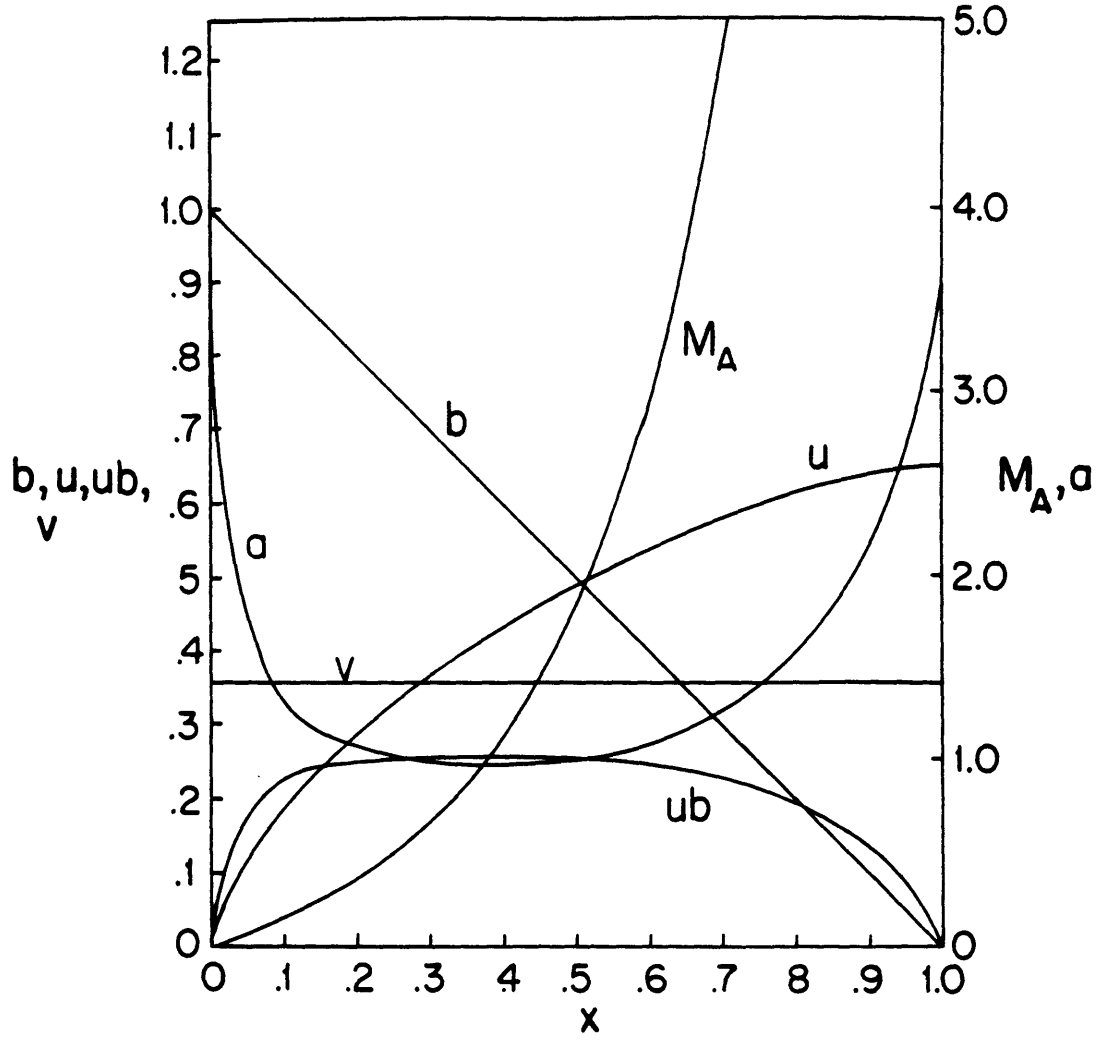

Figure A3.6: Distribution of Arcjet Parameters for the Inviscid Flared Channel at a Magnetic Reynolds' Number of Ten and an Argon Mass Flow Rate of 4 g/s

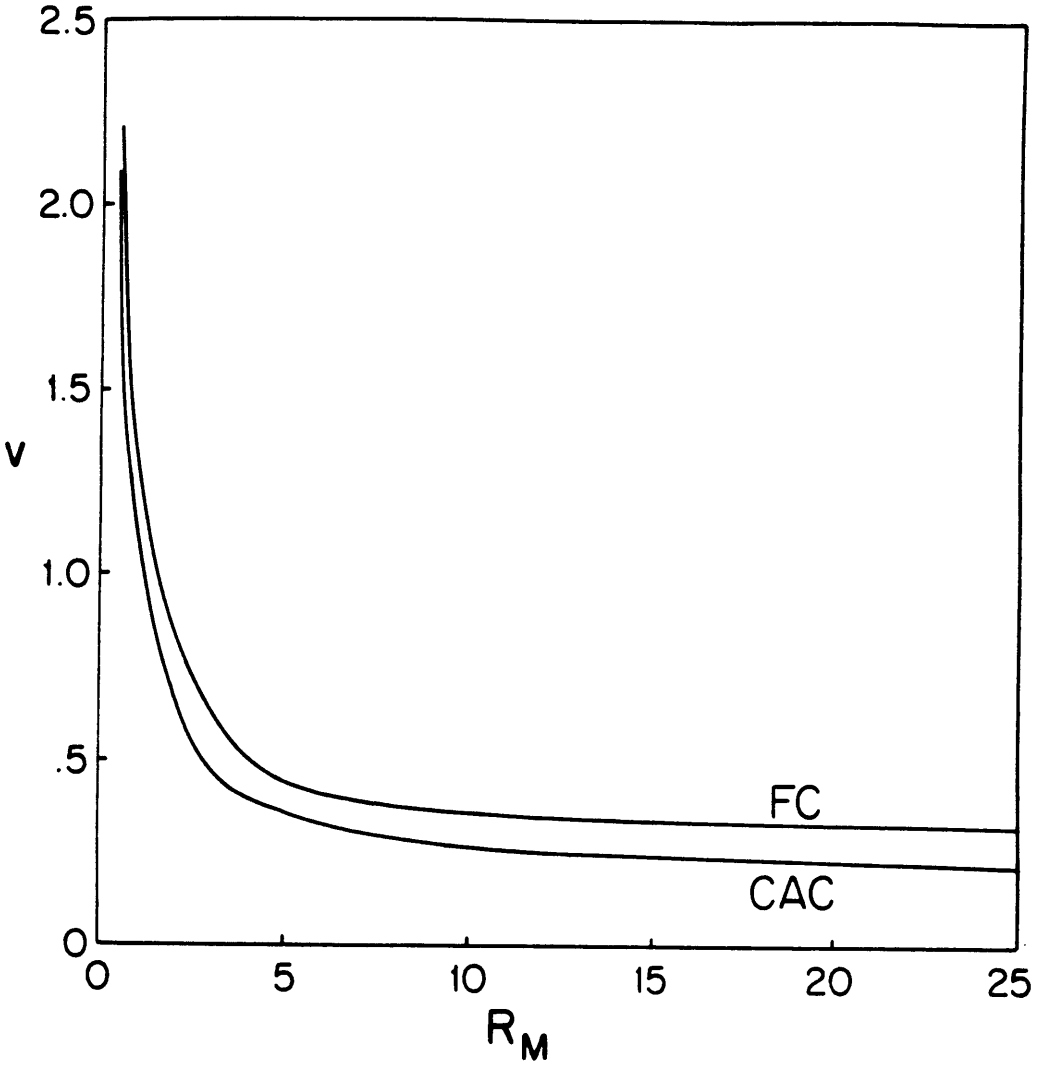

Figure A3.7: Nondimensional Voltage as a Function of Magnetic Reynolds' Number for Constant and Flared Geometries at an Argon Mass Flow Rate of 4 g/s

infinite. In the case of finite magnetic Reynolds' number flows, Ohmic dissipation is important, so the choking speed is close to, but not identically magnetosonic.

It is interesting to note that as the flow becomes more reactive (less dissipative), larger area variations are necessary in the flared channels to control the stronger inlet and exit current concentrations associated with higher magnetic Reynolds' number flows. The increased back emf tends to reduce the current carrying burden of most of the channel and load the two ends of the channel. Therefore, in order to keep the current density as specified, the interelectrode separation must increase.

The constant area channel behaves a little differently than one might expect. In this geometry, there is no explicit choking point. It is expected, from the infinite magnetic Reynolds' number example, that the whole channel is choked and little current is distributed through the channel body, or for a channel with a finite magnetic Reynolds' number, that the exit be the choking point. However, solution requires the artificial stipulation that the magnetic field go to zero at the exit. This satisfies the channel's length boundary condition explicit in Ohm's law. By forcing the magnetic field to zero, the behavior at the channel exit loses some of its physical meaning. At the exit, the local magnetosonic speed is zero in the limit as $\tau \to 0$, and the local magnetosonic number is infinite. The nondimensional equations for the constant area channel solution show that for $\tau=0$, all the magnetic pressure goes to plasma acceleration providing for a maximum velocity of 0.5. This is a

direct result from equation A3.12. But, in the numerical calculation, the local magnetoacoustic number is based on the local Alfven speed which is infinite at the exit, implying that the flow is magnetosonic somewhere upstream towards the middle of the channel. This is somewhat articial since the actual magnetoacoustic speed is a combination of the squares of the thermodynamic speed of sound and the Alfven speed, and although the Alfven speed goes to zero as the magnetic field decreases, the thermodynamic speed of sound does not and becomes dominant, keeping the local magnetoacoustic number finite. It so happens that as the magnetic Reynolds' number increases, the back emf approaches the electric field, and less acceleration occurs in the channel bulk, driving the magnetosonic passage further downstream.

The numerical results for both the constant area and variable area channels can be constructed into a voltage-current characteristic. This plot characterizes the transition from electrothermal to electromagnetic acceleration. Figure A3.8 is this plot drawn with log-log axes. Ohm's law, equation A2.6, shows that in the limit of low current, when there is little acceleration and the back emf is negligible, the local electric field goes directly with the applied current under the assumption of constant conductivity. At high magnetic Reynolds' numbers, the flow was shown to be purely reactive, and the voltage, in turn, is governed by the back emf. Under these circumstances, the voltage becomes proportional to the cube of the current and inversely proportional to the mass flow rate

$$\lim_{R_m \to \infty} V = \frac{J^3}{\dot{m}} \qquad \text{A3.1}$$

This behavior is indicated in figure A3.8 for both geometries, although

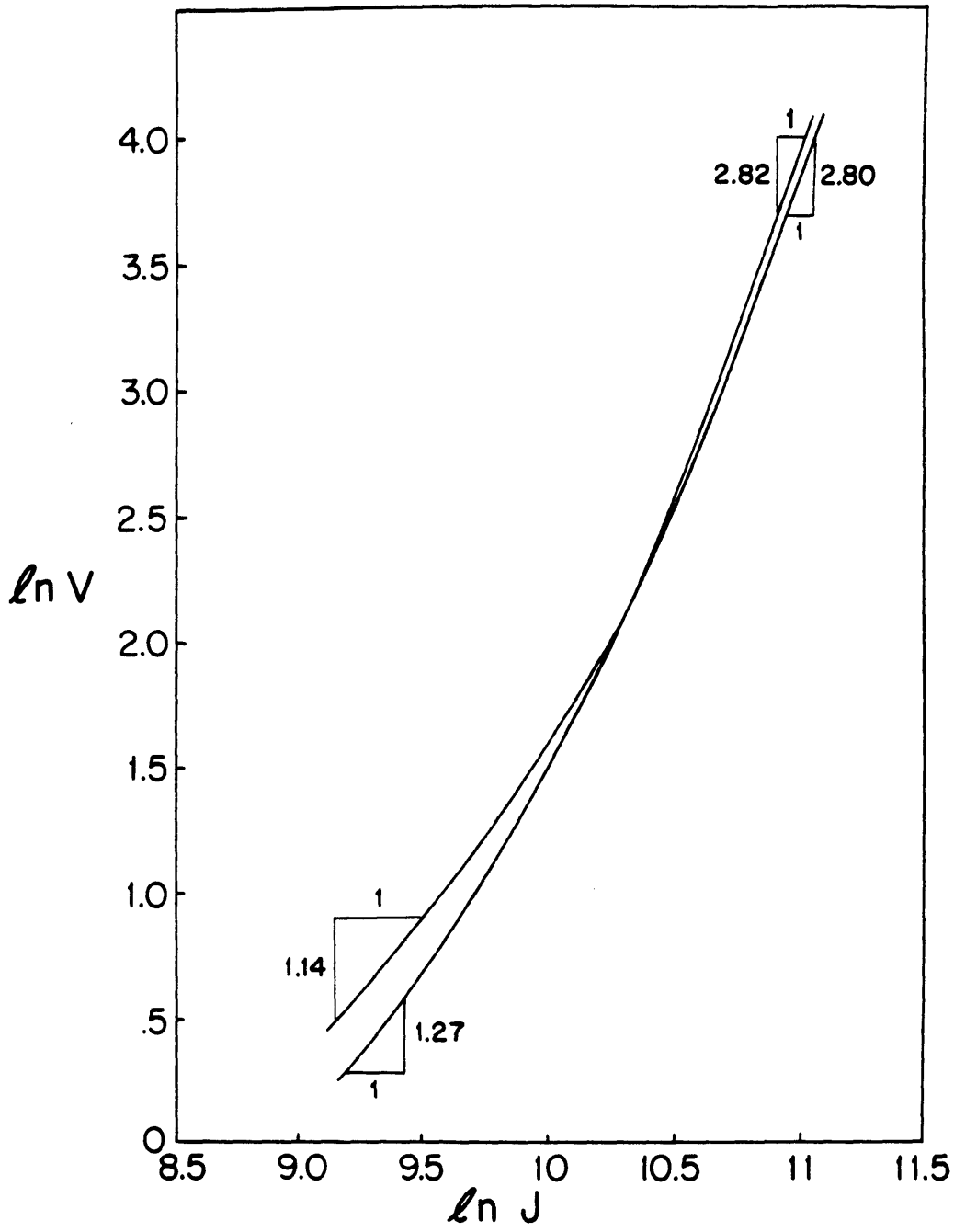

Figure A3.8: Logarithmic Plot of the Theoretical Voltage as a Function of Varied Thruster Current in the Constant and Flared Geometries at an Argon Mass Flow Rate of 4 g/s

the linear behavior is not quite demonstrated, most probably due to the magnitude of the magnetic Reynolds' numbers selected.

Without a more clear connection between the sonic passages, the plasma voltage, and the entrance conditions, solution of this numerical problem is difficult. It has been greatly simplified by neglecting the thermodynamic sonic passage which may be valid for the converging-diverging geometry, but is questionable for the constant area channels. The zeroth order channel behavior is not strongly affected by this limitation, and some of the anticipated discharge structures, indicated by experiment, are seen. These models presented so far, lack any significant two-dimensionality and therefore cannot be used to predict the occurrence of any anode related starvation and onset mechanisms. But the basic role of the magnetic Reynolds' number, for preonset flows or flows with applied electric fields (that cancel the Hall currents), is shown mathematically to demonstrate trends that are physically significant and applicable to MPD arcjet design.

Appendix 4: Derivation of an Approximate Two-Dimensional Solution to the MPD Induction Equation

A4.1: Introduction

One-dimensional models of the MPD arcjet have their utility in simplicity and ease in demonstrating some important overall parametric behavior. But by construction, they lack many of the significant features of two-dimensionality. The plasma discharge, because of the Hall effect, is at best, two-dimensional. The inclusion of an additional spatial dimension introduces significant complexity due to the strong coupling and nonlinear vector nature of the conservation equations. For solution, simplifications must be made.

These simplifications must be physically reasonable, otherwise model validity becomes questionable. Many simplifications may be severe enough for the model to be rendered so imprecise that it becomes merely a guideline, or only an approximate algebraic representation of the relation between the various physical discharge parameters.

The following model is based on the MHD fluid formulation outlined in Chapter II. It attempts to make a less restrictive jump to two-dimensionality than Baksht, at the same time eliminating strong two-dimensional effects by design (e.g. cylindricity). The ultimate validity of the model can be tested either by experiment, numerical simulation, or more detailed theory. Primary credit for this work goes to

Professor Manuel Martinez-Sanchez at MIT where it evolved during 1985.

A4.2: Simplification of the Induction and Momentum Equations

This derivation is carried out for the two-dimensional geometry shown in figure A4.1. An appropriate starting point for this derivation is the induction equation for a two-dimensional geometry expressed in equation A1.18 which is derived in Appendix 1

$$\frac{\partial^2 B}{\partial x^2} + \frac{\partial^2 B}{\partial y^2} + \frac{cB}{\rho^2}\left[\frac{\partial B}{\partial x}\frac{\partial \rho}{\partial y} - \frac{\partial B}{\partial y}\frac{\partial \rho}{\partial x}\right] = \mu_0 \sigma \rho \left(u \frac{\partial}{\partial x}\left(\frac{B}{\rho}\right) + v \frac{\partial}{\partial y}\left(\frac{B}{\rho}\right)\right) \quad \text{A4.1}$$

Strong two-dimensional effects can be simplified by the use of the "thin channel" assumption widely used in boundary layer theory. In the thin channel assumption, the characteristic axial dimension is much larger than the transverse dimension, allowing several terms with derivatives to be neglected. Under this assumption, the transverse magnetic diffusion term is of higher order than its axial counterpart except in the thin transition region commensurate with the distance associated with a magnetic Reynolds' number of unity. In this geometry, the thin channel also prevents significant transverse velocity from accumulating, which allows tranverse convection of the magetized plasma to be neglected in comparison to axial convection. This leaves the two-dimensional induction equation in the form

$$\frac{\partial^2 B}{\partial y^2} + \frac{cB}{\rho^2}\left[\frac{\partial B}{\partial x}\frac{\partial \rho}{\partial y} - \frac{\partial B}{\partial y}\frac{\partial \rho}{\partial x}\right] = \mu_0 \sigma \rho u \frac{\partial}{\partial x}\left(\frac{B}{\rho}\right) \quad \text{A4.2}$$

which will be further simplified by use of the momentum equation.

The inviscid steady-state MHD momentum equation can be written in vector form as

$$(\rho \vec{u} \cdot \nabla)\vec{u} = -\nabla p + \vec{J} \times \vec{B} \quad \text{A4.3}$$

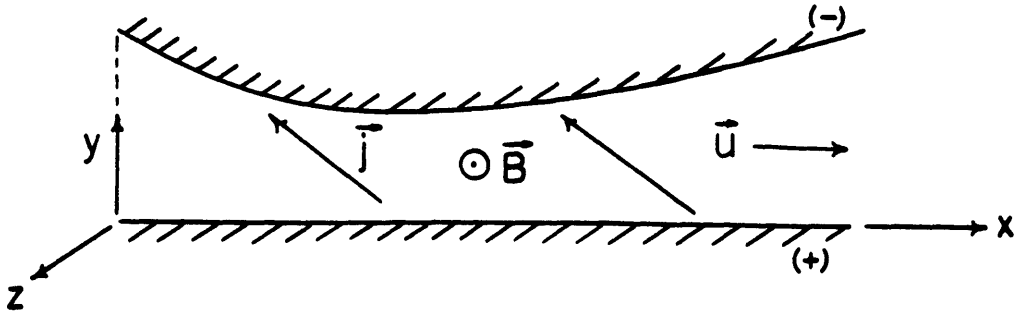

Figure A4.1: Two-Dimensional MPD Arcjet Geometry

Using Ampere's law

$$\nabla \times \vec{B} = \mu_0 \vec{j} \qquad \text{A4.4}$$

the momentum equation is written in component form

$$x: \quad \rho \left(u \frac{\partial u}{\partial x} + v \frac{\partial u}{\partial y} \right) = - \frac{\partial}{\partial x} \left(p + \frac{B^2}{2\mu_0} \right) \qquad \text{A4.5}$$

$$y: \quad \rho \left(u \frac{\partial v}{\partial x} + v \frac{\partial v}{\partial y} \right) = - \frac{\partial}{\partial y} \left(p + \frac{B^2}{2\mu_0} \right) \qquad \text{A4.6}$$

In the context of the thin channel assumption, these equations can be simplified to

$$x: \quad \rho u \frac{\partial u}{\partial x} = - \frac{\partial}{\partial x} \left(p + \frac{B^2}{2\mu_0} \right) \qquad \text{A4.7}$$

$$y: \quad 0 = - \frac{\partial}{\partial y} \left(p + \frac{B^2}{2\mu_0} \right) \qquad \text{A4.8}$$

The transverse momentum equation, equation A4.8, implies that hydrostatic equilibrium between the magnetic and thermodynamic pressures is reached, and that the total pressure,

$$\Pi(x) = p + \frac{B^2}{2\mu_0} \qquad \text{A4.9}$$

is a function only of the axial coordinate. This relation allows the Hall term in equation A4.2 to be rewritten directly in terms of the transverse partial derivative of the magnetic field and the ordinary derivative of the total pressure. With this additional simplification, the induction equation can be rewritten as

$$\frac{\partial^2 B}{\partial y^2} + \frac{\mu_0 c}{\rho^2} \frac{\partial \Pi}{\partial x} \frac{\partial \rho}{\partial y} = \mu_0 \sigma \rho u \frac{\partial}{\partial x} \left(\frac{B}{\rho} \right) \qquad \text{A4.10}$$

Expressing this induction equation in terms of the natural coordinate system (x,y) is inconvenient if the geometry of the device is an unknown. This theory is a design theory that, given a distribution of the total pressure, will ultimately produce a geometry. The total flow rate is a known parameter, so a more natural coordinate system is based on the axial coordinate and the stream function (x,Ψ). With this system, the limits of

Ψ are constant and also define the electrode boundaries.

The stream function is defined so that

$$\rho u = \frac{\partial \Psi}{\partial y} \quad \text{and} \quad \rho v = -\frac{\partial \Psi}{\partial x} \qquad \text{A4.11}$$

The derivatives in the (x,Ψ) coordinate system can be related to the derivatives in the (x,y) coordinate system by repeated use of the chain rule. For the differential element of an arbitrary function ω, the chain rule shows that

$$d\omega = \left(\frac{\partial \omega}{\partial x}\right)_{\Psi} dx + \left(\frac{\partial \omega}{\partial \Psi}\right)_{x} d\Psi \qquad \text{A4.12}$$

which (invoking the chain rule again for $d\Psi$) is

$$d\omega = \left(\frac{\partial \omega}{\partial x}\right)_{\Psi} dx + \left(\frac{\partial \omega}{\partial \Psi}\right)_{x} \left[\left(\frac{\partial \Psi}{\partial x}\right)_{y} dx + \left(\frac{\partial \Psi}{\partial y}\right)_{x} dy \right] \qquad \text{A4.13}$$

Rearranging and collecting terms gives

$$d\omega = \left[\left(\frac{\partial \omega}{\partial x}\right)_{\Psi} + \left(\frac{\partial \omega}{\partial \Psi}\right)_{x} \left(\frac{\partial \Psi}{\partial x}\right)_{y} \right] dx + \left(\frac{\partial \omega}{\partial \Psi}\right)_{x} \left(\frac{\partial \Psi}{\partial y}\right)_{x} dy \qquad \text{A4.14}$$

which is the same form as equation A4.12. Comparing the coefficients of equations A4.12 and A4.14, it is apparent that

$$\left(\frac{\partial}{\partial x}\right)_{y} = \left(\frac{\partial}{\partial x}\right)_{\Psi} + \left(\frac{\partial \Psi}{\partial x}\right)_{y} \left(\frac{\partial}{\partial \Psi}\right)_{x} = \left(\frac{\partial}{\partial x}\right)_{\Psi} - \rho v \left(\frac{\partial}{\partial \Psi}\right)_{x} \qquad \text{A4.15}$$

and

$$\left(\frac{\partial}{\partial y}\right)_{x} = \left(\frac{\partial \Psi}{\partial y}\right)_{x} \left(\frac{\partial}{\partial \Psi}\right)_{y} = \rho u \left(\frac{\partial}{\partial \Psi}\right)_{y} \qquad \text{A4.16}$$

In the spirit of this derivation, equation A4.15 becomes

$$\left(\frac{\partial}{\partial x}\right)_{y} = \left(\frac{\partial}{\partial x}\right)_{\Psi} \qquad \text{A4.17}$$

The induction equation, equation A4.10, and the axial momentum equation, equation A4.7, can now be rewritten in terms of the stream function leaving the two equations in the following forms:

$$\left[\frac{\partial}{\partial x}\left(\frac{B}{\rho}\right)\right]_{\Psi} = \frac{\partial}{\partial \Psi}\left(\frac{\rho u}{\mu_0 \sigma} \frac{\partial B}{\partial \Psi} - \frac{c}{\sigma \rho} \frac{d\Pi}{dx}\right) \qquad \text{A4.18}$$

and

$$\rho u \left(\frac{\partial u}{\partial x}\right)_{\Psi} = -\frac{d\Pi}{dx} \qquad \text{A4.19}$$

where c is a constant derived from the definition of the Hall parameter

$$\beta = \frac{eB}{m_e \nu} = c\,\frac{B}{\rho} \qquad \text{A4.20}$$

One can construct a solution to equation A4.18 based on an assumption that there is no axial current, $j_x = 0$, and that the initial diffusion layer is neglected. For this situation, there is no mechanism for transverse density variation, and B/ρ again becomes a convective constant. This assumption has a hidden implication since Ohm's law, written in two dimensions (neglecting contributions from the pressure gradient),

$$\vec{j} + \vec{j} \times \vec{\beta} = \sigma(\vec{E} + \vec{u}\times\vec{B}) \qquad \text{A4.21}$$

implies that an externally applied electric field must exist. This external field is required to mitigate the axial deflection of current caused by the Hall effect. For pre-onset operation, the axial deflection of current should be small due to the scaling of the Hall parameter with $J/\dot{m}$ implying that the applied field scales as $J^2/\dot{m}$. Below onset, the requisite local axial field should be smaller than its transverse counterpart. Herein lies the foundation for a perturbation solution to this two-dimensional problem. The solution for zero axial current, a "zeroth" order solution, may be perturbed so that the perturbation axial electric field exactly cancels the applied axial electric field required by the zeroth order solution. This perturbation model allows for an axial current distribution which arises from the perturbed zeroth order solution. This zeroth order solution is exactly the same as the solution for the one-dimensional model for infinite magnetic Reynolds' number presented in Appendix 2.

A4.3: Derivation of the Perturbation Equations

The following variables are perturbed in the prescribed manner

$$B = B^0 + B' \qquad \text{A4.22a}$$

$$\rho = \rho^0 + \rho' \qquad \text{A4.22b}$$

$$u = u^0 + u' \qquad \text{A4.22c}$$

$$\frac{B}{\rho} = \left(\frac{B}{\rho}\right)^0 \left(\frac{B'}{B} - \frac{\rho'}{\rho} \right) \qquad \text{A4.22d}$$

$$\rho u = \Gamma = \Gamma^0 + \Gamma' \qquad \text{A4.22e}$$

$$E = E^0 + E' \qquad \text{A4.22f}$$

Using A4.22a and A4.22b in the transverse momentum equation A4.8 leaves

$$\frac{B'}{B^0} = - \frac{\mu_0 P_0}{B_0^2} \frac{\rho'}{\rho^0} \qquad \text{A4.23}$$

This allows equation A4.22d to be expressed as

$$\left(\frac{B}{\rho}\right)' = - \left(\frac{B}{\rho}\right)^0 \left(1 + \frac{\mu_0 P_0}{B_0^2} \right) \frac{\rho'}{\rho^0} \qquad \text{A4.24}$$

At high interaction, this is approximately

$$\left(\frac{B}{\rho}\right)' = - \left(\frac{B}{\rho}\right)^0 \frac{\rho'}{\rho^0} \qquad \text{A4.25}$$

The induction and axial momentum equations can now rewritten as

$$- \left(\frac{B}{\rho}\right)_0 \frac{\partial \eta}{\partial x} = - \frac{\Gamma^0}{\sigma} \frac{RT}{(B/\rho)_0} \frac{\partial^2 \eta}{\partial \Psi^2} + \frac{m_i}{e} \frac{d\Pi}{dx} \frac{1}{\rho^0} \frac{\partial \eta}{\partial \Psi} \qquad \text{A4.26}$$

$$\frac{\partial}{\partial x} \left[u^0 \left(\frac{\Gamma'}{\Gamma^0} - \eta \right) \right] = \frac{\Gamma'}{\Gamma^{0\,2}} \frac{d\Pi}{dx} \qquad \text{A4.27}$$

where

$$\eta = \frac{\rho'}{\rho^0} \qquad \text{A4.28}$$

Since there is no net external axial electric field, equation A4.22f serves to connect the perturbation solution with the zeroth order solution via Ohm's law. It has the form

$$\mu_0 \sigma E_x{}^0 = \Gamma^0 \frac{\partial B'}{\partial \Psi} - c \left(\frac{B}{\rho}\right)_0 \frac{\partial B'}{\partial x} + c \left(\frac{B}{\rho}\right)_0 \frac{\rho'}{\rho^0} \frac{\partial B^0}{\partial x} = - \mu_0 \sigma E_x{}' \qquad \text{A4.29}$$

or, in terms of η

$$-\mu_0 \sigma E_x^0 = -\Gamma^0 \frac{\mu_0 RT}{(B/\rho)_0} \frac{\partial \eta}{\partial \Psi} + c \left(\frac{B}{\rho}\right)_0 \frac{\partial B^0}{\partial x} \eta + c\mu_0 RT \frac{\partial \eta}{\partial x} \qquad \text{A4.30}$$

A particular solution for η is readily found. By assuming a constant value for η_p, equation A4.30 shows that

$$\eta_p = \frac{\sigma E_x^0}{(j_y \beta)^0} = 1 \qquad \text{A4.31}$$

which leaves solution for the homogeneous problem and then for the momentum perturbation in equation A4.27.

A4.3.1: The Homogeneous Solution

Equations A4.26 and A4.27 are quite difficult to solve in their present forms. Further simplifications can reduce both equations to separable and solvable partial differential equations using Fourier transform methods. The equations exhibit complex behavior due the form of the η coefficients. If the coefficients were constant, then the equations would be more readily solved. In fact, the coefficient in front of the diffusion term contains Γ^0, which, near the throat of the MPD channel, can be approximated as constant. Since the mass flow rate is constant and the channel cross-sectional area is a minimum at the throat, this is also where the flux is a maximum. The coefficient in front of the Hall term contains $\frac{d\Pi}{dx} \frac{1}{\rho^0}$ which, for the condition of constant transverse current density and high interaction, is approximately constant throughout the channel. In the context of this derivation, these assumptions are perfectly reasonable, as long as it is realized that in regions of larger interelectrode separation, the model is less robust due to the increasing importance of the neglected diffusion terms. Given these assumptions, the

induction equation takes the form

$$a \frac{\partial^2 \eta_H}{\partial \Psi^2} + b \frac{\partial \eta_H}{\partial \Psi} = \frac{\partial \eta_H}{\partial x} \qquad \text{A4.32}$$

where

$$a = \frac{RT\langle \Gamma^0 \rangle}{(B/\rho)_0^2 \sigma} \qquad \text{A4.33}$$

and

$$b = \frac{c}{(B/\rho)\sigma} \left\langle \frac{1}{\rho^0} \frac{d\Pi}{dx} \right\rangle \qquad \text{A4.34}$$

Here $\langle\rangle$ denotes axially averaged quantities. Equation A4.32 is a parabolic partial differential equation which requires an initial transverse specification of η_H for solution. This model is also subject to electrode boundary conditions where, in the thin channel approximation, the electrodes can support no axial electric field. In a sheathless model (such as this one), no sheaths are present to support an axial variation of electrode fall. Therefore E_x must be zero at the electrode boundaries. This electrode boundary condition is also the plasma boundary condition, so at the anode and cathode

$$\left(r \frac{\partial \eta_H}{\partial \Psi} - s \frac{\partial \eta_H}{\partial x} + t\eta_H = 0 \right)_{\Psi=0,G} \qquad \text{A4.35}$$

where

$$r = \langle \Gamma^0 \rangle \frac{\mu_0 RT}{(B/\rho)_0}, \quad s = c\mu_0 RT, \quad t = -c \left(\frac{B}{\rho}\right)_0 \frac{\partial B^0}{\partial x} \qquad \text{A4.36}$$

and G is the total value of the stream function.

A4.3.2: Solution for the System Eigenvalues

Equation A4.32 is solved by separation of variables where

$$\eta_H = X(x)Y(\Psi) \qquad \text{A4.37}$$

Two equations, each in a single variable, result. These are

$$a \frac{\partial^2 Y}{\partial \Psi^2} + b \frac{\partial Y}{\partial \Psi} + \lambda_n Y = 0 \qquad \text{A4.38}$$

$$\frac{\partial X}{\partial x} + \lambda_n X = 0 \qquad \text{A4.39}$$

where λ_n are the eigenvalues of the system. The general solution is

$$X_n = e^{-\lambda_n x} \qquad \text{A4.40}$$

$$Y_n = A_n^+ \; e^{r_n^+ \Psi} + A_n^- \; e^{r_n^- \Psi} \qquad \text{A4.41}$$

where

$$r_n^{+,-} = \frac{-b \pm \sqrt{b^2 - 4a\lambda_n}}{2a} \qquad \text{A4.42}$$

Substitution of this general solution into the expressions for the boundary conditions will allow solution for each λ_n

$$r \sum e^{-\lambda_n x}(A_n^+ \; r_n^+ \; e^{r_n^+ \Psi} + A_n^- \; r_n^- \; e^{r_n^- \Psi}) + s \sum \lambda_n \; e^{-\lambda_n x}(A_n^+ \; e^{r_n^+ \Psi} + A_n^- \; e^{r_n^- \Psi}) + t \sum \lambda_n \; e^{-\lambda_n x}(A_n^+ \; e^{r_n^+ \Psi} + A_n^- \; e^{r_n^- \Psi}) = 0 \qquad \text{A4.43}$$

To solve for a particular λ_n, one must note that all λ_n and r_n are not functions of the independent variables. Equation A4.43 must be satisfied uniquely for all λ_n and r_n independent of axial location. Therefore, the axial coordinate contribution can be eliminated by evaluating equation A4.43 at the entrance, $x = 0$. This leaves the following two equations which must be solved simultaneously for the eigenvalues

$$(r r_n^+ + s\lambda_n + t) \; A_n^+ + (r r_n^- + s\lambda_n + t) \; A_n^- = 0 \qquad \text{A4.44}$$

$$(r r_n^+ + s\lambda_n + t) \; A_n^+ \; e^{r_n^+ G} + (r r_n^- + s\lambda_n + t) \; A_n^- \; e^{r_n^- G} = 0 \qquad \text{A4.45}$$

These simultaneous equations can be rewritten into a matrix form to help identify the conditions for solution. This form

$$\begin{bmatrix} 1 & 1 \\ e^{r_n^+ G} & e^{r_n^- G} \end{bmatrix} \begin{bmatrix} (r r_n^+ + s\lambda_n + t) \; A_n^+ \\ (r r_n^- + s\lambda_n + t) \; A_n^- \end{bmatrix} = 0 \qquad \text{A4.46}$$

can be satisfied in two different ways. The determinant of the first matrix is zero, or both elements of the second matrix are identically zero. The first condition states that

$$r_n^+ - r_n^- = \frac{2\pi n}{G} i \qquad \text{A4.47}$$

implying an infinite summation series of sine and cosine terms. Solving equation A4.47 with equation A4.42 for the eigenvalues gives

$$\lambda_n = \frac{b^2}{4a} + \frac{\pi^2 a}{G^2} n^2 \qquad \text{A4.48}$$

Further substitution of equation A4.47 into equation A4.44, shows that the ratio of A_n^- to A_n^+, denoted K_n, is

$$K_n = \frac{s\lambda_n + t - \frac{br}{2a}}{\frac{n\pi r}{G}} \qquad \text{A4.49}$$

It can be shown through substitution, that the boundary conditions cannot always be satisfied for n=0, except for certain trivial degenerate cases. This implies that the summation series extends from n=1 to infinity.

If the second matrix in equation A4.46 is exactly zero, then one of two conditions must exist. Either

$$rr_n^+ + s\lambda_n + t = 0 \quad \text{and} \quad A_n^- = 0 \qquad \text{A4.50}$$

or

$$A_n^+ = 0 \quad \text{and} \quad rr_n^- + s\lambda_n + t = 0 \qquad \text{A4.51}$$

These conditions imply that two more eigenvalues and eigenfunctions exist for a complete definition of η. Solving these two equations for λ_n gives the two additional eigenvalues

$$\lambda_{-1,-2} = \frac{r}{a} \frac{(bs - r - \frac{2a}{r} ts) \pm \sqrt{(bs - r)^2 + 4ats}}{2s^2} \qquad \text{A4.52}$$

The discriminant is greater than zero, since a, t, and s are all positive

quantities, so that the eigenvalues are real and distinct. The behavior of these eigenvalues can be seen by plotting the equation

$$rr_n^{+,-} + s\lambda_n + t = 0 \qquad \text{A4.53}$$

as a function of λ_n for the values of t that provide for two real roots. This behavior is seen in figure A4.2. Depending on the magnitude of t, there are either two real roots corresponding to the r_n^+ branch, or one root for both branches. From this figure, one of the roots is large and negative, but both eigenvalues are less than the eigenvalue defined by equation A4.48, corresponding to n=0. These eigenvalues correspond to the lowest values and are subscripted -1 and -2. The general form of the homogeneous and particular solution for η now becomes

$$\eta(x,\Psi) = 1 + e^{-\frac{b\Psi}{2a}}\{ C_{-2}\, e^{-\lambda_{-2}x}\, e^{(\frac{b}{2a} + r_{-2})\Psi} + C_{-1} e^{-\lambda_{-1}x}\, e^{(\frac{b}{2a} + r_{-1})\Psi} + \sum_{n=1}^{\infty} C_n e^{-\lambda_n x} (\cos\frac{n\pi\Psi}{G} - K_n \sin\frac{n\pi\Psi}{G}) \} \qquad \text{A4.54}$$

where

$$r_{-1,-2} = -\frac{s\lambda_{-1,2} + t}{r} \qquad \text{A4.55}$$

where r_{-1} and r_{-2} are the corresponding r values for the -1, and -2 eigenvalues.

A4.3.3: Calculation of the Fourier Coefficients

For solution, all values of C_n and K_n must be calculated. Normally, standard Fourier orthogonalization is utilized. However, this method must be modified for use in this derivation. In this model, the eigenvalues appear explicitly in the electrode boundary conditions whereas in the standard Fourier orthogonality condition the boundary conditions are

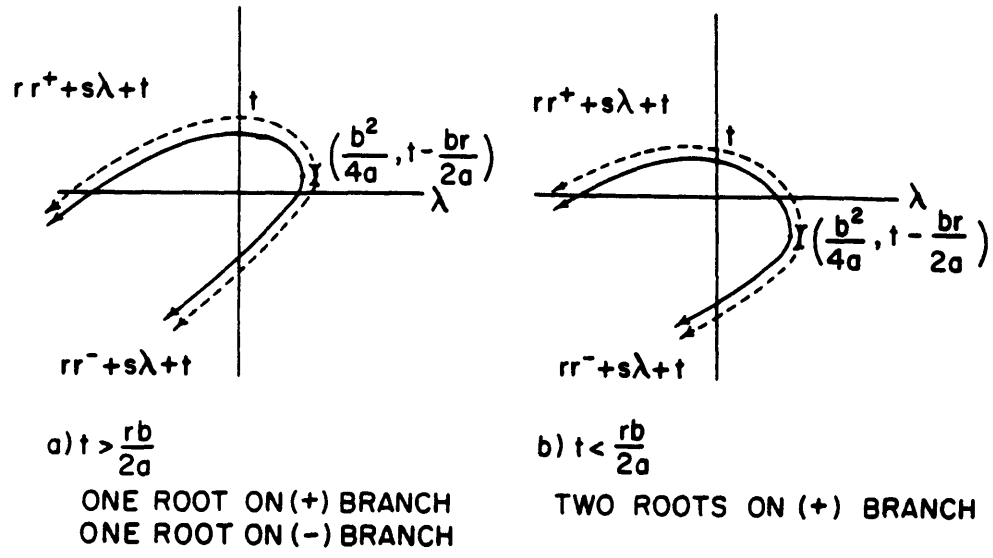

Figure A4.2: Behavior of the System Eigenvalues

simple. The normal orthogonalization technique, derived from a Sturm-Liouville boundary value problem, must be recast for the boundary conditions found in this formulation.

In an orthogonality condition, the coefficients in an infinite series are uniquely determined by multiplying the terms in a series by an orthogonal function, normally a function of an index (which signifies the position of the term in the infinite series) and an independent variable. When integrated over the domain of the orthogonal function, the only term remaining in the infinite series is that term sharing the same index as the orthogonal function. This provides a simple recursion technique for the determination of the unknown coefficients which are functions only of the index.

For the solution of equation A4.54, the portion of η, excluding the -1 and -2 eigenvalues, is replaced into equation A4.38 yielding

$$\frac{d}{d\Psi}\left(a\, e^{\frac{b}{a}\Psi} \frac{dY_n}{d\Psi} \right) + \lambda_n e^{\frac{b}{a}\Psi} Y_n = 0 \qquad \text{A4.56}$$

with the boundary condition

$$r \frac{dY_n}{d\Psi} + (s\lambda_n + t)\, Y_n = 0 \quad \text{on } \Psi = 0, G \qquad \text{A4.57}$$

for a given eigenfunction Y_n

$$Y_n = e^{-\frac{b}{2a}\Psi}\left(\cos\frac{n\pi\Psi}{G} - K_n \sin\frac{n\pi\Psi}{G}\right) \qquad \text{A4.58}$$

By rewriting equation A4.56 in terms of the m^{th} eigenvalue, two identical differential equations, one in terms of Y_n and the other in terms of Y_m, are found. Each equation is multiplied by the other eigenfunction, and

then one is subtracted from the other, leaving

$$(\lambda_n - \lambda_m)e^{\frac{b}{a}\psi} Y_n Y_m + Y_m \frac{d}{d\psi}(ae^{\frac{b}{a}\psi}\frac{dY_n}{d\psi}) - Y_n \frac{d}{d\psi}(ae^{\frac{b}{a}\psi}\frac{dY_m}{d\psi}) = 0 \quad \text{A4.59}$$

Integrating equation A4.59 from the anode to the cathode gives

$$(\lambda_n - \lambda_m)\int_0^G e^{\frac{b}{a}\psi} Y_n Y_m \, d\psi + [\, a\, e^{\frac{b}{a}\psi}(Y_m \frac{dY_n}{d\psi} - Y_n \frac{dY_m}{d\psi})\,]_0^G = 0 \quad \text{A4.60}$$

which, after combination with the electrode boundary conditions, can be written in terms of the Dirac delta function

$$(\lambda_n - \lambda_m)\int_0^G e^{\frac{b}{a}\psi}\{\, 1 - \frac{as}{r}[\,\delta(G) - \delta(0)\,]\,\} Y_n Y_m \, d\psi = 0 \quad \text{A4.61}$$

This shows that for $n \neq m$, Y_n and Y_m are orthogonal on the interval $\langle 0,G \rangle$ with respect to a weighting function

$$g(\psi) = e^{\frac{b}{a}\psi}\{\, 1 - \frac{as}{r}[\,\delta(G) - \delta(0)\,]\,\} \quad \text{A4.62}$$

The equation for the density perturbation evaluated at x=0, excluding the -1 and -2 terms, can be rewritten in a form more suitable for solution

$$f(\psi) = [\eta(x=0,\psi) - 1]\, e^{-\frac{b}{2a}\psi} = \sum_{n=1}^{\infty} C_n (\cos\frac{n\pi\psi}{G} - K_n \sin\frac{n\pi\psi}{G}) \quad \text{A4.63}$$

Rewriting equation A4.54 at x=0 in terms of $f(\psi)$, excluding the -1 and -2 terms, and integrating with the new orthogonality condition allows solution for the modified Fourier coefficients, C_n. This gives

$$\int_0^G \{1 - \frac{as}{r}[\delta(G) - \delta(0)]\}(\cos\frac{n\pi\psi}{G} - K_n \sin\frac{n\pi\psi}{G})(\cos\frac{m\pi\psi}{G} - K_n \sin\frac{m\pi\psi}{G})d\psi = 0 \quad \text{A4.64}$$

for $n \neq m$ and

$$\int_0^G f(\psi)\{1 - \frac{as}{r}[\delta(G) - \delta(0)]\}(\cos\frac{n\pi\psi}{G} - K_n \sin\frac{n\pi\psi}{G})d\psi =$$

$$C_n \int_0^G \{1 - \frac{as}{r}[\delta(G) - \delta(0)]\}(\cos\frac{n\pi\psi}{G} - K_n \sin\frac{n\pi\psi}{G})^2 d\psi \quad \text{A4.65}$$

for n=m. A simple specification of $f(\varphi)$ allows immediate calculation of the modified Fourier coefficients. Two integrals may be defined to simplify the expression for C_n. These are

$$A_n = \frac{2}{G}\int_0^G f(\varphi)\cos\frac{n\pi\varphi}{G}\,d\varphi \qquad \text{A4.66}$$

and

$$B_n = \frac{2}{G}\int_0^G f(\varphi)\sin\frac{n\pi\varphi}{G}\,d\varphi \qquad \text{A4.67}$$

A simple expression can be written for C_n by integrating the second integral in equation A4.65 and rewriting the first integral in terms of A_n and B_n. This results in the following equation

$$C_n = \frac{A_n - K_n B_n - \frac{2}{G}\frac{as}{r}[(-1)^n f(G) - f(0)]}{1 + K_n^2} \qquad \text{A4.68}$$

for n = 1, 2, ..., ∞.

The same derivation is applied to the -1 and -2 eigenvalues. In this case, the eigenfunctions are

$$Y_{-1,-2} = e^{-\frac{b\varphi}{2a}} e^{(\frac{b}{2a} + r_{-1,-2})\varphi} \qquad \text{A4.69}$$

The same orthogonal function, $g(\varphi)$, can be applied to these eigenfunctions. The constants $C_{-1,-2}$ are found after a similar integration is completed, with the results shown below

$$C_{-1,-2} = \frac{-2r'_{-1,-2}r}{(e^{2r'_{-1,-2}G}-1)(2asr'_{-1,-2}-r)}\int_0^G f(\varphi)\{1-\frac{as}{r}[\delta(G)-\delta(0)]\}e^{r'_{-1,-2}\varphi}d\varphi \qquad \text{A4.70}$$

where

$$r'_{-1,-2} = \frac{b}{2a} + r_{-1,-2} \qquad \text{A4.71}$$

Substitution of typical values into equation A4.52 shows that the

eigenvalue corresponding to the -2 term has a large negative value. In the η series, this corresponds to a divergent term. This is physically not allowed. To cancel this divergent term, the function, $f(\Psi)$, must be appropriately chosen. The first nontrivial function for $f(\Psi)$ is provided by a linear expression for the density perturbation with a zero transverse mean. This corresponds to an initial density perturbation

$$\eta(0,\Psi) = m\left(\Psi - \frac{G}{2}\right) \qquad \text{A4.72}$$

or

$$f(\Psi) = \left(m\Psi - \frac{mG+2}{2}\right) e^{\frac{b\Psi}{2a}} \qquad \text{A4.73}$$

where m is a constant to be determined. Substitution of equation A4.73 into the integral in equation A4.70 allows the value for m to be calculated by expressing the condition that $C_{-2} = 0$:

$$m = \left[\frac{1}{\frac{b}{2a} + r'_{-2}} - \frac{as}{r}\right]\left[\frac{G}{2}\left\{\frac{1}{\frac{b}{2a} + r'_{-2}} - \frac{as}{r}\right\} - \frac{1}{\left(\frac{b}{2a} + r'_{-2}\right)^2}\right]^{-1} \qquad \text{A4.74}$$

Now that an initial profile for the density perturbation has been determined, the modified Fourier coefficients for all the other index values can be derived from the integral expressions.

For n=-1,

$$C_{-1} = \frac{-2r'_{-1}r}{(e^{2r'_{-1}G} - 1)(2asr'_{-1} - r)}\left\{ mGe^{\left(\frac{b}{2a}+r'_{-1}\right)G}\left[\frac{1}{\frac{b}{2a} + r'_{-1}} - \frac{as}{r}\right] - \left[e^{\left(\frac{b}{2a}+r'_{-1}\right)G} - 1\right]\left[\frac{mG+2}{2}\left(\frac{1}{\frac{b}{2a} + r'_{-1}} - \frac{as}{r}\right) + \frac{m}{\left(\frac{b}{2a} + r'_{-1}\right)^2}\right]\right\} \qquad \text{A4.75}$$

For all other n, the intermediate integrals, A_n and B_n, are first computed using the function for $f(\Psi)$ specified in equation A4.73 with the value for

m calculated in equation A4.74. This gives

$$A_n = \frac{1}{\left(\frac{b}{2a}\right)^2 + \left(\frac{n\pi}{G}\right)^2} \left\{ \frac{mb}{a} (-1)^n e^{\frac{bG}{2a}} + \frac{2m}{G} \left((-1)^n e^{\frac{bG}{2a}} - 1 \right) \left[\frac{\left(\frac{n\pi}{G}\right)^2 - \left(\frac{b}{2a}\right)^2}{\left(\frac{b}{2a}\right)^2 + \left(\frac{n\pi}{G}\right)^2} - \frac{b}{2a} \frac{mG+2}{2m} \right] \right\} \qquad \text{A4.76}$$

and

$$B_n = \frac{\frac{n\pi}{G}}{\left(\frac{b}{2a}\right)^2 + \left(\frac{n\pi}{G}\right)^2} \left\{ \left((-1)^n e^{\frac{bG}{2a}} - 1 \right) \left[\frac{\frac{2mb}{aG}}{\left(\frac{b}{2a}\right)^2 + \left(\frac{n\pi}{G}\right)^2} + \frac{mG+2}{G} \right] - 2m (-1)^n e^{\frac{bG}{2a}} \right\} \qquad \text{A4.77}$$

which are then substituted into equation A4.68.

A4.3.4: Calculation of the Momentum Perturbation

Now that the density perturbation has been derived, the momentum perturbation can be calculated. Substituting the momentum perturbation

$$\xi = \frac{\Gamma'}{\Gamma^0} \qquad \text{A4.78}$$

into equation A4.20 gives

$$\frac{\partial}{\partial x} \left[u^0 \left(\xi - \eta \right) \right] = \frac{\xi}{\Gamma^0} \frac{d\Pi}{dx} \qquad \text{A4.79}$$

Expanding out equation A4.79 gives

$$\frac{\partial \xi}{\partial x} + \xi \left[\frac{\partial}{\partial x}(\ln u^0) - \frac{1}{\Gamma^0 u^0} \frac{d\Pi}{dx} \right] = \frac{\partial \eta}{\partial x} + \eta \frac{\partial}{\partial x}(\ln u^0) \qquad \text{A4.80}$$

The bracketed term can be simplified by the zeroth order momentum equation

$$\Gamma^0 \frac{\partial u^0}{\delta x} = - \frac{d\Pi}{dx} \qquad \text{A4.81}$$

leaving

$$\frac{\partial \xi}{\partial x} + 2\xi \frac{\partial}{\partial x}(\ln u^0) = \frac{\partial \eta}{\partial x} + \eta \frac{\partial}{\partial x}(\ln u^0) \qquad \text{A4.82}$$

The complete solution to equation A4.82 consists of both homogeneous and particular solutions. The homogeneous solution satisfies the equation

$$\frac{\partial \xi}{\partial x} = - 2\xi \frac{\partial}{\partial x}(\ln u^0) \qquad \text{A4.83}$$

which is satisfied by

$$\xi_H = \frac{\gamma(\Psi)}{u^{0\,2}} \qquad \text{A4.84}$$

Substituting a particular solution of the form

$$\xi_P = \frac{\gamma(x,\Psi)}{u^{0\,2}} \qquad \text{A4.85}$$

into equation A4.82 gives a differential equation for $\gamma(x,\Psi)$,

$$\frac{\partial \gamma}{\partial x} = \frac{\partial}{\partial x}(\eta u^{0\,2}) - \eta u^0 \frac{\partial u^0}{\partial x} \qquad \text{A4.86}$$

Recalling that, to zeroth order, the quantities

$$u^0 \frac{\partial u^0}{\partial x} = -\frac{d\Pi}{dx}\frac{1}{\rho^0} \simeq \text{constant} \qquad \text{A4.87}$$

allow equation A4.86 to be integrated to

$$\xi(x,\Psi) = \frac{u^{0\,2}(0)}{u^{0\,2}(x)}\,[\,\xi(0,\Psi) - \eta(0,\Psi)\,] + \eta(x,\Psi) + \frac{1}{u^{0\,2}}\left\langle\frac{d\Pi}{dx}\frac{1}{\rho^0}\right\rangle \int_0^x \eta\, dx \qquad \text{A4.88}$$

where

$$\int_0^x \eta\, dx = x - e^{-\frac{b\Psi}{2a}}\Big\{\frac{C_{-1}}{\lambda_{-1}}\, e^{\left(\frac{b}{2a} + r_{-1}\right)\Psi}\left(e^{-\lambda_{-1}x} - 1\right) + \sum_{n=1}^{\infty}\frac{C_{-n}}{\lambda_{-n}}\left(e^{-\lambda_n x} - 1\right)\left(\cos\frac{n\pi\Psi}{G} - K_n \sin\frac{n\pi\Psi}{G}\right)\Big\} \qquad \text{A4.89}$$

Complete solution requires an initial specification for ξ. This is a free specification in the context of this parabolic model. The specification of $\xi(0,\Psi)$ is arbitrary, however, it ultimately determines the cold gas inlet boundary condition in a real channel. Therefore, it is perfectly reasonable to assume that $\xi(0,\Psi)$ is exactly zero (transversally uniform inlet mass flow).

Once the momentum and density perturbations are known, the channel height can be calculated from the continuity equation. The channel height,

$$h(x) = \int_0^G \frac{\partial \Psi}{\Gamma} = \int_0^G \frac{1}{\Gamma^0}(1 - \xi)\, d\Psi \qquad \text{A4.90}$$

is immediately integrable with the help of equation A4.87, becoming

$$h(x) = \frac{G}{\Gamma^0} - \frac{1}{\Gamma^0}\frac{u^{0\,2}(0)}{u^{0\,2}(x)}\left\{\int_0^G \xi(0,\mathcal{P})\,d\mathcal{P} - \int_0^G \eta(0,\mathcal{P})\,d\mathcal{P}\right\} - \frac{1}{\Gamma^0}\int_0^G \eta(0,\mathcal{P})\,d\mathcal{P} - \frac{1}{\Gamma^0}\frac{1}{u^{0\,2}}\left\langle\frac{d\Pi}{dx}\frac{1}{\rho^0}\right\rangle\int_0^G\int_0^x \eta\,dx\,d\mathcal{P} \qquad \text{A4.91}$$

where

$$\int_0^G \eta\,d\mathcal{P} = G + \frac{C_{-1}}{r_{-1}}e^{-\lambda_{-1}x}\left(e^{r_{-1}G} - 1\right) + \sum_{n=1}^{\infty}\frac{1}{\left(\frac{b}{2a}\right)^2 + \left(\frac{n\pi}{G}\right)^2}\frac{C_n}{\lambda_n}e^{-\lambda_n x}\left(e^{-\frac{bG}{2a}}(-1)^n - 1\right)\left(K_n\frac{n\pi}{G} - \frac{b}{2a}\right) \qquad \text{A4.92}$$

and

$$\int_0^G\int_0^x \eta\,dx\,d\mathcal{P} = xG - \frac{C_{-1}}{\lambda_{-1}}\frac{1}{r_{-1}}\left(e^{r_{-1}G} - 1\right)\left(e^{-\lambda_{-1}x} - 1\right) - \sum_{n=1}^{\infty}\frac{1}{\left(\frac{b}{2a}\right)^2 + \left(\frac{n\pi}{G}\right)^2}\frac{C_n}{\lambda_n}\left(e^{-\lambda_n x} - 1\right)\left(e^{-\frac{bG}{2a}}(-1)^n - 1\right)\left(K_n\frac{n\pi}{G} - \frac{b}{2a}\right) \qquad \text{A4.93}$$

The solution for the approximate two-dimensional model is now complete. The perturbed solutions are added to the zeroth order solutions defined by the infinite magnetic Reynolds' number model in Appendix 2.

A4.4: An Estimation of Onset

The previous model can be further simplified to show a rough prediction of the onset limitation. This is done to verify that the predicted parametric behavior corresponds to that found in empirical studies.

In equation A4.70, an initial specification of η is necessary to cancel the divergent term in the infinite series. Assume that an $\eta(0,\mathcal{P})$ was selected orthogonal not only to the -2 term but to all of the terms in

the infinite expansion. This would leave

$$\eta(x,\Psi) = 1 + C_{-1} e^{-\lambda_{-1} x} + r_{-1} \Psi \qquad \text{A4.94}$$

If this is to have zero mean, then

$$C_{-1} = \frac{- r_{-1}}{e^{r_{-1}} - 1} \qquad \text{A4.95}$$

At the anode inlet corner,

$$\eta(0,0) = 1 + C_{-1} \qquad \text{A4.96}$$

An approximate onset condition occurs when the density at this location goes to zero, which corresponds to

$$\eta(0,0) = -1 \qquad \text{A4.97}$$

or

$$C_{-1} \cong -2 \qquad \text{A4.98}$$

This leads to

$$r_{-1} = -1.593 \qquad \text{A4.99}$$

which can be expanded from its definition in equation A4.55 to show that the onset current scales approximately with the square root of the mass flow rate and inversely with the 0.2 power of the molecular weight.

$$J^* \sim 2.5^{0.1} \dot{m}^{0.5} \left(\frac{w^5 L}{h^{*7}} \right)^{0.1} \frac{(RT)^{0.2}}{\sigma^{0.1} \mu_0^{0.6} M^{0.2}} \qquad \text{A4.100}$$

This is in remarkable agreement with experiment. The behavior predicted by equation A4.100, deviates slightly from empirical data and zeroth order theory which shows that the the onset current varies inversely with the 0.25 power of the molecular weight.

A4.5: A Numerical Example

It is difficult, if not impossible, to deduce the trends exhibited in this approximate two-dimensional model. For this reason, a numerical example is prudent. A FORTRAN program was written for use on an IBM compatible personal computer and is found in Appendix 11. From this code, it is possible to design an MPD channel based on specific inputs.

This code is a design code and is only valid for a single operating point--that is, for a single specification of current and flow rate. A specific geometry is determined by the initial parameters so that a thruster could be designed to operate far below onset (based on anode starvation) which would give one geometry, or designed closer to onset which would give a completely different geometry. The accuracy of the design is questionable, due to the strong assumptions made in the derivation of the model; however, significant trends are demonstrated that appear to accurately describe the general phenomenology of two-dimensional MPD arcjet operation.

This model requires a specification for the total pressure distribution, $\Pi(x)$. This specification is arbitrary, but an appropriate selection would be one that implies an approximately constant axial current density distribution. This selection enables the arcjet designer to minimize the local current concentrations associated with flows at high magnetic Reynolds' numbers, which may help decrease local electrode erosion by minimizing the local ohmic heating. This specification leads to the following form of the total pressure

$$\Pi(x) = \Pi(0) \left(1 - \frac{x}{L}\right)^2 \qquad \text{A4.101}$$

where $\Pi(0)$ is based on the initial values of magnetic field and density. For solution, the following parameters are chosen:

$$\sigma = 3300 \text{ mhos/m}$$

$$T = 12000 \text{ K}$$

$$B(0) = 0.059 \text{ Tesla}$$

$$G = 0.01 \text{ kg/ms}$$

$$L = 0.12 \text{ m}$$

$$\rho(0) = 8.0 \times 10^{-5} \text{ kg/m}^3 \qquad \text{A4.102}$$

The simulation stops when the magnetic field goes negative at the anode defining the actual length of the thruster. These parameters give a thruster about 9 cm long, operating at a mass flow rate of 3.95 g/s at approximately 43,365 A.

The values for the coefficients in the differential equation, equation A4.32, and the boundary conditions, equation A4.35, are computed to be

$$a = 5.421 \times 10^{-4}$$

$$b = 0.3041$$

$$r = 1.658 \times 10^{-3}$$

$$s = 8.580 \times 10^{-3}$$

$$t = 0.5049 \qquad \text{A4.103}$$

Figure A4.3 shows the values for the eigenvalues, the series coefficients and the exponential coefficients for the first twenty terms. The results of the calculation are presented in figure A4.4 to A4.14. Figure A4.4 shows the interelectrode separation as a function of distance, figure A4.5 shows the magnetic field distribution through the channel; figure A4.6,

n	λ_n	K_n	C_n	r_n
-2	-.10575D+03		0	.24270D+03
-1	.27585D+02		-.34737D+01	-.44730D+03
1	.96162D+02	.16605D+01	.17674D+01	
2	.25666D+03	.21522D+01	-.20234D+00	
3	.52417D+03	.29037D+01	.78696D-01	
4	.89868D+03	.37200D+01	-.16500D-01	
5	.13802D+04	.45624D+01	.11766D-01	
6	.19687D+04	.54177D+01	-.34189D-02	
7	.26642D+04	.62805D+01	.31926D-02	
8	.34667D+04	.71479D+01	-.10996D-02	
9	.43763D+04	.80184D+01	.11888D-02	
10	.53928D+04	.88910D+01	-.45379D-03	
11	.65163D+04	.97653D+01	.53748D-03	
12	.77468D+04	.10641D+02	-.21973D-03	
13	.90843D+04	.11517D+02	.27694D-03	
14	.10529D+05	.12394D+02	-.11889D-03	
15	.12080D+05	.13272D+02	.15674D-03	
16	.13739D+05	.14150D+02	-.69802D-04	
17	.15504D+05	.15028D+02	.95214D-04	
18	.17377D+05	.15907D+02	-.43624D-04	
19	.19357D+05	.16786D+02	.61114D-04	
20	.21443D+05	.17665D+02	-.28644D-04	

Figure A4.3: Eigenvalues, Series Coefficients, and Other Important Parameters in the η Series

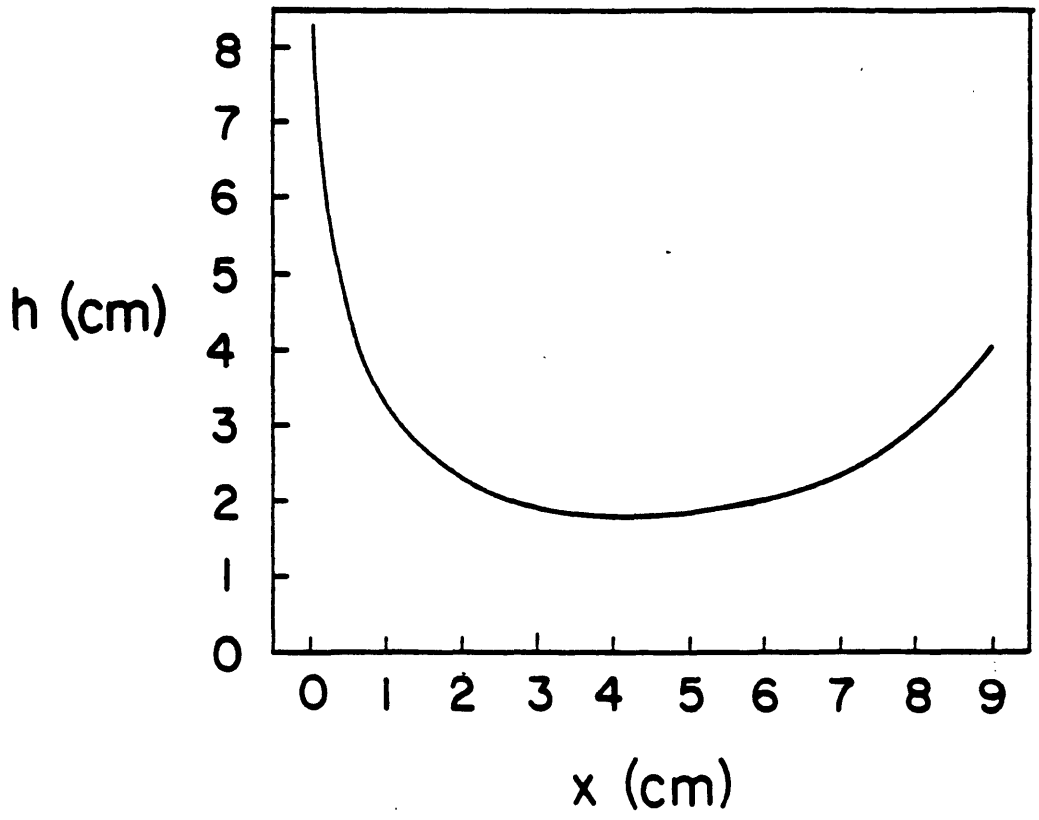

Figure A4.4: Calculated Variation of the Interelectrode Separation at 43 kA and an Argon Mass Flow Rate of 4 g/s

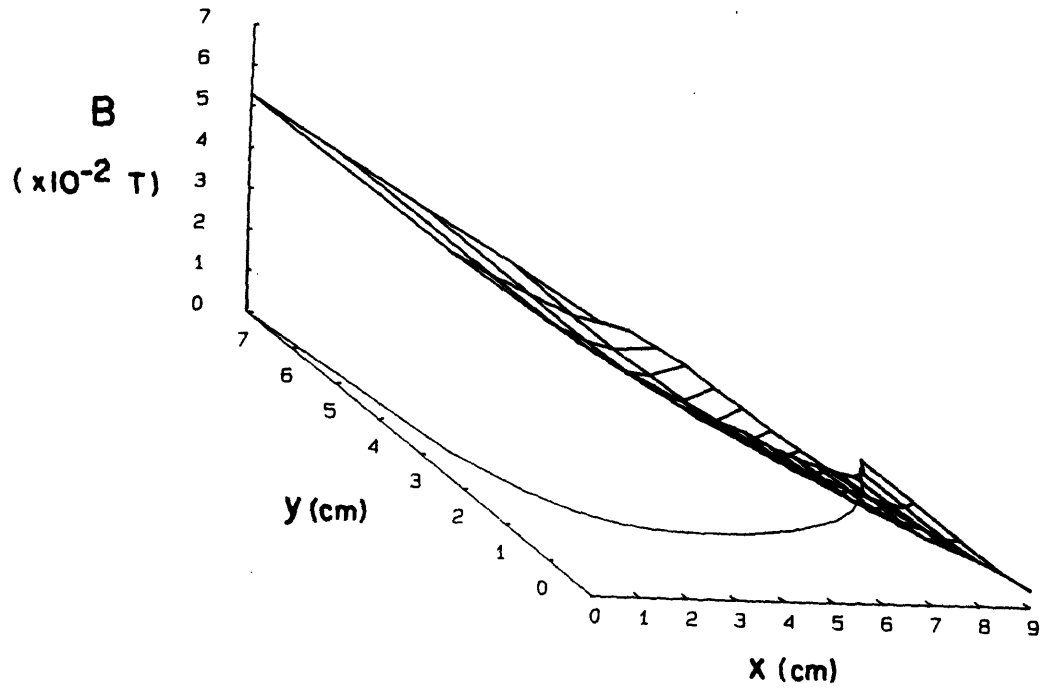

Figure A4.5: Theoretical Variation of the Magnetic Field Throughout the Channel at 43 kA and an Argon Mass Flow Rate of 4 g/s

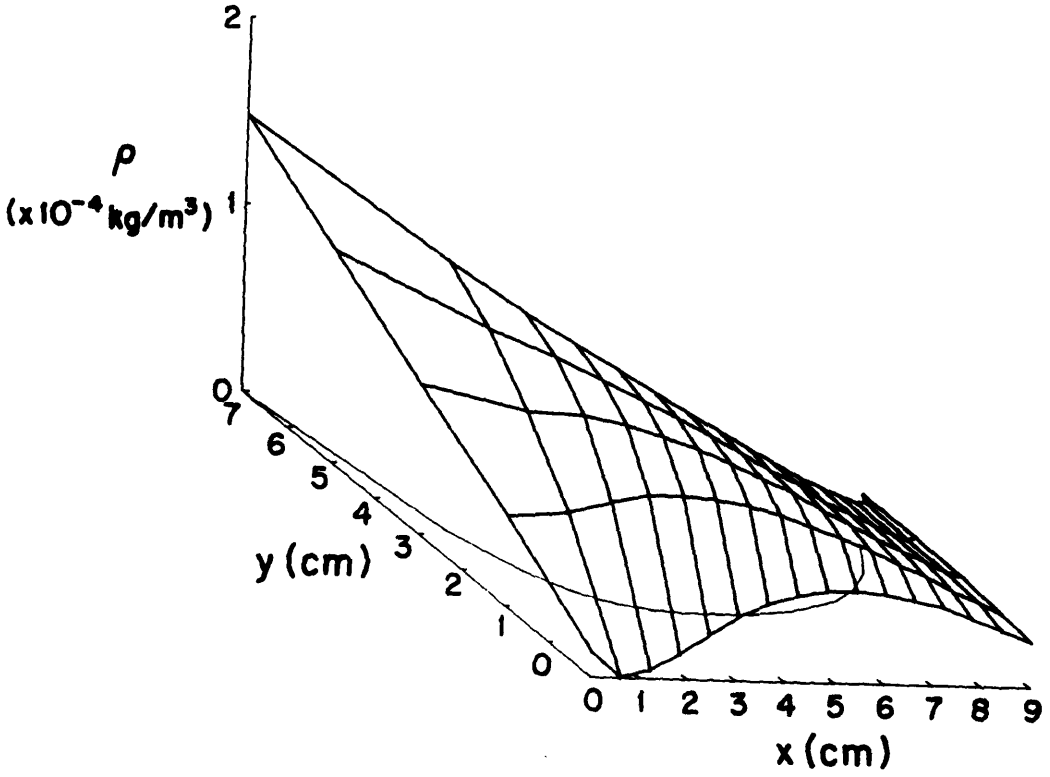

Figure A4.6: Theoretical Variation of the Plasma Density Throughout the Channel at 43 kA and an Argon Mass Flow Rate of 4 g/s

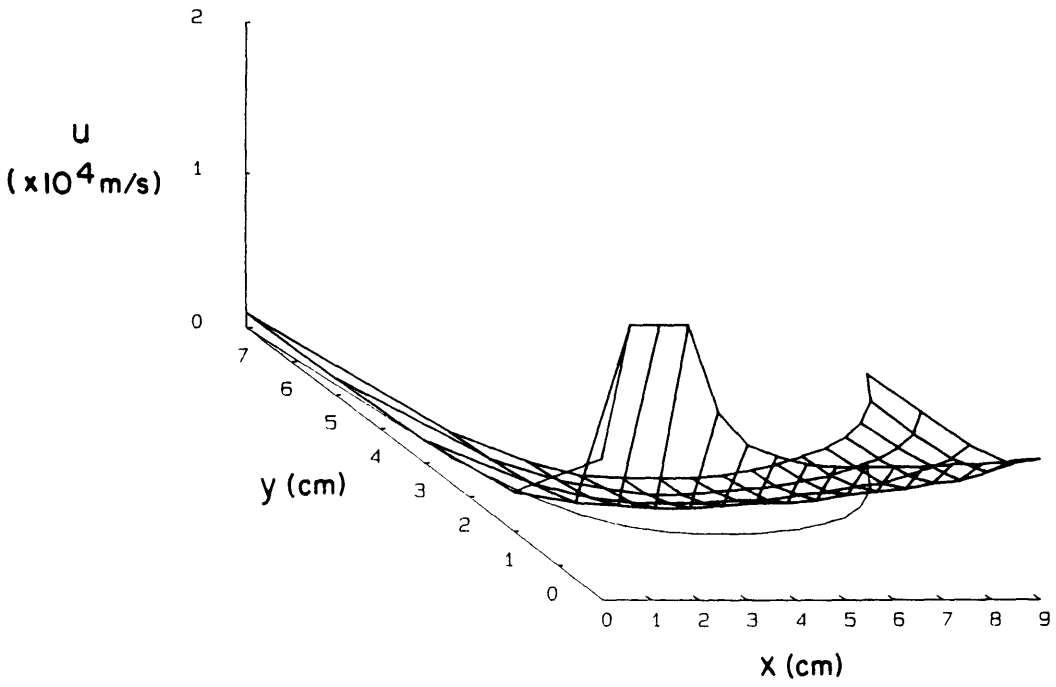

Figure A4.7: Theoretical Variation of the Plasma Velocity Throughout the Channel at 43 kA and an Argon Mass Flow Rate of 4 g/s

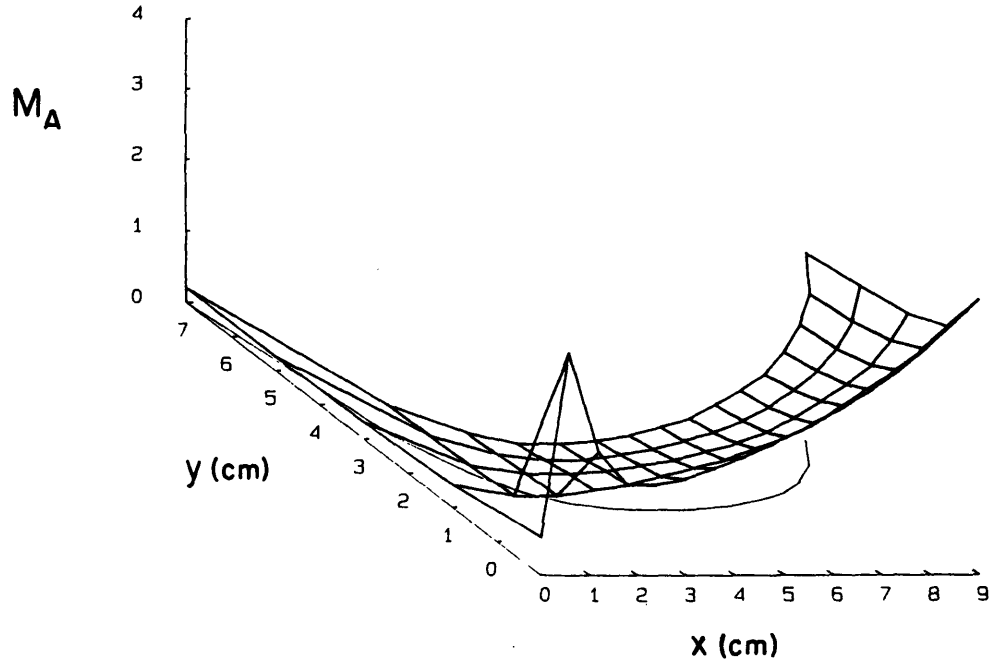

Figure A4.8: **Theoretical Variation of the Magnetoacoustic Number Throughout the Channel at 43 kA and an Argon Mass Flow Rate of 4 g/s**

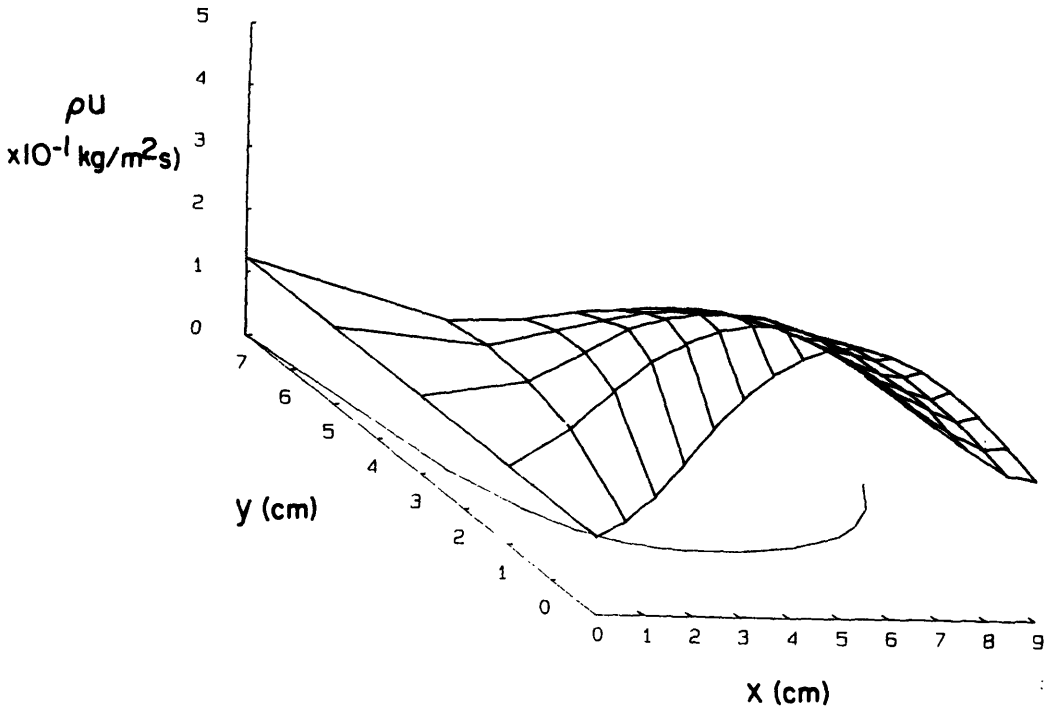

Figure A4.9: Theoretical Variation of the Momentum Throughout the Channel at 43 kA and an Argon Mass Flow Rate of 4 g/s

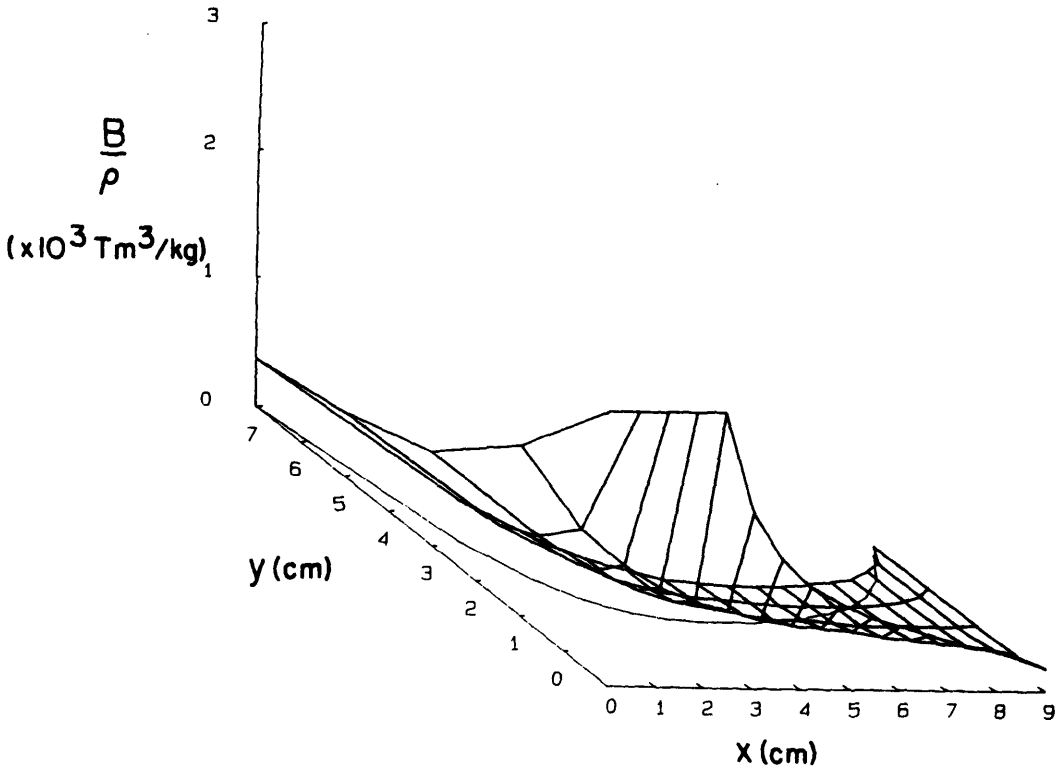

Figure A4.10: Theoretical Variation of B/ρ Throughout the Channel at 43 kA and an Argon Mass Flow Rate of 4 g/s

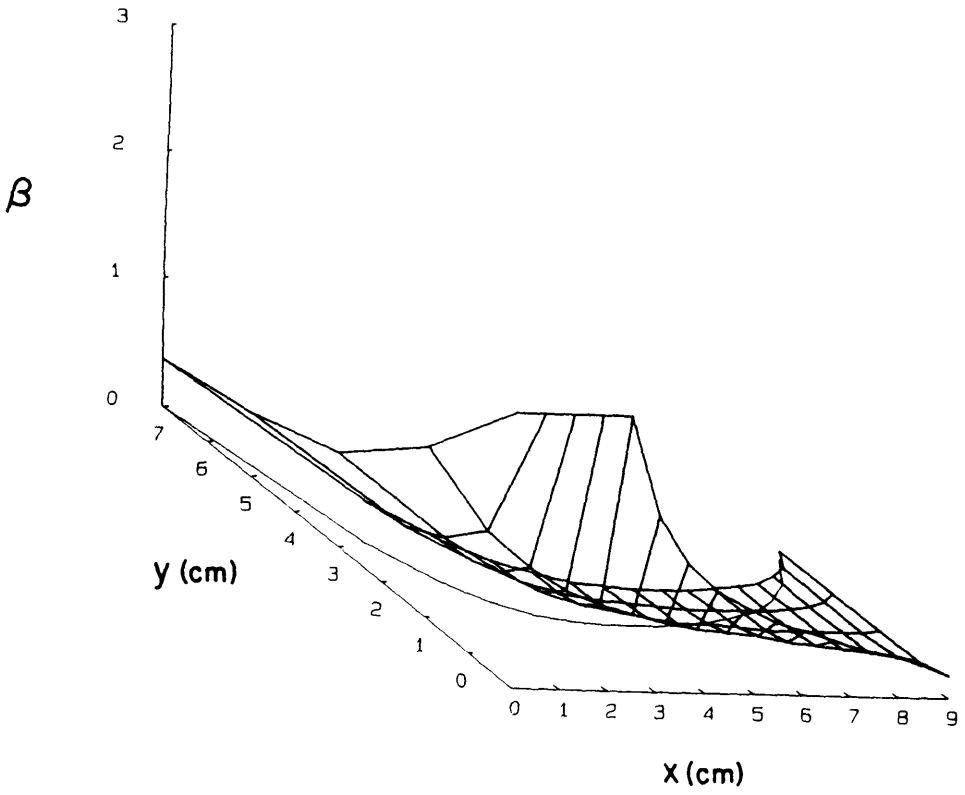

Figure A4.11: Theoretical Variation of the Hall Parameter Throughout the Channel at 43 kA and an Argon Mass Flow Rate of 4 g/s

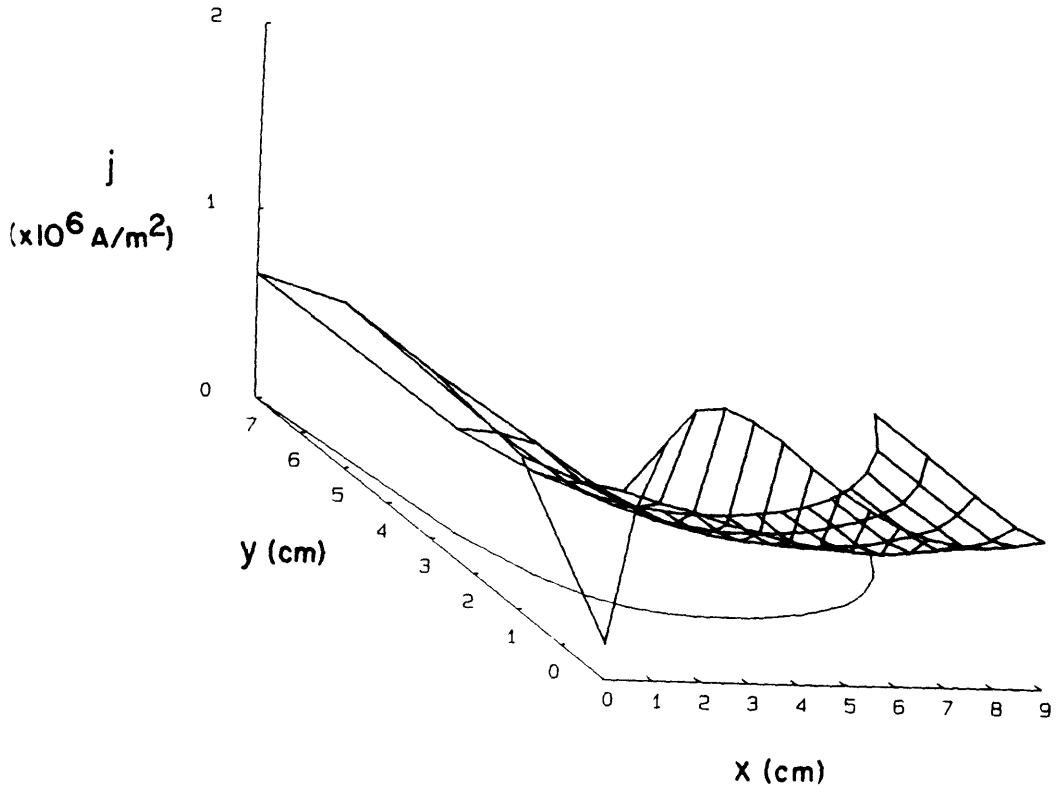

Figure A4.12: Theoretical Variation of the Total Current Density Throughout the Channel at 43 kA and an Argon Mass Flow Rate of 4 g/s

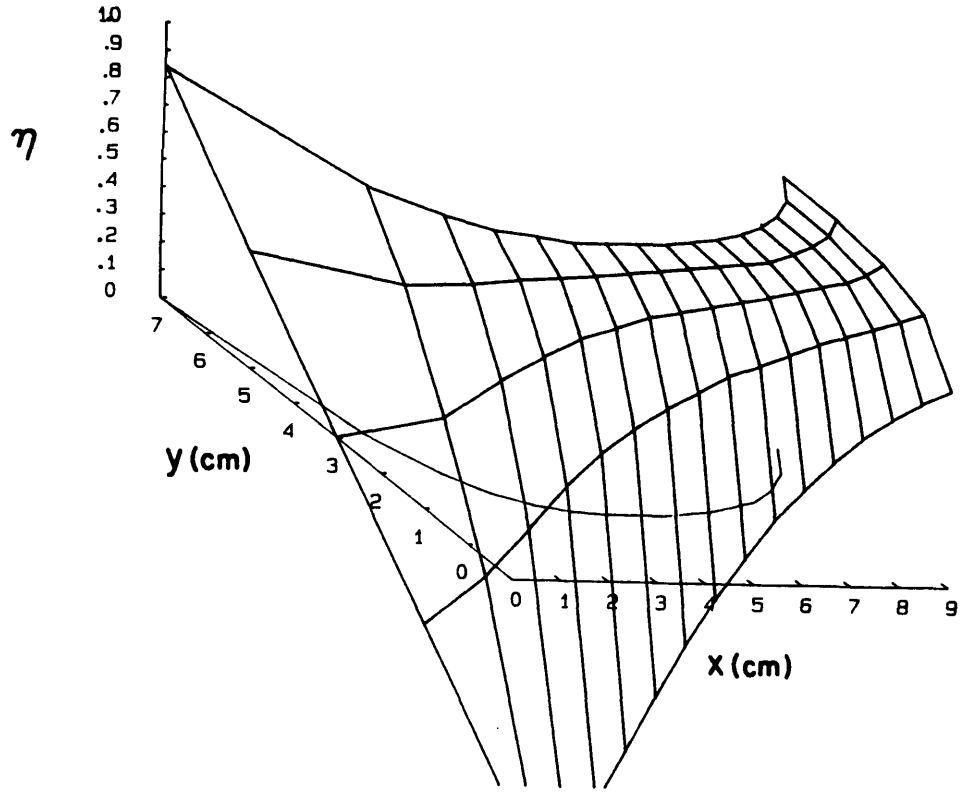

Figure A4.13: Theoretical Variation of η Throughout the Channel at 43 kA and an Argon Mass Flow Rate of 4 g/s

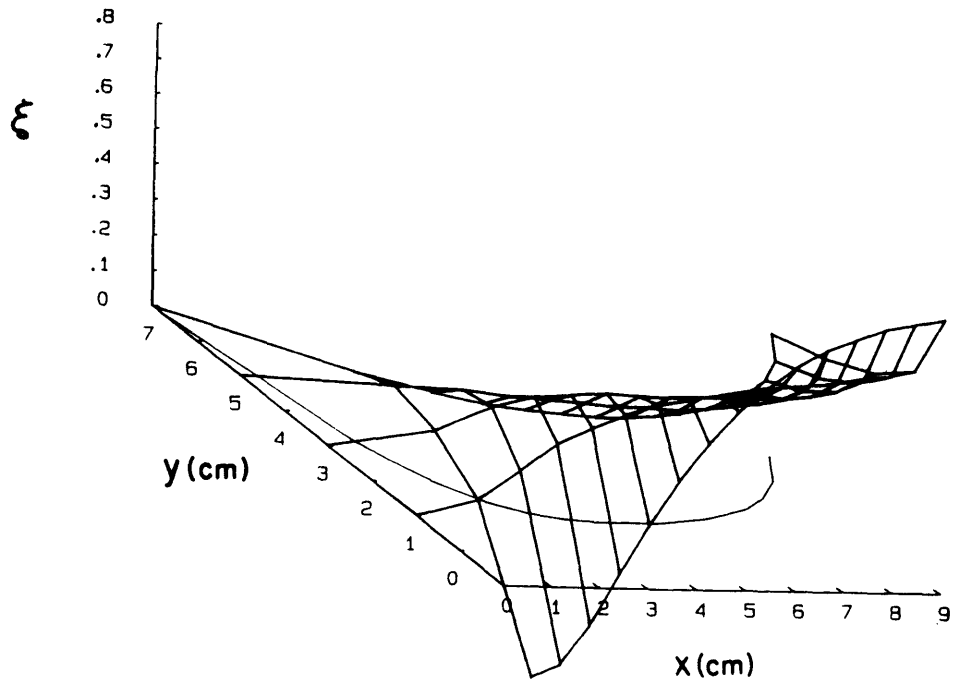

Figure A4.14: Theoretical Variation of ξ Throughout the Channel at 43 kA and an Argon Mass Flow Rate of 4 g/s

the density distribution; figure A4.7, the velocity distribution; figure A4.8, the local magnetoacoustic number; figure A4.9, the momentum distribution; figure A4.10, the distribution of B/ρ; figure A4.11, the Hall parameter distribution; figure A4.12, the current density distibution; figure A4.13, the η distribution; and figure A4.14, the ξ distribution.

Examination of these figures shows some interesting behavior. The initial parameters were selected so that the density went to zero somewhere along the anode. Therefore, this channel is operating at onset.

As expected, the interelectrode separation, shown in figure A4.4, indicates a converging-diverging section. The entrance and exit variation are quite severe but expected, since the initial velocity is small and the exit density is low. There is significant deviation from the zeroth order solution. This is indicative of large perturbations since the electrode separation is ultimately calculated from the density perturbation.

The variation of the magnetic field in figure A4.5 shows a generally monotonically decreasing behavior for increasing axial distance. The transverse behavior is somewhat different from experimental results which show increasing magnetic field near the cathode. This is due to the two-dimensional formulation. Regardless of geometry, the axial component of the current must point in the upstream direction. In the absence of cylindrical effects, this can only occur for increasing magnetic field in the direction of the anode.

The density, as expected, increases towards the cathode (figure A4.6). This is attributed to the pumping force which acts to pressurize

the cathode. In the axial direction, the density tends to decrease except near the anode. As stated previously, the density is seen to go to zero at a specific anode location. In this case, the onset condition appears only near the anode root. After the density drops to zero, the anode becomes less rarefied and may actually be locally above onset. After the throat region, the density, once again, decreases.

The velocity distribution shows a generally increasing trend with increasing axial distance. In the onset region, the local velocity is very large. In fact, the velocity appears to be elevated along the entire anode region where the flow is more rarefied. Since no transverse transport of fluid is allowed in this formulation, rarefaction in a given streamtube requires an increase in the velocity in order to satisfy mass conservation. A more appropriate measure is the local magnetoacoustic number. In figure A4.7, the local magnetoacoustic number is about 1.10 to 1.15 at the throat. According to the high interaction models presented in Appendix 3, the magnetoacoustic number at this location should be near unity, exactly unity for $R_n \to \infty$. Martinez-Sanchez notes that for finite interaction, the magnetoacoustic number at the throat should be a little higher than unity. This reflects the finite contribution of the electrothermal thrust.[27] The flow through the remaining channel increases to an exit magnetoacoustic number of about three, which is a reasonable value for any gas dynamic nozzle.

Figure A4.9 shows that the momentum is maximum near the throat of the channel. This is expected from the conservation of mass which requires an increase in momentum for a decrease in area. Its variation is not too

severe, which is good, since in this formulation, one of the constants in equation A4.34 assumes that the momentum is relatively constant throughout the channel.

The variations in magnetic field and density imply that the quantity B/ρ is very large at the anode root. This is shown in figure A4.10. Elsewhere, it tends to be a well behaved, axially decreasing quantity.

The Hall parameter behaves identically as B/ρ except that it has a different scaling. The Hall parameter is very large at the anode root indicating, as expected, poor electron collisionality. Values exceeding one are seen in this region. Elsewhere, the Hall parameter drops to more reasonable values near 0.4.

The local current density, which is the magnitude of the current density vector, has an odd shape due to the effect of the Hall Parameter. As seen in figure A4.12, the current density is low at the anode root but increases rapidly in the onset region. This behavior is due to the strong contribution by the axial current due to the high Hall Parameter. This is visualized in figure A4.15 which shows a plot of the magnitude and direction of the local current density vector. At the anode root, the entrance boundary conditions disallow any significant axial current. Otherwise, the current distribution is about constant throughout the channel. This is anticipated since the total pressure specification, $\Pi(x)$ is quadratic, and, for high interaction, is approximately the magnetic pressure.

The variation of η in figure A4.13 shows that the density perturbation is not really a very small parameter for this specification

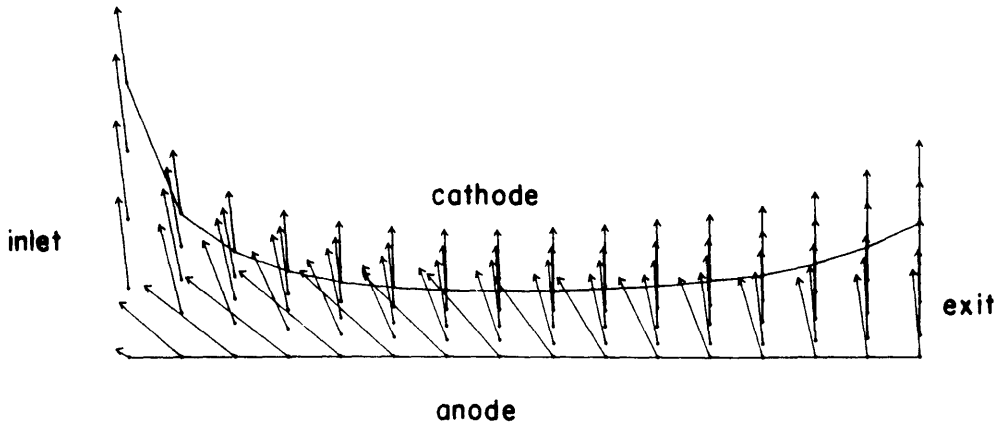

Figure A4.15: Magnitude and Direction of the Current Density Vector Throughout the Calculated Channel at 43 kA and an Argon Mass Flow Rate of 4 g/s

of initial parameters. This is to be anticipated since this channel was designed for the density to disappear somewhere along the anode, and to satisfy this, η must go to -1 at some location. This indicates that the validity of this model is somewhat questionable for these operational parameters. However, the anticipated discharge trends have been demonstrated, so although numerical fidelity may be questionable, the results of the model are quite encouraging.

The ξ variations are smaller than η and are therefore more believable in the perturbation sense. However, ξ is based on η and is therefore its numerical fidelity is also questionable. The interesting trend in this perturbation is that it is axially increasing indicating that the local momentum is greater than the zeroth order momentum except in the anode root region. This is anticipated since the perturbation channel separation is significantly smaller than the zeroth order separation.

Appendix 5: Design of the L-C Ladder System

Creation of a reasonable square current pulse can be achieved with a carefully designed electrical network consisting of inductors and capacitors in a ladder arrangement as described in Chapter III.

The MPD arcjet has been designed to operate at current levels up to 60 kA. It is desirable to operate at or below this current level without charging the capacitors to their full voltage. It is also necessary to have a pulse length of sufficient duration to provide for a quasi-steady operation. Barnett indicates that the transient to steady-state near the onset level can be significant--on the order of a millisecond in the worst case.[12] However, below onset, this transient does not appear to exceed 150 μs.

In the ideal L-C network, the characteristic pulse width is

$$\tau = 2n(LC)^{1/2} \qquad \text{A5.1}$$

where n is the number of stages. If the desired pulse width is 1.0 ms, the required inductance is about 15.6 μH for an eight stage ladder; however, given the capacitor maximum voltage, this inductor value provides for insufficient current. A 10 μH inductor significantly raises the value for steady-state current while only decreasing the pulse width by about 80%. To test the performance of a network designed with these parameters, a model of an L-C ladder was designed. The circuit diagram is shown in figure A5.1. This circuit diagram shows a ladder comprised of eight independently switched stages. As previously described, General Electric

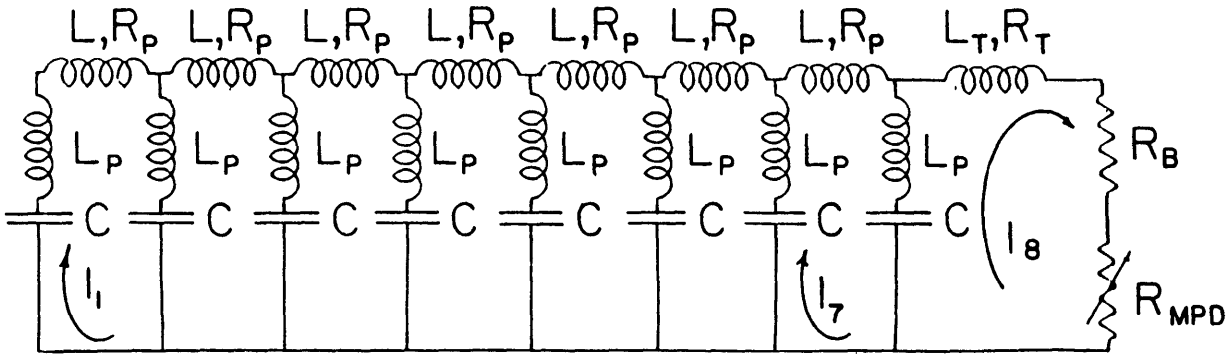

Figure A5.1: Eight Stage L-C Ladder Fired by a Single Ignitron

Ignitrons (high voltage mercury switches) can be triggered at any time during the discharge. The longest pulse is achieved by only triggering ignitron #8. This will provide a characteristic pulse length of approximately one millisecond, however the output current level is only about 35 kA. Another desirable scheme is to trigger both ignitrons #1 and #8 simultaneously. This acts to halve the pulse duration, while increasing the output current. Both of these cases will be treated in this appendix.

In this circuit analysis, the parasitic resistance of each inductor was estimated and included. The estimated magnitude of the parasitic resistance associated with each capacitor/parasitic inductor was negligible and was not included in the overall circuit model. A final terminating inductor with an inductance twice the value of each stage inductance may be placed at the end of the circuit. This inductor tends to slow the circuit's characteristic rise time, but Black found that it helps cut the overshoot associated with this type of L-C ladder.[43]

The impedance of the ladder, closed by a single Ignitron, can be estimated to first order as

$$Z = \left(\frac{L}{C}\right)^{1/2} \qquad \text{A5.2}$$

which at 0.2 Ω (for an eight stage ladder) is greater than the few milliohms expected in the MPD arcjet. To prevent severe ringing of the line voltage, a matching resistor is required. When the two Ignitrons are closed simultaneously, the impedance is halved, but the circuit still requires a matching resistor.

A5.1: Derivation of the L-C Ladder Equations

Using Kirchoff's Laws, the loop current equations for each stage can be written. The loop current equation, following the sign convention of positive current in the clockwise direction (refer to figure A5.1), is shown as follows

$$\ddot{I}_1 - \frac{L_p}{L + 2L_p}\ddot{I}_2 = \frac{I_2 - 2I_1}{(L + 2L_p)C} - \frac{R}{L + 2L_p}\dot{I}_1 \qquad \text{A5.3}$$

The expression for the second stage as well as stages three to seven (replacing the appropriate subscripts) is

$$\ddot{I}_2 - \frac{L_p}{L + 2L_p}\ddot{I}_1 - \frac{L_p}{L + 2L_p}\ddot{I}_3 = \frac{1}{(L + 2L_p)C}(I_1 + I_3 - 2I_2) - \frac{R}{L + 2L_p}\dot{I}_2 \qquad \text{A5.4}$$

and the expression for the current through the final stage is

$$\ddot{I}_8 - \frac{L_p}{L_p + L_T}\ddot{I}_7 = \frac{I_7 - I_8}{(L_p + L_T)C} - \frac{R_T + R_L}{L_p + L_T}\dot{I}_8 \qquad \text{A5.5}$$

Here I_1 through I_8 represent the loop currents (the "dotted" variables represent the time derivatives of the quantities with the order of the derivative equal to the number of dots), L, L_p, and L_T are the stage inductance, parasitic inductance, and terminating inductance, R is each inductor's parasitic resistance, R_L is the matched load resistance, R_T is the terminating resistance, and C is the stage capacitance.

This system is comprised of eight second order coupled ordinary differential equations. Solution requires sixteen initial conditions. At

t=0, no current flows so $I_1(0)=I_2(0)=\ldots=I_8(0)=0$ and, when the discharge is initially triggered, $\dot{I}_1(0)=\dot{I}_2(0)=\ldots=\dot{I}_7(0)=0$ and $\dot{I}_8 = \frac{CV_C}{L_P + L_T}$ where V_C is the charging voltage of the bank.

The differential equations can be written in a slightly more convenient vector form

$$\underline{A}\ddot{\underline{I}} = \underline{B} \qquad \text{A5.6}$$

where $\underline{A}$ is a coefficient matrix, $\ddot{\underline{I}}$ is the vector composed of the second derivatives of the loop currents with respect to time, and $\underline{B}$ is a vector composed of elements that are functions of the loop currents and their first derivatives. This matrix differential equation is further modified to take advantage of convenient numerical integration procedures. The new form is

$$\underline{A}'\underline{x} = \underline{B}' \qquad \text{A5.7}$$

where $\underline{A}'$ and $\underline{B}'$ are modified matrices of sizes 2n by 2n and 2n by 1 respectively, and $\underline{x}$ is a column vector comprised of the vector $\underline{\dot{I}}$ catenated to the vector $\underline{I}$. Inverting this equation leaves

$$\underline{x} = \underline{C} \qquad \text{A5.8}$$

where

$$\underline{C} = \underline{A}'^{-1}\underline{B}' \qquad \text{A5.9}$$

which is now amenable to numerical integration.

From equations A5.3 to A5.7, $\underline{A}'$ can be written in a sparse banded matrix

$$
\begin{bmatrix}
1 & 0 & 0 & 0 & 0 & 0 & 0 & 0 & 0 & 0 & 0 & 0 & 0 & 0 & 0 & 0 \\
0 & 1 & 0 & 0 & 0 & 0 & 0 & 0 & 0 & 0 & 0 & 0 & 0 & 0 & 0 & 0 \\
0 & 0 & 1 & 0 & 0 & 0 & 0 & 0 & 0 & 0 & 0 & 0 & 0 & 0 & 0 & 0 \\
0 & 0 & 0 & 1 & 0 & 0 & 0 & 0 & 0 & 0 & 0 & 0 & 0 & 0 & 0 & 0 \\
0 & 0 & 0 & 0 & 1 & 0 & 0 & 0 & 0 & 0 & 0 & 0 & 0 & 0 & 0 & 0 \\
0 & 0 & 0 & 0 & 0 & 1 & 0 & 0 & 0 & 0 & 0 & 0 & 0 & 0 & 0 & 0 \\
0 & 0 & 0 & 0 & 0 & 0 & 1 & 0 & 0 & 0 & 0 & 0 & 0 & 0 & 0 & 0 \\
0 & 0 & 0 & 0 & 0 & 0 & 0 & 1 & 0 & 0 & 0 & 0 & 0 & 0 & 0 & 0 \\
0 & 0 & 0 & 0 & 0 & 0 & 0 & 0 & 1 & \frac{-L_p}{L+2L_p} & 0 & 0 & 0 & 0 & 0 & 0 \\
0 & 0 & 0 & 0 & 0 & 0 & 0 & 0 & \frac{-L_p}{L+2L_p} & 1 & \frac{-L_p}{L+2L_p} & 0 & 0 & 0 & 0 & 0 \\
0 & 0 & 0 & 0 & 0 & 0 & 0 & 0 & 0 & \frac{-L_p}{L+2L_p} & 1 & \frac{-L_p}{L+2L_p} & 0 & 0 & 0 & 0 \\
0 & 0 & 0 & 0 & 0 & 0 & 0 & 0 & 0 & 0 & \frac{-L_p}{L+2L_p} & 1 & \frac{-L_p}{L+2L_p} & 0 & 0 & 0 \\
0 & 0 & 0 & 0 & 0 & 0 & 0 & 0 & 0 & 0 & 0 & \frac{-L_p}{L+2L_p} & 1 & \frac{-L_p}{L+2L_p} & 0 & 0 \\
0 & 0 & 0 & 0 & 0 & 0 & 0 & 0 & 0 & 0 & 0 & 0 & \frac{-L_p}{L+2L_p} & 1 & \frac{-L_p}{L+2L_p} & 0 \\
0 & 0 & 0 & 0 & 0 & 0 & 0 & 0 & 0 & 0 & 0 & 0 & 0 & \frac{-L_p}{L+2L_p} & 1 & \frac{-L_p}{L+2L_p} \\
0 & 0 & 0 & 0 & 0 & 0 & 0 & 0 & 0 & 0 & 0 & 0 & 0 & 0 & \frac{-L_p}{L_T+L_p} & 1
\end{bmatrix}
$$

A5.10

and $\underline{B}'$ can be written as

$$\begin{bmatrix} \dot{I}_1 \\ \dot{I}_2 \\ \dot{I}_3 \\ \dot{I}_4 \\ \dot{I}_5 \\ \dot{I}_6 \\ \dot{I}_7 \\ \dot{I}_8 \\ \frac{1}{(L+2L_p)C}(I_2 - 2I_1) - \frac{R}{L+2L_p}\dot{I}_1 \\ \frac{1}{(L+2L_p)C}(I_1 + I_3 - 2I_2) - \frac{R}{L+2L_p}\dot{I}_2 \\ \frac{1}{(L+2L_p)C}(I_2 + I_4 - 2I_3) - \frac{R}{L+2L_p}\dot{I}_3 \\ \frac{1}{(L+2L_p)C}(I_3 + I_5 - 2I_4) - \frac{R}{L+2L_p}\dot{I}_4 \\ \frac{1}{(L+2L_p)C}(I_4 + I_6 - 2I_5) - \frac{R}{L+2L_p}\dot{I}_5 \\ \frac{1}{(L+2L_p)C}(I_5 + I_7 - 2I_6) - \frac{R}{L+2L_p}\dot{I}_6 \\ \frac{1}{(L+2L_p)C}(I_6 + I_8 - 2I_7) - \frac{R}{L+2L_p}\dot{I}_7 \\ \frac{1}{(L_T+L_p)C}(I_7 - I_8) - \frac{R_T+R_l}{L_T+L_p}\dot{I}_8 \end{bmatrix} \qquad \text{A5.11}$$

Integration of this second order system can be accomplished by using Runge-Kutta integration techniques. Code utilizing a fourth order accurate Runge-Kutta integrator was written and included in Appendix 11.

For inductor values of 10 μH, a final inductor of 20 μH, and a charging voltage of 20,000 V, a maximum current pulse for this eight stage

bank is found and is shown in figure A5.2.

Larger current values can be achieved by simultaneously triggering ignitrons #1 and #8. In this case, the matrices $\underline{A}'$ and $\underline{B}'$ have a slightly different form. This is readily seen in the equivalent loop current diagram shown in figure A5.3. In this case, there are now nine loop currents since the load is fed from both sides of the ladder. But by symmetry, no current will flow in the middle section so $I_5=0$ as does all its derivatives. This leaves $\underline{A}'$ in the following sparse banded form

$$\begin{bmatrix}
1 & 0 & 0 & 0 & 0 & 0 & 0 & 0 & 0 & 0 & 0 & 0 & 0 & 0 & 0 & 0 \\
0 & 1 & 0 & 0 & 0 & 0 & 0 & 0 & 0 & 0 & 0 & 0 & 0 & 0 & 0 & 0 \\
0 & 0 & 1 & 0 & 0 & 0 & 0 & 0 & 0 & 0 & 0 & 0 & 0 & 0 & 0 & 0 \\
0 & 0 & 0 & 1 & 0 & 0 & 0 & 0 & 0 & 0 & 0 & 0 & 0 & 0 & 0 & 0 \\
0 & 0 & 0 & 0 & 1 & 0 & 0 & 0 & 0 & 0 & 0 & 0 & 0 & 0 & 0 & 0 \\
0 & 0 & 0 & 0 & 0 & 1 & 0 & 0 & 0 & 0 & 0 & 0 & 0 & 0 & 0 & 0 \\
0 & 0 & 0 & 0 & 0 & 0 & 1 & 0 & 0 & 0 & 0 & 0 & 0 & 0 & 0 & 0 \\
0 & 0 & 0 & 0 & 0 & 0 & 0 & 1 & 0 & 0 & 0 & 0 & 0 & 0 & 0 & 0 \\
0 & 0 & 0 & 0 & 0 & 0 & 0 & 0 & 1 & \frac{-L_p}{L+2L_p} & 0 & 0 & 0 & 0 & 0 & \frac{-L_T}{L+2L_p} \\
0 & 0 & 0 & 0 & 0 & 0 & 0 & 0 & \frac{-L_p}{L+2L_p} & 1 & \frac{-L_p}{L+2L_p} & 0 & 0 & 0 & 0 & 0 \\
0 & 0 & 0 & 0 & 0 & 0 & 0 & 0 & 0 & \frac{-L_p}{L+2L_p} & 1 & \frac{-L_p}{L+2L_p} & 0 & 0 & 0 & 0 \\
0 & 0 & 0 & 0 & 0 & 0 & 0 & 0 & 0 & 0 & \frac{-L_p}{L+2L_p} & 1 & 0 & 0 & 0 & 0 \\
0 & 0 & 0 & 0 & 0 & 0 & 0 & 0 & 0 & 0 & 0 & 0 & 1 & \frac{-L_p}{L+2L_p} & 0 & 0 \\
0 & 0 & 0 & 0 & 0 & 0 & 0 & 0 & 0 & 0 & 0 & 0 & \frac{-L_p}{L+2L_p} & 1 & \frac{-L_p}{L+2L_p} & 0 \\
0 & 0 & 0 & 0 & 0 & 0 & 0 & 0 & 0 & 0 & 0 & 0 & 0 & \frac{-L_p}{L_T+L_p} & 1 & \frac{-L_p}{L_T+L_p} \\
0 & 0 & 0 & 0 & 0 & 0 & 0 & 0 & \frac{-L_T}{L_T+L_p} & 0 & 0 & 0 & 0 & 0 & \frac{-L_T}{L_T+L_p} & 1
\end{bmatrix}$$

A5.12

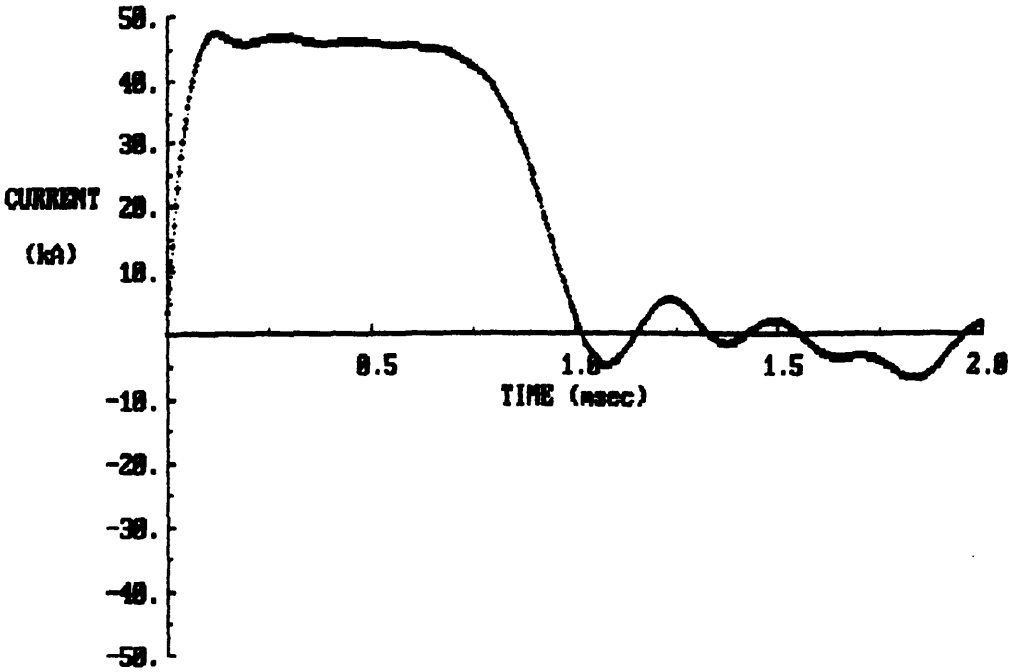

Figure A5.2: Theoretical Current Pulse from the Eight Stage L-C Ladder Fired by a Single Ignitron

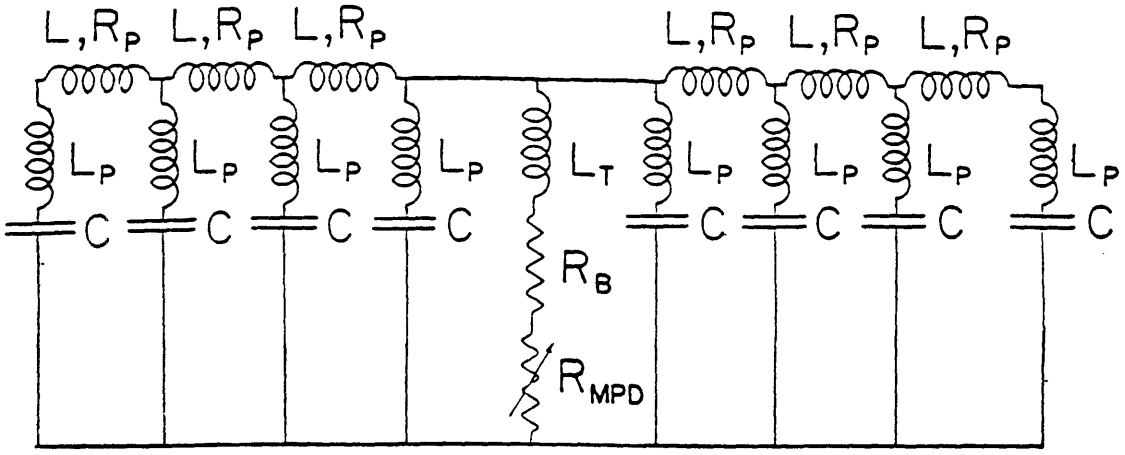

Figure A5.3: Eight Stage L-C Ladder Fired by Two Ignitrons

and $\underline{B}'$ as

$$\begin{bmatrix} \dot{I}_1 \\ \dot{I}_2 \\ \dot{I}_3 \\ \dot{I}_4 \\ \dot{I}_6 \\ \dot{I}_7 \\ \dot{I}_8 \\ \dot{I}_9 \\ \frac{1}{(L+L_T)C}(I_2 - I_1) - \frac{R_L+R_T}{L+2L_p}(\dot{I}_1 - \dot{I}_9) \\ \frac{1}{(L+2L_p)C}(I_1 + I_3 - 2I_2) - \frac{R}{L+2L_p}\dot{I}_2 \\ \frac{1}{(L+2L_p)C}(I_2 + I_4 - 2I_3) - \frac{R}{L+2L_p}\dot{I}_3 \\ \frac{1}{(L+2L_p)C}(I_3 - 2I_4) - \frac{R}{L+2L_p}\dot{I}_4 \\ \frac{1}{(L+2L_p)C}(I_7 - 2I_6) - \frac{R}{L+2L_p}\dot{I}_6 \\ \frac{1}{(L+2L_p)C}(I_6 + I_8 - 2I_7) - \frac{R}{L+2L_p}\dot{I}_7 \\ \frac{1}{(L_T+L_p)C}(I_7 + I_9 - 2I_8) - \frac{R}{L_T+L_p}\dot{I}_8) \\ \frac{1}{(L_T+L_p)C}(I_1 - I_9) - \frac{R_T+R_L}{L_T+L_p}(\dot{I}_9 - \dot{I}_8) \end{bmatrix} \qquad \text{A5.13}$$

with the appropriate initial conditions

$$I_1 = I_2 = \ldots = I_9 = 0 \;;\; \dot{I}_1 = \dot{I}_2 = \ldots = \dot{I}_8 = 0 \quad \text{and} \quad \dot{I}_9 = \frac{V_C}{2L_T + L_p} \qquad \text{A5.14}$$

In the design of this network, it is important to ensure that voltage reversals on the capacitors are well within their prescribed limits to

prevent physical damage. A typical plot of the voltage trace across a capacitor initially charged to 20,000 V is seen in figure A5.4 and shows that these reversals are not too severe.

A5.2: Design of the Inductors

Proper inductor design is quite important to the performance of the system. These inductors must be designed to have the requisite inductance, a low resistance so that the L/R decay of the system is negligible in comparison to the L-C time constant, and they must be strong enough to prevent deformation from the magnetic force during each pulse. To minimize the resistance of the inductor, it is necessary to first determine how much of the conductor participates in current conduction over the duration of the event. To do this, the transient skin depth of the conducting medium must be estimated. The skin depth is a measure of the penetration of an electromagnetic wave into a conducting medium and is defined as

$$\delta = \left(\frac{2}{\omega\sigma\mu_0}\right)^{1/2} \qquad \text{A5.15}$$

where ω is the angular frequency. For copper at a frequency of 10 kHz, this quantity is approximately 0.7 mm.[44] The conducting material has an internal resistance of

$$R_L = \frac{L}{\sigma A} \qquad \text{A5.16}$$

which must be small so as not to induce a significant resistive decay into the system. From iterative considerations including material cost, ease in construction, and size, a helical inductor design, based on data in Grover, was deemed appropriate.[45] Eight turns of #0000 EGR-Hypalon

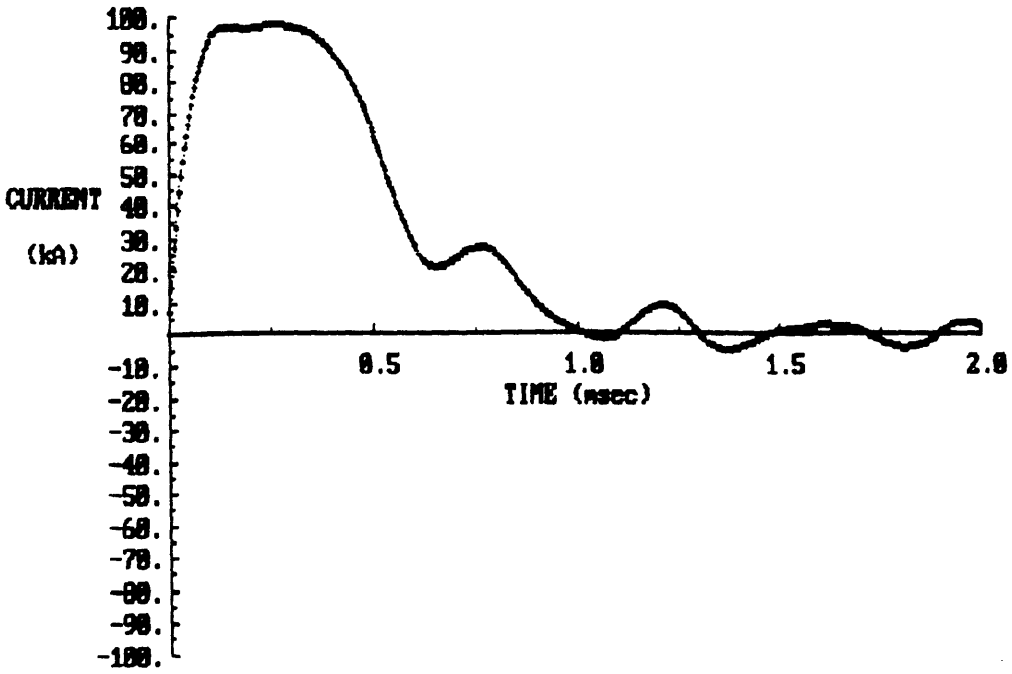

Figure A5.4: Theoretical Current Pulse from the Eight Stage L-C Ladder Fired by Two Ignitrons

insulated copper wire were wrapped around a six inch diameter PVC mandrel. The resulting inductor has an approximate inductance of 10.1 μH and an approximate parasitic resistance of about three milliohms. The impulse felt by each inductor is, at most, about 10 pound-seconds which should be carried easily by the material. Since the inductors are heavy and not completely rigid, a fiberglass cladding is used for additional containment and strength.

A5.3: Design of the Matching Resistor and Thruster Connection

The matching resistor was constructed out of a forty gallon garbage can filled with a copper sulfate solution. Two large copper plates separated by a four inch gap (for the 0.2 Ω resistor) or a two inch gap (for the 0.12 Ω resistor) are immersed into the solution whose concentration is tuned to the required resistance. The resistor is not difficult to tune and its large capacity prevents significant temperature variation. Over the course of a single day, over fifty shots were fired at about 13 kV charge, and the resistor temperature rose only 10 K.

The MPD arcjet is connected to the pulse forming network through ten sixty foot RG 213/U coaxial cables. This is to minimize both the inductive and resistive losses inherent to long transmission lines. The initial capacitive effects of the transmission line damp out so rapidly that they are of no major concern for this experiment and are not included in this analysis.

Appendix 6: MIT/RDA MPD Arcjet Schematics

This appendix contains the mechanical drawings of the MPD arcjet and the three cathodes used in this experiment. Complete drawings for the system are not provided but are on file at R&D Associates, Washington Research Laboratory in Alexandria, Virginia.

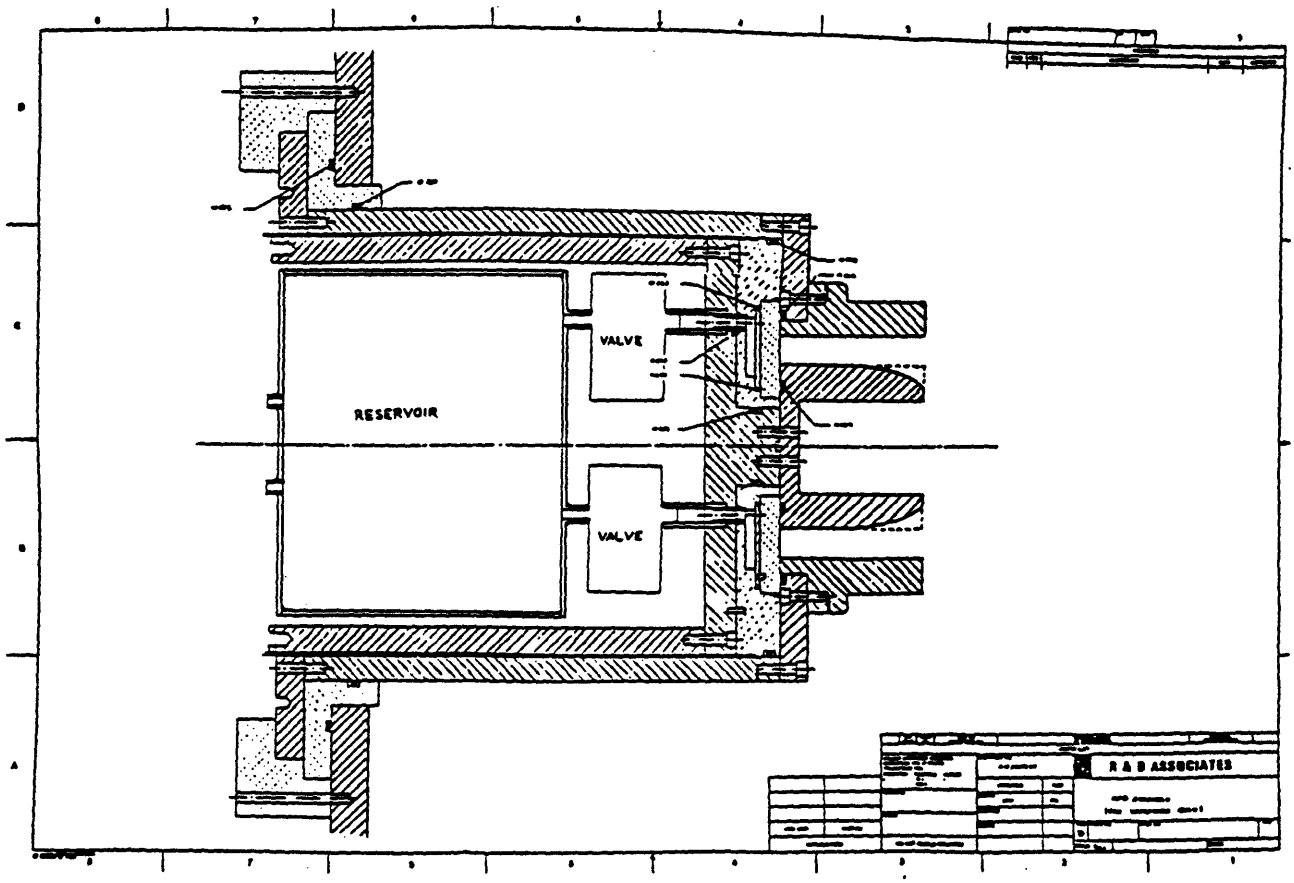

Figure A6.1: MPD Arcjet Assembly Drawing

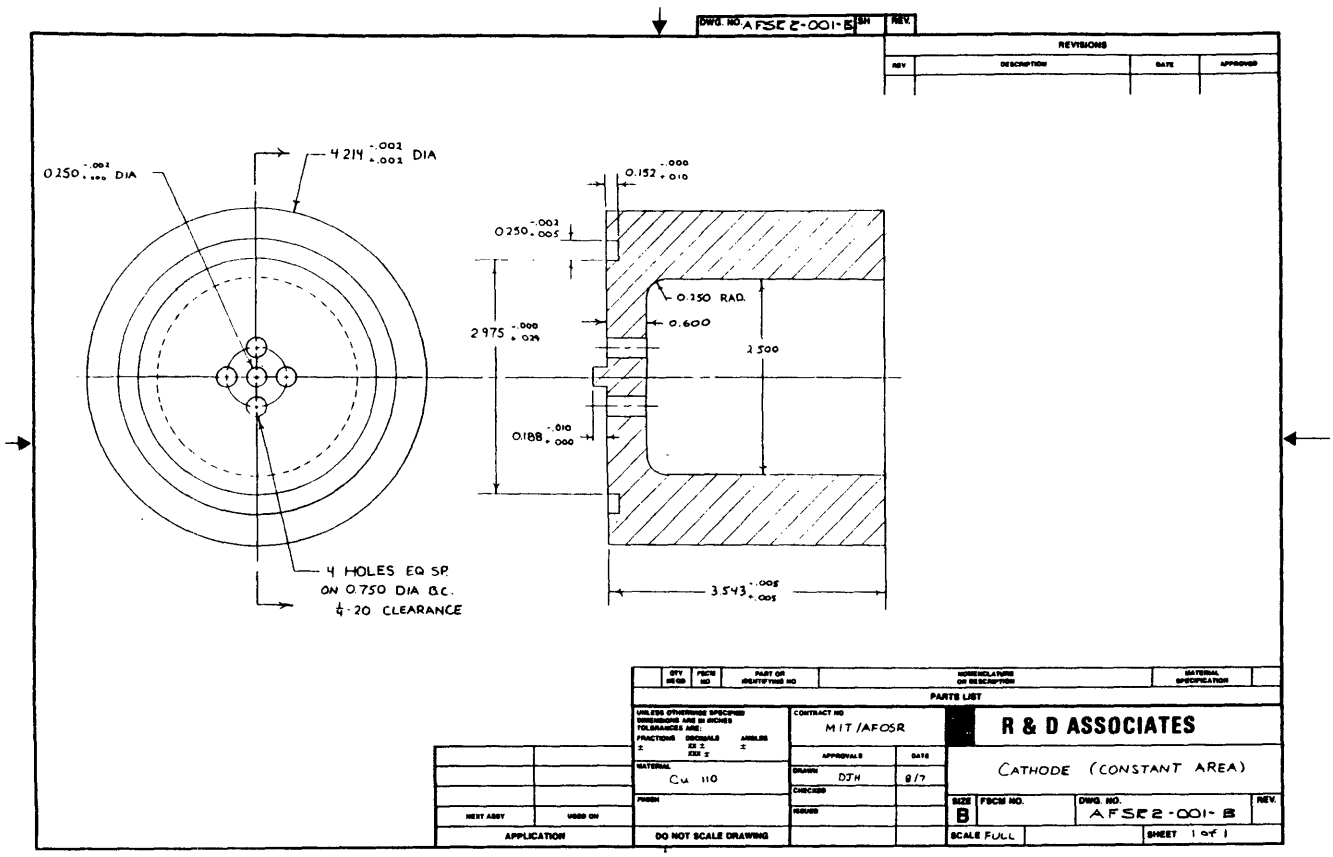

Figure A6.2: Constant Area Cathode

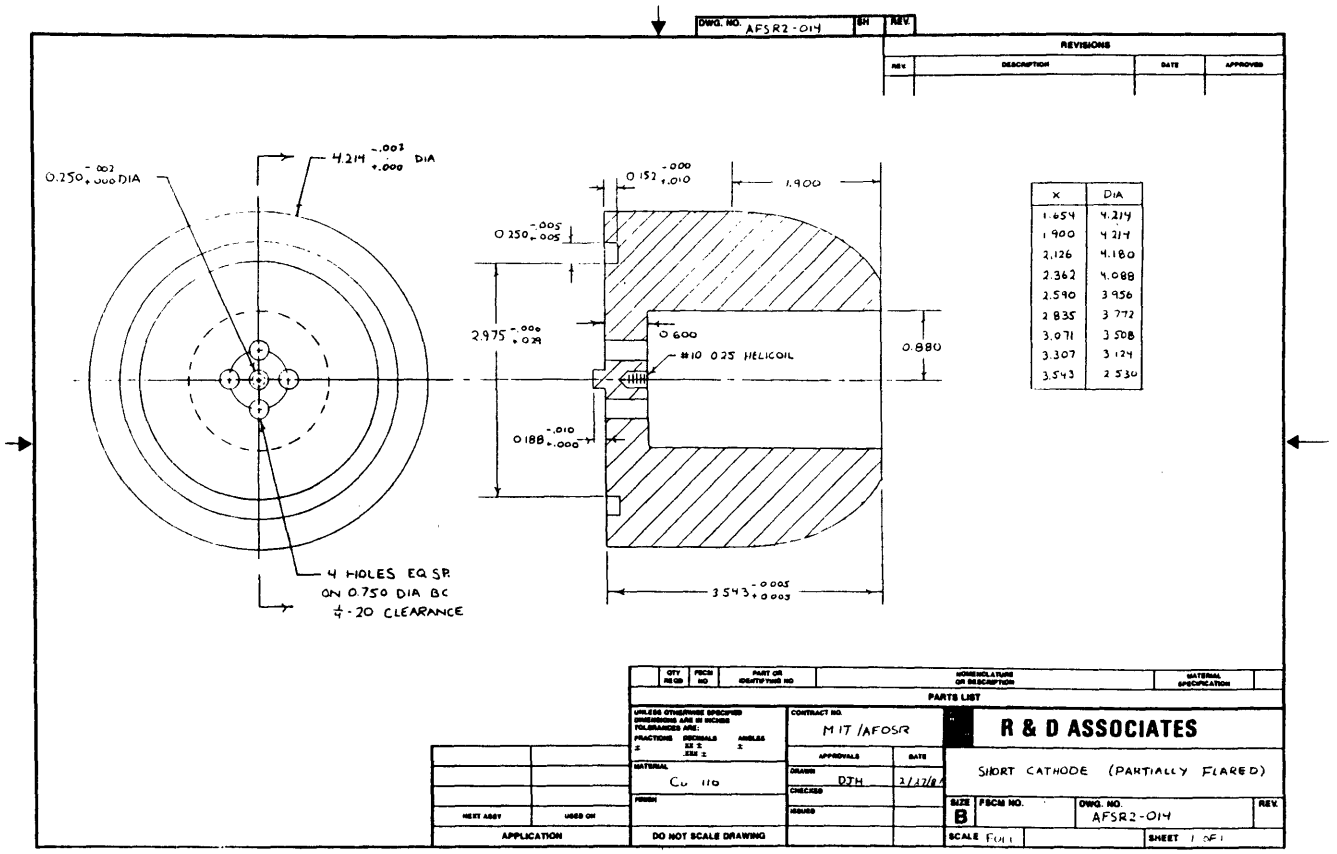

Figure A6.3: Partially Flared Cathode

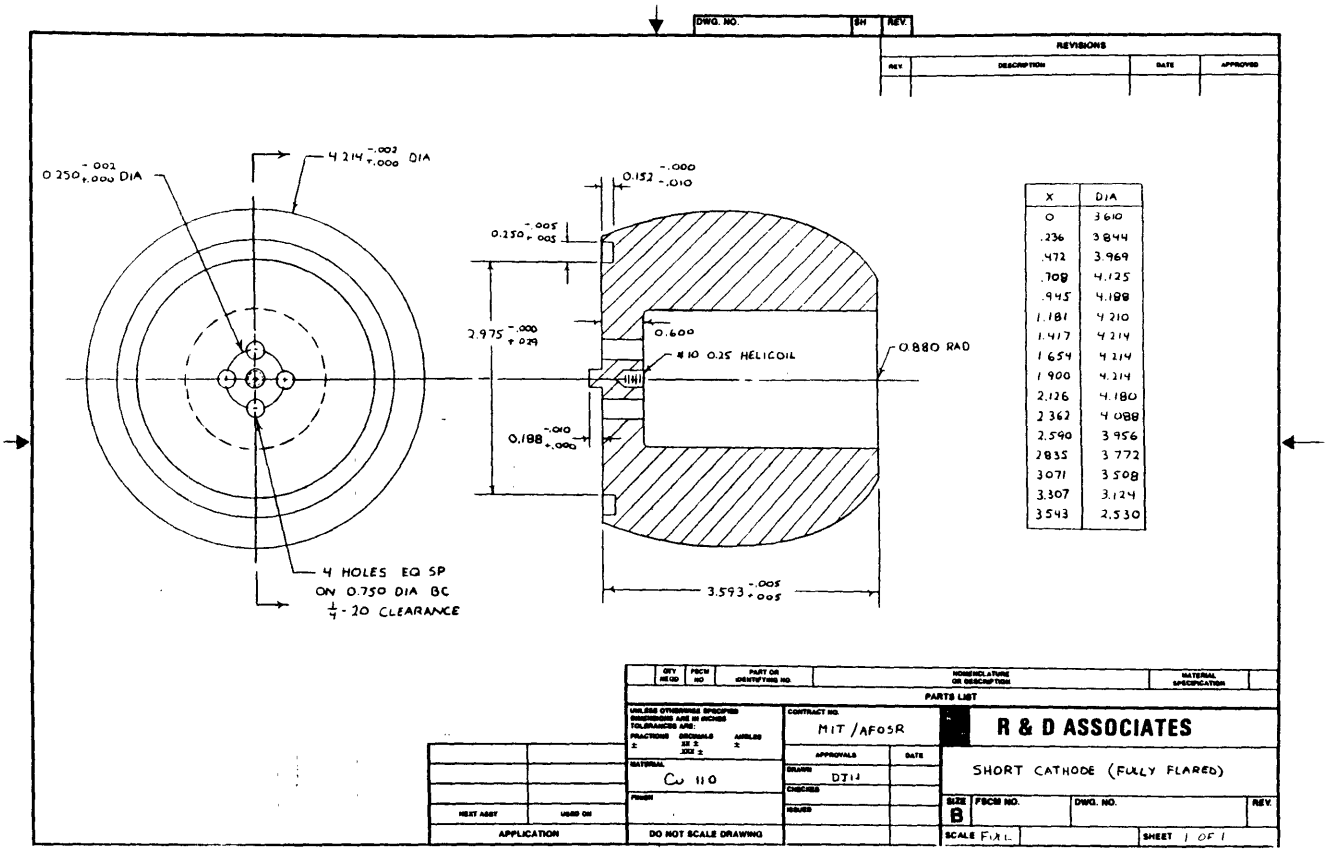

Figure A6.4: Fully Flared Cathode

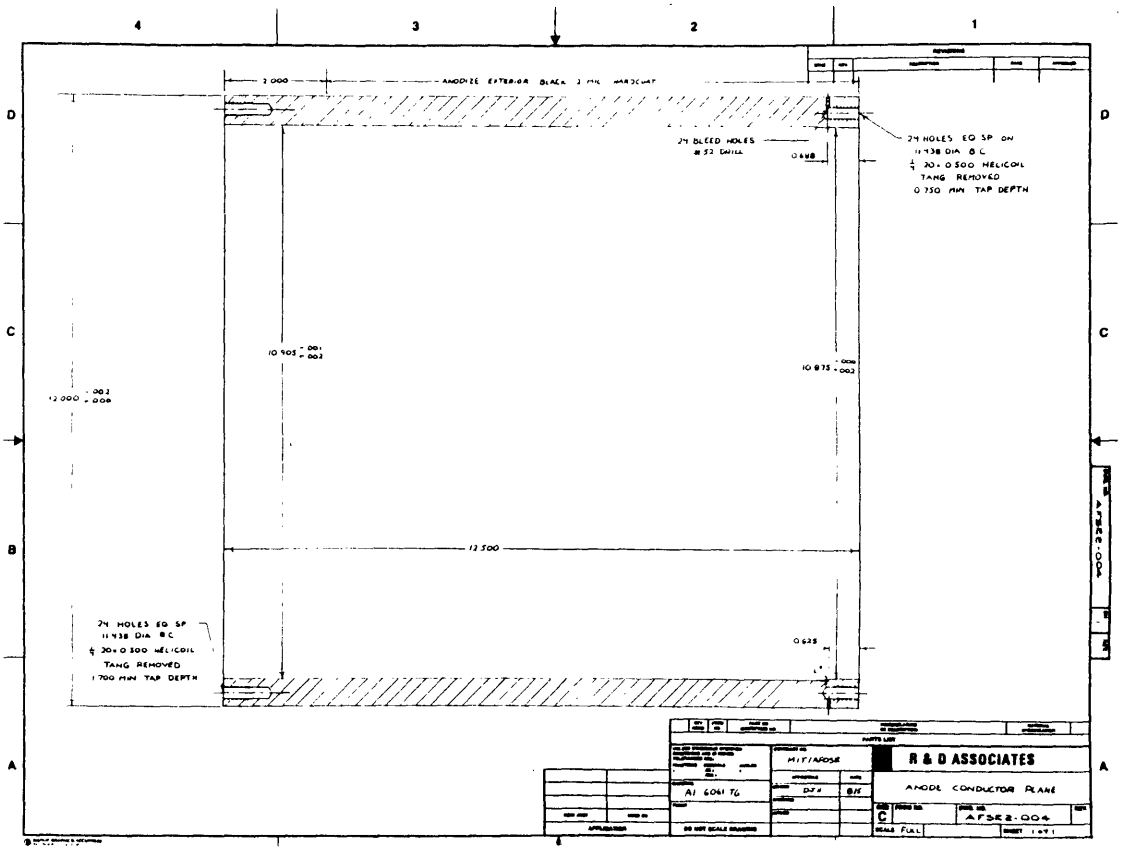

Figure A6.5: Anode Conductor Plane

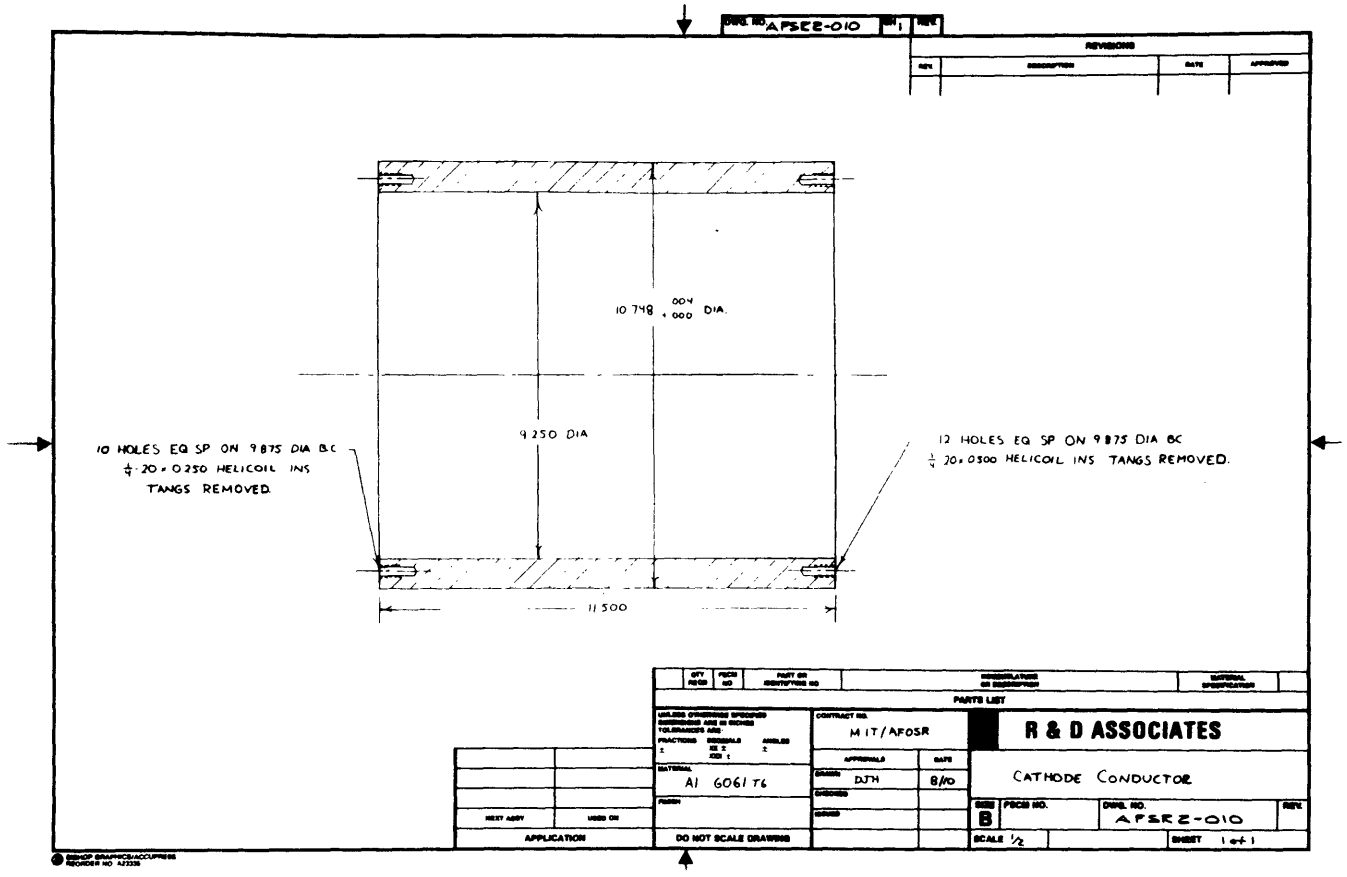

Figure A6.6: Cathode Conductor

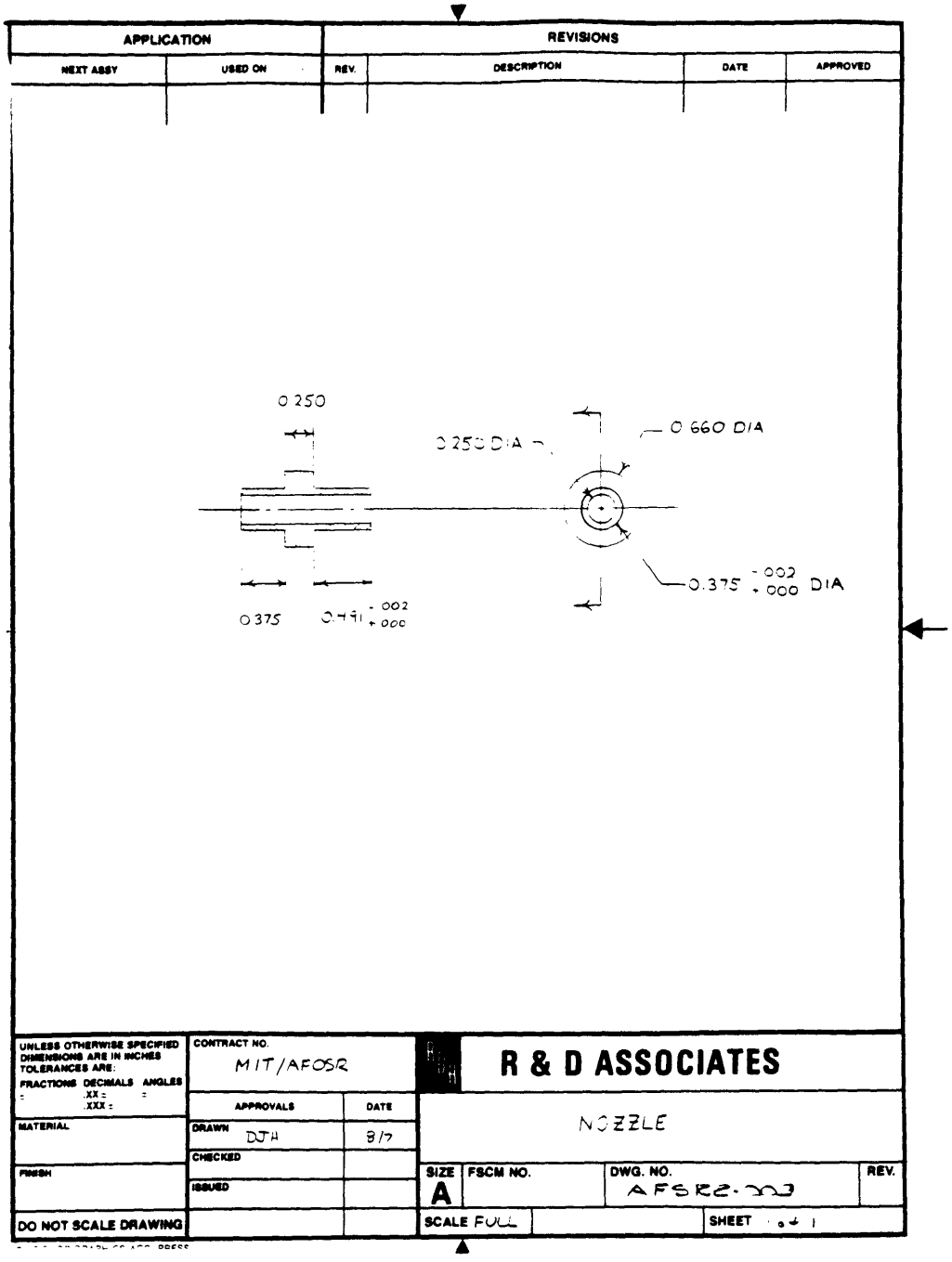

Figure A6.7: Nozzle

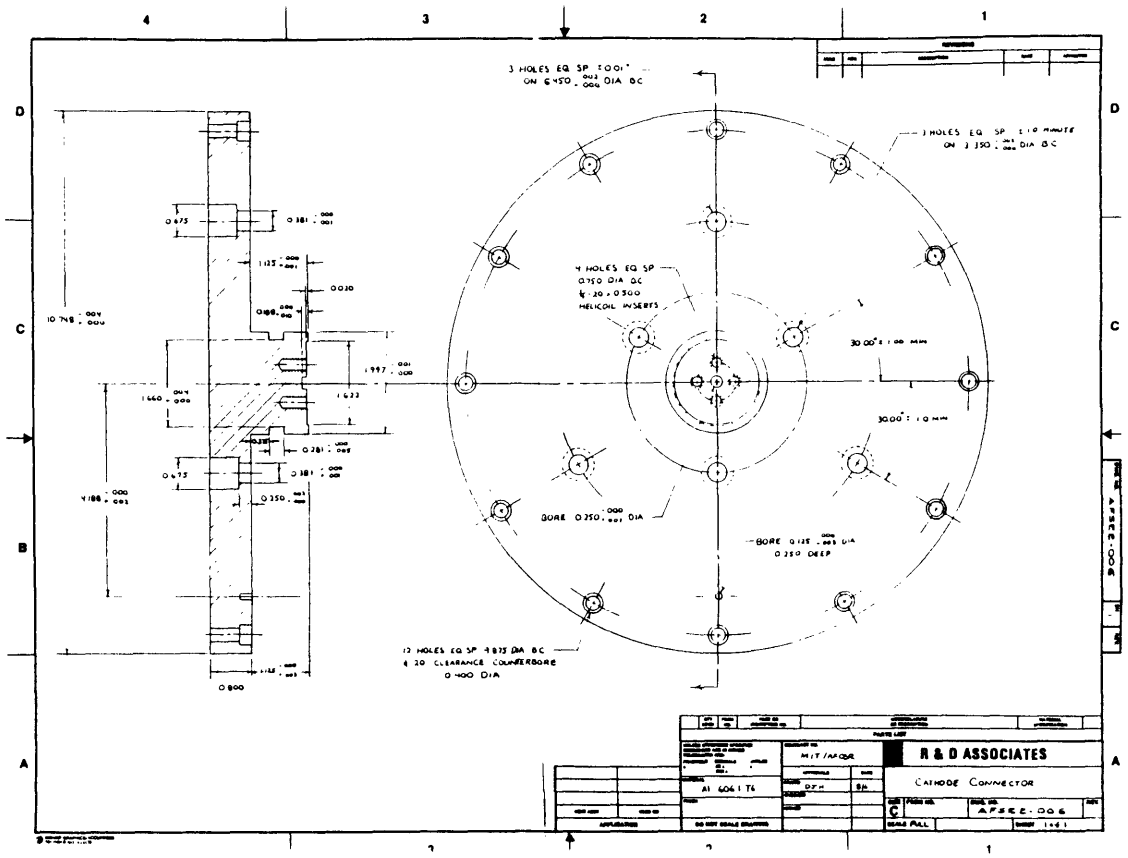

Figure A6.8: Cathode Connector

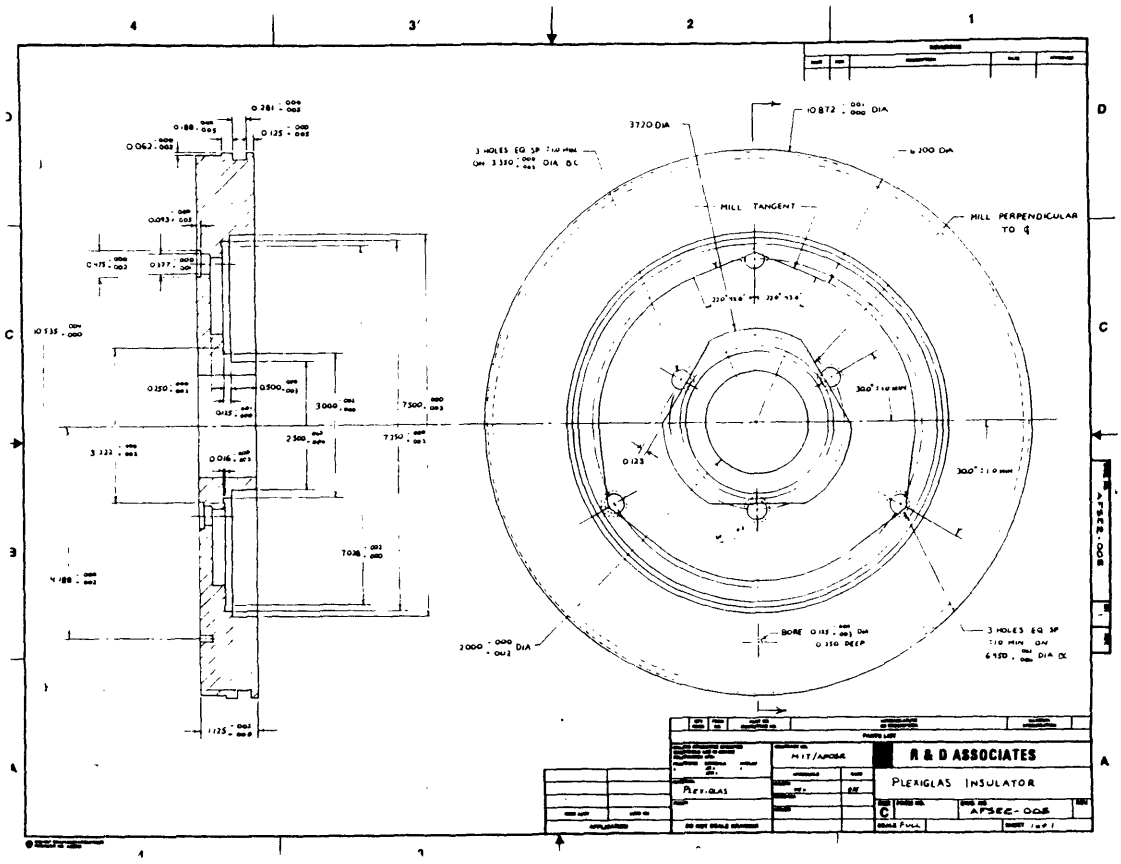

Figure A6.9: Plexiglas Insulator

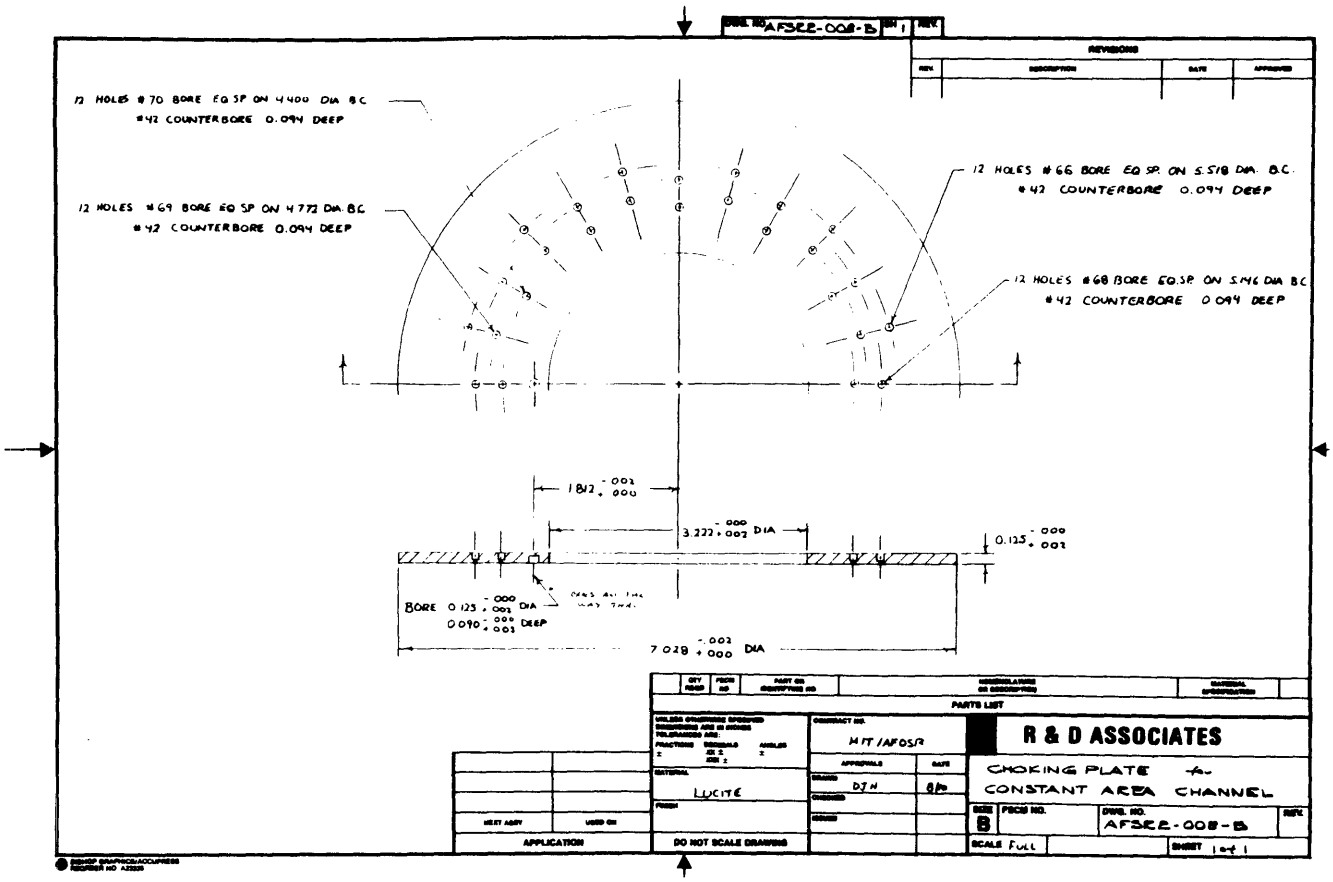

Figure A6.10: Choking Plate

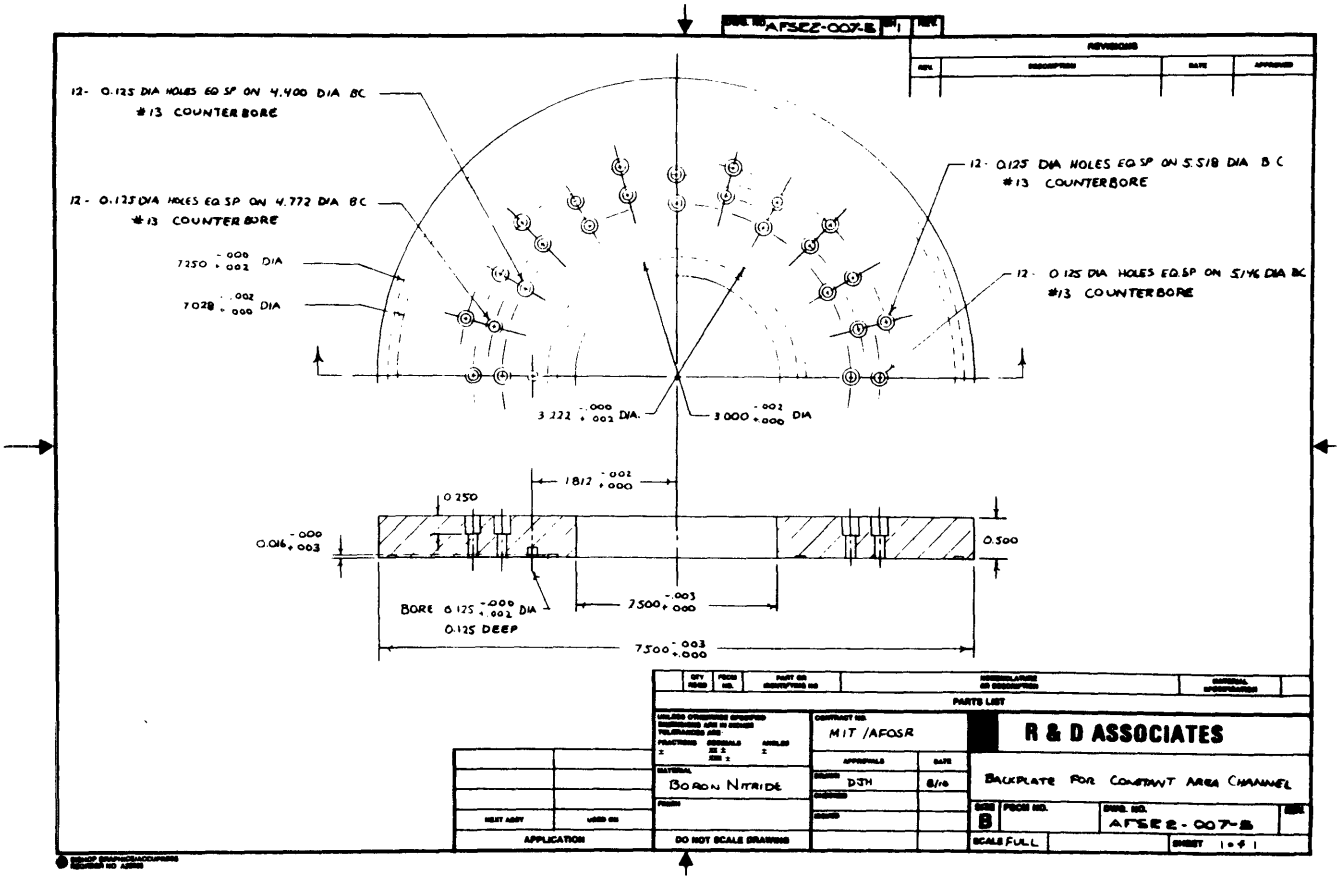

Figure A6.11: Insulator Backplate

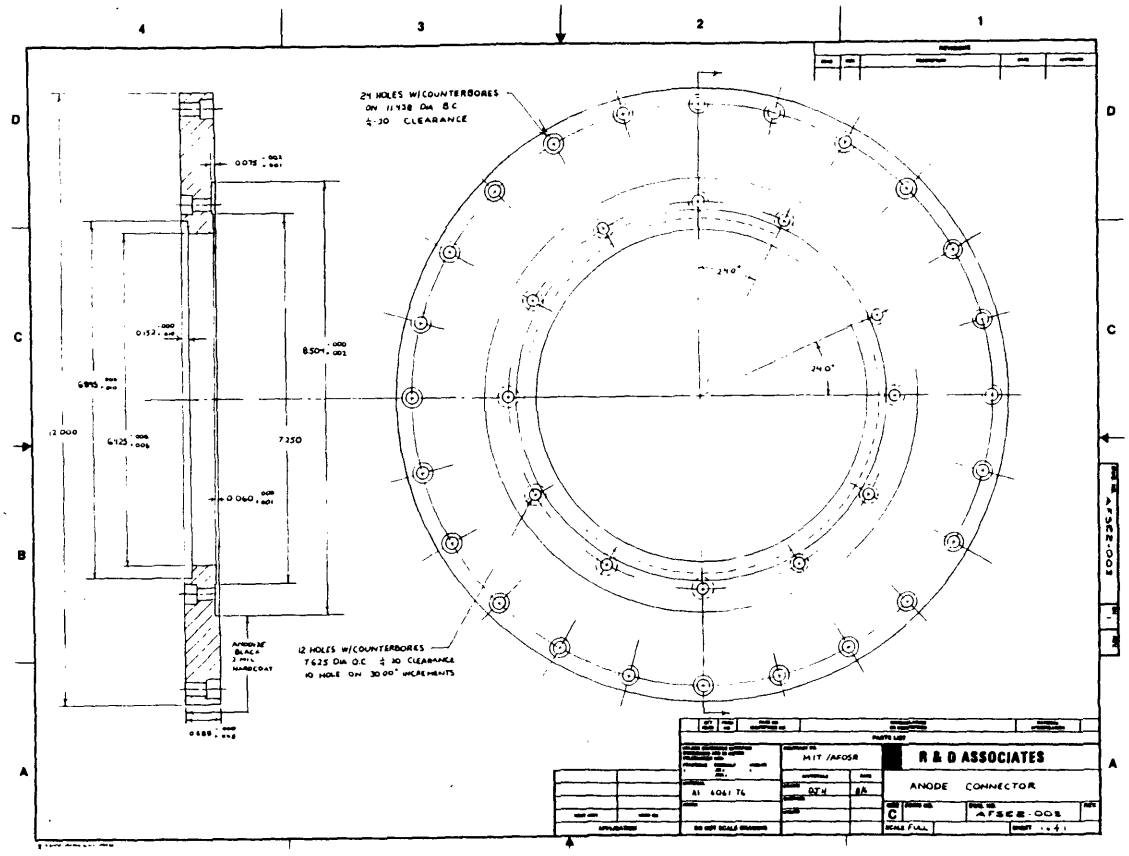

Figure A6.12: Anode Connector

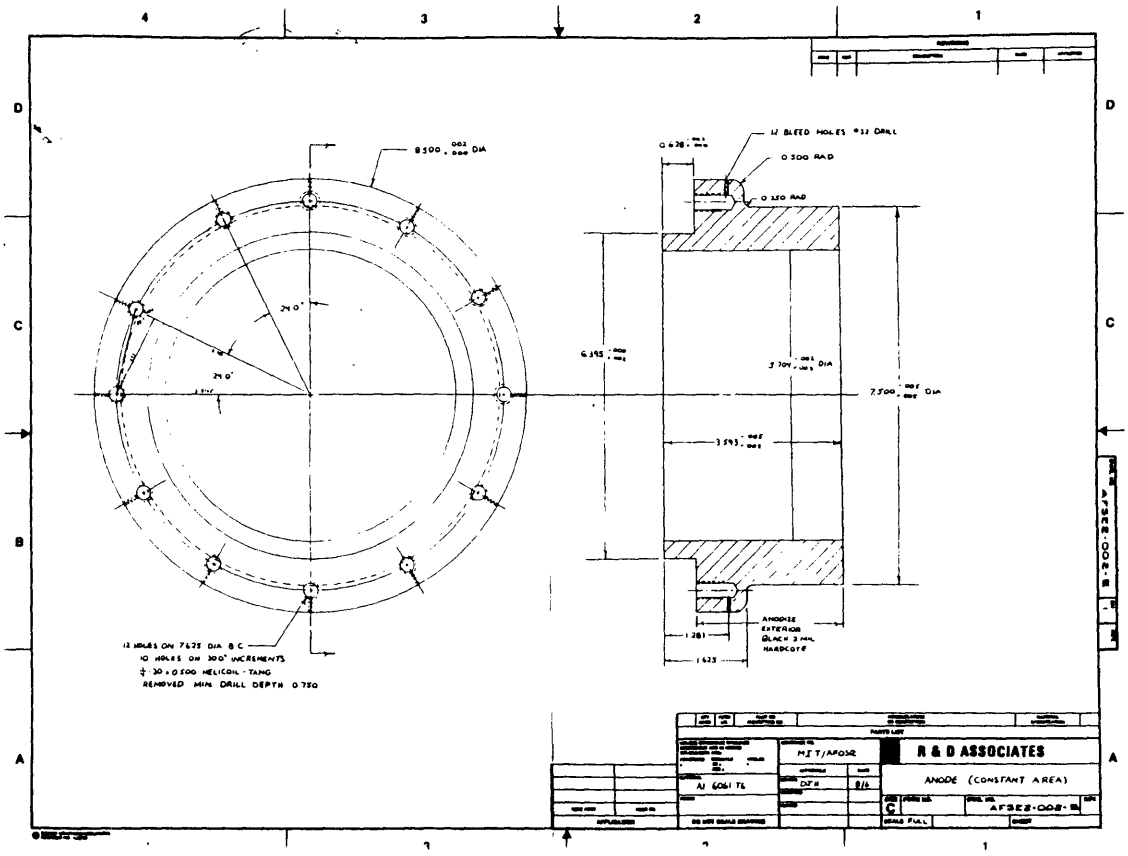

Figure A6.13: Anode

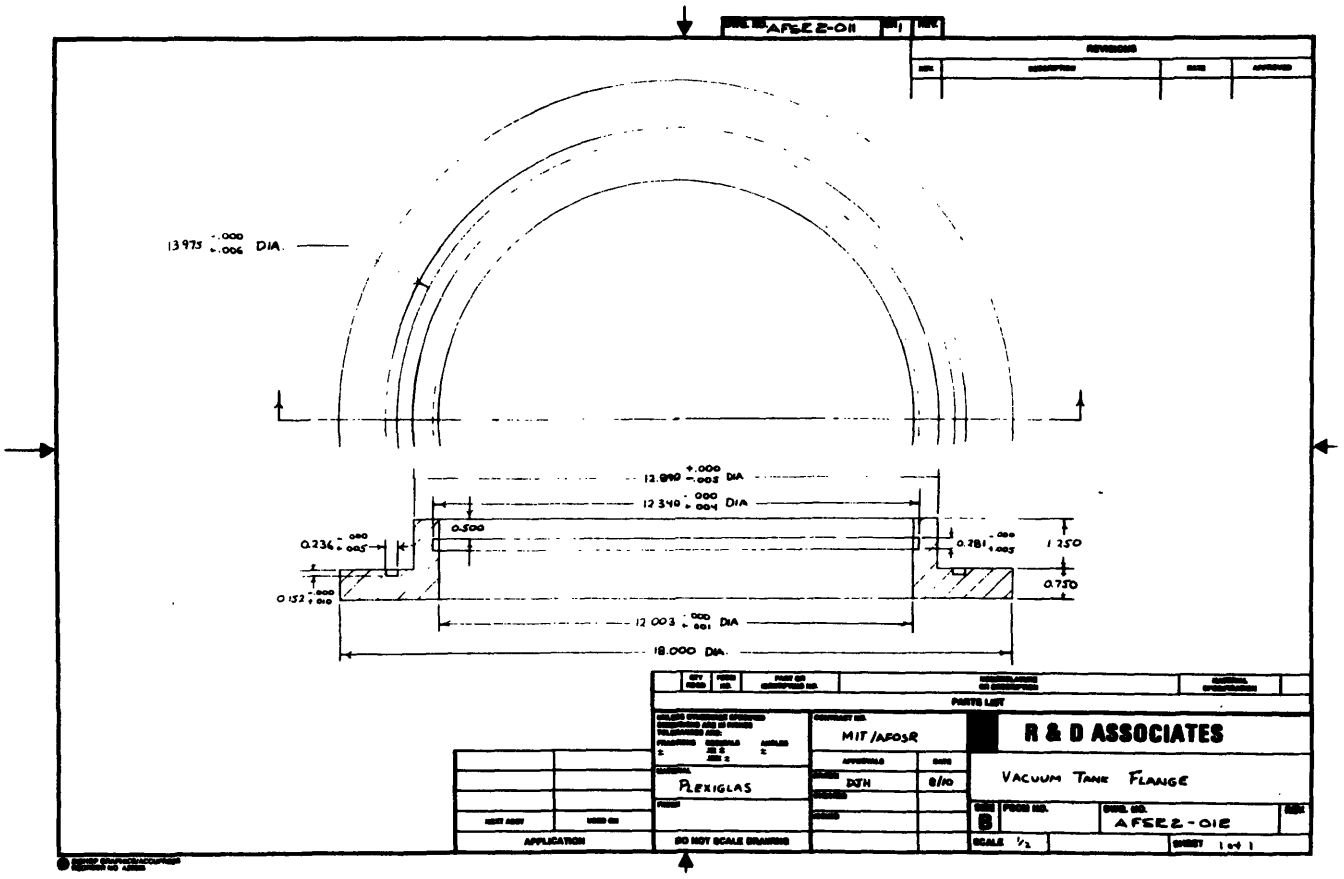

Figure A6.14: Vacuum Tank Flange

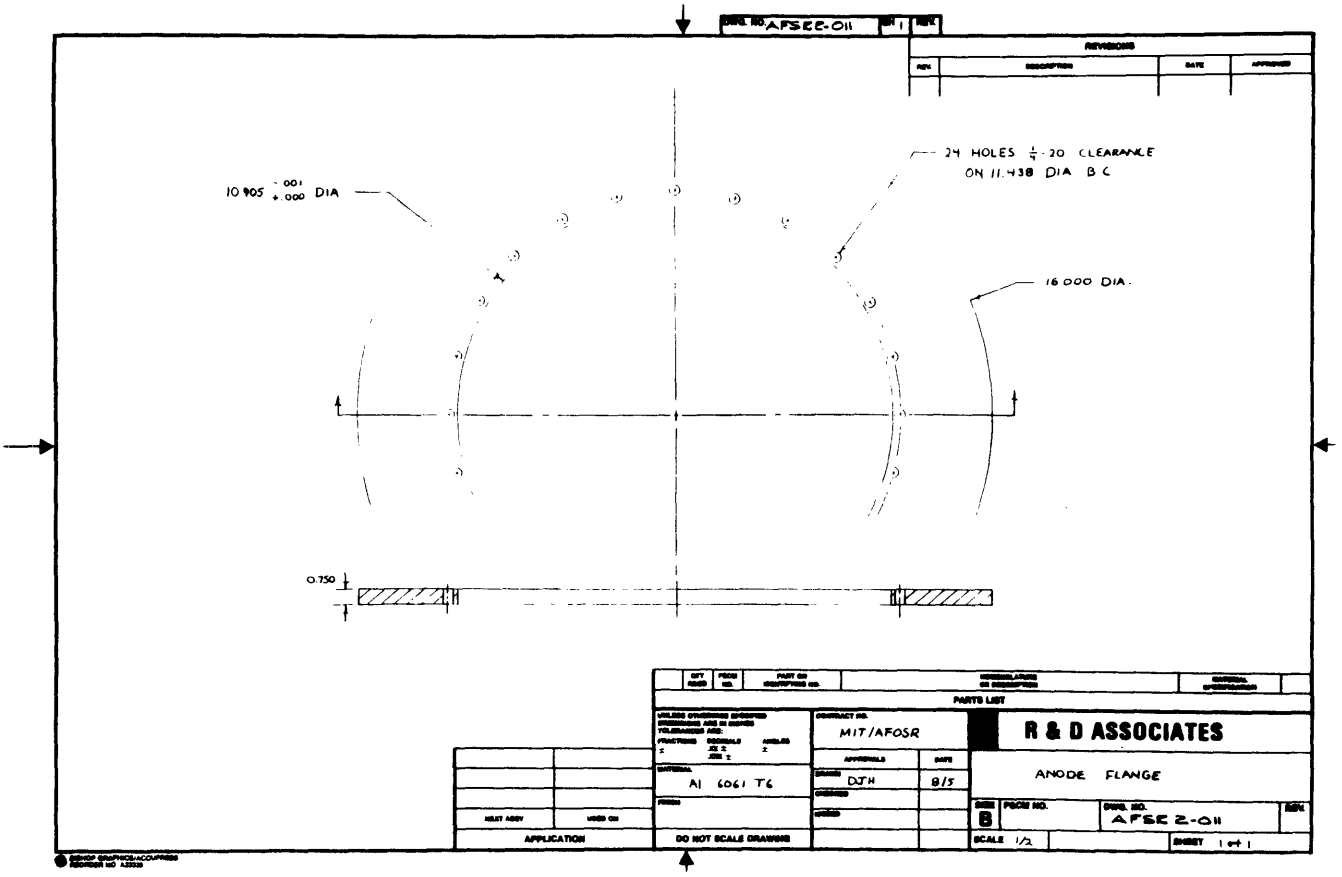

Figure A6.15: Anode Flange

Appendix 7: Determination of the Steady State and Oscillogram Data Reduction

A7.1: Determination of the Steady State

Terminal measurements play an important role in the diagnosis of the arcjet. The two terminal measurements, voltage and total current, are overall operational parameters which give rise to analysis of the transient behavior of the discharge, shot to shot reproducibility, the thruster impedance, the power provided to the discharge, and many other features. The transition to onset has also been characterized by these measurements.[3,12] In this work, the terminal voltage and total current are used primarily to verify thruster performance and repeatability. Oscillograms of these quantities are also indispensable for the determination of the establishment of quasi-steady operation.

Typical oscillograms of an MPD discharge are seen in figures A7.1 and A7.2. Figure A7.1 shows the total current pulse delivered to the arcjet as well as the response of the magnetic field probe residing within the discharge. Figure A7.2 shows the terminal voltage along with the floating potential, also measured from within the device.

In these figures, a discharge initiation transient appears to last approximately 200 μs before a quasi-steady voltage is reached. During this transient, which appears to be geometry dependent, the terminal voltage has an initial large spike immediately following Ignitron closure, after which the voltage is depressed significantly below its quasi-steady value. The voltage then slowly increases to a plateau before the discharge termination transient. Correspondingly, the magnetic field

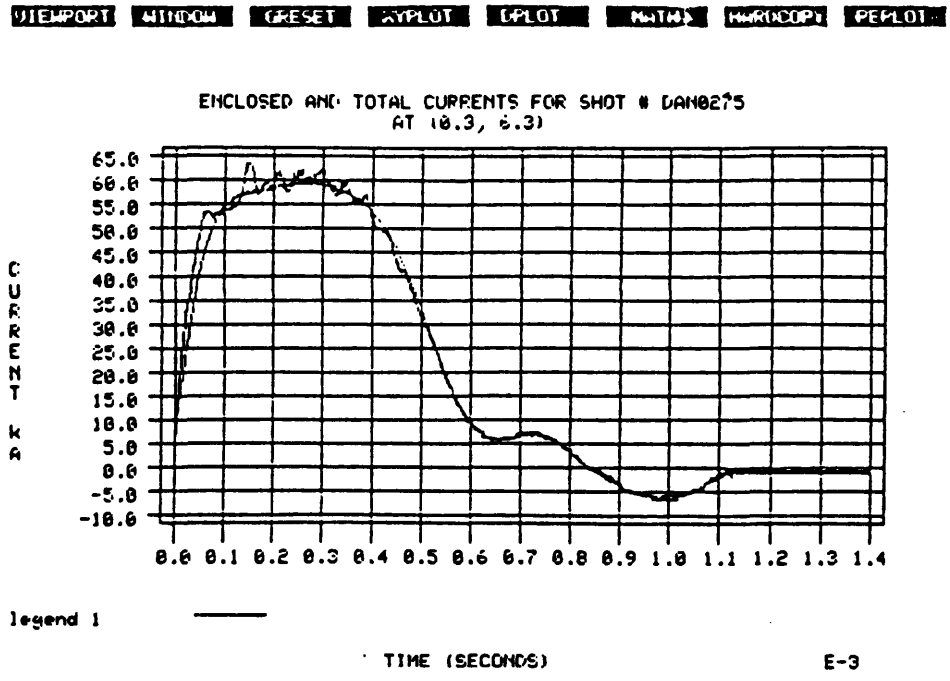

Figure A7.1: Typical Oscillogram of the Total and Enclosed Currents at 60 kA and an Argon Mass Flow Rate of 4 g/s

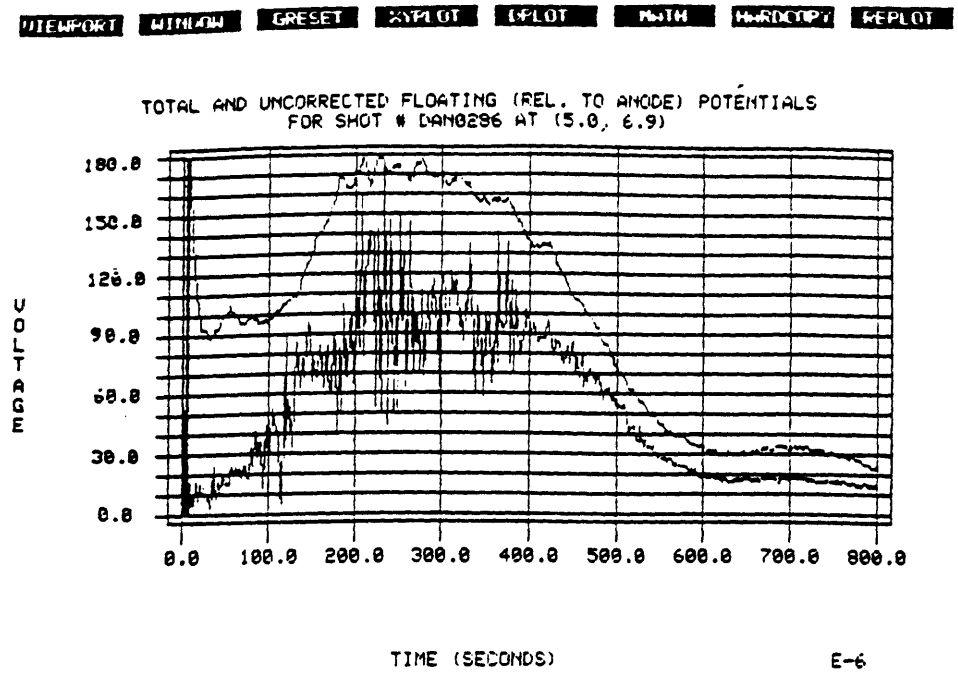

Figure A7.2: Typical Oscillogram of the Total and Floating Potentials at 60 kA and an Argon Mass Flow Rate of 4 g/s

probe shows a large overshoot in this startup transient. The initial spike of current at a very low voltage may indicate the presence of a strong concentrated arc that may become more diffuse with time. Evidence of arcing can be seen in some photographs of the different discharges which, in the case of an integrated photograph, shows large arc spots on both the anode and cathode, or in the case of the microchannel plate photographs show arcs and other transient asymmetric behavior. Data from the integrated photographs are more difficult to understand because of the lack of temporal resolution. It is unclear whether all of the asymmetric behavior seen in these photographs occurs during the initiation or termination transients or during quasi-steady operation. At termination, there are also large and fast changes in voltage and current both in polarity and magnitude due to ringing in the circuit which could account for localized arcing.

Barnett forwards a different theory for these voltage transients which were also observed in his doctoral work at Princeton.[12] Barnett used a stepped current pulse as the input waveform to the MPD arcjet in order to study the arcjet's transition to the onset of significant voltage hash. The initial step was set below this onset level, while the final step was several kiloamps above it. He noticed that the initial discharge transient appears significantly only at current levels at or above onset, and he believes that this is a plasmadynamic discharge effect where the discharge adjusts its impedance. In his experiment, the impedance of the arcjet was significantly lower than that of the power supply (as in this experiment). Therefore the current source was "stiff" and not strongly

affected by the varying arcjet impedance. From this, he concluded that there are two significant voltage transients—a fast one attributable to an adjustment of the voltage at varying current and constant impedance, and a slow one attributable to a constant current adjustment at varying impedance. These arise from a study of his transient voltage and current data. There it was seen that the total voltage transient to quasi-steady operation was significantly longer than the current transient to quasi-steady operation. He claims that this adjustment time is that time required by the thruster to establish an equilibrium magnetic field distribution through convective and diffusive means, and that at onset, the discharge takes longer to equilibrate to steady-state operation. For his arcjet, this initiation transient was seen to be primarily a plume related phenomenon, perhaps due to the Princeton benchmark geometry which enables large convection of magnetic field into the discharge plume. In this region, he noted significant floating potential oscillations which were not as strong, if present at all, in the upstream portion of the channel.

In this experiment, similar data are seen throughout the channels although more predominantly in the downstream portions of the flared channels. The significant difference with these thrusters is that they have very small magnetized plumes that are harder to diagnose reproducibly. But, the characteristics of the transient data do have some similarities with Barnett's data. One implication of Barnett's hypothesis is that longer channels may have longer discharge equilibration times, so that longer current pulses may be necessary to allow for quasi-steady

operation. This may be important for pulsed arcjet operation since the transient discharge may not be representative of the steady-state arcjet models.

Since the quasi-steady operation of the arcjets in this study is relatively short lived, the MPD arcjet cannot be diagnosed at any arbitrary time. It is important to measure the discharge when the terminal characteristics as well as the plasma characteristics are not influenced by the startup and termination transients. Otherwise significant biases, such as those due to voltage contributions from the changing input current waveform or those due to the changing plasma inductance, could affect the accuracy of the various discharge measurements (which already have significant associated error bars). After a considerable data sample was analyzed, it was determined that an average signal over the discharge period from 220 to 320 μs provides an appropriate characterization of the discharge. Now that the quasi-steady state has been determined, the steady-state characteristics can be measured.

A7.2: Oscillogram Data Reduction

Now that the measurement interval has been determined, it is important to describe the technique used in the reduction of the oscillogram data. The parameters that were recorded on the oscillograms were total voltage, total current, floating potential inside the arcjet, and enclosed current inside the arcjet.

A7.2.1: Current Measurements in the MPD Arcjet

Oscillograms record voltages, not currents, so one must know the appropriate conversion factors for the various types of signals being recorded. In the case of the total current measurement, the toroidal Rogowski loop was calibrated against a previously calibrated Rogowski loop and determined to have a calibration constant of 1.304×10^{-2} kA/Vμs. When used with an integrator having a characteristic integration time constant of 377 μs, its calibration becomes 4.916 kA/V. Since the data was recorded on a Tektronix system with a data analysis computer, this conversion factor was programmed into the system. The resulting oscillogram for the total current trace is shown in figure A7.3. This trace shows that the current pulse is very flat in the region of 220 to 320 μs. In this region, the total current is approximately 59.5 kA. The lack of noise on this signal is due to the large impedance of the power supply and the small impedance of the arcjet which necessitates a large ballast resistor to match the impedances. The ballast resistor has an impedance about fifty times that of the MPD arcjet, so the power supply is not strongly affected by the changing impedance of the arcjet. Hence the power supply can be considered a stiff current source, free from MPD induced noise. Therefore the waveform found in figure A7.3 is very reproducible. Unfortunately this cannot be said about the measurement of enclosed current from inside the arcjet.

Enclosed current is measured from a small Rogowski loop placed inside a quartz tube which is moved throughout the discharge channel. This probe measures the changing magnetic field at a specific radial location in the

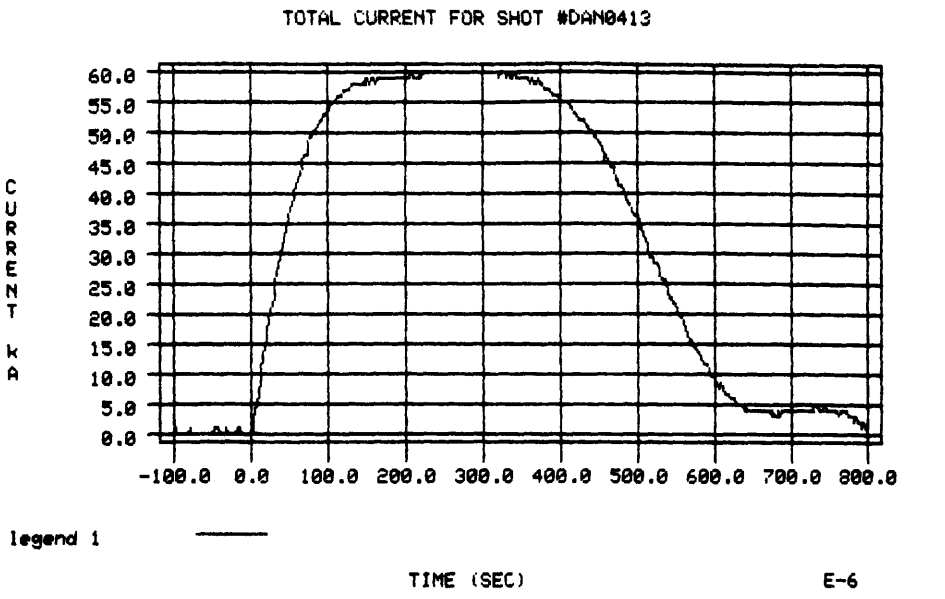

Figure A7.3: Total Current Pulse Provided to the MPD Arcjets for a 12 kV Charge

discharge, and with the help of Ampere's law, allows for a calculation of enclosed current (refer to Chapter III). These probes are small and are exposed to a harsh environment so their lifetime is limited. As a result, numerous probes were used to measure the discharge. Each probe had to be calibrated in a special device that oriented the probe accurately and provided a magnetic field of known strength at a specific location. A typical calibration constant for one of these probes is 1.444 kA/Vcmμs. When used with an integrator with a characteristic time of 3.47 μs, the typical calibration constant becomes 5.343 kA/Vcm. Once again, the Tektronix system can convert the probe data automatically given a conversion factor and the probe's radial position, so that no manual conversion is necessary.

Since the total current signal is so smooth and free from noise, it is possible to divide the enclosed current signal by the total current signal. This provides a trace that is the ratio of the two signals, which is the desired form for the enclosed current maps found in Chapter IV. Two examples of these traces are shown in figure A7.4. The first trace is taken in the partially flared channel at the cathode, two centimeters from the backplate. The second is also from the partially flared channel but is in the exit plane, at a radial distance of 6.3 cm. From these traces it is easy to see that over the period of 220-320 μs the probe signal 2 cm from the backplate shows an enclosed current ratio of about 0.48 with an uncertainty of about $\pm$ 0.06, which translates to an uncertainty of $\pm$ 12.5% from the mean measurement. At the exit, the measurement of the enclosed current is 0.2 of the total current with an uncertainty of $\pm$ 0.06, which

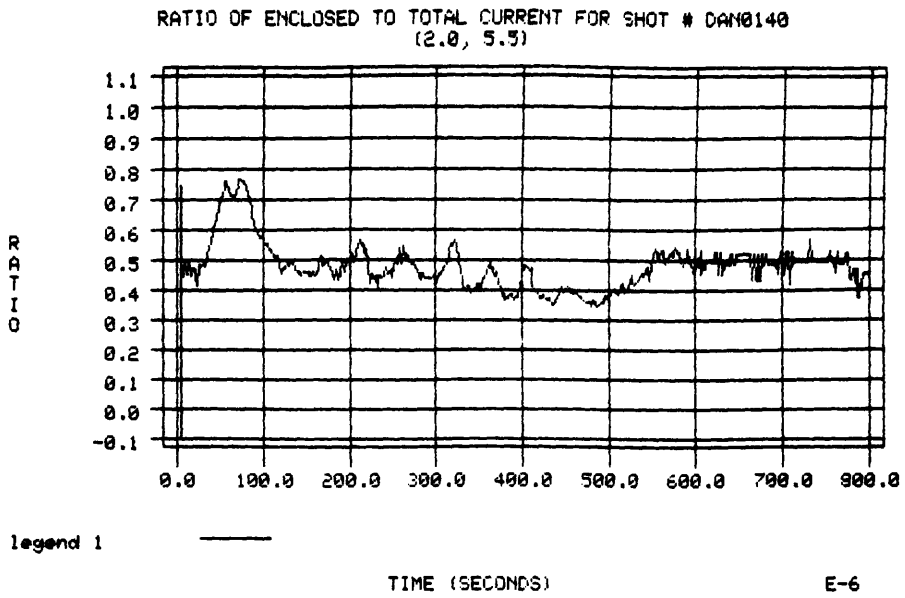

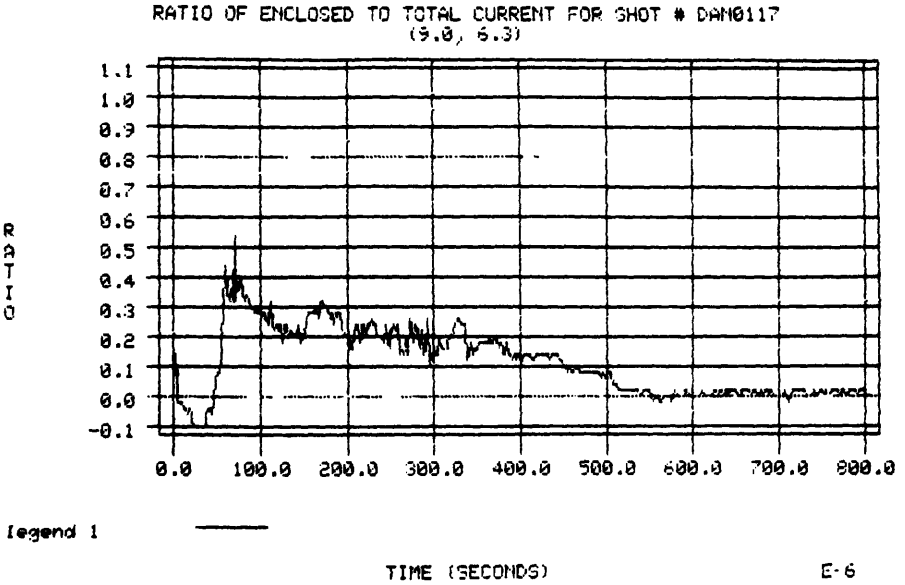

Figure A7.4: Ratio of Enclosed to Total Current at Two Locations in the Partially Flared Channel at 60 kA and an Argon Mass Flow Rate of 4 g/s

corresponds to an uncertainty of ± 30% from the measured mean value.

A7.2.2: Voltage Measurements in the MPD Arcjet

Measuring the voltage and floating potential is not as clean as the procedure for measuring the current. Recalling figure IV.7, presented here as figure A7.5, representative total voltage traces for each channel at 60 kA and an argon mass flow rate of 4 g/s are shown. Only the trace from the constant area channel looks quasi-steady. These traces were taken from a 1000:1 voltage probe placed at the entrance to the channel. The Tektronix system automatically accounted for the probe reduction.

These traces show that the transient nature of the discharge really prevent one to ascribe a characteristic voltage. Rather, one must attempt to define a mean voltage with a characteristic uncertainty that is a combined measure of the discharge transience and measurement error. These are also very difficult to separate and will not be done in this analysis.

Adhering to the steady-state determination based on the previous analysis of the voltage and current waveforms, the voltage for the constant area channel is approximately 137 ± 5 V, or an error of ± 4% from the mean; the waveform from the partially flared channel gives 165 ± 9 V, or an error of ± 6% from the mean; the waveform from the fully flared channel gives 163 ± 30 V, or an uncertainty of ± 19% from the mean. This uncertainty is unfortunate, but is typical due to the transient nature of the discharge at an operating point of 60 kA at an argon mass flow rate of 4 g/s.

Floating potential measurements are even noisier than the terminal voltage measurements. A Langmuir probe is exposed to the plasma and is

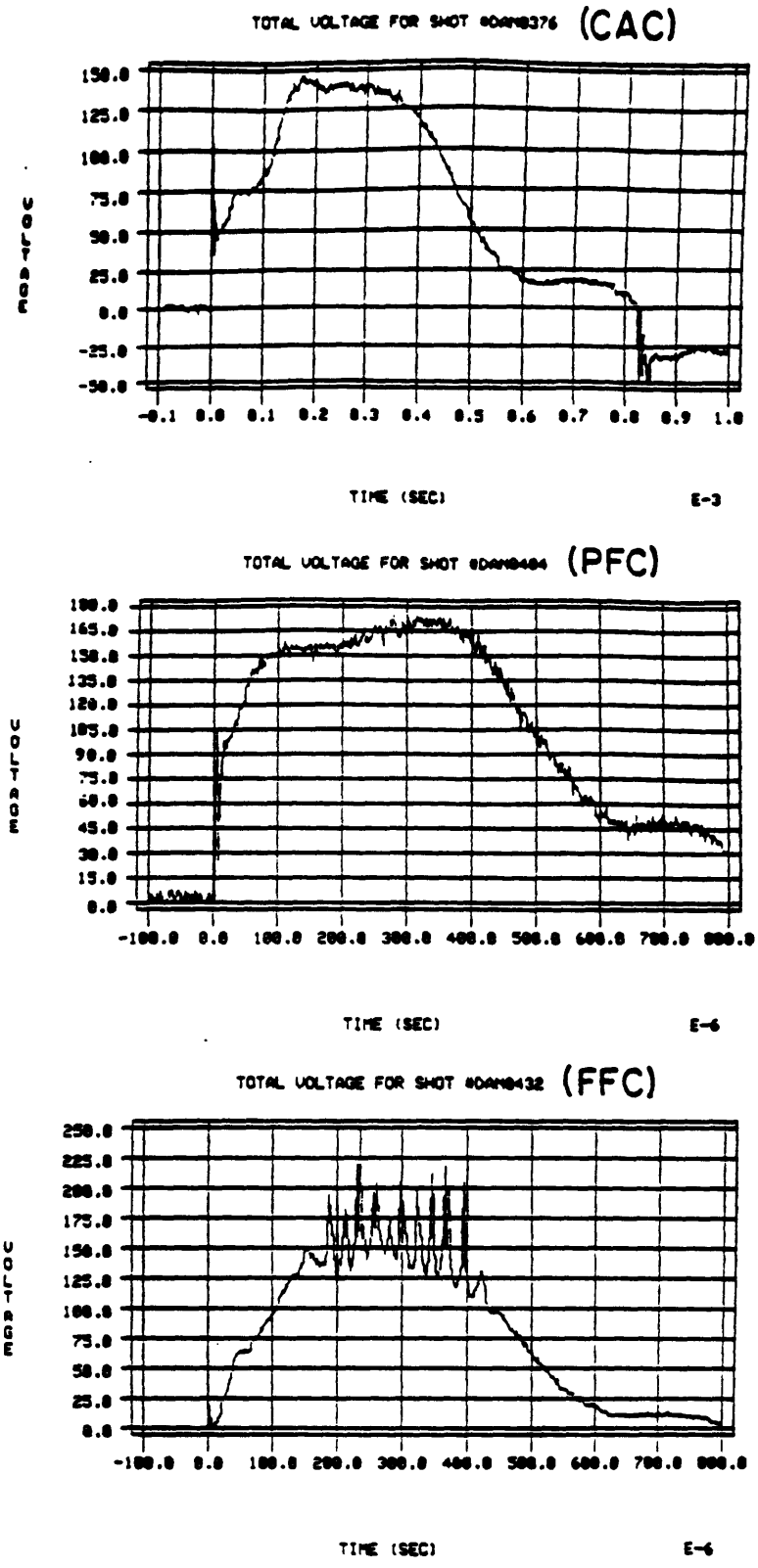

Figure A7.5: Voltage Characteristics for the Three Different Geometries for an Argon Mass Flow Rate of 4 g/s and a Current Level of 60 kA

allowed to float. It is measured relative to the anode through a 1000:1 voltage probe. This was done to protect instrumentation because the power supply required the cathode to be brought to negative high voltage and the anode at zero volts. Examples of floating potential probe measurements are shown in figure A7.6. Both of these traces are taken from the fully flared channel which has the noisiest of traces for the three channels. The first trace is taken at a distance of 6.3 cm from the insulator backplate just off the surface of the cathode. The second is taken at a distance of 7.3 cm from the insulator just off of the anode. These traces illustrate the difficulty in the measurement of the floating potential. The first trace measures out to 140 ± 30 V, or an uncertainty of ± 22% from the mean. The second trace gives 38 ± 65 V, or an uncertainty of 170 %. This latter measurement is not too typical but does occur and usually takes a series of discharges to get more precise measurements of the mean voltage. In order to map floating potential contours so that zero volts corresponds to the cathode, it is necessary to subtract the floating potential from the total potential and then divide by the total potential. Uncertainty propagation requires that the subtraction operation cause the two uncertainties to be added and the division requires that the final uncertainty is the square root of the sum of the square of the uncertainties. So if the voltage trace for the flared channel from figure A7.5 is combined with the first trace in figure A7.6, the following results for the floating potential are reached:

$$\%V = \frac{V_T - V_F}{V_T} \qquad \text{A7.1}$$

$$\%V_{error} = ((s_T + s_F)^2 + s_T^2)^{1/2}\ \%V \qquad \text{A7.2}$$

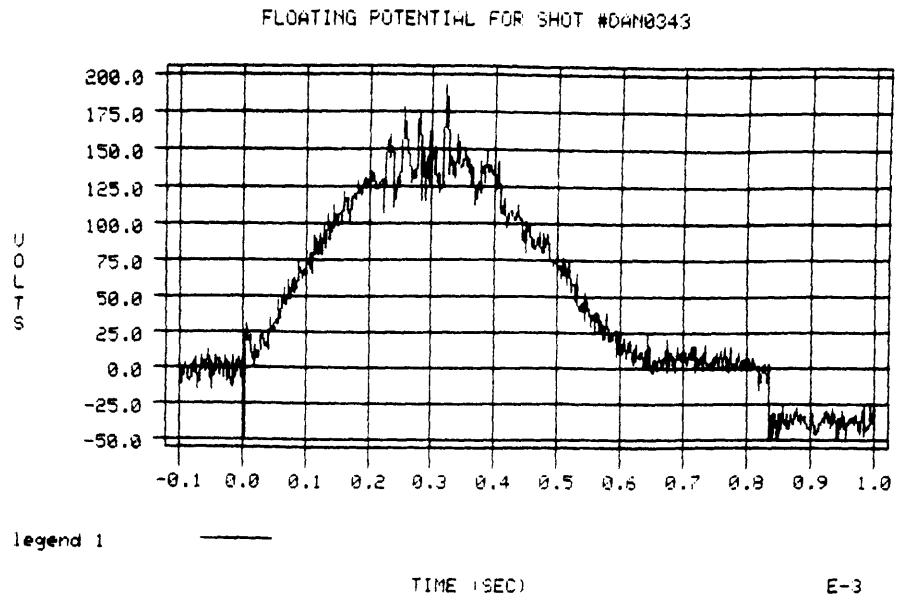

a) Near cathode

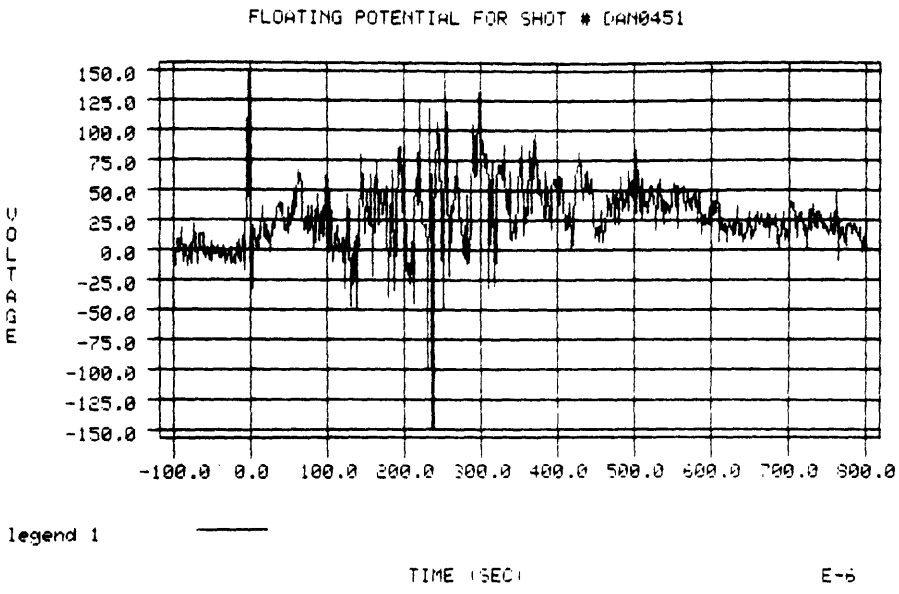

b) Near anode

Figure A7.6: Floating Potentials at Two Locations in the Fully Flared Channel at 60 kA and an Argon Mass Flow Rate of 4 g/s

where s_T and s_F are the relative uncertainties of the terminal and floating potential measurements leaving

$$V_T = 163 \pm 30 \text{ V} \; ; \; V_F = 140 \pm 30 \text{ V} \; ; \; \%V = 0.14 \; ;$$

$$s_T = \frac{30}{163} = 0.184 \; ; \; s_F = \frac{30}{140} = 0.214 \; ;$$

$$\%V_{error} = 0.44 \; \%V = 0.06 \qquad \text{A7.3}$$

which is considerably large. The error on the mean can be reduced by repetitive shots, but these errors are to be expected from data for the fully flared channel. If the uncertainty on the terminal voltage were decreased to ± 5V, then $\%V_{error}$ would be reduced to ± 0.25 %V = 0.04.

This error analysis shows that future measurements of the floating potential should probably be measured relative to the cathode. This would minimize the uncertainty by not measuring across the noisy anode region for every floating potential measurement. This would require a modification to the floating potential probe to protect the diagnostic circuitry from the cathode, which is the "hot" electrode in the present arcjet.

Appendix 8: An Approximate Cylindrical Model for Anode Depletion

In this appendix, an approximate model for the onset of anode depletion is derived for a channel with concentric cylindrical electrodes. The approach is based on the work by Baksht, et. al. in reference 13 except that it is derived for a channel with a discharge structure that varies radially.

This derivation is based on a thruster with a high aspect ratio cylindrical planform as shown in figure A8.1. In this geometry, there are three directions forming the normal coordinate system. These include a radial axis (r), an azimuthal axis (θ), and an axial axis (x).

The geometry is sufficiently narrow to allow for the thin channel assumption

$$\frac{\partial}{\partial r} >> \frac{\partial}{\partial x} \qquad \text{A8.1}$$

to be used throughout the derivation.

This derivation is begun by assuming a steady-state, constant electrical conductivity plasma, at a constant temperature. The governing equations of motion are the continuity equation, conservation of momentum, equation of state for a fully ionized perfect gas, Ohm's law, and Maxwell's laws as shown below

$$\nabla\cdot(\rho\vec{u}) = 0 \qquad \text{A8.2}$$

$$\rho(\vec{u}\cdot\nabla)\vec{u} = -\nabla p + \vec{J}\times\vec{B} \qquad \text{A8.3}$$

$$p = 2n_e kT \qquad \text{A8.4}$$

$$\vec{J} + \vec{J}\times\vec{\beta} = \sigma\left(\vec{E} + \frac{1}{en_e}\nabla p_e + \vec{u}\times\vec{B}\right) \qquad \text{A8.5}$$

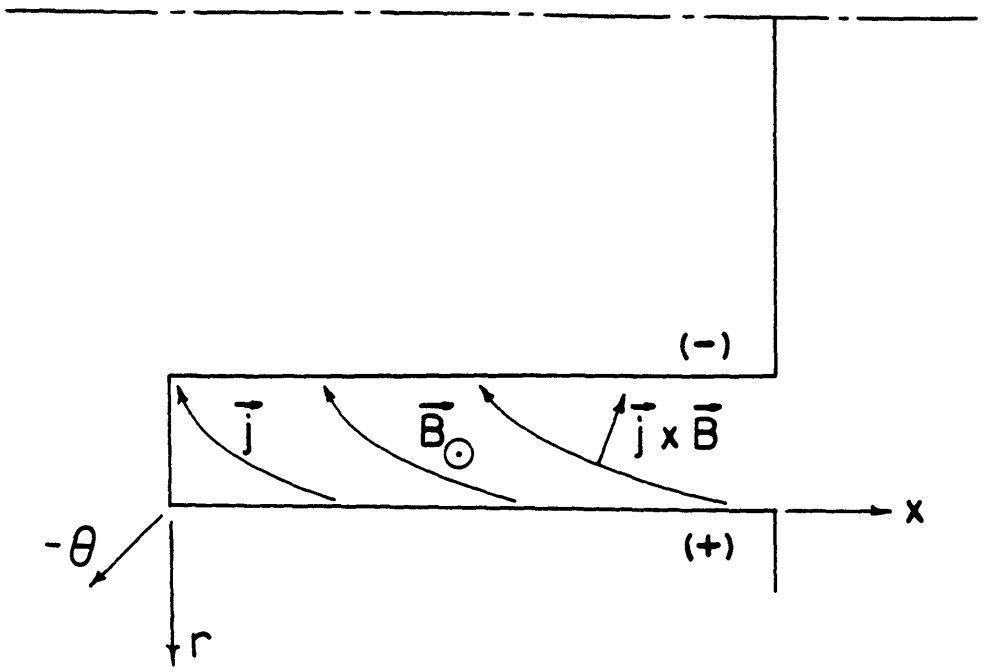

Figure A8.1: Cylindrical Geometry

$$\nabla \times \vec{B} = \mu_0 \vec{j} \qquad \text{A8.6}$$

$$\nabla \cdot \vec{B} = 0 \qquad \text{A8.7}$$

$$\nabla \times \vec{E} = 0 \qquad \text{A8.8}$$

For this geometry, equation A8.8 implies that the axial electric field is smaller than the radial electric field, or

$$\frac{E_x}{E_r} \sim \frac{h}{L} \qquad \text{A8.9}$$

and the geometry does not allow for significant accumulation of radial flow velocity, so

$$\frac{u_r}{u_x} \sim \frac{h}{L} \qquad \text{A8.10}$$

These assumptions allow equations A8.3 and A8.5 to be broken into two parts, one of which contains only derivatives in the radial direction, and one which contains derivatives only in the axial direction. The latter set of differential equations propagates radial averages of the various quantities, and the other equations that vary only in r determine the structure and the average value of the specific quantities.

In order that all physical quantities have positive values, the direction is taken into account prior to any algebraic manipulation so that

$$\vec{j} = (-\, j_r,\ 0,\ -\, j_x)$$

$$\vec{B} = (0,\ -\, B,\ 0)$$

$$\vec{E} = (-\, E_r,\ 0,\ -\, E_x)$$

$$\vec{\beta} = (0,\ -\, \beta,\ 0) \qquad \text{A8.11}$$

Under these assumptions, Ohm's law can be shown to separate into the following two equations

$$j_r = \frac{1}{1 + \beta^2}\, \sigma \left(E_r - uB - \frac{kT}{e} \frac{\partial}{\partial r} (\ln n_e) \right) \qquad \text{A8.12}$$

$$j_x = \frac{\beta}{1+\beta^2}\,\sigma\,\left(E_r - uB - \frac{kT}{e}\frac{\partial}{\partial r}(\ln n_e)\right) \qquad \text{A8.13}$$

or

$$j_x = \beta\, j_r \qquad \text{A8.14}$$

The Hall parameter is defined as

$$\beta = \frac{\sigma B}{e n_e} \qquad \text{A8.15}$$

allowing the transverse momentum balance to be expressed as

$$2kT\frac{\partial n_e}{\partial r} = -\frac{\sigma}{e}\frac{j_r B^2}{n_e} \qquad \text{A8.16}$$

Equations A8.6 and A8.7 imply that

$$\nabla\cdot\vec{j} = 0 \qquad \text{A8.17}$$

which, for the thin channel assumption implies that

$$r j_r = \text{constant} = r_a\, j_r(x, r_a) \qquad \text{A8.18}$$

where the current density at the anode is simply the mean thermal flux of electrons to the anode

$$j_r(x, r_a) = \frac{e n_a \langle c\rangle}{4} \qquad \text{A8.19}$$

Here the quantity $\langle c\rangle$ is the mean thermal speed of the electrons and is equal to

$$\langle c\rangle = \left(\frac{8kT}{\pi m_e}\right)^{1/2} \qquad \text{A8.20}$$

Equation A8.16 can be integrated directly, resulting in the following equation for the electron density

$$n_e^2(x,r) = n_e^2(x, r_c) - \frac{\sigma}{ekT}\, r_a\, j_r(x, r_a) B^2 \ln\left(\frac{r_a}{r_c}\right) \qquad \text{A8.21}$$

At anode starvation, the electron density at the anode is much less than at the cathode

$$n_e(x, r_a) \ll n_e(x, r_c) \qquad \text{A8.22}$$

so the electron density at the cathode in equation A8.21 can be

approximated as

$$n_e(x,r_c) = \left(\frac{\sigma}{ekT} r_a j_r(x,r_a) B^2 \right)^{1/2} \left(\ln \left(\frac{r_a}{r_c} \right) \right)^{1/2} \qquad \text{A8.23}$$

This equation for the electron density is now integrated across the channel to get the mean electron density which will be used in the axial differential equations

$$\langle n_e(x) \rangle = \frac{2}{r_a^2 - r_c^2} \int_{r_c}^{r_a} \left(\frac{\sigma}{ekT} r_a j_r(x,r_a) B^2 \right)^{1/2} \left(-\ln \left(\frac{r}{r_a} \right) \right)^{1/2} r\,dr \qquad \text{A8.24}$$

This equation is not directly integrable, but with approximate techniques can be easily integrated. The natural log term can be rewritten as

$$\ln \left(\frac{r}{r_a} \right) = \ln \left(1 - \frac{r_a - r}{r_a} \right) \qquad \text{A8.25}$$

and a small parameter ϵ may be defined as

$$\epsilon = \frac{r_a - r}{r_a} \qquad \text{A8.26}$$

The natural log can now be approximated as

$$\ln \left(\frac{r}{r_a} \right) \simeq -\epsilon + \frac{1}{2}\epsilon^2 \qquad \text{A8.27}$$

and the integral in equation A8.24 can be transformed into the following form

$$\langle n_e(x) \rangle = \frac{2}{r_a^2 - r_c^2} \left(\frac{\sigma}{ekT} r_a j_r(x,r_a) B^2 \right)^{1/2} \int_{\frac{r_c}{r_a}}^{1} \left(\frac{1}{2} - \frac{1}{2} \left(\frac{r}{r_a} \right)^2 \right)^{1/2} \frac{r}{r_a} d\left(\frac{r}{r_a} \right) \qquad \text{A8.28}$$

which can be readily integrated. Once integrated,

$$\langle n_e(x) \rangle = \frac{2^{1/2}}{6} \left(\frac{r_a^2 - r_c^2}{r_a^2} \right)^{1/2} \left(\frac{\sigma \langle c \rangle}{kT} r_a B^2 n_e(x,r_a) \right)^{1/2} \qquad \text{A8.29}$$

Now that the transverse structure and average of the electron density is determined, the axial variation of the transversely averaged quantities can be calculated. From now on, the <> notation will be dropped.

The axial component of the momentum equation (equation A8.3) can be rewritten in terms of the magnetic pressure (equation A8.6) and combined with the one-dimensional continuity equation to provide the following integrable differential equation

$$\frac{\dot{m}}{A}\frac{du}{dx} = -\frac{dp}{dx} - \frac{d}{dx}\left(\frac{B^2}{2\mu_0}\right) \qquad \text{A8.30}$$

Neglecting the thermodynamic pressure in comparison to the magnetic pressure is not necessary for integration but is required for the ultimate solution of this model. The velocity

$$u(x) = \frac{A}{2\dot{m}\mu_0}\left(B^2(0) - B^2(x)\right) + u(0) \qquad \text{A8.31}$$

can be substituted into the one-dimensional continuity equation

$$n_e(x) = \frac{\dot{m}}{u(x)Am_i} \qquad \text{A8.32}$$

and solved to give the electron density at the anode as a function of x with the additional assumption that u(0) is small

$$n_e(x,r_a) = 64\,\frac{r_a}{r_a^2 - r_c^2}\,\frac{kT}{\sigma\langle c\rangle}\left(\frac{\dot{m}}{A}\right)^4\left(\frac{\mu_0}{m_i}\right)^2\frac{1}{B^2(x)\left(B^2(0) - B^2(x)\right)^2} \qquad \text{A8.33}$$

The only remaining unknown quantity is the axial variation of the magnetic field. The axial component of Ampere's Law

$$\frac{\partial B}{\partial x} = -\mu_0 j_r \qquad \text{A8.34}$$

is used to calculate this variation. In this equation, j_r is a transversely averaged quantity and is calculated by integrating the expression for j_r, equation A8.18, across the annular surface. This gives a value for j_r, written below in average brackets, as

$$\langle j_r\rangle = \frac{r_a}{r_a + r_c}\,j_r(x,r_a) = \frac{r_a}{r_a + r_c}\,\frac{en_e(x,r_a)\langle c\rangle}{4} \qquad \text{A8.35}$$

Combining equations A8.33 to A8.35 gives

$$\frac{\partial B}{\partial x} = -16 \frac{r_a^2}{(r_a + r_c)(r_a^2 - r_c^2)} \frac{\mu_0 ekT}{\sigma} \left(\frac{\dot{m}}{A}\right)^4 \left(\frac{\mu_0}{m_i}\right)^2 \frac{1}{B^2(x)(B^2(0) - B^2(x))^2} \qquad \text{A8.36}$$

Integration of this is straightforward, leaving a solution of the form

$$\frac{1}{7} B^7(x) - \frac{2}{5} B^2(0)B^5(x) + \frac{1}{3} B^4(0)B^3(x) - \frac{8}{105} B^7(0) = -16 \frac{r_a^2}{(r_a + r_c)(r_a^2 - r_c^2)} \frac{\mu_0 ekT}{\sigma} \left(\frac{\dot{m}}{A}\right)^4 \left(\frac{\mu_0}{m_i}\right)^2 x \qquad \text{A8.37}$$

which is solved iteratively for the axial value of the magnetic field. By specifying the initial magnetic field, which is actually a specification of the total current, the thruster length is determined as that distance, L, where the magnetic field goes to zero. Therefore, either the length or the total current may be specified and are not independent. This is shown in the following equation which expresses the relationship between the initial magnetic field and the thruster length given the mass flow rate, plasma temperature, electrical conductivity, and electrode radii

$$B(0) = \left(210 \frac{r_a^2}{(r_a + r_c)(r_a^2 - r_c^2)} \frac{\mu_0 ekT}{\sigma} \left(\frac{\dot{m}}{A}\right)^4 \left(\frac{\mu_0}{m_i}\right)^2 L\right)^{1/7} \qquad \text{A8.38}$$

The value for the entrance magnetic field is related to the total thruster current through Ampere's law. For this cylindrical geometry, the value of the magnetic field at the anode is

$$B(0, r_a) = \frac{\mu_0 I}{2\pi r_a} \qquad \text{A8.39}$$

but, the magnetic field in equation A8.38 is averaged over the entrance annulus and is slightly larger due to the cylindrical geometry

$$B(0) = \frac{\mu_0 I}{\pi (r_a + r_c)} \qquad \text{A8.40}$$

Equation A3.38 can now be rewritten to predict the current at which anode starvation is predicted for a specified cylindrical channel

$$I = \left(210 \pi^7 \frac{r_a^2 (r_a + r_c)^5}{r_a - r_c} \frac{ekT}{\mu_0^4 \sigma} \frac{1}{m_i^2} \left(\frac{\dot{m}}{A}\right)^4 L\right)^{1/7} \qquad \text{A8.41}$$

The onset voltage can also be predicted. If the thrust is equated to the directed momentum of the accelerated plasma

$$F = \dot{m}u \qquad \text{A8.42}$$

and the kinetic power of the beam is equated to the total power provided to the thruster,

$$JV = \frac{1}{2}\frac{F^2}{\dot{m}} \qquad \text{A8.43}$$

the total voltage can be calculated with the aid of equation A8.31 which predicts the exhaust velocity of the plasma. Assuming u(0) is small

$$V = \frac{1}{8}\frac{\mu^2 A^2 J^3}{\pi^4 (r_a + r_c)^4 \dot{m}} \qquad \text{A8.44}$$

which varies as $I^3/\dot{m}$ -- expected of a electromagnetically dominated plasma accelerator. With equation A8.41, the voltage varies as

$$V = \frac{210^{3/7}}{8\pi^{4/7}}\frac{\mu_0^{2/7}}{(r_a + r_c)^{10/7}}\left(\frac{ekTLr_a^2}{m_i^2\sigma}\right)^{3/7} A^{-1/7}\,\dot{m}^{5/7} \qquad \text{A8.45}$$

The axial voltage distribution may also be calculated from equation A8.12. This equation can be rewritten in terms of the radial component of the electric field

$$E_r = \frac{1+\beta^2}{\sigma} j_r + uB + \frac{kT}{e}\frac{\partial}{\partial r}(\ln n_e) \qquad \text{A8.46}$$

The pressure gradient term must again be averaged over the transverse distance. The derivative of the natural log term can be calculated using equations A8.21 and A8.23 and is

$$\frac{\partial}{\partial r}(\ln n_e) = \frac{1}{r}\frac{1}{\ln\frac{r}{r_a}} \qquad \text{A8.47}$$

Once again, this can be integrated over the annular section with the perturbation scheme in equation A8.27 leaving

$$\left\langle\frac{\partial}{\partial r}(\ln n_e)\right\rangle = -\frac{2r_a}{r_a^2 - r_c^2}\ln\left(\frac{2r_a - r_c}{r_c}\right) \qquad \text{A8.48}$$

If the voltage is just the average electric field multiplied by the

channel height, equation A8.46 can be rewritten for the voltage as a function of the local magnetic field

$$V(B(x)) = \frac{16r_a^2}{(r_a + r_c)^2} \frac{ekT}{\sigma^2} \left(\frac{\dot{m}}{A}\right)^4 \left(\frac{\mu_0}{m_i}\right)^2 \frac{1}{B^2(x)(B^2(0) - B^2(x))^2} -$$

$$\frac{r_a}{r_a + r_c} \frac{2kT}{e} \ln\left(\frac{2r_a - r_c}{r_c}\right) + \frac{A}{2\dot{m}\mu_0} (B^2(0) - B^2(x))B(x)(r_a - r_c) \quad \text{A8.49}$$

The voltage may be calculated as a function of distance once the average axial magnetic field distribution has been determined.

For the following parameters:

$$\begin{aligned} T &= 11{,}000 \text{ K} \\ \sigma &= 3000 \text{ mho/m} \\ \dot{m} &= 0.004 \text{ kg/s} \\ m_i &= 6.646 \times 10^{-26} \text{ kg} \\ r_a &= 0.072 \text{ m} \\ r_c &= 0.053 \text{ m} \\ L &= 0.09 \text{ m} \end{aligned} \quad \text{A8.50}$$

this model predicts the onset current to be 31,165 A and the onset voltage to be about 3.5 volts.

The same procedure may be followed for a two-dimensional channel with the following results for onset current and voltage

$$J = w \left(\frac{945}{8} \frac{ekT}{\mu_0^4 \sigma} \frac{1}{m_i^2} \left(\frac{\dot{m}}{A}\right)^4 \frac{L}{h} \right)^{1/7} \quad \text{A8.51}$$

where w is an effective channel width, d is the electrode separation, and

$$V = \frac{1}{8} \left(\frac{945}{8}\right)^{3/7} \frac{\mu_0^{2/7}}{w} \left(\frac{ekTL}{\sigma m_i^2 h}\right)^{3/7} A^{2/7} \dot{m}^{5/7} \quad \text{A8.52}$$

The channel area can be expressed as

$$A = wh \quad \text{A8.53}$$

so that

$$V = \frac{1}{8} \left(\frac{945}{8}\right)^{3/7} \frac{\mu_0^{2/7}}{w^{4/7}} \left(\frac{ekTL}{\sigma m_i^2}\right)^{3/7} A^{-1/7} \dot{m}^{5/7} \quad \text{A8.54}$$

For w = 0.39 m and h = 0.019 m, these equations predict onset to occur at 33,378 A and 4.4 volts. The calculated voltages are quite low when compared to the calculated axial potential variation defined by equation

A8.49 and plotted in figure V.2. In fact, the 4.4 volts corresponds quite well to the midchannel back emf component of equation A8.49. Unfortunately, most of the voltage calculated in equation A8.49 is taken up by the Ohmic and Hall contributions and not by the back emf.

Cylindrical effects are shown to reduce the onset limit. This makes sense since radial variation increases the average pumping force which acts depletes the anode. In both cases, the onset voltage and current are increased with decreased channel area. This also makes sense since a smaller channel area requires a steeper density gradient for anode starvation. So as the electrodes become closer, starvation is more difficult.

Appendix 9: Derivation of Approximate Thrust Equations for Arcjets With Flared Geometries

To estimate the performance of the various arcjet channels used in this experiment, it is useful to derive equations to calculate the approximate electromagnetic thrust generated by each device.

The electromagnetic thrust is simply the volumetric integral of the $\vec{J}x\vec{B}$ body force

$$F_{em} = \iiint \vec{J}x\vec{B}\, dV \qquad A9.1$$

The electromagnetic component of the arcjet's thrust is only one component of the total thrust. There is also a contribution from ordinary gas expansion due to the heating of the plasma as well as the negative contribution from fluid friction. In this approximation, the latter two effects will be neglected since they are of a lower order.

Equation A9.1 can be transformed to a surface integral which states that the thrust is the integral of the magnetic pressure over the thruster surface

$$F_{em} = \iint \frac{B^2}{2\mu_0} \vec{n}\, dA \qquad A9.2$$

where $\vec{n}$ is the outward pointing normal to the local surface. In the arcjet, there are two components of the electromagnetic force, one which is directed in the axial direction and is directly contributory to the sensible thrust, and another which is directed in the radial direction and indirectly contributes to the total thrust. The radial thrust acts to

pressurize the cathode and pumps fluid into a region of higher magnetic field where acceleration is more efficient. This higher pressure region also adds to the thrust through ordinary gas expansion. This term is more difficult to analyze accurately, and will be neglected in this approximation.

In this experiment, three different geometries have been designed. The first channel has a constant interelectrode separation, the second has an initial section with a constant separation followed by a flared section, and the third channel has a converging-diverging section.

A9.1: Derivation of the Axial Thrust for the Constant Area Channel

In the constant area channel, the integral presented in equation A9.2 is almost trivial to evaluate. For this channel, it was noted that almost no current left the channel and attached onto the external faces of the electrodes. Because of this, the only contribution to the axial force is the portion of the control volume adjacent to the backplate. For this geometry, the internal distribution of current is immaterial since it does not affect the integration. Ampere's law shows that the magnetic field along this surface varies inversely with radius and directly with the total current

$$B(0,r) = \frac{\mu_0 J}{2\pi r} \qquad \text{A9.3}$$

which leads to the following integral for the axial electromagnetic force

$$F_x = \frac{\mu_0}{4\pi} J^2 \int_{r_c}^{r_a} r^{-1}\, dr \qquad \text{A9.4}$$

which is directly integrable, leaving

$$F_x = \frac{\mu_0}{4\pi} J^2 \ln\left(\frac{r_a}{r_c}\right) \qquad \text{A9.5}$$

If current leaves the channel and attaches to the cathode face, then this equation is modified slightly by an additional constant since the magnetic field is stronger at a smaller radius. This will be neglected since very little current attaches to the cathode face, and its distribution, which is important, is unknown.

A similar derivation will be done for the flared channels, however it is more difficult since the flaring contributes to the thrust and the irregular interelectrode separation must be accounted for.

A9.3: Derivation of the Axial Thrust for the Fully Flared Channel

An approximate thrust equation for the fully flared channel may be derived based on several simplifying assumptions. In this derivation, a constant axial current density distribution, is selected. This, as shown in chapter II, leads to a specific interelectrode separation. For simplicity, a parabolic converging-diverging section is chosen with a separation specified through selection of inlet and throat electrode radii and throat position. These assumptions are presented mathematically in the following equations

$$B(x,r) = \frac{\mu_0 J}{2\pi r} \left(1 - \frac{x}{L} \right) \qquad \text{A9.6}$$

where the enclosed current is independent of radius and

$$r_c = r_c^* - \left(r_c^* - r_{c0} \right)\left(\frac{x - x^*}{x^*} \right)^2 \qquad \text{A9.7}$$

where the starred quantities refer to the throat location, r_c refers to the cathode radius, and r_{c0} refers to the initial cathode radius. Equation A9.4 can now be rewritten to take into account the contributions from the flaring of the cathode

$$F_{z,cathode} = \frac{\mu_0}{4\pi} J^2 \int_0^L \left(1 - \frac{x}{L} \right)^2 \frac{d \ln r_c}{dx} dx \qquad A9.8$$

where

$$\frac{d \ln r_c}{dx} = -2 \left(r_c^* - r_{c0} \right) \left(\frac{x - x^*}{x^{*2}} \right) \qquad A9.9$$

The integral portion of equation A9.8 can be nondimensionalized to the form

$$G_{ffc} = f^2 \int_{g-1}^{g} \left(g - \xi \right)^2 \frac{2\xi d\xi}{1 - f^2 \xi^2} \qquad A9.10$$

where

$$\xi = \frac{x - x^*}{L}, \quad g = 1 - \frac{x^*}{L}, \quad \text{and} \quad f^2 = \frac{r_c^* - r_{c0}}{r_c^*} \left(\frac{L}{x^*} \right)^2 \qquad A9.11$$

Equation A9.10 can be integrated after some algebraic simplification with the result

$$G_{ffc} = (1+2g) - \frac{(1-fg)^2}{f^2} \ln \frac{1-fg}{1-f(g-1)} - \frac{(1+fg)^2}{f^2} \ln \frac{1+fg}{1+f(g-1)} \qquad A9.12$$

The axial electromagnetic force is now the sum of equation A9.5 with the contribution due to the flared nozzle

$$F_z = \frac{\mu_0}{4\pi} J^2 \left(\ln \left(\frac{r_s}{r_{c0}} \right) + G_{ffc} \right) \qquad A9.13$$

The effect of flaring is readily seen to increase the thrust by the dependence of the thrust with the logarithm of the inverse of the initial cathode radius, r_{c0} in the natural log term. From equation A9.12, the contribution to the thrust from flaring is not immediately apparent but depends on whether the entrance flare (which is negatively contributory to the total thrust) is stronger than the divergent section at the exit.

A9.3: Derivation of the Axial Thrust for the Partially Flared Channel

The behavior of the partially flared channel can be estimated from the previous approximation to the fully flared channel. In this case, there is no initial converging section, so this derivation can be

considered a degenerate case of the fully flared channel approximation.

For the partially flared channel, the throat occurs at the channel entrance, so

$$g = 1 \quad \text{and} \quad r_c^* = r_{c0} \tag{A9.14}$$

The parameter f in equation A9.11 can be rewritten with the use of equation A9.7 evaluated at the exit. From equation A9.7,

$$\frac{L}{x^*} = 1 + \left(\frac{r_c^* - r_{cL}}{r_c^* - r_{c0}} \right)^{1/2} \tag{A9.15}$$

so that

$$f^2 = \frac{r_c^* - r_{c0}}{r_c^*} \left(1 + \left(\frac{r_c^* - r_{cL}}{r_c^* - r_{c0}} \right)^{1/2} \right) \tag{A9.16}$$

In the limit as $r_c^* \rightarrow r_{c0}$,

$$f^2 = \frac{r_c^* - r_{cL}}{r_c^*} \tag{A9.17}$$

and

$$G_{pfc} = 3 - \left(\frac{1 - f}{f} \right)^2 \ln (1 - f) - \left(\frac{1 + f}{f} \right)^2 \ln (1 + f) \tag{A9.18}$$

A9.4: Estimation of Thruster Voltage

Once the thrust of the appropriate channel is estimated, the channel voltage can be easily approximated. If it is assumed that the total power delivered to the channel is put into the kinetic power of the plasma, then

$$V = \frac{1}{2} \frac{F^2}{\dot{m} J} \tag{A9.18}$$

Therefore, the voltage of the constant area channel is approximately

$$V_{cac} = \frac{1}{2} \frac{J^3}{\dot{m}} \left(\frac{\mu_0}{4\pi} \ln\left(\frac{r_a}{r_c} \right) \right)^2 \tag{A9.19}$$

the voltage of the partially flared channel is approximately

$$V_{pfc} = \frac{1}{2} \frac{J^3}{\dot{m}} \left(\frac{\mu_0}{4\pi} \left(\ln \left(\frac{r_a}{r_{c0}} \right) + G_{pfc} \right) \right)^2 \tag{A9.20}$$

and the voltage of the fully flared channel is approximately

$$V_{ffc} = \frac{1}{2} \frac{J^3}{\dot{m}} \left(\frac{\mu_0}{4\pi} \left(\ln \left(\frac{r_a}{r_{c0}} \right) + G_{ffc} \right) \right)^2 \tag{A9.21}$$

Appendix 10: Transport Effects in MPD Flows

This section is devoted to a simplified study of the performance limiting effects in an MPD arcjet channel due to the presence of fluid friction. The formulation steers away from any kinetic treatment by channeling those kinetics into a coefficient of viscosity, μ, which can be treated as a function of ionization fraction, temperature, and pressure. This relationship arises from the dependence of the viscosity on the collision frequency. Since the collision frequency depends on a collisional cross section, which varies significantly as Coulomb collisions become dominant, strong variation is to be expected. The equilibrium variation of μ with ionization fraction and temperature, at a pressure of 100 kPa is shown in figure A10.1.[32] From this figure, a sharp decrease in viscosity occurs at an equilibrium ionization fraction of about 25 %. From this figure it appears that viscous dissipation is more likely to occur in cooler channels where the ionization fraction is low and the viscosity is high. But, at higher temperatures, a higher ionization fraction is expected, and viscous effects may be negligible in all but very high aspect ratio channels.

Viscosity's strong ionization fraction and temperature dependence does not enable one, in the spirit of an approximate one-dimensional analysis, to neglect an energy equation. Previous data and analysis show that the temperature in a typical arcjet is approximately constant, except in the initial ionization layer, and this experimentally determined

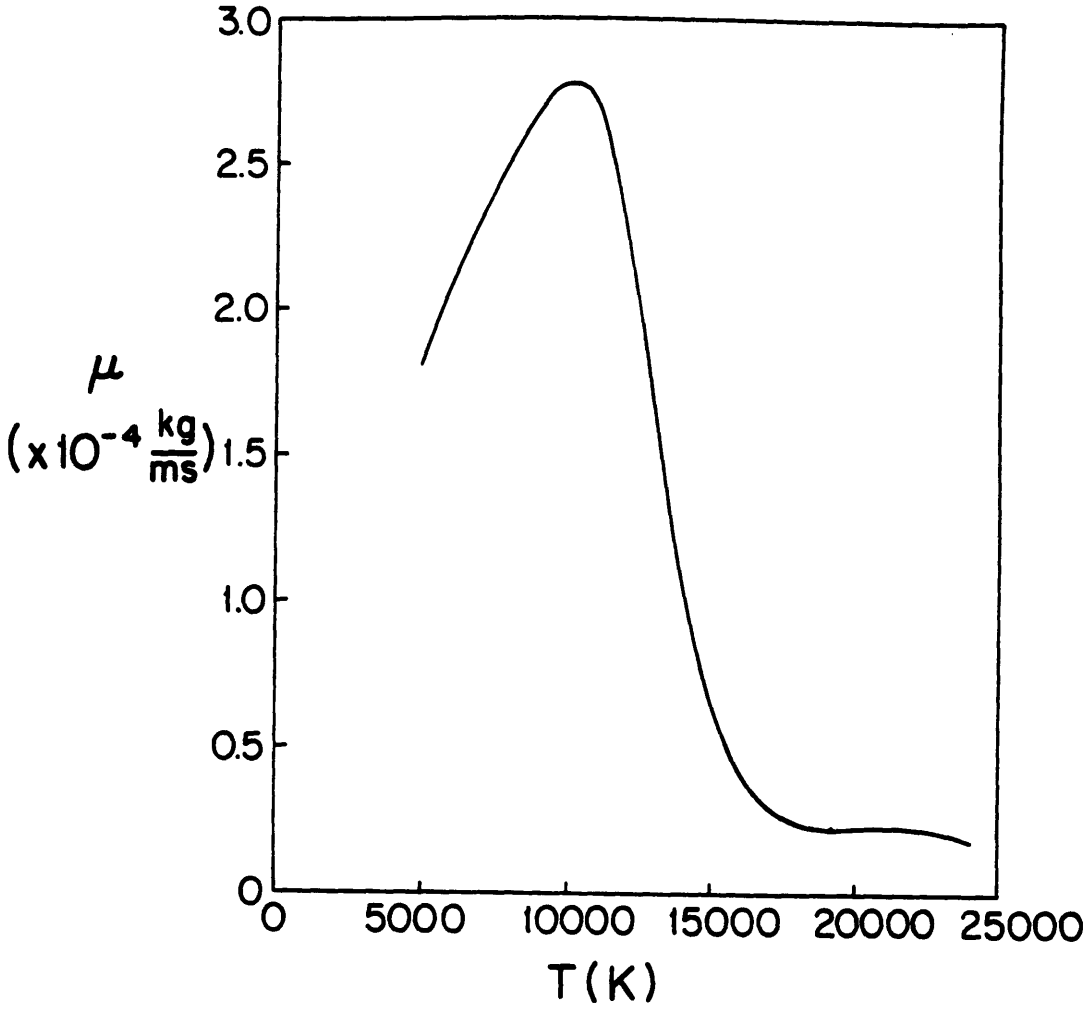

Figure A10.1: Viscosity of an Equilibrium Argon Plasma at Atmospheric Atmospheric Pressure

temperature corresponds to the region where viscosity varies rapidly.[14,34] Therefore, depending on the local dissipation, the channel will either be mostly viscous, mixed, or inviscid. This complicates the system of equations by requiring calculation of the ionization fraction and temperature for a nonequilibrium plasma. Because of the rapid variations in plasma temperature and viscosity, care must be taken to accurately calculate the plasma state or significant error may result. Fortunately, the variation of μ with enthalpy is nearly linear in the ionization range, so that one can keep a reasonable record of its development. This is important since the inherent simplifications in this one-dimensional analysis only allow for an approximation of arcjet behavior. To model the device with an approximate energy equation in order to capture the rapid decrease in viscosity will not necessarily yield an increase in simulation accuracy due to the strong nonequilibrium processes present in real arcjet flows, but it is a first step.

Viscous effects modify only the momentum equation, which can be rewritten in a one-dimensional form as

$$\rho u A \frac{du}{dx} + A \frac{d}{dx}\left(p + \frac{B^2}{2\mu_0}\right) = -2 w \tau_w \qquad \text{A10.1}$$

Here the viscous effects are modeled as losses to the wall via a wall shear stress τ_w. The coefficient of 2 in front of the wall shear stress accounts for the frictional loss at both electrodes while w accounts for the depth of the channel. This equation assumes that the anode and cathode boundary layers are fluid-dynamically equivalent. The skin friction at the wall can be estimated by assuming a constant transverse

distribution of viscous sources so that

$$q = \frac{d}{dy} \left(\mu \frac{du}{dy} \right) \qquad \text{A10.2}$$

where u, in this equation is the axial velocity at a given transverse position and q is the strength of the viscous sources. Equation A10.2 can be integrated directly, and, with the no slip boundary conditions at (x,0) and (x,H), the transverse velocity is expressed as

$$u(x,y) = \frac{q}{2\mu} \left(y^2 - Hy \right) \qquad \text{A10.3}$$

The average transverse velocity, once again denoted by u, is

$$u(x) = - \frac{qH^2}{12\mu} \qquad \text{A10.4}$$

The wall shear stress, τ_w, now becomes

$$\tau_w = \mu \left(\frac{du}{dy} \right)_w = \frac{6\mu u}{H} \qquad \text{A10.5}$$

Substituting equation A10.5 into A10.1, and using the previous nondimensionalization scheme, a new momentum equation

$$\frac{du}{dx} + a \frac{d}{dx} \left(\tau\rho + \frac{b^2}{2} \right) = - f \frac{u}{a} \qquad \text{A10.6}$$

is derived where the friction factor, f, is defined by

$$f = \frac{12 \, w^2 L \mu}{A_0 \dot{m}} \qquad \text{A10.7}$$

Equation A10.7 shows the dependence of the viscous term on the thruster aspect ratio, flow rate, and viscosity. Thinner channels have larger values for the friction factor. For the calculation of this parameter, the only unknown is the variation in viscosity.

In a gas allowing for single ionization, the viscosity is approximately

$$\mu = \frac{1}{2} \lambda_n n_n m_n c_n + \frac{1}{2} \lambda_i n_i m_i c_i \qquad \text{A10.8}$$

where the mean free paths are defined as

$$\lambda_n = \frac{1}{n_n Q_{n\,n} + n_i Q_{i\,n}} \quad \text{and} \quad \lambda_i = \frac{1}{n_n Q_{n\,i} + n_i Q_{i\,i}} \qquad \text{A10.9}$$

For the anticipated plasma conditions, several approximations regarding the collisional cross sections may be made. For the most part, the neutral-neutral cross section is much smaller than the Coulomb cross section, and the neutral-ion (ion-neutral) cross section is approximately equal to the neutral-neutral cross section

$$Q_{ii} >> Q_{nn} \quad \text{and} \quad Q_{in} = Q_{ni} \simeq Q_{nn} \qquad \text{A10.10}$$

allowing the viscosity to be approximated as

$$\mu \simeq \frac{1}{2} \frac{n_n}{n_i + n_n} \frac{m_n c_n}{Q_{nn}} + \frac{1}{2} \frac{n_n}{n_n + \frac{n_n Q_{ii}}{Q_{in}}} \frac{m_i c_i}{Q_{nn}} \qquad \text{A10.11}$$

which can be written in terms of the ionization fraction, α,

$$\alpha = \frac{n_i}{n_i + n_n} \qquad \text{A10.12}$$

leaving

$$\mu = \mu_n \left\{ (1 - \alpha) + \frac{\alpha}{(1-\alpha) + \alpha \frac{\mu_n}{\mu_i}} \right\} \qquad \text{A10.13}$$

This equation is quadratic for the viscosity of the neutral species. The viscosity due to the ionic species can be calculated from an equation given in reference (29) as

$$\mu_i = \frac{0.406 \ (4\pi\epsilon_0)^2 \ (m_i)^{1/2} \ (kT)^{5/2}}{Z^4 e^4 \ \ln \Lambda} \qquad \text{A10.14}$$

where ln Λ is the Spitzer logarithm and is weakly dependent on the pressure. This term, defined as the natural log of the ratio of the Debye length and the impact parameter, can be expressed as

$$\Lambda = 1.24 \times 10^7 \ (\frac{T^3}{n_e})^{1/2} \qquad \text{A10.15}$$

or, in a more appropriate form

$$\Lambda = 1.24 \times 10^7 \ (\frac{T^3 m_i}{\alpha \rho})^{1/2} \qquad \text{A10.16}$$

This derivation implies that at high ionization fractions, the viscosity of the plasma becomes predominantly ionic and rises as indicated by the

temperature behavior of the viscosity in equation A10.14. In reality, multiple ionization can occur. Similar equations based on the single and double ion viscosities, as well as the ionization fraction for multiple species, can be derived with the result that the viscosity of the doubly ionized species moderates the total viscosity and begins to dominate at significant ionization fractions. Although the temperature dependence is the same and is also given by equation A10.14, the total viscosity is decreased due to the increased mean free path of the multiply ionized ion. This trend is reflected by the non-unity value for Z in equation A10.14. Therefore, instead of having a viscosity that increases once single ionization is complete, the viscosity continues to decrease due to additional ionization.

Given the variation of the viscosity from figure A10.1, the neutral viscosity can be determined for any ionization model. For this approximation, only single ionization is allowed, and the calculated variation of the neutral viscosity based on this data and model is shown in figure A10.2. The strange behavior noted at high temperatures is due to the high ionization fraction of the single species, the increasing ion viscosity, and the lack of multiple ionization. Once the local ionization fraction and the local temperature are determined, the plasma viscosity can be calculated based on the mixture scheme presented in equation A10.13.

In order to characterize the plasma state and calculate the viscosity, a simple energy equation can be derived based on the enthalpy of the plasma. An overall one-dimensional conservation of energy equation

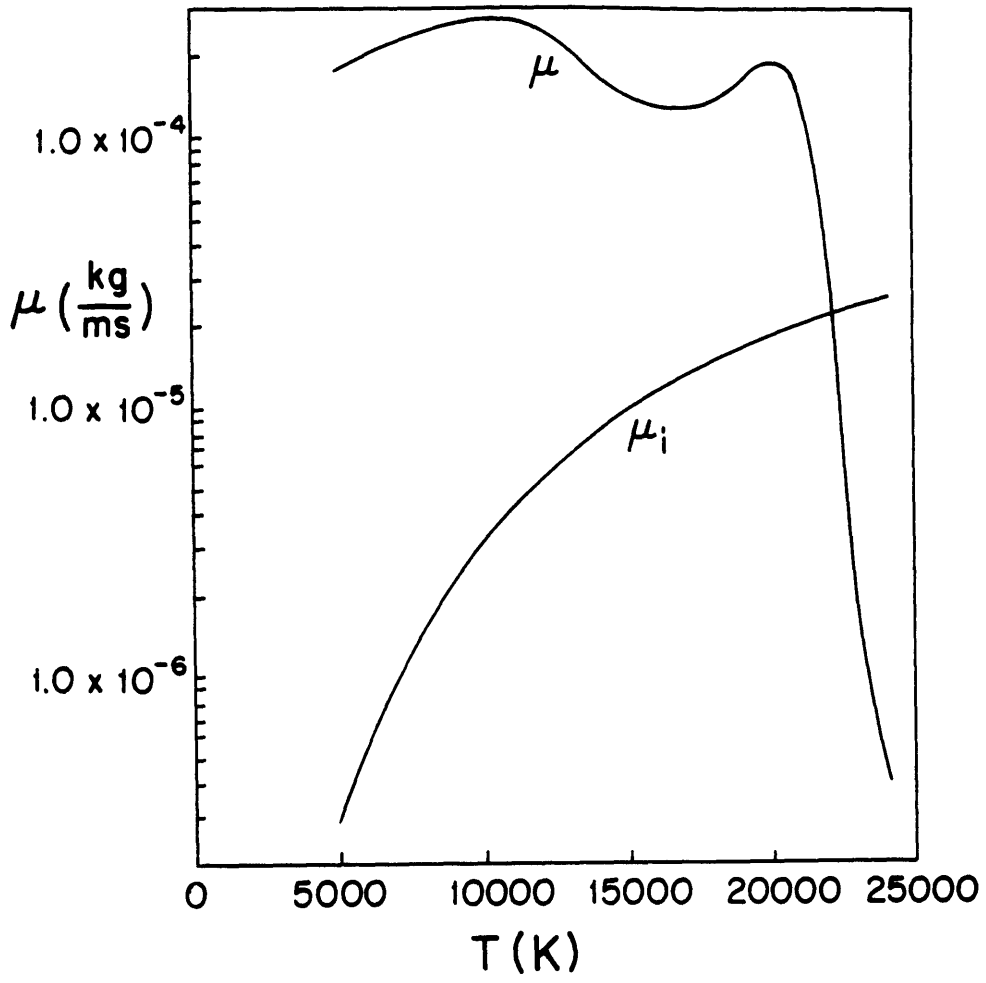

Figure A10.2: Viscosity of Neutral and Singly Ionized Argon as a Function of Temperature

can be written in terms of the enthalpy

$$\rho u \frac{d}{dx} \left(h + \frac{u^2}{2} \right) = j_y E_y \qquad \text{A10.17}$$

where the above quantities are dimensional. In this equation the electrical work is balanced by the convection of enthalpy and kinetic energy. Thermal conduction and other loss mechanisms such as radiation transport will not be considered. With the continuity equation and Ampere's law, equations II.1 and II.6, equation A10.17 can be rewritten as

$$\frac{d}{dx} \left(h + \frac{u^2}{2} \right) = - \frac{E_y A}{\mu_0 \dot{m}} \frac{dB}{dx} \qquad \text{A10.18}$$

For all channels, the product AE_y is constant and the equation becomes algebraic for h

$$h + \frac{u^2}{2} + \frac{E_y A}{\mu_0 \dot{m}} B = \left(h + \frac{u^2}{2} + \frac{E_y A}{\mu_0 \dot{m}} B \right)_0 \qquad \text{A10.19}$$

In order to calculate the viscosity, two state variables are required--the easiest being temperature and ionization fraction. By definition, the enthalpy is

$$h = e_i + \frac{P}{\rho} \qquad \text{A10.20}$$

where e_i is the internal energy, and is a combination of two terms, one representing the thermal energy associated with the three degrees of freedom of a single atom gas, and the other represents the amount of energy invested in the plasma ionization. This changes equation A10.20 into

$$h = \frac{3}{2} \frac{kT}{m_i} + \frac{\alpha e V_i}{m_i} + \frac{P}{\rho} \qquad \text{A10.21}$$

With the equation of state, equation II.3, this equation becomes

$$h = \frac{3}{2} \frac{kT}{m_i} + \frac{\alpha e V_i}{m_i} + RT \qquad \text{A10.22}$$

For a partially ionized gas, R can be expressed as

$$R = \frac{(\alpha+1)k}{m_i} \qquad \text{A10.23}$$

so that

$$h = \left(\alpha + \frac{5}{2} \right) \frac{kT}{m_i} + \frac{\alpha e V_i}{m_i} \qquad \text{A10.24}$$

This equation now relies on a specific model detailing the relationship between the ionization fraction and temperature. Heimerdinger found that an energy equation including dissipation, ionization, wall recombination, heat transfer, and radiative losses provides for a plasma temperature that plateaus at about 12,000 K and ionization fractions between 0.5 and 0.8 for a channel with a constant interelectrode separation.[14] Since the enthalpy changes with axial distance, the ionization fraction also changes, but differently from an equilibrium situation due to the strong nonequilibrium effects. Under equilibrium conditions, as the temperature increases, the ionization fraction tends to unity, and without additional ionization, recombination, or other loss mechanisms, the plasma temperature increases artificially with any enthalpy increase. These effects tend to decrease the viscosity prematurely, so the equilibrium condition is not the best characterization of the plasma.

One can model a nonequilibrium condition for the plasma discharge by creating an electron conservation equation based on balancing simple recombination mechanisms with the local plasma ionization. This can be approached by assuming that the local rate of production of electrons is equilibrated by the ambipolar diffusion of charged particles to the walls where recombination occurs. The local rate of production of electrons is the net result of the ionization from two body interactions and the recombination from the corresponding three body mechanism in the plasma

bulk. These can expressed as

$$\dot{n}_e = \Omega(T_e)\, n_e \left(n_e \frac{n_e^{*2}}{n_n^{*}} - n_e^2 \right) \qquad \text{A10.25}$$

where the "starred" ratio is the condition based on Saha equilibrium, and $\Omega(T_e)$ is an empirically determined constant by Bates[29] given as

$$\Omega(T_e) = \frac{1.09\times10^{-20}}{T_e^{9/2}} \qquad \text{A10.26}$$

The net rate of production of electrons is exactly the divergence of the electron current density

$$\nabla \cdot \vec{J}_e = - e \dot{n}_e \qquad \text{A10.27}$$

which, in the thin channel approximation, simplifies to

$$\frac{\partial j_{e,y}}{\partial y} = - e \dot{n}_e \qquad \text{A10.28}$$

The ambipolar diffusion of electrons is defined as

$$n_e \vec{v}_e = \mu_i \frac{k(T_e+T_i)}{e} \frac{\partial n_e}{\partial y} \simeq 2 \mu_i \frac{kT}{e} \frac{\partial n_e}{\partial y} \qquad \text{A10.29}$$

where μ_i is the ion mobility. Equation A10.27 can be rewritten using equation A10.29 as

$$\frac{\partial j_{e,y}}{\partial y} = - 2\mu_i kT_e \frac{\partial^2 n_e}{\partial y^2} \qquad \text{A10.30}$$

where it is also assumed that the electron temperature is transversally constant. This diffusion term can be approximated by a uniform set of sources in the same manner as with the viscosity, with the result that

$$\frac{\partial j_{e,y}}{\partial y} \simeq \frac{24\, \mu_i kT_e n_e}{H^2} \qquad \text{A10.31}$$

The ion mobility is defined as

$$\mu_i = \frac{e}{\Sigma\, \nu_{i\,n}\, \mu_{i\,n}} \qquad \text{A10.32}$$

where charged particle collisions are not included. This expression can be simplified further since there are only collisions between single ions and neutrals, the reduced mass is half of the ionic mass, and the

collision frequency is

$$\nu_{in} = n_n Q_{in} \langle c_{in} \rangle \qquad \text{A10.33}$$

where the mean thermal speed for the ion-neutral collision is

$$\langle c_{in} \rangle = \left(\frac{16kT}{\pi m_i} \right)^{1/2} \qquad \text{A10.34}$$

The ion-neutral collision cross section is approximated as constant at about 5×10^{-19} m^2 so that the ion mobility is inversely proportional to the neutral number density and the square root of the temperature. If the electron, ion, and neutral temperatures are assumed to be identical, the Saha condition can be written in terms of the temperature and densities as

$$\frac{n_e^{*2}}{n_n^*} = 2 \frac{Q_{i,int}}{Q_{n,int}} \left(\frac{2\pi m_e kT}{h_p^2} \right)^{3/2} \exp\left(- \frac{eV_i}{kT} \right) \qquad \text{A10.35}$$

The ratio of internal to atomic partition functions for first ionization is identically 1/2 so equation A10.35 simplifies a little further. The electron conservation equation can now be rewritten in terms of the density, ionization fraction, temperature, and channel cross sectional area, leaving

$$\frac{12\, w^2}{A^2 Q_{in}} \left(\frac{\pi k}{m_i}\right)^{1/2} = \frac{1.09 \times 10^{-20} \rho^3}{m_i^{\,3} T^6} (1-\alpha) \left\{ (1-\alpha) \left(\frac{2\pi m_e kT}{h_p^2}\right)^{3/2} \frac{m_i}{\rho} \exp\left(- \frac{eV_i}{kT}\right) - \alpha^2 \right\} \qquad \text{A10.36}$$

Equation A10.36 has a very interesting behavior. In figure A10.3, the relationship between temperature and ionization fraction is seen for varying pressure. One interesting feature is that there is a temperature limit below which the equality cannot be satisfied. This corresponds to the "glow" limit which requires that there exist a minimum electron temperature for the discharge to be sustained. In addition to this, for a given pressure, there is a maximum allowable ionization fraction. The

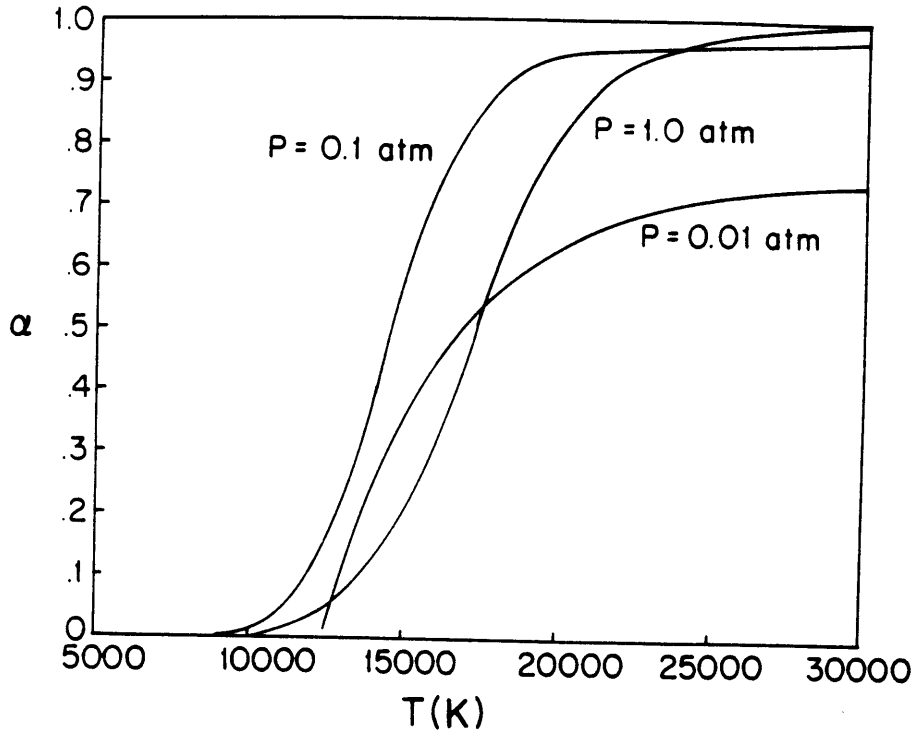

Figure A10.3: Nonequilibrium Variation of the Ionization Fraction of Argon With Varying Temperature and Pressure

variation of the curves with pressure are somewhat unexpected and are due to the varying influence of each source or sink term in the electron balance. At low densites and temperatures, the ambipolar diffusion term is very strong and cannot be balanced by the production and three body recombination. This imbalance acts to establish the glow limit and discharge extinction.

From figure A10.3, it appears that the nonequilibrium plasma is probably at a high enough ionization fraction so that the MPD channel is beyond the range of significant viscous losses.

The previous equations detailing the plasma state can be readily nondimensionalized with the additional relations

$$h' = \left(\frac{\dot{m}\mu_0}{B_0^2 A^*}\right)^2 \quad ; \quad V_i' = \frac{e}{m_i}\left(\frac{\dot{m}\mu_0}{B_0^2 A^*}\right)^2 V_i \quad ; \quad T' = \frac{k}{m_i}\left(\frac{\dot{m}\mu_0}{B_0^2 A^*}\right)^2 V_i \qquad \text{A10.37}$$

These allow the differential equation for the enthalpy, equation A10.18, the expression for the enthalpy in a one-dimensional channel, equation A10.19, the expression for the temperature in terms of enthalpy and ionization fraction, equation A10.24, to be rewritten as follows

$$h' + \frac{u'^2}{2} + eb = \left(h' + \frac{u'^2}{2} + eb \right)_0 \qquad \text{A10.38}$$

$$T' = \frac{h' - \alpha V_i'}{\alpha + 2.5} \qquad \text{A10.39}$$

It is now possible to simultaneously solve equations A10.39 and a long nondimensional form of equation A10.36 for the temperature and ionization fraction given the enthalpy, and then calculate the approximate viscosity.

Once temperature and ionization fraction information is available, it becomes possible to lower the restriction of constant conductivity in Ohm's law (equation II.6). The electric conductivity, σ, can be expressed

as

$$\sigma = \frac{e^2 n_e}{m_e \nu_{ei}} \qquad \text{A10.40}$$

provided that Coulomb collisions play the dominant role in the electron transport process. The Coulombic collision frequency is the product of the electron density, Coulomb cross section, and mean thermal speed between the charged species

$$\nu_{ei} = n_e Q_{ei} \langle c_e \rangle \qquad \text{A10.41}$$

where

$$Q_{ei} = \frac{2.95 \times 10^{-10} \ln \Lambda}{T_e^2} \qquad \text{A10.42}$$

and

$$\langle c_e \rangle = \left(\frac{8kT_e}{\pi m_e} \right)^{1/2} \qquad \text{A10.43}$$

The Coulomb cross section is weakly dependent on density (from the Spitzer logarithm, $\ln \Lambda$) and inversely proportional to the energy or temperature.[29] The mean thermal speed in equation A10.43 differs from the mean thermal speed in equation A10.32 because the reduced mass of electron collisions is, effectively, the electron mass. Under these assumptions, the electric conductivity can be approximated by

$$\sigma = \sigma_{ref} \left(\frac{T}{T_{ref}} \right)^{3/2} \qquad \text{A10.44}$$

since the variations in the Spitzer logarithm are small. The equilibrium variation of conductivity with temperature is seen in figure A10.4 and the reference quantities can be selected from any point on the curve where the conductivity has the behavior noted in equation A10.44

Numerical solution is performed in the same manner as solution to the previous inviscid cases. Sonic passage is again neglected by assuming that τ is small. For a constant area channel, the iteration is based on

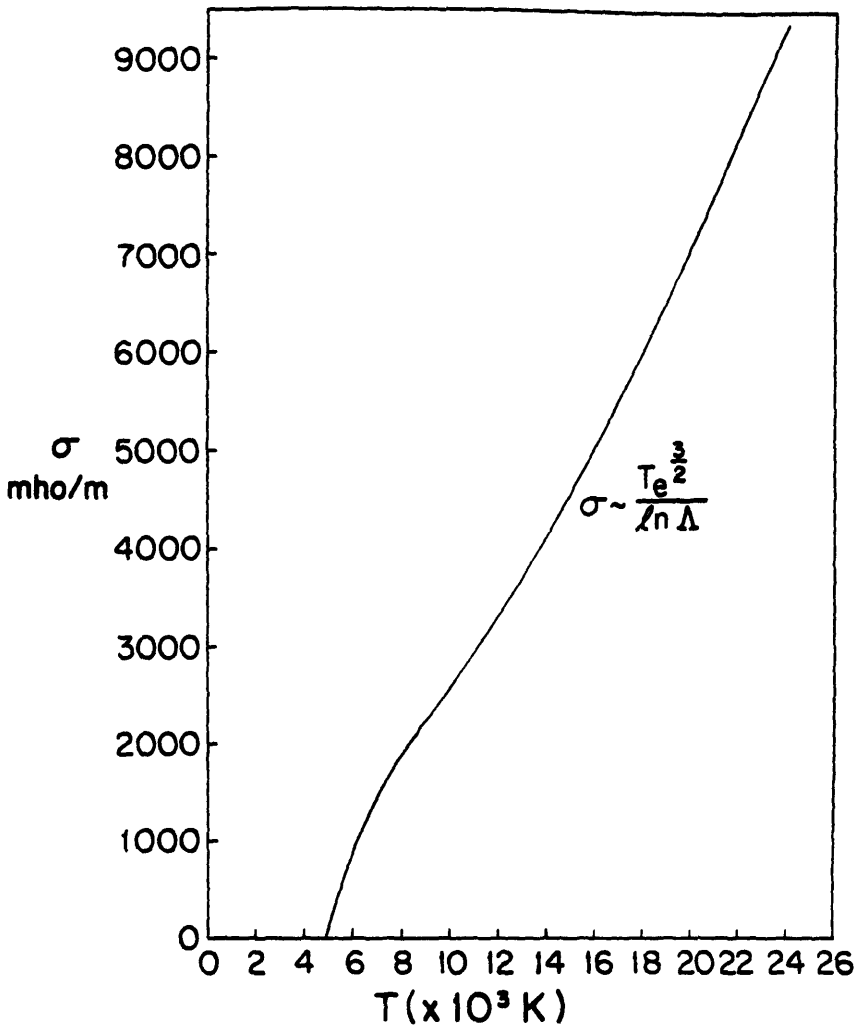

Figure A10.4: Variation of Electrical Conductivity for an Equilibrium Argon Plasma

zero field at the exit; for the flared channel, and iteration is based on the requisite minimum area for the channel throat.

Figures A10.5 to A10.7 show the variation of channel temperature, ionization fraction, viscosity, and electric conductivity in the constant area channel for the three magnetic Reynolds' numbers, and figure A10.8 to A10.10 show the corresponding values for the flared channel. These figures show that the arcjet temperature is maintained relatively constant for the conditions of R_m=1. In this case, the viscosity remains fairly constant at a very high value. At a magnetic Reynolds' number of five, the temperature never plateaus, the ionization fraction is high, and the viscosity drops rapidly near the end of the channel. In the channel with a magnetic Reynolds' number of ten, the temperature climbs very quickly and the viscosity drops drastically. It is interesting to note that at 24,000 K, the simulation fails to continue calculating the temperature, ionization fraction, and viscosity. The reason for this is purely artificial. By not allowing for multiple ionization, the temperature rises with enthalpy. So above about two electron volts, the temperature and ionization fraction results are very questionable. Spectroscopically, the double ion is rarely seen, so plasma temperatures are probably not any higher than two electron volts. Regardless, the viscosity at this point is almost nonexistant, so the channel behaves as is the flow were inviscid.

The effect of viscosity and variable conductivity can be seen in figures A10.11 to A10.15. Figures A10.11 and A10.12 show the velocity deficit due to viscous effects, figure A10.13 shows the effect of variable

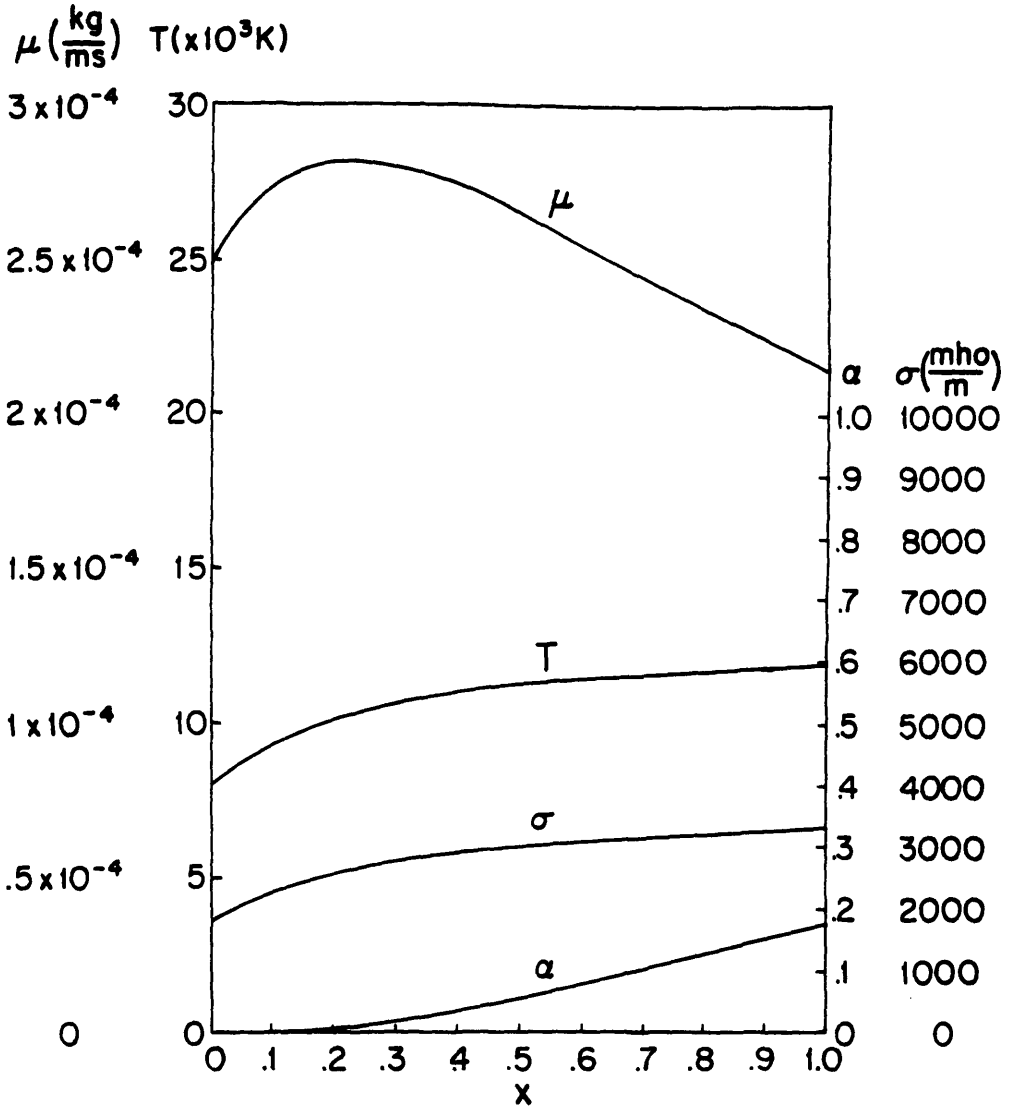

Figure A10.5: Variation of Plasma Viscosity, Temperature, Ionization Fraction, and Conductivity in the Constant Area Channel at a Magnetic Reynolds' Number of One and an Argon Mass Flow Rate of 4 g/s

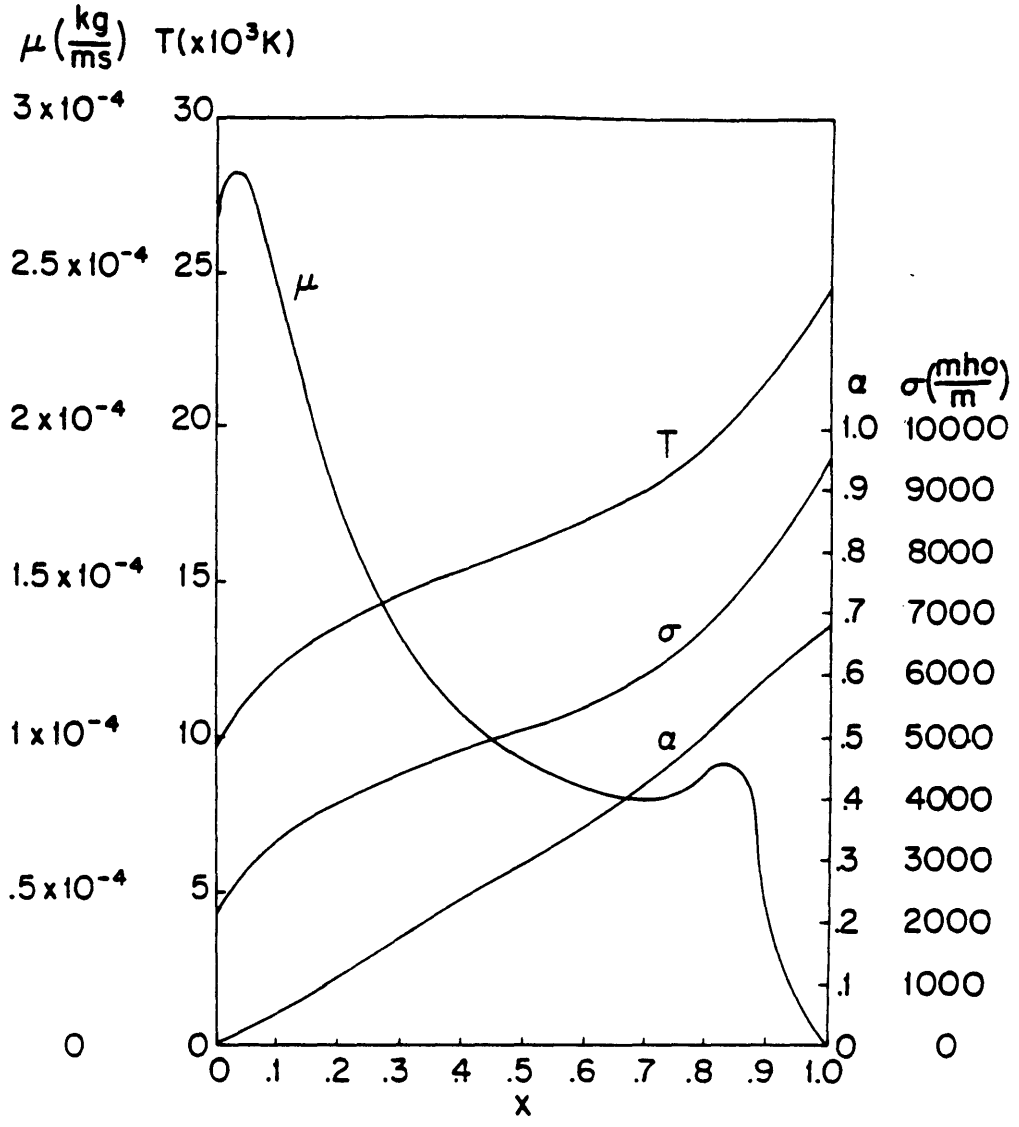

Figure A10.6: Variation of Plasma Viscosity, Temperature, Ionization Fraction, and Conductivity in the Constant Area Channel at a Magnetic Reynolds' Number of Five and an Argon Mass Flow Rate of 4 g/s .

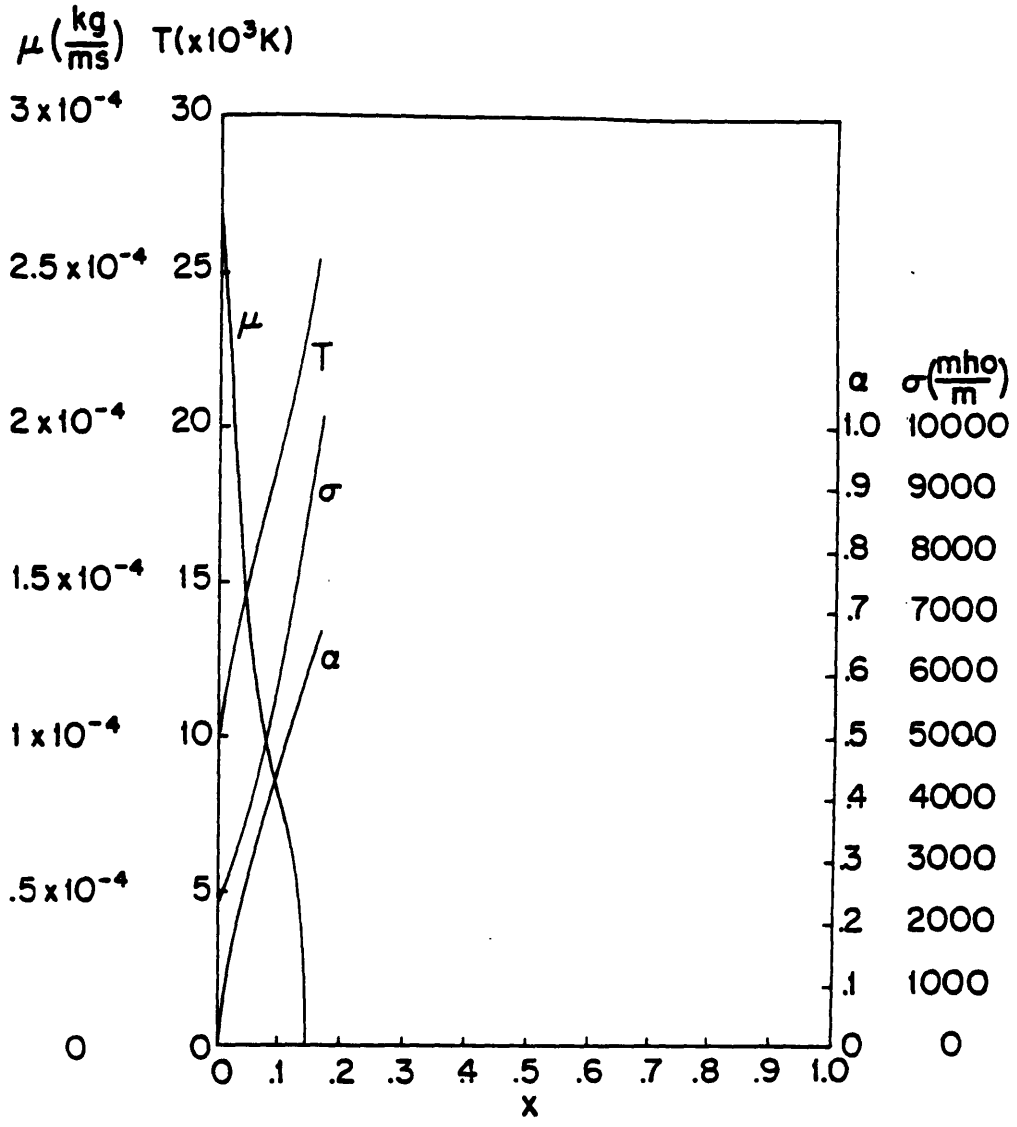

Figure A10.7: Variation of Plasma Viscosity, Temperature, Ionization Fraction, and Conductivity in the Constant Area Channel at a Magnetic Reynolds' Number of Ten and an Argon Mass Flow Rate of 4 g/s

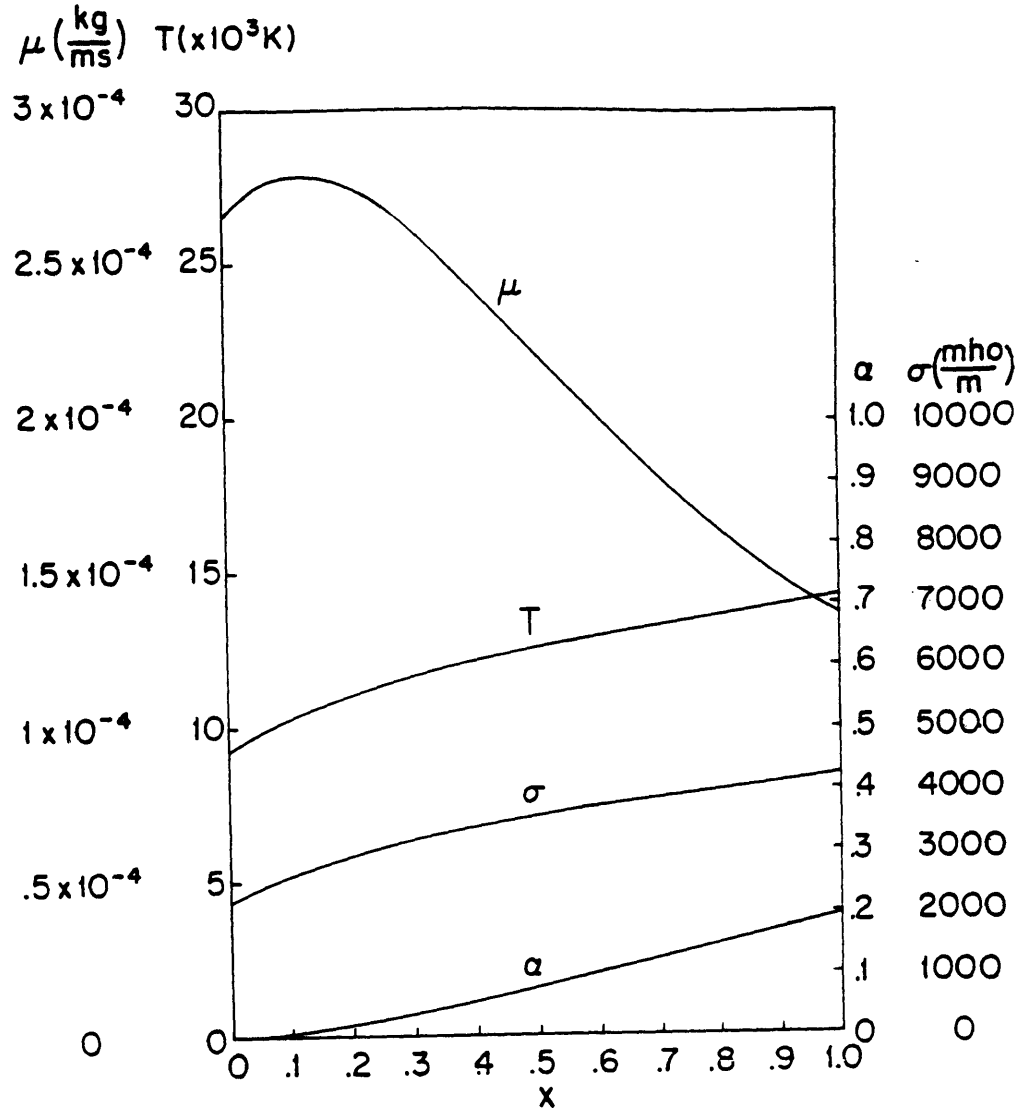

Figure A10.8: Variation of Plasma Viscosity, Temperature, Ionization Fraction, and Conductivity in the Flared Channel at a Magnetic Reynolds' Number of One and an Argon Mass Flow Rate of 4 g/s

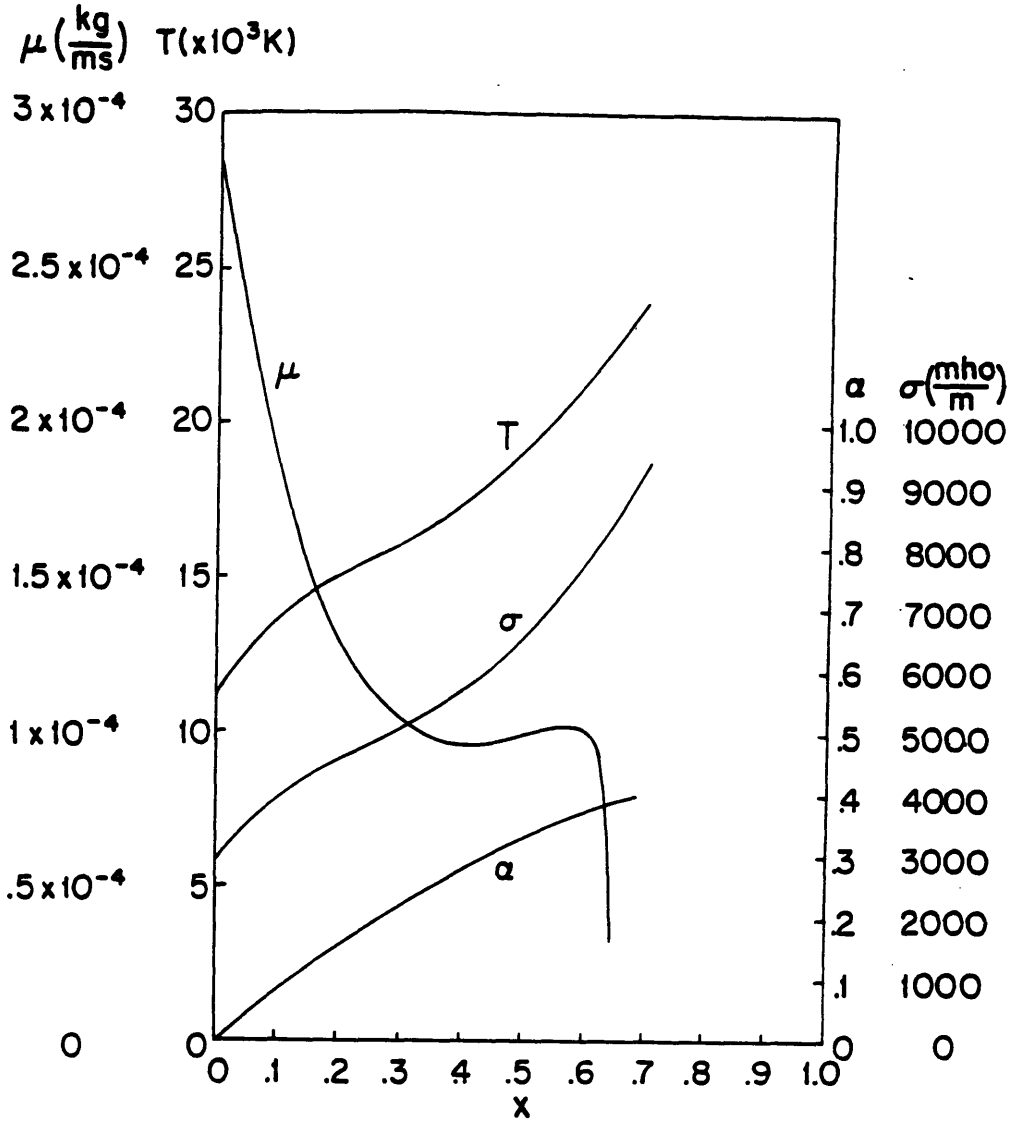

Figure A10.9: Variation of Plasma Viscosity, Temperature, Ionization Fraction, and Conductivity in the Flared Channel at a Magnetic Reynolds' Number of Five and an Argon Mass Flow Rate of 4 g/s

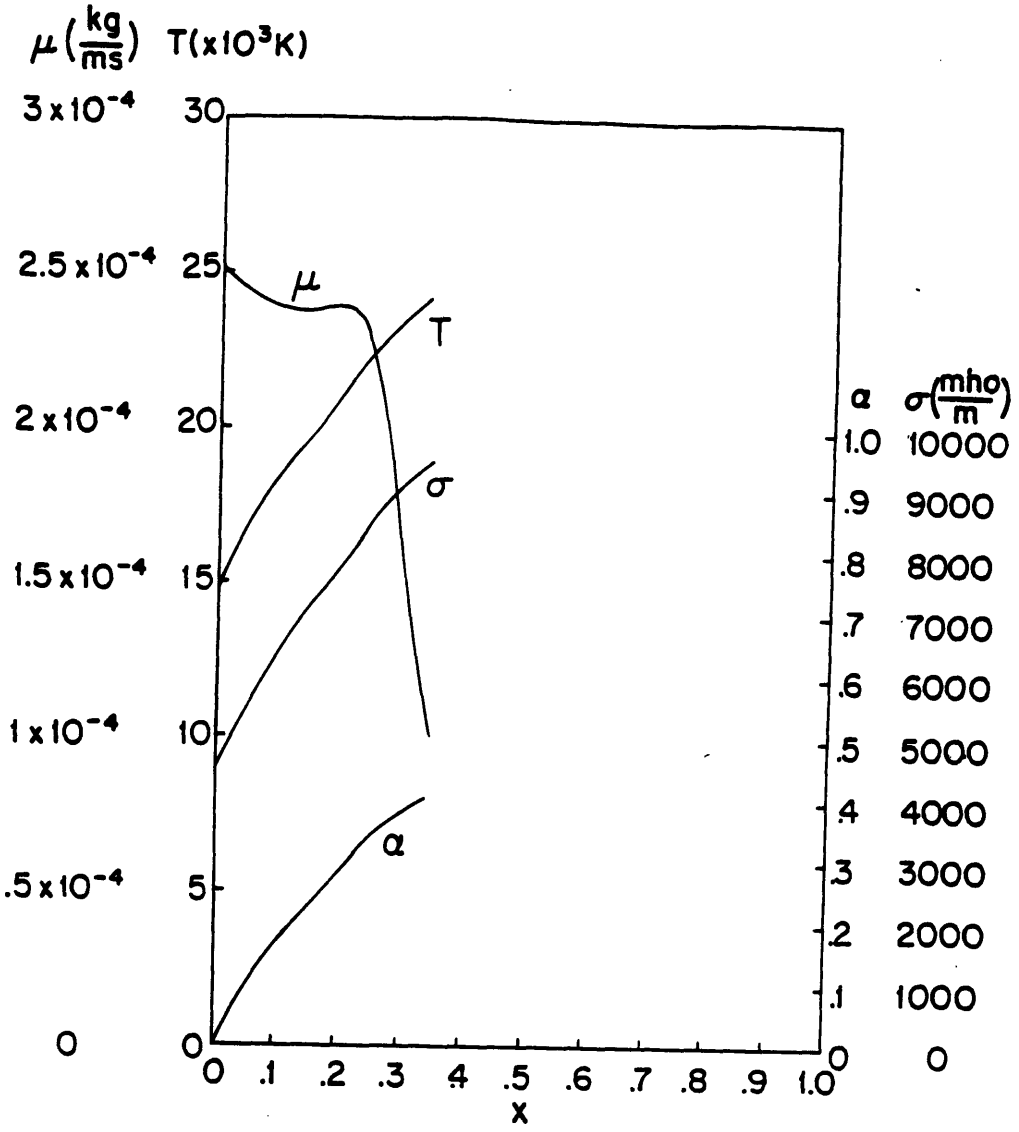

Figure A10.10: Variation of Plasma Viscosity, Temperature, Ionization Fraction, and Conductivity in the Flared Channel at a Magnetic Reynolds' Number of Ten and an Argon Mass Flow Rate of 4 g/s

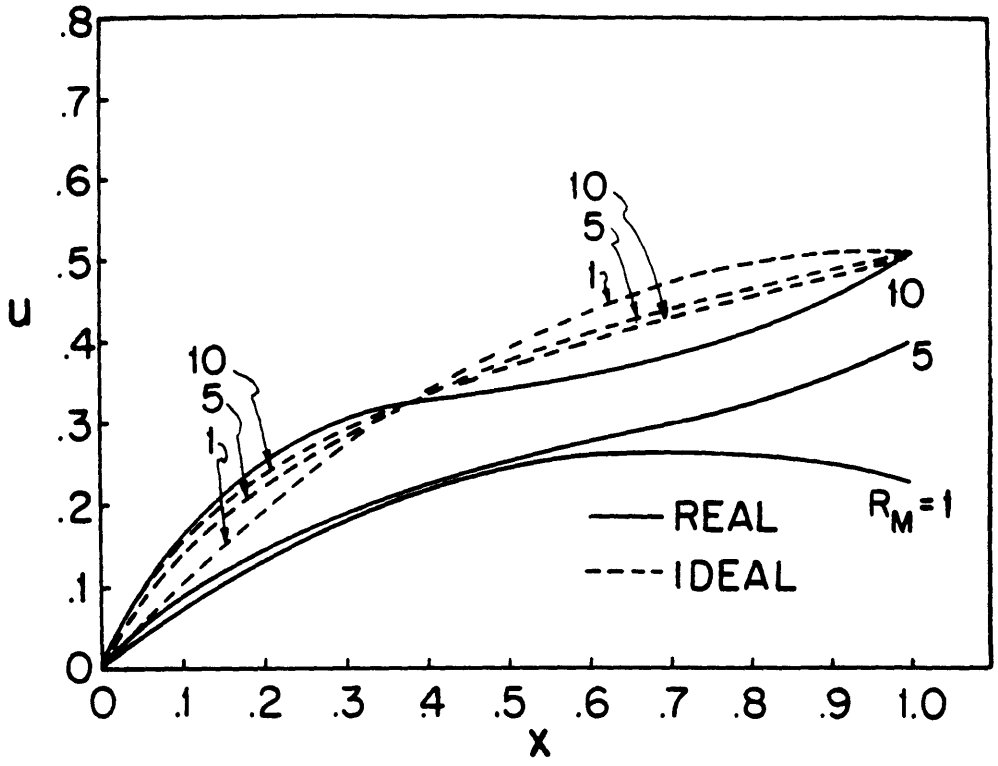

Figure A10.11: Plasma Velocity for Ideal and Real Flows in the Constant Area Channel at Various Magnetic Reynolds' Numbers and an Argon Mass Flow Rate of 4 g/s

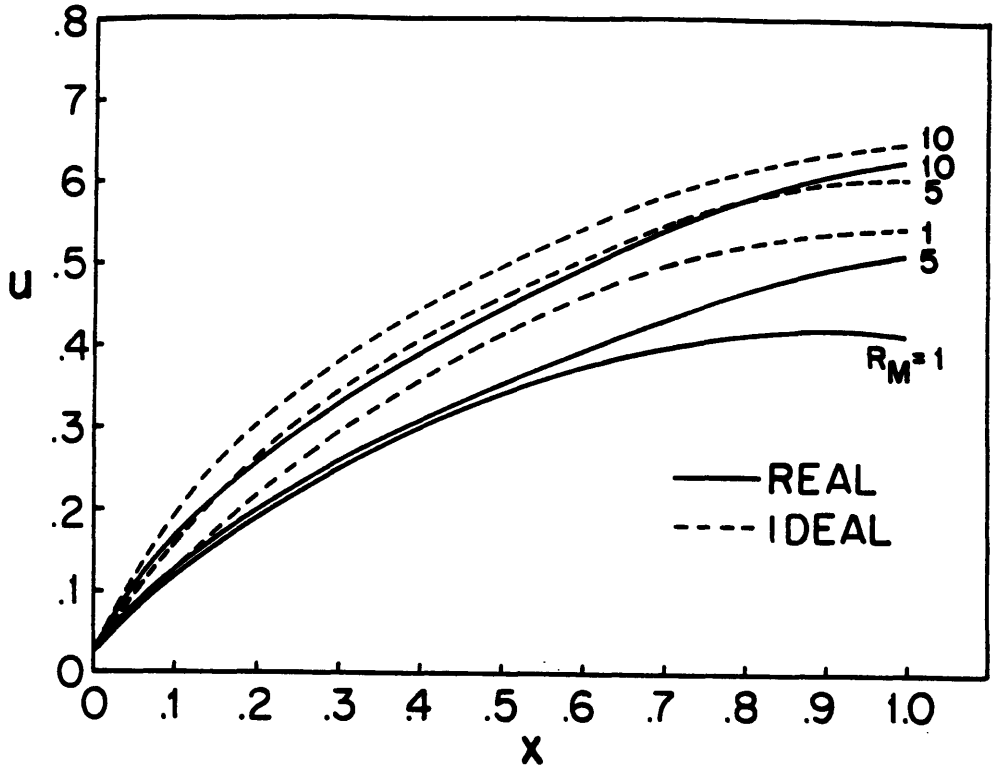

Figure A10.12: Plasma Velocity for Ideal and Real Flows in the Flared Channel at Various Magnetic Reynolds' Numbers and an Argon Mass Flow Rate of 4 g/s

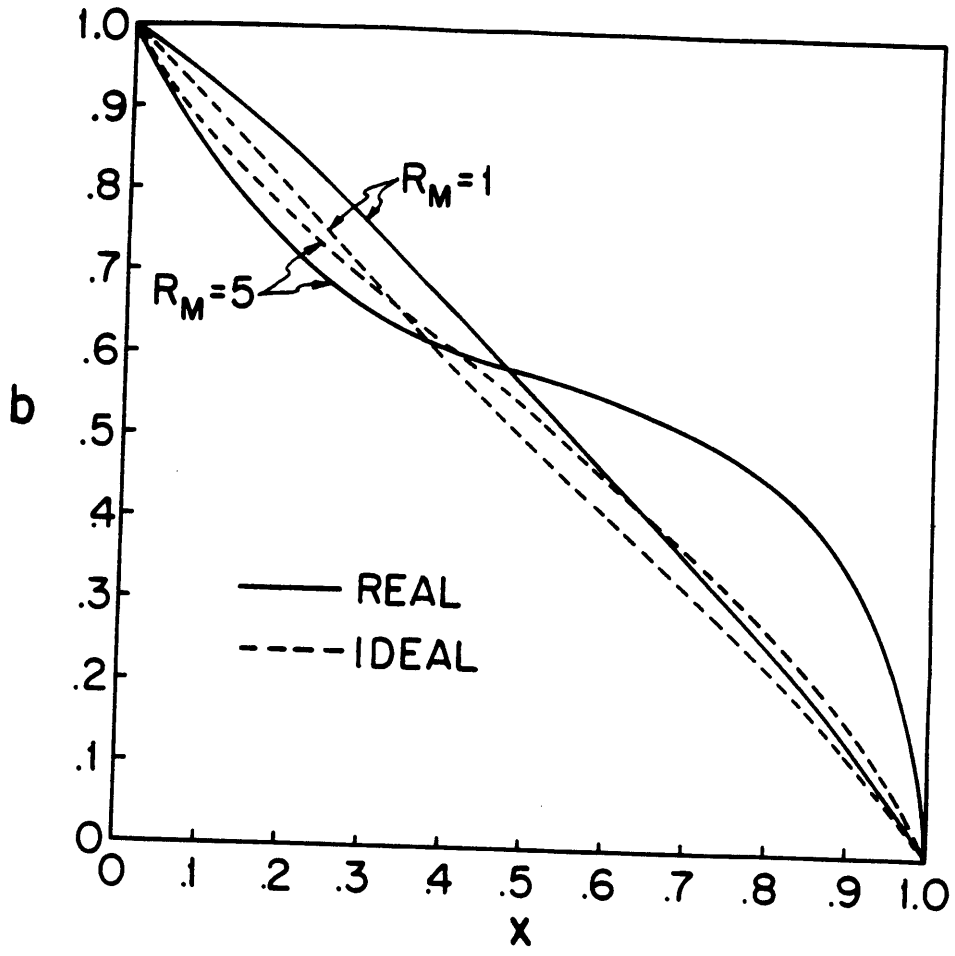

Figure A10.13: Magnetic Field Distribution in the Constant Area Channel for Real and Ideal Plasma Flows at Various Magnetic Reynolds' Numbers and an Argon Mass Flow Rate of 4 g/s

R_m	Constant Area Channel		Flared Channel	
	Ideal	Real	Ideal	Real
1	1.133	1.245	1.216	1.535
5	0.346	0.243	0.444	0.313
10	0.257	0.212	0.361	0.269

Figure A10.14: Nondimensional Voltage as a Function of Magnetic Reynolds' Number for Ideal and Real Gas Flows

R_m	Constant Area Channel	Flared Channel
1	0.204	0.568
5	0.624	0.707
10	1.000	0.912

Figure A10.15: Relative Efficiencies Based on the Ratio of Real to Ideal Exhaust Kinetic Power as a Function of Magnetic Reynolds' Number

conductivity on the distribution of magnetic field in the constant area channel, figure A10.14 tabulates the inviscid-constant conductivity voltages with the viscous-variable conductivity voltages, and figure A10.15 shows the calculated "efficiencies" of the two types of channels based on the exhaust kinetic power.

In figure A10.11, the difference between channels is quite apparent. Viscous effects are more apparent for a magnetic Reynolds' number of one since the temperature and viscosity do not vary significantly. For this case, the viscous effects actually cause the velocity to decrease near the channel exit. For a magnetic Reynolds' number of five, the viscosity is lower but since the velocity is slightly higher, the effects are still strongly seen. The velocity does not decrease near the exit, and this is primarily due to the fact that the temperature is elevated so the conductivity increases and the viscosity goes to zero. The higher conductivity increases the local $\vec{j}x\vec{B}$ force and, in the absence of friction, enables the plasma to accelerate rapidly. For the case of the magnetic Reynolds' number of ten, the channel is effectively inviscid and the conductivity is significantly elevated. Because of this, there is no significant viscous loss and the channel is effectively operating at a higher magnetic Reynolds' number.

The constant area channel data is interesting, but its accuracy is questionable. Of course, any one-dimensional analysis is questionable, but neglecting the thermodynamic pressure and sonic passage strongly affects the overall channel behavior. In the cases where temperature and conductivity vary rapidly, such effects are magnified and really cannot be

neglected. Therefore, the model of the flared channel exhibits more believable behavior since the converging-diverging sections act to reduce the gradients and mitigate the mechanisms which lead to strong sonic choking effects.

Figures A10.8 to A10.10 exhibit the same behavior as seen in figures A10.5 through A10.7, and figure A10.12 shows similar trends to those found in figure A10.11 except that the behavior at magnetic Reynolds' number of five and ten follow more smoothly their inviscid counterparts. The initial strong effect of viscosity causes a deficit in velocity that is never made up throughout the remainder of the channel. It is interesting to note that although the friction term is directly proportional to the viscosity and the velocity, it is the magnitude of the viscosity that ultimately controls the loss. As the plasma accelerates for all but the slowest of channels, the plasma heats up to the point where it behaves more like an inviscid flow.

The effect of the variation in conductivity is shown in figure A10.13 which exhibits the redistribution of the magnetic field in the constant area channel. For a magnetic Reynolds' number of one, there is only small deviation from the ideal model. This is due to the decreased conductivity from the slightly depressed plasma temperature. At a magnetic Reynolds' number of ten, there is significant variation reminiscent of higher magnetic Reynolds' number flows. This is appropriate since the plasma temperature, and therefore conductivity, is significantly higher.

Figure A10.14 shows a comparison between the voltage for an ideal channel and one with the real effects of viscosity and variable

conductivity. Except for the channel with real gas effects at reference magnetic Reynolds' number of unity, all of the real voltages are lower. This reflects not only the viscous losses which lower the back emf, but also the increased conductivity which lowers the Ohmic contribution to the voltage. For the more dissipative constant area channel, the voltage is predominantly Ohmic. Since the conductivity is decreased from the ideal case, the mean magnetic Reynolds' number may be slightly less than one, and the resulting the Ohmic voltage contribution is increased.

These channels can be compared by defining a relative efficiency as the ratio of the real gas exhaust kinetic power to the inviscid exhaust power. Figure A10.15 shows these results and demonstrates that the deficiencies are more strongly noted for low magnetic Reynolds' numbers and decreases as the magnetic Reynolds' number increases. This is primarily due to the diminished importance of the viscous losses as the flow is heated allowing it to become more reactive.

This model can only be used as a guideline to estimate the importance of friction in the operation of various geometries. Greater fidelity requires a more substantial model of the arcjet--not only more independent dimensions, but a more accurate description of the plasma boundary layers and plasma state, and a more careful treatment of the thruster thermodynamics.

Appendix 11: Computer Codes

The following computer codes are used throughout this dissertation to simulate MPD channel flows and L-C Ladder configurations. The code is written for use on the IBM PC or PC compatible and is either written in PC-Basic or MS-FORTRAN.

A11.1: Code for the One-Dimensional Constant Area Channel

The following BASIC code is used to calculate the operation of both ideal and real plasma flows in MPD Channels presented in Appendices 3 and 10. The code becomes ideal by setting f=0 at the end of the subroutine where it is calculated and by eliminating the temperature dependence in the conductivity. The magnetic Reynold's number can be varied by changing the variable RM.

```
10 REM 1-D REAL GAS MPD SIMULATION WITH FINITE RM FOR CONSTANT AREA
       CHANNEL
20 REM REVISED OCTOBER 13, 1987
30 REM
40 DIM B(101),U(101),KU(4),X(101),E(101),AREA(101),RHO(101),TEMP(101)
50 DIM ALPHA(101),TV(20),MU(20),Y2(20),TU(20),GAM(20),TA(20),TB(20),
   TC(20)
60 DIM TR(20),FV(101)
70 REM
80 REM INPUT VALUES FOR THE TABULATED VISCOSITY
90 REM
100 DATA 5,6,7,8,9,10,11,12,13,14,15,16,17,18,19,20,21,22,23,24
110 DATA 1.81,2.07,2.28,2.50,2.69,2.83,2.84,2.60,2.17,1.74,1.44,1.31,
    1.32,1.33 ,1.62,1.99,1.81,.351,.0176,.00407
120 REM
130 REM SET INITIAL CONDITIONS AND NONDIMENSIONAL PARAMETERS
140 REM
```

```
150 B0=1!:U0=.01:H0=.58:RM=21:N=50!:H=1!/N:X0=0!:F=0!:A0=1!
160 SIG=3300!:L=9.000001E-02:MU0=.0000004*3.14159:MDOT=.004:
    AD=.0074:WD=AD/.019
170 MI=6.646E-26:CHARG=1.6E-19:BD=(RM*MDOT/(SIG*L*AD))^.5
180 REM CALCULATE THE TOTAL CURRENT
190 CURR=(RM*MDOT*WD*WD/(SIG*L*AD*MU0*MU0))^.5
200 PRINT CURR
210 REM
220 REM CALCULATE NONDIMENSIONAL PARAMETERS
230 REM
240 VCONST=(RM/(SIG*L))*(RM*MDOT/(SIG*L*AD))^.5*AD/(MU0*WD)
250 PRINT"INPUT MPD VOLTAGE"
260 INPUT V:CONST=V/VCONST:E(1)=CONST
270 HNON=(BD*BD*AD/(MU0*MDOT))^2:VI=CHARG*15.775/(MI*HNON)
280 TREF=MI*HNON/1.38E-23:RREF=MU0*(MDOT/(BD*AD))^2
290 TC=1.38E-23*12000/(MI*HNON)
300 REM
310 REM DEFINE FUNCTIONS
320 REM
330 DEF FNDB(BT,UT)=-1!*RM*(TNEW/TC)^1.5*(CONST-UT*BT)
340 DEF FNDU(BT,UT)=-1!*((BT*FNDB(BT,UT))+(F*UT))
350 DEF FNDH(BT,UT,ET)=H0+(U0*U0/2!)+E(1)-((UT*UT/2!)+(ET*BT))
360 DEF FNT(ALF,ENT)=(ENT-(ALF*VI))/(ALF+2.5)
370 DEF FNNON(ALF,RHO,T)=1!-2.187E+31*((RREF*RHO)^3/(TREF*T)^5)*(1!-ALF)
    *((.0001601*(1!-ALF)*(TREF*T)^1.5*EXP(-VI/T)/(RREF*RHO))-ALF^2)
380 B(1)=B0:U(1)=U0:X(1)=X0:RHO(1)=1!/U0:AREA(1)=A0
390 BT=B0:UT=U0:RHO0=1!/U0:ALPHA(1)=.001:TEMP(1)=2.89238E-04:TOL=.01
400 RHOT=RHO0:ENT=H0
410 ALPHA(1)=0
420 LPRINT "RM = ",RM,"VOLTAGE = ",V,"H0 = ",H0
430 LPRINT
440  LPRINT"          X           B             U          ALPHA          T
MU"
450 LPRINT
460 REM
470 REM DISCRETIZE THE VISCOSITY
480 REM
490 GOSUB 1190
500 GOSUB 880
510 FV(1)=MUCOR:TEMP(1)=TNEW
520 REM
530 REM DO RUNGE KUTTA INTEGRATION
540 REM
550 FOR I=1 TO N
560 UT=U0:XT=X0:BT=B0
570 KU(1)=H*FNDU(BT,UT):KB(1)=H*FNDB(BT,UT)
580 UT=U0+(KU(1)/2!):XT=X0+(H/2!):RHOT=1!/UT
590 BT=B0+(KB(1)/2!)
600 ENT=FNDH(BT,UT,CONST)
```

```
610 GOSUB 880
620 KU(2)=H*FNDU(BT,UT):KB(2)=H*FNDB(BT,UT)
630 UT=U0+(KU(2)/2!):XT=X0+(H/2!):RHOT=1!/UT
640 BT=B0+(KB(2)/2!)
650 ENT=FNDH(BT,UT,CONST)
660 GOSUB 880
670 KU(3)=H*FNDU(BT,UT)
680 UT=U0+KU(3):XT=X0+H:KB(3)=H*FNDB(BT,UT):RHOT=1!/UT
690 BT=B0+KB(3)
700 ENT=FNDH(BT,UT,CONST)
710 GOSUB 880
720 KU(4)=H*FNDU(BT,UT):KB(4)=H*FNDB(BT,UT)
730 U0=U0+(KU(1)+KU(2)+KU(2)+KU(3)+KU(3)+KU(4))/6!
740 B0=B0+(KB(1)+KB(2)+KB(2)+KB(3)+KB(3)+KB(4))/6!
750 X0=X0+H:RHO0=1!/U0:RHOT=RHO0
760 ENT=FNDH(BT,UT,CONST)
770 GOSUB 880
780 B(I+1)=B0:U(I+1)=U0:X(I+1)=X(I)+H:RHO(I+1)=RHO0:ALPHA(I+1)=ANEW:
    TEMP(I+1)=TNEW:FV(I+1)=MUCOR:IF (MUCOR<0!) THEN FV(I+1)=0
790 NEXT I
800 FOR I=1 TO N+1
810 LPRINT USING "#.#####^^^^_ ";X(I),B(I),U(I),ALPHA(I),
    TEMP(I)*MI*HNON/1.38E-23,FV(I)
820 NEXT I
830 BEEP
840 LPRINT
850 LPRINT"VCONST = ",CONST
860 END
870 REM
880 REM SUBROUTINE TO CALCULATE A CONSISTENT TEMPERATURE AND IONIZATION
890 REM FRACTION
900 REM
910 TLIM=TNEW*MI*HNON/1.38E-23
920 IF (TLIM>24000!) THEN RETURN
930 A1=ALPHA(I)
940 AMAX=ENT/VI
950 IF ((A2<.01) AND (A2>0)) THEN A2=2!*A2 ELSE A2=(A1+AMAX)/2!
960 T1=FNT(A1,ENT):T2=FNT(A2,ENT)
970 F1=FNNON(A1,RHOT,T1)
980 F2=FNNON(A2,RHOT,T2)
990 IF ((A1=0) AND (F1>TOL)) THEN PRINT"INITIAL ENTHALPY TOO LOW":STOP
1000 IF (ABS(F1)<=TOL) THEN GOTO 1150
1010 IF (ABS(F2)<=TOL) THEN GOTO 1160
1020 IF (ABS((F1-F2)/F1)<.0001) THEN TNEW=T1:ANEW=A1:GOTO 1170
1030 IF (F1>F2) AND (F2>0) THEN GOTO 1070
1040 IF (F1<F2) AND (F1>0) THEN GOTO 1080
1050 IF (F1>0) AND (F2<0) THEN GOTO 1090
1060 IF (F2>0) AND (F1<0) THEN GOTO 1120
1070 A1=A2:GOTO 950
1080 A2=A1:A1=A1/2!:GOTO 960
```

```
1090 ANEW=(A1+A2)/2!:TNEW=FNT(ANEW,ENT):EFNEW=FNNON(ANEW,RHOT,TNEW)
1100 IF (EFNEW>0) THEN A1=ANEW:F1=EFNEW:T1=TNEW ELSE A2=ANEW:F2=EFNEW:
     T2=TNEW
1110 GOTO 1000
1120 ANEW=(A1+A2)/2!:TNEW=FNT(ANEW,ENT):EFNEW=FNNON(ANEW,RHOT,TNEW)
1130 IF (EFNEW>0) THEN A2=ANEW:F2=EFNEW:T2=TNEW ELSE
     A1=ANEW:F1=EFNEW:T1=TNEW
1140 GOTO 1000
1150 ANEW=A1:TNEW=T1:GOTO 1170
1160 ANEW=A2:TNEW=T2:GOTO 1170
1170 GOSUB 1430
1180 RETURN
1190 REM
1200 REM SUBROUTINE TO CALCULATE THE CUBIC SPLINE INTERPOLANT
1210 REM
1220 FOR I=1 TO 20:READ TV(I):NEXT I
1230 FOR I=1 TO 20:READ MU(I):NEXT I
1240 FOR I=1 TO 20:TV(I)=TV(I)*1000!:MU(I)=MU(I)/10000!:NEXT I
1250 FOR I=1 TO 20:TB(I)=1:NEXT I
1260 TA(1)=0:TA(20)=0:TC(1)=0:TC(20)=0:TR(1)=0:TR(20)=0
1270 FOR I=2 TO 19
1280 TA(I)=(TV(I)-TV(I-1))/(2!*(TV(I+1)-TV(I-1)))
1290 TC(I)=(TV(I+1)-TV(I))/(2!*(TV(I+1)-TV(I-1)))
1300 TR(I)=3!*((MU(I+1)-MU(I))/(TV(I+1)-TV(I))-(MU(I)-MU(I-1))/
     (TV(I)-TV(I-1)))/(TV(I+1)-TV(I-1))
1310 NEXT I
1320 BET=1
1330 TU(1)=TR(1)
1340 FOR I=2 TO 20
1350 GAM(I)=TC(I-1)/BET
1360 BET=TB(I)-TA(I)*GAM(I)
1370 TU(I)=(TR(I)-TA(I)*TU(I-1))/BET
1380 NEXT I
1390 FOR I=19 TO 1 STEP -1
1400 TU(I)=TU(I)-GAM(I+1)*TU(I+1)
1410 NEXT I
1420 RETURN
1430 REM
1440 REM SUBROUTINE TO DO THE INTERPOLATION
1450 REM
1460 FLAG=0
1470 TEM=TNEW*MI*HNON/1.38E-23
1480 FOR J=2 TO 20
1490 IF (FLAG=1) THEN GOTO 1510
1500 IF ((TEM<=TV(J)) AND (TEM>TV(J-1))) THEN KLO=J-1:KHI=J:FLAG=1
1510 NEXT J
1520 HH=TV(KHI)-TV(KLO)
1530 A1=(TV(KHI)-TEM)/HH
1540 B1=(TEM-TV(KLO))/HH
1550 MUNEW=A1*MU(KLO)+B1*MU(KHI)+((A1^3-A1)*TU(KLO)+(B1^3-B1)*
```

```
    Y2(KHI))*(HH^2)/6!
1560 IF (ANEW=0!) THEN ANEW=.0000001
1570 MUION=1.75E-16*TEM^2.5/LOG(3.196E-06*(TEM^3/(ANEW*RREF*RHOT))^.5)
1580 MUTMP=MUION/(MUNEW-MUION)
1590 MUCOR=MUNEW*((MUTMP+ANEW-ANEW^2)/(MUTMP+ANEW))
1600 F=12!*.154*9.000001E-02*MUCOR/(AD*MDOT)
1610 IF (F<0) THEN F=0
1620 RETURN
```

A11.2: Code for the One-Dimensional Flared Channel

This BASIC code models the one-dimensional ideal and real MPD channels presented in Appendices 3 and 10. The code becomes ideal by setting f=0 and by eliminating the temperature dependence in the conductivity. The magnetic Reynold's number can be varied by changing the variable RM.

```
10 REM 1-D REAL MPD SIMULATION WITH FINITE RM AND AREA VARIATION
20 REM REVISED OCTOBER 21, 1987
30 REM
40 DIM B(101),U(101),KU(4),KH(4),X(101),E(101),AREA(101),RHO(101),
     TEMP(101)
50 DIM ALPHA(101),TV(20),MU(20),Y2(20),TU(20),GAM(20),TA(20),TB(20),
   TC(20)
60 DIM TR(20),FV(101)
70 REM
80 REM INPUT VALUES FOR THE TABULATED VISCOSITY
90 REM
100 DATA 5,6,7,8,9,10,11,12,13,14,15,16,17,18,19,20,21,22,23,24
110 DATA 1.81,2.07,2.28,2.50,2.69,2.83,2.84,2.60,2.17,1.74,1.44,1.31,
    1.32,1.33,1.62,1.99,1.81,.351,.0176,.00407
120 REM
130 REM SET INITIAL CONDITIONS AND NONDIMENSIONAL PARAMETERS
140 REM
150 B0=1!:H0=.666:U0=.01:RM=1!:N=50!:H=1!/N:X0=0!:F=0!:
    A0=4!:WD=.00746/.019
160 SIG=3300!:L=9.000001E-02:MU0=.0000004*3.14159:MDOT=.004:AD=.00746
170 MI=6.646E-26:CHARG=1.6E-19:BD=(RM*MDOT/(SIG*L*AD))^.5
180 REM
190 REM CALCULATE NONDIMENSIONAL PARAMETERS
200 REM
```

```
210 VCONST=(RM/(SIG*L))*(RM*MDOT/(SIG*L*AD))^.5*AD/(MU0*WD)
220 PRINT "VCONST = ",VCONST
230 PRINT"INPUT MPD VOLTAGE"
240 INPUT V:CONST=V/VCONST:E(1)=CONST/A0
250 HNON=(BD*BD*AD/(MU0*MDOT))^2:VI=CHARG*15.775/(MI*HNON)
260 TREF=MI*HNON/1.38E-23:RREF=MU0*(MDOT/(BD*AD))^2
270 TC=1.38E-23*12000/(MI*HNON)
280 REM
290 REM DEFINE FUNCTIONS
300 REM
310 DEF FNDB(XT)=B0*(1!-XT)
320 DEF FNDU(XT,UT,AT)=(B0*AT*FNDB(XT))-(F*UT/AT)
330 DEF FNDH(XT,UT,ET,AT)=ET*AT-UT*FNDU(XT,UT,AT)
340 DEF FNT(ALF,ENT)=(ENT-(ALF*VI))/(ALF+2.5)
350 DEF FNNON(ALF,RHO,T)=1!-2.187E+31*((RREF*RHO)^3/(TREF*T)^5)*(1!-ALF)
    *((.0001601*(1!-ALF)*(TREF*T)^1.5*EXP(-VI/T)/(RREF*RHO))-ALF^2)
360 B(1)=B0:U(1)=U0:X(1)=X0:RHO(1)=1!/(A0*U0):AREA(1)=A0
370 BT=B0:UT=U0:RHO0=1!/(A0*U0):TEMP(1)=2.89238E-04:TOL=.01
380 RHOT=RHO0:ENT=H0
390 ALPHA(1)=0
400 PRINT "RM = ",RM,"VOLTAGE = ",V
410 PRINT "H0 = ",H0
420 PRINT
430  PRINT"          X          AREA          U          ALPHA          T
MU"
440 PRINT
450 GOSUB 1250
460 GOSUB 920
470 FV(1)=MUCOR:TEMP(1)=TNEW
480 REM
490 REM DO RUNGE KUTTA INTEGRATION
500 REM
510 FOR I=1 TO N
520 UT=U0:XT=X0:UT=U0:AT=A0:RHOT=RHO0:HT=H0
530 KU(1)=H*FNDU(XT,UT,AT):KH(1)=H*FNDH(XT,UT,ET,AT)
540 UT=U0+(KU(1)/2!):HT=H0+(KH(1)/2!):ET=UT*FNDB(XT)+
    (B0/(RM*(TNEW/TC)^1.5)):AT=CONST/ET:RHOT=1!/(UT*AT):XT=X0+(H/2!)
550 ENT=HT
560 GOSUB 920
570 KU(2)=H*FNDU(XT,UT,AT):KH(2)=H*FNDH(XT,UT,ET,AT)
580 UT=U0+(KU(2)/2!):HT=H0+(KH(2)/2!):ET=UT*FNDB(XT)+
    (B0/(RM*(TNEW/TC)^1.5)):AT=CONST/ET:RHOT=1!/(UT*AT):XT=X0+(H/2!)
590 ENT=HT
600 GOSUB 920
610 KU(3)=H*FNDU(XT,UT,AT):KH(3)=H*FNDH(XT,UT,ET,AT)
620 UT=U0+KU(3):HT=H0+KH(3):ET=UT*FNDB(XT)+
    (B0/(RM*(TNEW/TC)^1.5)):AT=CONST/ET:RHOT=1!/(UT*AT):XT=X0+H
630 ENT=HT
640 GOSUB 920
650 KU(4)=H*FNDU(XT,UT,AT):KH(4)=H*FNDH(XT,UT,ET,AT)
```

```
660 U0=U0+(KU(1)+KU(2)+KU(2)+KU(3)+KU(3)+KU(4))/6!
670 H0=H0+(KH(1)+KH(2)+KH(2)+KH(3)+KH(3)+KH(4))/6!
680 X0=X0+H:E0=U0*FNDB(X0)+(B0/(RM*(TNEW/TC)^1.5)):
    A0=CONST/E0:RHO0=1!/(U0*A0):RHOT=RHO0
690 ENT=H0
700 GOSUB 920
710 B(I+1)=FNDB(X0):U(I+1)=U0:X(I+1)=X(I)+H:E(I+1)=E0:
    AREA(I+1)=A0:RHO(I+1)=RHO0
720 PRINT E0,A0
730 FV(I+1)=MUCOR:TEMP(I)=TNEW
740 ALPHA(I+1)=ANEW
750 PRINT I
760 NEXT I
770 REM
780 REM FIND THROAT B
790 REM
800 AMIN=AREA(1)
810 FOR J=1 TO N:IF (AREA(J)>AMIN) GOTO 830
820 AMIN=AREA(J):BMIN=B(J)
830 NEXT J
840 FOR I=1 TO N+1
850 PRINT USING "#.#####^^^^_ ";X(I),AREA(I),U(I),ALPHA(I),
    TEMP(I)*MI*HNON/1.38E-23,FV(I)
860 NEXT I
870 PRINT
880 PRINT"VCONST = ",CONST
890 BEEP
900 END
910 REM
920 REM SUBROUTINE TO CALCULATE A CONSISTENT TEMPERATURE AND IONIZATION
930 REM FRACTION
940 REM
950 TLIM=TNEW*MI*HNON/1.38E-23
960 IF (TLIM>24000!) THEN RETURN
970 A1=ALPHA(I)
980 AMAX=ENT/VI
990 IF (AMAX>1) THEN AMAX=1
1000 IF ((A2<.01) AND (A2>0)) THEN A2=3!*A2 ELSE A2=(A1+AMAX)/2!
1010 IF (A2>AMAX) THEN A2=(A1+AMAX)/2!
1020 T1=FNT(A1,ENT):T2=FNT(A2,ENT)
1030 F1=FNNON(A1,RHOT,T1)
1040 F2=FNNON(A2,RHOT,T2)
1050 IF ((A1=0) AND (F1>TOL)) THEN PRINT"INITIAL ENTHALPY TOO LOW":STOP
1060 IF (ABS(F1)<=TOL) THEN GOTO 1210
1070 IF (ABS(F2)<=TOL) THEN GOTO 1220
1080 IF (ABS((F1-F2)/F1)<.0001) THEN TNEW=T1:ANEW=A1:GOTO 1230
1090 IF (F1>F2) AND (F2>0) THEN GOTO 1130
1100 IF (F1<F2) AND (F1>0) THEN GOTO 1140
1110 IF (F1>0) AND (F2<0) THEN GOTO 1150
1120 IF (F2>0) AND (F1<0) THEN GOTO 1180
```

```
1130 A1=A2:GOTO 1000
1140 A2=A1:A1=A1/2!:GOTO 1020
1150 ANEW=(A1+A2)/2!:TNEW=FNT(ANEW,ENT):EFNEW=FNNON(ANEW,RHOT,TNEW)
1160 IF (EFNEW>0) THEN A1=ANEW:F1=EFNEW:T1=TNEW ELSE A2=ANEW:
     F2=EFNEW:T2=TNEW
1170 GOTO 1060
1180 ANEW=(A1+A2)/2!:TNEW=FNT(ANEW,ENT):EFNEW=FNNON(ANEW,RHOT,TNEW)
1190 IF (EFNEW>0) THEN A2=ANEW:F2=EFNEW:T2=TNEW ELSE A1=ANEW:
     F1=EFNEW:T1=TNEW
1200 GOTO 1060
1210 ANEW=A1:TNEW=T1:GOTO 1230
1220 ANEW=A2:TNEW=T2:GOTO 1230
1230 GOSUB 1490
1240 RETURN
1250 REM
1260 REM SUBROUTINE TO CALCULATE THE CUBIC SPLINE INTERPOLANT
1270 REM
1280 FOR I=1 TO 20:READ TV(I):NEXT I
1290 FOR I=1 TO 20:READ MU(I):NEXT I
1300 FOR I=1 TO 20:MU(I)=MU(I)/10000!:TV(I)=TV(I)*1000!:NEXT I
1310 FOR I=1 TO 20:TB(I)=1:NEXT I
1320 TA(1)=0:TA(20)=0:TC(1)=0:TC(20)=0:TR(1)=0:TR(20)=0
1330 FOR I=2 TO 19
1340 TA(I)=(TV(I)-TV(I-1))/(2!*(TV(I+1)-TV(I-1)))
1350 TC(I)=(TV(I+1)-TV(I))/(2!*(TV(I+1)-TV(I-1)))
1360 TR(I)=3!*((MU(I+1)-MU(I))/(TV(I+1)-TV(I))-(MU(I)-MU(I-1))/
     (TV(I)-TV(I-1)))/(TV(I+1)-TV(I-1))
1370 NEXT I
1380 BET=1
1390 TU(1)=TR(1)
1400 FOR I=2 TO 20
1410 GAM(I)=TC(I-1)/BET
1420 BET=TB(I)-TA(I)*GAM(I)
1430 TU(I)=(TR(I)-TA(I)*TU(I-1))/BET
1440 NEXT I
1450 FOR I=19 TO 1 STEP -1
1460 TU(I)=TU(I)-GAM(I+1)*TU(I+1)
1470 NEXT I
1480 RETURN
1490 REM
1500 REM SUBROUTINE TO DO THE INTERPOLATION
1510 REM
1520 FLAG=0
1530 TEM=TNEW*MI*HNON/1.38E-23
1540 FOR J=2 TO 20
1550 IF (FLAG=1) THEN GOTO 1570
1560 IF ((TEM<=TV(J)) AND (TEM>TV(J-1))) THEN KLO=J-1:KHI=J:FLAG=1
1570 NEXT J
1580 HH=TV(KHI)-TV(KLO)
1590 A1=(TV(KHI)-TEM)/HH
```

```
1600 B1=(TEM-TV(KLO))/HH
1610 MUNEW=A1*MU(KLO)+B1*MU(KHI)+((A1^3-A1)*TU(KLO)+(B1^3-B1)*Y2(KHI))*
     (HH^2)/6!
1620 IF (ANEW=0!) THEN ANEW=.0000001
1630 MUION=1.75E-16*TEM^2.5/LOG(3.196E-06*(TEM^3/(ANEW*RREF*RHOT))^.5)
1640 MUTMP=MUION/(MUNEW-MUION)
1650 MUCOR=MUNEW*((MUTMP+ANEW-ANEW^2)/(MUTMP+ANEW))
1660 F=12!*.154*9.000001E-02*MUCOR/(AD*MDOT)
1670 IF (F<0) THEN F=0
1680 RETURN
```

A11.3: Approximate Two-Dimensional MPD Code

This FORTRAN code was used to calculate the results presented in Chapter II detailing the approximated two-dimensional MPD channel model.

```
$DEBUG
$LARGE
$NOFLOATCALLS
      PROGRAM TWOD
      IMPLICIT DOUBLE PRECISION (A-H,O-Z)
      DOUBLE PRECISION JTOTAL,JX,JY,KN,LAM,LAMM1,LAMM2,LENGTH,M,MDOT,
     &                 ME,MI,MOM,MU0
      LOGICAL FLAG,FLAG2
      COMMON/VARS/LENGTH,PI0
      DIMENSION AN(20),ARG(50,20),BFIELD(50,20),BN(20),BORHO(50,20),
     &          BZ(50),CN(20),ETA(50,10),ETAINT(50,10),ETADNT(50,10),
     &          ETATNT(50,10),H(50),HALL(50,20),JX(50,20),JTOTAL(50,20),
     &          JY(50,20),KN(20),LAM(20),MOM(50,20),PSI(50,10),
     &          RHO(50,20),RHOZ(50),UZ(50),VEL(50,20),X(50),Y(50,10)
      DATA BOLTZ/1.380662D-23/CHARGE/1.60219D-19/ME/9.10953D-30/
      DATA MI/6.645D-26/PI/3.14159265/MU0/1.256637D-6/RGAS/415.7/
      DATA SIGMA/3300./TEMP/12000./
C     OPEN(1000,FILE='PARAMS.DAT',STATUS='NEW')
      OPEN(1100,FILE='B.DAT',STATUS='NEW')
      OPEN(1200,FILE='RHO.DAT',STATUS='NEW')
      OPEN(1300,FILE='VEL.DAT',STATUS='NEW')
      OPEN(1400,FILE='JX.DAT',STATUS='NEW')
      OPEN(1500,FILE='JY.DAT',STATUS='NEW')
      OPEN(1600,FILE='JTOTAL.DAT',STATUS='NEW')
C     OPEN(1700,FILE='BOR.DAT',STATUS='NEW')
      OPEN(1700,FILE='HALL.DAT',STATUS='NEW')
      OPEN(1800,FILE='HEIGHT.DAT',STATUS='NEW')
      OPEN(1900,FILE='ETA.DAT',STATUS='NEW')
      OPEN(2000,FILE='PSI.DAT',STATUS='NEW')
```

```
      OPEN(2100,FILE='Y.DAT',STATUS='NEW')
C     OPEN(2200,FILE='ANGLE.DAT',STATUS='NEW')
      OPEN(2200,FILE='MOM.DAT',STATUS='NEW')
C
C     THIS PROGRAM DOES THE CALCULATION ON THE APPROXIMATE
C     TWO DIMENSIONAL MODEL OF THE THIN CHANNEL MPD.
C
C     WRITTEN 2/2/87 BY DAN HEIMERDINGER
C     REVISED 3/31/87 BY DAN HEIMERDINGER
C
C
C     PARAMETER LIST:
C        SYSTEM CONSTANTS:
C           BOLTZ = BOLTZMANN CONSTANT
C           C = COEFFICIENT IN THE HALL PARAMETER DEFINITION
C           CHARGE = FUNDAMENTAL CHARGE
C           ME = ELECTRON REST MASS
C           MI = ION MASS
C           MU0 = PERMEABILITY OF FREE SPACE
C           PI = THE CONSTANT PI
C           RGAS = THE UNIVERSAL GAS CONSTANT FOR SINGLY IONIZED ARGON
C           SIGMA = PLASMA CONDUCTIVITY
C           TEMP = PLASMA TEMPERATURE
C        ARRAYS:
C           AN(N) = FIRST MODIFIED FOURIER COEFFICIENT
C           ARG(NNN,NN) = ARGUMENT OF THE CURRENT DENSITY VECTOR
C           BFIELD(NNN,NN) = MAGNETIC FIELD
C           BN(N) = SECOND MODIFIED FOURIER COEFFICIENT
C           BORHO(NNN,NN) = B/RHO
C           BZ(NNN) = ZEROTH ORDER MAGNETIC FIELD
C           CN(N) = FIRST SUMMATION SERIES COEFFICIENTS
C           ETA(NNN,NN) = DENSITY PERTURBATION
C           ETAINT(NNN,NN) = AXIAL INTEGRAL OF ETA
C           ETADNT(NNN) = DOUBLE INTEGRATION OF ETA OVER X AND PSI
C           ETATNT(NNN,NN) = TRANSVERSE INTEGRATION OF ETA OVER PSI
C           H(NNN) = AXIAL HEIGHT DISTRIBUTION
C           JTOTAL(NNN,NN) = TOTAL CURRENT DENSITY
C           JX(NNN,NN) = AXIAL CURRENT DENSITY
C           JY(NNN,NN) = TRANSVERSE CURRENT DENSITY
C           KN(N) = SECOND SUMMATION SERIES COEFFICIENTS
C           LAM(N) = EIGENVALUES
C           MOM(NNN,NN) = MOMENTUM
C           PSI(NNN,NN) = MOMENTUM PERTURBATION
C           RHOZ(NNN) = ZEROTH ORDER DENSITY
C           RHO(NNN,NN) = DENSITY
C           UZ(NNN) = ZEROTH ORDER VELOCITY
C           VEL(NNN,NN) = VELOCITY
C           X(NNN) = AXIAL (STREAMWISE) COORDINATE
C           Y(NNN,NN) = HEIGHT MATRIX
C
```

```
C       FUNCTIONS:
C           DPIDX(X) = DERIVATIVE OF THE TOTAL PRESSURE
C           PIFUN(X) = TOTAL PRESSURE (STATIC AND MAGNETIC)
C
C       VARIABLES
C           A = CONSTANT IN FRONT OF SECOND ORDER PHI TERM IN ETA D.E.
C           B = CONSTANT IN FRONT OF FIRST ORDER PHI TERM IN ETA D.E.
C           BOR = ZEROTH ORDER B/RHO
C           BO = MAGNETIC FIELD AT CHANNEL ENTRANCE
C           CM1 = C SUB -1 CONSTANT
C           DBDXAV = AVERAGE VALUE OF DB/DX FOR THE ZEROTH ORDER
C           DPHI = TRANSVERSE STREAM FUNCTION STEP
C           DX = AXIAL STEP IN LENGTH
C           ETASUM = SUMMATION OF THE ETA SERIES
C           FLAG = CONDITIONAL FLAG
C           FLAG2 = CONDITIONAL FLAG
C           G = STREAM FUNCTION AT CATHODE
C           GAMOAV = AXIALLY AVERAGE OF THE ZEROTH ORDER MOMENTUM
C           IMAX = THE VALUE OF III WHEN B AT ANODE GOES NEGATIVE
C           LAMM1 = -1 EIGENVALUE
C           LAMM2 = -2 EIGENVALUE
C           LENGTH = CHANNEL LENGTH
C           M = SLOPE OF THE ENTRANCE PROFILE OF ETA
C           MDOT = MASS FLOW RATE
C           N = TOTAL NUMBER OF TERMS IN THE INFINITE SERIES
C           NN = NUMBER OF TRANSVERSE POINTS
C           NNN = NUMBER OF AXIAL POINTS
C           PHI = TRANSVERSE COORDINATE
C           PIO = THE VALUE OF PI AT THE ENTRANCE
C           PORAV = <(DPI/DX)/RHOZ>
C           R = CONSTANT IN FRONT OF FIRST ORDER PHI TERM IN ETA B.C.
C           RA = ANODE RADIUS
C           RHOUAV = AVERAGE VALUE OF RHOZ*UZ
C           RHOO = DENSITY AT CHANNEL ENTRANCE
C           RM1 = R FOR -1 EIGENVALUE
C           RM2 = R FOR -2 EIGENVALUE
C           RPM1 = R PRIME FOR -1 EIGENVALUE
C           RPM2 = R PRIME FOR -2 EIGENVALUE
C           S = CONSTANT IN FRONT OF FIRST ORDER X TERM IN ETA B.C.
C           SUM = ETA SUM FROM I=1 TO N
C           SUM1 = PSI SUM FROM I=1 TO N
C           SUM2 = ETATNT SUM FROM I=1 TO N
C           SUM3 = ETADNT SUM FROM I=1 TO N
C           T = CONSTANT IN FRONT OF ETA TERM IN ETA B.C.
C           TOTCUR = APPROXIMATE TOTAL CURRENT
C           UO = VELOCITY AT CHANNEL ENTRANCE
C           W = CHANNEL "MIDLINE" CIRCUMFERENCE
C
C     INPUT PARAMETERS
C
```

```
      WRITE(*,*)' INPUT B0, LENGTH, RHO0*10000'
      READ(*,*) B0,LENGTH,RHO0
      WRITE(*,*)
      RHO0 = RHO0/10000.
      N = 10
      NN = 5
      NNN = 21
      BOR = B0/RHO0
      RA = .072
      G=0.01
      X(1) = 0.0
      U0=1500.
      BZ(1) = B0
      RHOZ(1) = RHO0
      UZ(1) = U0
      W = 2.0*(.054+(.072-.054)/2.0)*PI
      PI0 = RHO0*RGAS*TEMP+(B0*B0/(2.0*MU0))
      DX=LENGTH/DBLE(NNN-1)
      RHOUAV=0.0
C
C     CALCULATE THE ZEROTH ORDER SOLUTION
C
      DO 10 I=2,(NNN-1)
         X(I)=X(I-1)+DX
         RHOZ(I) = (DSQRT((RGAS*TEMP)**2 + 4.0*(BOR*BOR)*PIFUN(X(I))/
     &              (2.*MU0)) - (RGAS*TEMP))/(BOR*BOR/MU0)
         UZ(I) = DSQRT((U0*U0) +(2.* RGAS*TEMP*DLOG(RHO0/RHOZ(I))) +
     &            (2.*BOR*BOR*(RHO0-RHOZ(I))/MU0))
         BZ(I) = BOR*RHOZ(I)
         RHOUAV = RHOZ(I)*UZ(I)+RHOUAV
10    CONTINUE
      RHOUAV=RHOUAV/DBLE(NNN-2)
      X(NNN)=LENGTH
C
C     CALCULATE THE COEFFICIENTS IN THE LINEARIZED INDUCTION EQUATION
C     AND IN THE LINEARIZED BOUNDARY CONDITION
C
      C = MI*SIGMA/CHARGE
      PORAV=0.0
      DBDXAV=0.0
      DO 20 I=2,(NNN-1)
      DBDXAV=DBDXAV+(BZ(I+1)-BZ(I-1))/(2.0*DX)
      PORAV=PORAV+DPIDX(X(I))/RHOZ(I)
20    CONTINUE
      PORAV=PORAV/DBLE(NNN-2)
      DBDXAV=DBDXAV/DBLE(NNN-2)
      A = RGAS*TEMP*RHOUAV/(SIGMA*BOR*BOR)
      B = -C*PORAV/(SIGMA*BOR)
      R = MU0*RGAS*TEMP*RHOUAV/BOR
      S = C*MU0*RGAS*TEMP
```

```
      T = -C*BOR*DBDXAV
C
C     CALCULATE THE EIGENVALUES AND SUMMATION SERIES COEFFICIENTS
C
      LAMM1 = (R/(2.*A*S*S))*((B*S-(R+(2.*A*T*S/R)))+DSQRT((B*S-R)**2
     &        + 4.*A*T*S))
      LAMM2 = (R/(2.*A*S*S))*((B*S-(R+(2.*A*T*S/R)))-DSQRT((B*S-R)**2
     &        + 4.*A*T*S))
      TMP1 = B/(2.*A)
      RM1 = - ((S*LAMM1+T)/R)
      RM2 = - ((S*LAMM2+T)/R)
      RPM1 = TMP1 + RM1
      RPM2 = TMP1 + RM2
      TMP2 = 1./(TMP1+RPM2)
      TMP3 = TMP1+RPM1
      M=(TMP2-(A*S/R))/((G*(TMP2-(A*S/R))/2.)-(TMP2*TMP2))
      CM1 = (-2.*RPM1*R/((DEXP(2.*RPM1*G)-1.)*(2.*A*S*RPM1-R))) *
     &      ((M*G*DEXP(TMP3*G)*((1./TMP3)-(A*S/R))) -
     &      (DEXP(TMP3*G)-1.)*(((M*G+2.)/2.)*((1./TMP3)-(A*S/R))+
     &      (M/(TMP3*TMP3))))
      TMP4 = DEXP(B*G/(2.*A))
      DO 30 I=1,NN
30       PSI(1,I) = 0.0
      DO 40 I=1,N
         LAM(I) = (B*B/(4.*A)) + (A*PI*PI*DBLE(I*I)/(G*G))
         KN(I) = (S*LAM(I) + T - (B*R/(2.*A)))/(PI*R*DBLE(I)/G)
         TMP5 = DBLE(I)*PI/G
         TMP6 = 1./(TMP1*TMP1 + TMP5*TMP5)
         AN(I) = TMP6*(((M*B/A)*TMP4*(-1.)**I) +
     &           (2.*M/G)*(TMP4*((-1.)**I)-1.)*(TMP6*(TMP5*TMP5-
     &           TMP1*TMP1) - TMP1*(M*G+2.)/(2.*M)))
         BN(I) = TMP6*TMP5*((((TMP4*(-1.)**I)-1.)*
     &           ((TMP6*2.*M*B/(A*G)) + ((M*G+2.)/G))) -
     &           2.*M*TMP4*(-1.)**I)
         CN(I) = (AN(I) - (KN(I)*BN(I)+(A*S/(R*G))*
     &           (((-1.)**I)*(M*G-2.)*TMP4 + (M*G+2.))))/(1.+KN(I)*KN(I))
40    CONTINUE
C
C     CALCULATE THE PERTURBATION SOLUTIONS
C
      DPHI=G/DBLE(NN-1)
C
C     AXIAL ITERATION
C
      FLAG = .TRUE.
      FLAG2 = .TRUE.
      DO 90 III=1,(NNN-1)
C
C     TRANSVERSE ITERATION
C
```

```
      PHI = 0.0
      DO 80 II=1,NN
         SUM = 0.0
         SUM1 = 0.0
         SUM2 = 0.0
         SUM3 = 0.0
         JX(III,II) = -RGAS*TEMP*CM1*RM1*DEXP(RM1*PHI-LAMM1*X(III))
     &                /BOR
         JY(III,II) = JX(III,II)*LAMM1/RM1
         DO 60 I=1,N
            SUM = SUM + CN(I)*DEXP(-LAM(I)*X(III))*
     &           (DCOS(DBLE(I)*PI*PHI/G) -
     &           KN(I)*DSIN(DBLE(I)*PI*PHI/G))
            SUM1 = SUM1 + (CN(I)/LAM(I))*(DEXP(-LAM(I)*X(III))-1.0)*
     &           (DCOS(DBLE(I)*PI*PHI/G) -
     &           KN(I)*DSIN(DBLE(I)*PI*PHI/G))
            TMP5 = DBLE(I)*PI/G
            TMP6 = TMP1*TMP1 + TMP5*TMP5
            SUM2 = SUM2 + CN(I)*DEXP(-LAM(I)*X(III))*
     &           (DEXP(-TMP1*PHI)*((TMP5*KN(I)-TMP1)*DCOS(TMP5*PHI)
     &           +(TMP1*KN(I)+TMP5)*DSIN(TMP5*PHI)) -
     &           (TMP5*KN(I)-TMP1))/TMP6
            SUM3 = SUM3 + (CN(I)/LAM(I))*(DEXP(-LAM(I)*X(III))-1.0)*
     &           (DEXP(-TMP1*PHI)*((TMP5*KN(I)-TMP1)*DCOS(TMP5*PHI)
     &           +(TMP1*KN(I)+TMP5)*DSIN(TMP5*PHI)) -
     &           (TMP5*KN(I)-TMP1))/TMP6
            JX(III,II) = JX(III,II)+(DEXP(-(TMP1*PHI+LAM(I)*X(III)))*
     &                   CN(I)*( (TMP5-TMP1*KN(I))*DSIN(TMP5*PHI) +
     &                   (TMP5*KN(I)+TMP1)*DCOS(TMP5*PHI)))*
     &                   RGAS*TEMP/BOR
            JY(III,II) = JY(III,II)-(DEXP(-(TMP1*PHI+LAM(I)*X(III)))*
     &                   CN(I)*LAM(I)*(DCOS(DBLE(I)*PI*PHI/G) -
     &                   KN(I)*DSIN(DBLE(I)*PI*PHI/G)))*RGAS*TEMP/BOR
            WRITE(*,50) III,II,I
50          FORMAT('+',3I5)
60       CONTINUE
         ETA(III,II) = 1.0 + DEXP(-B*PHI/(2.*A))*(CM1*
     &                 DEXP(RPM1*PHI-LAMM1*X(III)) + SUM)
         ETAINT(III,II) = X(III) - DEXP(-B*PHI/(2.*A))*((CM1/LAMM1)*
     &                 DEXP(RPM1*PHI)*(DEXP(-LAMM1*X(III))-1.) +
     &                 SUM1)
         ETATNT(III,II) = PHI + (CM1/RM1)*(DEXP(RM1*PHI)-1.)*
     &           DEXP(-LAMM1*X(III)) + SUM2
         ETADNT(III,II) = X(III)*PHI - (  (CM1/(LAMM1*RM1))*
     &                 (DEXP(RM1*PHI)-1.)*(DEXP(-LAMM1*X(III))-1.)
     &                 + SUM3)
         PSI(III,II) = ((UZ(1)/UZ(III))**2)*(PSI(1,II)-ETA(1,II)) +
     &                 ETA(III,II) + (PORAV/(UZ(III)*UZ(III)))*
     &                 ETAINT(III,II)
         BFIELD(III,II) = BZ(III)-(RGAS*TEMP*MU0/BOR)*ETA(III,II)
```

```
            IF((II.EQ.NN).AND.(BFIELD(III,II).LT.0.0).AND.FLAG) THEN
               FLAG = .FALSE.
               WRITE(*,70) BFIELD(III,II),X(III)
70             FORMAT(' B GOES TO ',D12.5,' AT X = ',D12.5)
               WRITE(*,*)
            ENDIF
            IF((II.EQ.1).AND.(BFIELD(III,II).LT.0.0).AND.FLAG2) THEN
               IMAX = III-1
               FLAG2 = .FALSE.
            ENDIF
            RHO(III,II) = RHOZ(III)*(1.+ETA(III,II))
            BORHO(III,II) = BFIELD(III,II)/RHO(III,II)
            HALL(III,II) = C*BORHO(III,II)
            MOM(III,II) = (RHOZ(III)*UZ(III))*(1.0+PSI(III,II))
            VEL(III,II) = MOM(III,II)/RHO(III,II)
            JX(III,II) = RHOZ(III)*UZ(III)*JX(III,II)
            JY(III,II) = JY(III,II) - DPIDX(X(III))/BZ(III)
            JTOTAL(III,II) = DSQRT(JX(III,II)**2+JY(III,II)**2)
            Y(III,II) = (PHI-((ETATNT(III,II)-(UZ(1)/UZ(III))**2*M*PHI*
     &                  0.5*(PHI-G))+PORAV*ETADNT(III,II)/UZ(III)**2))/
     &                  (RHOZ(III)*UZ(III))
            ARG(III,II) = DATAN(JY(III,II)/JX(III,II))*180./PI
            IF ((JY(III,II).GT.0.).AND.(JX(III,II).LT.0.0))
     &         ARG(III,II) = ARG(III,II) + 180.
            IF ((JY(III,II).LT.0.).AND.(JX(III,II).LT.0.0))
     &         ARG(III,II) = ARG(III,II) - 180.
            PHI = PHI+DPHI
80       CONTINUE
       H(III) = (G - (ETATNT(III,NN) + PORAV*ETADNT(III,NN)/UZ(III)**2))/
     &          (RHOZ(III)*UZ(III))
90     CONTINUE
C
C      CALCULATE APPROXIMATE OVERALL PARAMETERS
C
       TOTCUR=0.0
       DO 100 I=2,IMAX-1
100       TOTCUR = 2.0*JTOTAL(I,1)+TOTCUR
       TOTCUR = RA*PI*(TOTCUR+JTOTAL(1,1)+JTOTAL((IMAX-1),1))*DX
       WRITE(*,110) TOTCUR
110    FORMAT(' TOTCUR = ',D12.5,' AMPS')
       MDOT = W*RHOZ(1)*UZ(1)*H(1)
       WRITE(*,120) MDOT
120    FORMAT(' MDOT = ',D12.5,' KG/SEC')
C
C      WRITE DATA TO FILES
C
       GOTO 185
       WRITE(1000,130) B0
130    FORMAT(' B0 = ',F12.5)
       WRITE(1000,140) LENGTH
```

```
140   FORMAT(' SCALE LENGTH = ',F12.5)
      WRITE(1000,150) G
150   FORMAT(' G = ',F12.5)
      WRITE(1000,160) X(IMAX-1)
160   FORMAT(' THRUSTER LENGTH = ',F12.5)
      WRITE(1000,170) MDOT
170   FORMAT(' MDOT = ',F12.5)
      WRITE(1000,180) TOTCUR
180   FORMAT(' TOTAL CURRENT = ',F12.5)
185   DO 200 I=1,(NNN-1)
         DO 190 J=1,NN,5
            WRITE(1100,210) BFIELD(I,J),BFIELD(I,J+1),BFIELD(I,J+2),
     &                      BFIELD(I,J+3),BFIELD(I,J+4)
            WRITE(1200,210) RHO(I,J),RHO(I,J+1),RHO(I,J+2),RHO(I,J+3),
     &                      RHO(I,J+4)
            WRITE(1300,210) VEL(I,J),VEL(I,J+1),VEL(I,J+2),VEL(I,J+3),
     &                      VEL(I,J+4)
            WRITE(1400,210) JX(I,J),JX(I,J+1),JX(I,J+2),JX(I,J+3),
     &                      JX(I,J+4)
            WRITE(1500,210) JY(I,J),JY(I,J+1),JY(I,J+2),JY(I,J+3),
     &                      JY(I,J+4)
            WRITE(1600,210) JTOTAL(I,J),JTOTAL(I,J+1),JTOTAL(I,J+2),
     &                      JTOTAL(I,J+3),JTOTAL(I,J+4)
C            WRITE(1700,210) BORHO(I,J),BORHO(I,J+1),BORHO(I,J+2),
C     &                      BORHO(I,J+3),BORHO(I,J+4)
            WRITE(1700,210) HALL(I,J),HALL(I,J+1),HALL(I,J+2),
     &                      HALL(I,J+3),HALL(I,J+4)
            WRITE(1900,210) ETA(I,J),ETA(I,J+1),ETA(I,J+2),ETA(I,J+3),
     &                      ETA(I,J+4)
            WRITE(2000,210) PSI(I,J),PSI(I,J+1),PSI(I,J+2),PSI(I,J+3),
     &                      PSI(I,J+4)
            WRITE(2100,210) Y(I,J),Y(I,J+1),Y(I,J+2),Y(I,J+3),Y(I,J+4)
C            WRITE(2200,210) ARG(I,J),ARG(I,J+1),ARG(I,J+2),ARG(I,J+3),
C     &                      ARG(I,J+4)
            WRITE(2200,210) MOM(I,J),MOM(I,J+1),MOM(I,J+2),MOM(I,J+3),
     &                      MOM(I,J+4)
190         CONTINUE
         WRITE(1800,220) X(I),H(I)
200   CONTINUE
210   FORMAT(5D12.5)
220   FORMAT(2F12.5)
      END

      DOUBLE PRECISION FUNCTION PIFUN(X)
      DOUBLE PRECISION LENGTH,PI0,X
      COMMON/VARS/LENGTH,PI0
      PIFUN = PI0*(1.-X/LENGTH)**2
      RETURN
      END
```

```
      DOUBLE PRECISION FUNCTION DPIDX(X)
      DOUBLE PRECISION LENGTH,PIO,X
      COMMON/VARS/LENGTH,PIO
      DPIDX = -2.0*PIO*(1.-X/LENGTH)/LENGTH
      RETURN
      END
```

A11.4: FORTRAN Code for the L-C Ladder Triggered by a Single Ignitron

This code models the L-C ladder network triggered by a single Ignitron, Ignitron #1, as detailed in Chapter III and in Appendix 5.

```
$DEBUG
$NOFLOATCALLS
$LARGE
      PROGRAM LCBANK
      IMPLICIT DOUBLE PRECISION (A-H,O-Z)
      DOUBLE PRECISION L,LP,LPNON
      LOGICAL FLAG
      DIMENSION A(8,8),Y(16),RESULT(17,501),VOLT(8,501)
      COMMON/RESIST/RES,RL,L,LP,C
      COMMON/VOLTS/VCHARG,CAP,VOLT,PIND,FLAG
C
C     OPEN OUTPUT FILES
C
      OPEN(2000,FILE='XARR.TXT',STATUS='NEW')
      OPEN(3000,FILE='YARR.TXT',STATUS='NEW')
      OPEN(4000,FILE='V1.TXT',STATUS='NEW')
      OPEN(5000,FILE='V2.TXT',STATUS='NEW')
      OPEN(6000,FILE='V3.TXT',STATUS='NEW')
      OPEN(7000,FILE='V4.TXT',STATUS='NEW')
      OPEN(8000,FILE='V5.TXT',STATUS='NEW')
      OPEN(9000,FILE='V6.TXT',STATUS='NEW')
      OPEN(9200,FILE='V7.TXT',STATUS='NEW')
      OPEN(9400,FILE='V8.TXT',STATUS='NEW')
C
C     THIS PROGRAM CALCULATES THE RESPONSE OF AN L-C LADDER POWER
C     SUPPLY INCLUDING EFFECTS OF PARASITIC INDUCTANCE AND RESISTANCE
C
C     REVISED 7/28/86 BY DJH
C     REVISED 2/13/86 BY DJH
C
      C=2.5D-4
      CAP=C
      WRITE(*,*)'INPUT INDUCTANCE IN uH'
```

```
      READ(*,*) L
      L=L*1.D-6
      WRITE(*,*)'INPUT PARASITIC INDUCTANCE IN uH'
      READ(*,*) LP
      LP=LP*1.D-6
      PIND=LP
      WRITE(*,*)'INPUT PARASITIC RESISTANCE IN OHMS'
      READ(*,*) RES
      WRITE(*,*)'INPUT LOAD RESISTANCE IN OHMS (INPUT 100. FOR MATCHED)'
      READ(*,*) RL
      IF (DABS((RL/100.)-1.).LT.0.01) RL=DSQRT(L/C)
      LPNON=LP/(L+2.*LP)
      WRITE(*,*) ' INPUT CHARGING VOLTAGE'
      READ(*,*) VCHARG
      WRITE(*,*) ' INPUT NUMBER OF TIME STEPS'
      READ(*,*) NDIVS
      WRITE(*,*) ' INPUT FINAL TEST TIME'
      READ(*,*) XF
      WRITE(*,*)' OUTPUT CAP. VOLTAGE (1) OR CAP. + PARASITIC INDUCTOR
     &VOLTAGE (2)'
      READ(*,*) IFLAG
      IF(IFLAG.EQ.1) THEN
        FLAG=.FALSE.
      ELSE
        FLAG=.TRUE.
      ENDIF
C
C     CREATE AN "A" MATRIX FOR THE STATE EQUATION:
C          A * IDOUBLEDOT = F(I,IDOT)
C
      DO 10 I=1,8
      DO 20 J=1,8
20       A(I,J)=0.0
10    CONTINUE
      DO 30 I=1,8
30    A(I,I)=1.0
      DO 40 I=2,7
        A(I,I+1)=-LPNON
        A(I,I-1)=-LPNON
40    CONTINUE
      A(1,2)=-LPNON
      A(8,7)=-LP/(2.*L+LP)
C
C     CALL MATRIX INVERSION ROUTINE TO DO AN IN PLACE MATRIX
C     INVERSION OF A
C
      ZTOL=1.0D-8
      NA=8
      CALL MATINV(NA,A,ZTOL)
      X0=0.0
```

```
      NEQ=16
C
C     CREATE PROPER INPUTS FOR SUBROUTINE RKSYS
C
      NEQP1=17
      NDIVP1=NDIVS+1
      DO 21 I=1,15
        Y(I)=0.0
21    CONTINUE
      Y(16)= VCHARG/(2.*L+LP)
      CALL RKSYS(A,NEQ,NEQP1,NDIVS,NDIVP1,X0,XF,Y,RESULT,ZTOL)
      DO 50 I=1,NDIVP1
C
C     WRITE DATA TO FILES
C
      WRITE(2000,62)RESULT(1,I)
      WRITE(3000,62)RESULT(9,I)
      WRITE(4000,62)VOLT(1,I)
      WRITE(5000,62)VOLT(2,I)
      WRITE(6000,62)VOLT(3,I)
      WRITE(7000,62)VOLT(4,I)
      WRITE(8000,62)VOLT(5,I)
      WRITE(9000,62)VOLT(6,I)
      WRITE(9200,62)VOLT(7,I)
      WRITE(9400,62)VOLT(8,I)
60    FORMAT(2D12.5)
62    FORMAT(D12.5,',')
50    CONTINUE
      END

      SUBROUTINE RKSYS(A,NEQ,NEQP1,NDIVS,NDIVP1,X0,XF,Y,RESULT,ZTOL)
      IMPLICIT DOUBLE PRECISION(A-H,O-Z)
      DOUBLE PRECISION LP
      LOGICAL FLAG
      DIMENSION A(8,8),Y(16),Y0(16),YP(16),DYP(16),RKTEMP(3,16),
     &          RESULT(17,501),CURR(8),VC(8),VOLT(8,501)
      COMMON/VOLTS/VCHARG,C,VOLT,LP,FLAG
C
C     THIS SUBROUTINE INTEGRATES A SET OF FIRST ORDER DIFFERENTIAL
C     EQUATIONS WRITTEN IN MATRIX-STATE VARIABLE FORM
C
C                              XDOT = A*X
C
C     THIS SUBROUTINE DOES A FIXED STEP FOURTH ORDER RUNGE KUTTA
C     ANALYSIS ON A SYSTEM OF FIRST ORDER ORDINARY DIFFERENTIAL
C     EQUATIONS.
C
C     NEQ --------- NUMBER OF ROWS AND COLUMNS  OF  A  (NUMBER  OF  FIRST
ORDER
C                   DIFFERENTIAL EQUATIONS)
```

```
C     NEQP1 ------ NUMBER OF FIRST ORDER DIFFERENTIAL EQUATIONS + 1
C       A ---------- DIFFERENTIAL EQUATION STATE COEFFICIENT MATRIX (NEQ
BY
C                  NEQ)
C     NDIVS ------ NUMBER OF POINTS TO BE STORED **** THE NUMBER OF
C                  ITERATION STEPS IS GOVERNED BY NEND WHICH IS A SIMPLE
C                  CONSTANT MULTIPLIED BY NDIVS ****
C     NDIVP1 ----- NUMBER OF POINTS TO BE STORED + 1
C     X0 --------- INDEPENDENT VARIABLE STARTING POINT
C     XF --------- INDEPENDENT VARIABLE END POINT
C     Y ---------- VECTOR OF DEPENDENT VARIABLES, LENGTH NEQ
C     RESULT ----- RESULT ARRAY; NEQ+1 ROWS, NDIVS+1 COLUMNS
C                  THE FIRST ROW IS THE INDEPENDENT VARIABLE
C                  SUBSEQUENT ROWS ARE THE DEPENDENT VARIABLES
C     ZTOL ------- TEST FOR ZERO EQUIVALENCE
C
C     IN THE FOLLOWING PROGRAM, CURR, VOLT, AND VC, AND FLAG ARE
C     APPLICATION SPECIFIC AS IS THE COMMON BLOCK /VOLTS/.  THE VOLTAGE
C     EITHER ACROSS CAPACITORS (IF FLAG=FALSE) OR ACROSS THE CAPACITORS
C     AND PARASITIC INDUCTORS (FLAG=TRUE).
C
C     REVISED 7/26/86 BY DJH
C
C     ERROR TRAPPING
C
      IF (NDIVS.LE.0) THEN
         WRITE(*,1)
         RETURN
      ENDIF
      IF (NDIVS.NE.NDIVP1-1) THEN
         WRITE(*,2)
         RETURN
      ENDIF
      IF (NEQ.NE.NEQP1-1) THEN
         WRITE(*,3)
         RETURN
      ENDIF
      IF (DABS(X0-XF).LT.ZTOL) THEN
         WRITE(*,5)
         WRITE(*,6)
         RETURN
      ENDIF
      WRITE(*,7)
C
C     BEGIN PROGRAM
C
C     INITIALIZE VARIABLES AND ARRAYS
C
      NEND=NDIVS
      DELX = (XF-X0)/DBLE(NEND)
```

```
      WRITE(*,*) ' DELX = ',DELX
      WRITE(*,*)
      RESULT(1,1) = XO
      II=1
      DO 11 L=1,NEQ
         RESULT(L+1,1) = Y(L)
         YP(L)=0.0
   11 CONTINUE
C
C     APPLICATION SPECIFIC ADDITION TO CALCULATE INTERMEDIATE VOLTAGE
C
      DO 122 I=1,8
      VC(I)=VCHARG
      VOLT(I,1)=VCHARG
      CURR(I)=Y(I)
  122 CONTINUE
C
C     END APPLICATION SPECIFIC ADDITION
C
      DO 90 I=1,NEND
C
C     FIRST RUNGE-KUTTA STEP
C
         DO 20 J=1,NEQ
   20       YO(J) = Y(J)
         CALL RKSVAL(NEQ,A,X,YO,YP)
         DO 25 J=1,NEQ
            RKTEMP(1,J) = YP(J)
   25    CONTINUE
C
C        SECOND AND THIRD RUNGE-KUTTA STEPS
C
         X = XO + DELX/2.0
         DO 50 K=2,3
            DO 30 J=1,NEQ
   30          Y(J) = YO(J) + DELX*RKTEMP(K-1,J)/2.0
            CALL RKSVAL(NEQ,A,X,Y,YP)
            DO 40 J=1,NEQ
   40          RKTEMP(K,J) = YP(J)
   50    CONTINUE
C
C        FOURTH RUNGE-KUTTA STEP
C
         X = XO+DELX
         DO 60 J=1,NEQ
   60       Y(J) = YO(J) + DELX*RKTEMP(3,J)
         CALL RKSVAL(NEQ,A,X,Y,YP)
         DO 70 J=1,NEQ
            Y(J) = YO(J) + DELX*(RKTEMP(1,J)+YP(J)+2.0*
     &              (RKTEMP(2,J)+RKTEMP(3,J)))/6.0
```

```
 70      CONTINUE
C
C        APPLICATION SPECIFIC FUNCTION TO CALCULATE THE
C        VOLTAGE THROUGH A TRAPEZOIDAL INTEGRATION METHOD.
C        THIS REQUIRES STORAGE OF THE PREVIOUS VALUES OF THE
C        CURRENT IN VECTOR CURR.
C
         IF(I.NE.1) THEN
            DO 76 J=1,8
            IF (J.EQ.1) THEN
              VC(J)=VC(J)-DELX*(CURR(J)+Y(J))/(2.*C)
            ELSE
              VC(J)=VC(J)-DELX*((CURR(J)-CURR(J-1))+(Y(J)-Y(J-1)))/
     &              (2.*C)
            ENDIF
76          CONTINUE
         ENDIF
         DO 77 J=1,8
77          CURR(J)=Y(J)
C
C        END OF THE APPLICATION SPECIFIC SECTION
C
C        FILL UP RESULT ARRAYS
C
C        THE MOD STATEMENT IS NECESSARY IF NDIVS IS NOT EQUAL TO NEND
C
         IF(MOD(I,1).EQ.0) THEN
            II=II+1
            RESULT(1,(II+1)) = X
            DO 80 L=1,NEQ
               RESULT((L+1),(II+1)) = Y(L)
               IF (FLAG) THEN
                  IF(L.EQ.1) THEN
                     VOLT(1,(II+1))=VC(L)+LP*Y(L+8)
                  ELSE
                     VOLT(L,(II+1))=VC(L)+LP*(Y(L+8)-Y(L+7))
                  ENDIF
               ELSE
                  VOLT(L,(II+1))=VC(L)
               ENDIF
80          CONTINUE
         ENDIF
         XO = X
C
C        COUNTER TO SHOW ITERATION
C
         IF(MOD(I,100).EQ.0) THEN
            WRITE(*,8) I
         ENDIF
 90   CONTINUE
```

```
C
C     ERROR MESSAGES
C
    1  FORMAT(' *** ERROR: NUMBER OF DIVISIONS IS NOT GREATER THAN 0 ***
     & ')
    2  FORMAT(' **** ERROR: NDIVS IS NOT ONE LESS THAN NDIVP1 ****')
    3  FORMAT(' NEQ IS NOT ONE LESS THAN NEQP1')
    5  FORMAT(' **** ERROR: START AND END POINTS (X0 AND XF) ARE THE SAME
     & GIVEN ****')
    6  FORMAT(' ****
     & ZTOL  ****')
    7  FORMAT('    ')
    8  FORMAT('+BE PATIENT, FORTRAN PROGRAM IS RUNNING  ',I5)
       RETURN
       END

       SUBROUTINE RKSVAL(NEQ,A,X,Y,YP)
       IMPLICIT DOUBLE PRECISION(A-H,O-Z)
       DOUBLE PRECISION L,LP,LCON
       DIMENSION A(8,8),Y(16),YP(16),BVEC(8)
       COMMON/RESIST/R,RL,L,LP,C
C
C     THIS SUBROUTINE CALCULATES THE VALUES OF THE DERIVATIVE MATRIX,
C     YP, IN THE MATRIX STATE EQUATION
C
C                              YP = A*Y
C
C     NEQ ------ NUMBER OF ROWS IN A AND B AND NUMBER OF COLUMNS IN A
C     A ------- COEFFICIENT MATRIX OF THE DIFFERENTIAL EQUATIONS
C     X ------- INDEPENDENT VARIABLE
C     Y ------- VECTOR OF DEPENDENT VARIABLES (LENGTH NEQ)
C     YP ------ VECTOR OF DERIVATIVES (LENGTH NEQ)
C
       LCON=L+2.*LP
       DO 1 I=1,8
1        YP(I)=Y(I+8)
       BVEC(1)=((Y(2)/C)-((2.*Y(1)/C)+R*YP(1)))/LCON
       BVEC(8)=((Y(7)/C)-((Y(8)/C)+(2.*R+RL)*YP(8)))/(LP+2.*L)
       DO 5 I=2,7
5         BVEC(I)=((Y(I-1)/C)+(Y(I+1)/C)-((2.*Y(I)/C)+
     &           (R*YP(I))))/(L+2.*LP)
       DO 10 I=9,16
10        YP(I) = 0.0
       DO 30 I=1,8
       DO 20 J=1,8
20        YP(8+I)=YP(8+I)+A(I,J)*BVEC(J)
30     CONTINUE
       RETURN
       END
```

```
      SUBROUTINE MATINV(N,A,ZTOL)
      IMPLICIT DOUBLE PRECISION (A-H,O-Z)
      DIMENSION A(8,8),MR(8),MC(8)
C
C     SUBROUTINE MATINV FINDS THE MATRIX INVERSE OF A
C     NON-SINGULAR 2-D MATRIX OF X AND Y VALUES
C
C     N--------NUMBER OF ROWS OR COLUMNS IN MATRIX
C     ARRAY---MATRIX WHERE INITIAL VALUES ARE ENTERED AND ANSWER IS
C             RETURNED
C     ZTOL----TOLERANCE FOR QUANTITY ZERO
C
C     REVISED 7/26/86 BY DJH
C
      DO 100 I=1,N
         MR(I) = I
         MC(I) = I
100   CONTINUE
C
C     FIND THE FIRST PIVOT
C
      MPIVI = 1
      MPIVJ = 1
      DO 200 I=1,N
         DO 300 J=1,N
            IF (DABS(A(I,J)).GT.DABS(A(MPIVI,MPIVJ))) THEN
               MPIVI = I
               MPIVJ = J
            ENDIF
300      CONTINUE
200   CONTINUE
C
C     BEGIN MATRIX INVERSION
C
      DO 400 I=1,N
         L = MR(I)
         MR(I) = MR(MPIVI)
         MR(MPIVI) = L
         L = MC(I)
         MC(I) = MC(MPIVJ)
         MC(MPIVJ) = L
C
C     CHECK THAT THE PIVOT IS NOT ZERO
C
         IF(DABS(A(MR(I),MC(I))).LT.ZTOL)THEN
            WRITE(*,1000)
            RETURN
         ENDIF
C
         DO 500 J=N,1,-1
```

```
            IF(I.NE.J)THEN
               A(MR(I),MC(J)) = A(MR(I),MC(J))/A(MR(I),MC(I))
            ENDIF
500       CONTINUE
          PIVOT = 0.0
          A(MR(I),MC(I)) = 1.0/A(MR(I),MC(I))
          DO 600 K=1,N
             IF(I.NE.K)THEN
                DO 700 J=N,1,-1
                   IF(I.NE.J)THEN
                      A(MR(K),MC(J)) =  A(MR(K),MC(J))-A(MR(I),MC(J))*
     &                                  A(MR(K),MC(I))
                      IF (K.GT.I.AND.J.GT.I.AND.DABS(A(MR(K),MC(J)))
     &                   .GE.DABS(PIVOT)) THEN
                         MPIVI = K
                         MPIVJ = J
                         PIVOT = A(MR(K),MC(J))
                      ENDIF
                   ENDIF
700             CONTINUE
                A(MR(K),MC(I)) = -1.0*A(MR(I),MC(I))*A(MR(K),MC(I))
             ENDIF
600       CONTINUE
400    CONTINUE
C
C      REARRANGE THE ROWS THEN THE COLUMNS TO THEIR PROPER ORDER
C
       CALL PERMUT(A,MR,MC,N,1)
       CALL PERMUT(A,MC,MR,N,0)
C
C      ERROR MESSAGES
C
1000   FORMAT(' THE MATRIX IS SINGULAR, A ZERO PIVOT WAS FOUND')
       RETURN
       END

       SUBROUTINE PERMUT(ARRAY,MS,MD,N,NCHNG)
       IMPLICIT DOUBLE PRECISION(A-H,O-Z)
       DIMENSION ARRAY(N,N),MS(N),MD(N),NTAG(8),LOC(8)
C
C      SUBROUTINE PERMUT PERMUTES A MATRIX ACCORDING TO THE PERMUTATION
C      VECTORS CONTAINED IS MS AND MD
C
C      ARRAY---THE MATRIX TO BE PERMUTED, SERVES AS INPUT AND OUTPUT
C      MS------SOURCE LOCATION FOR ARRAY ELEMENT
C      MD------DESTINATION LOCATION FOR ARRAY ELEMENT
C      N-------NUMBER OF ROWS OR COLUMNS IN MATRIX
C      NCHNG---WHEN NCHNG IS 1 THE ROWS ARE REARRANGED, ELSE THE COLUMNS
C              ARE REARRANGED
C
```

```
      DO 100 I=1,N
         NTAG(I) = I
         LOC(I) = I
100   CONTINUE
      DO 200 I=1,N
         M = MS(I)
            J = LOC(M)
            K = MD(I)
            IF(J.NE.K)THEN
               DO 300 NP=1,N
                  IF(NCHNG.EQ.1)THEN
                     W = ARRAY(J,NP)
                     ARRAY(J,NP) = ARRAY(K,NP)
                     ARRAY(K,NP) = W
                  ELSE
                     W = ARRAY(NP,J)
                     ARRAY(NP,J) = ARRAY(NP,K)
                     ARRAY(NP,K) = W
                  ENDIF
300            CONTINUE
               NTAG(J) = NTAG(K)
               NTAG(K) = M
               LOC(M) = LOC(NTAG(J))
               LOC(NTAG(J)) = J
         ENDIF
200   CONTINUE
      RETURN
      END
```

A11.5: FORTRAN Code for the L-C Ladder Triggered by Two Ignitrons

The following is the source code for the L-C ladder network triggered by Ignitrons #1 and #8 as detailed in Chapter III and Appendix 6.

```
$DEBUG
$LARGE
      PROGRAM SHORT
      IMPLICIT DOUBLE PRECISION (A-H,O-Z)
      DOUBLE PRECISION L,LP,LPNON,LF
      LOGICAL FLAG
      DIMENSION A(8,8),Y(16),RESULT(17,501),VOLT(8,501)
      COMMON/RESIST/RES,RL,L,LP,C,LF
      COMMON/VOLTS/VCHARG,CAP,VOLT,PIND,FLAG
C
C     OPEN OUTPUT FILES
```

```
C
      OPEN(2000,FILE='XARR.TXT',STATUS='NEW')
      OPEN(3000,FILE='YARR.TXT',STATUS='NEW')
      OPEN(4000,FILE='V1.TXT',STATUS='NEW')
      OPEN(5000,FILE='V2.TXT',STATUS='NEW')
      OPEN(6000,FILE='V3.TXT',STATUS='NEW')
      OPEN(7000,FILE='V4.TXT',STATUS='NEW')
      OPEN(8000,FILE='V5.TXT',STATUS='NEW')
      OPEN(9000,FILE='V6.TXT',STATUS='NEW')
      OPEN(9200,FILE='V7.TXT',STATUS='NEW')
      OPEN(9400,FILE='V8.TXT',STATUS='NEW')
C
C     THIS PROGRAM CALCULATES THE RESPONSE OF AN L-C LADDER POWER
C     SUPPLY INCLUDING EFFECTS OF PARASITIC INDUCTANCE AND RESISTANCE.
C     THIS VERSION CALCULATES THE WAVEFORM FOR A FOUR STAGE LADDER
C     ARRANGEMENT WITH A FINAL INDUCTOR EQUAL TO ALL THE INTERMEDIATE
C     INDUCTORS
C
C     REVISED 2/18/87 BY DJH
C
      C=2.5D-4
      CAP=C
      WRITE(*,*)'INPUT INDUCTANCE, FINAL INDUCTANCE IN uH'
      READ(*,*) L,LF
      L=L*1.D-6
      LF=LF*1.D-6
      WRITE(*,*)'INPUT PARASITIC INDUCTANCE IN uH'
      READ(*,*) LP
      LP=LP*1.D-6
      PIND=LP
      WRITE(*,*)'INPUT PARASITIC RESISTANCE IN OHMS'
      READ(*,*) RES
      WRITE(*,*)'INPUT LOAD RESISTANCE IN OHMS (INPUT 100. FOR MATCHED)'
      READ(*,*) RL
      IF (DABS((RL/100.)-1.).LT.0.01) RL=DSQRT((L)/C)
      LPNON=LP/(L+2.*LP)
      WRITE(*,*) ' INPUT CHARGING VOLTAGE'
      READ(*,*) VCHARG
      WRITE(*,*) ' INPUT NUMBER OF TIME STEPS'
      READ(*,*) NDIVS
      WRITE(*,*) ' INPUT FINAL TEST TIME'
      READ(*,*) XF
      WRITE(*,*)' OUTPUT CAP. VOLTAGE (1) OR CAP. + PARASITIC INDUCTOR
     &VOLTAGE (2)'
      READ(*,*) IFLAG
      IF(IFLAG.EQ.1) THEN
        FLAG=.FALSE.
      ELSE
        FLAG=.TRUE.
      ENDIF
```

```
C
C     CREATE AN "A" MATRIX FOR THE STATE EQUATION:
C          A * IDOUBLEDOT = F(I,IDOT)
C
      DO 10 I=1,8
      DO 20 J=1,8
20       A(I,J)=0.0
10    CONTINUE
      DO 30 I=1,8
30    A(I,I)=1.0
      DO 40 I=2,7
        A(I,I+1)=-LPNON
        A(I,I-1)=-LPNON
40    CONTINUE
      A(1,2)=-LP/(LF+LP)
      A(1,8)=-LF/(LF+LP)
      A(4,5)=0.
      A(5,4)=0.
      A(8,1)=-LF/(LF+LP)
      A(8,7)=-LP/(LF+LP)
C
C     CALL MATRIX INVERSION ROUTINE TO DO AN IN PLACE MATRIX
C     INVERSION OF A
C
      ZTOL=1.0D-8
      NA=8
      CALL MATINV(NA,A,ZTOL)
      X0=0.0
      NEQ=16
C
C     CREATE PROPER INPUTS FOR SUBROUTINE RKSYS
C
      NEQP1=17
      NDIVP1=NDIVS+1
      DO 21 I=1,16
        Y(I)=0.0
21    CONTINUE
      Y(9)= -VCHARG/(2.*LF+LP)
      Y(16)= VCHARG/(2.*LF+LP)
      CALL RKSYS(A,NEQ,NEQP1,NDIVS,NDIVP1,X0,XF,Y,RESULT,ZTOL)
      DO 50 I=1,NDIVP1
C
C     WRITE DATA TO FILES
C
      WRITE(2000,62)RESULT(1,I)
      TEMP=RESULT(9,I)-RESULT(2,I)
      WRITE(3000,62)TEMP
      WRITE(4000,62)VOLT(1,I)
      WRITE(5000,62)VOLT(2,I)
      WRITE(6000,62)VOLT(3,I)
```

```
      WRITE(7000,62)VOLT(4,I)
      WRITE(8000,62)VOLT(5,I)
      WRITE(9000,62)VOLT(6,I)
      WRITE(9200,62)VOLT(7,I)
      WRITE(9400,62)VOLT(8,I)
60    FORMAT(2D12.5)
62    FORMAT(D12.5,',')
50    CONTINUE
      END

      SUBROUTINE RKSYS(A,NEQ,NEQP1,NDIVS,NDIVP1,X0,XF,Y,RESULT,ZTOL)
      IMPLICIT DOUBLE PRECISION(A-H,O-Z)
      DOUBLE PRECISION LP
      LOGICAL FLAG
      DIMENSION A(8,8),Y(16),Y0(16),YP(16),DYP(16),RKTEMP(3,16),
     &          RESULT(17,501),CURR(8),VC(8),VOLT(8,501)
      COMMON/VOLTS/VCHARG,C,VOLT,LP,FLAG
C
C     THIS SUBROUTINE INTEGRATES A SET OF FIRST ORDER DIFFERENTIAL
C     EQUATIONS WRITTEN IN MATRIX-STATE VARIABLE FORM
C
C                              XDOT = A*X
C
C     THIS SUBROUTINE DOES A FIXED STEP FOURTH ORDER RUNGE KUTTA
C     ANALYSIS ON A SYSTEM OF FIRST ORDER ORDINARY DIFFERENTIAL
C     EQUATIONS.
C
C     NEQ -------- NUMBER OF ROWS AND COLUMNS  OF  A  (NUMBER  OF  FIRST
ORDER
C                  DIFFERENTIAL EQUATIONS)
C     NEQP1 ------ NUMBER OF FIRST ORDER DIFFERENTIAL EQUATIONS + 1
C       A ---------- DIFFERENTIAL EQUATION STATE COEFFICIENT MATRIX (NEQ
BY
C                  NEQ)
C     NDIVS ------ NUMBER OF POINTS TO BE STORED **** THE NUMBER OF
C                  ITERATION STEPS IS GOVERNED BY NEND WHICH IS A SIMPLE
C                  CONSTANT MULTIPLIED BY NDIVS ****
C     NDIVP1 ----- NUMBER OF POINTS TO BE STORED + 1
C     X0 --------- INDEPENDENT VARIABLE STARTING POINT
C     XF --------- INDEPENDENT VARIABLE END POINT
C     Y ---------- VECTOR OF DEPENDENT VARIABLES, LENGTH NEQ
C     RESULT ----- RESULT ARRAY; NEQ+1 ROWS, NDIVS+1 COLUMNS
C                  THE FIRST ROW IS THE INDEPENDENT VARIABLE
C                  SUBSEQUENT ROWS ARE THE DEPENDENT VARIABLES
C     ZTOL ------- TEST FOR ZERO EQUIVALENCE
C
C     IN THE FOLLOWING PROGRAM, CURR, VOLT, AND VC, AND FLAG ARE
C     APPLICATION SPECIFIC AS IS THE COMMON BLOCK /VOLTS/.  THE VOLTAGE
C     EITHER ACROSS CAPACITORS (IF FLAG=FALSE) OR ACROSS THE CAPACITORS
C     AND PARASITIC INDUCTORS (FLAG=TRUE).
```

```
C
C     REVISED 8/25/87 BY DJH
C
C     ERROR TRAPPING
C
      IF (NDIVS.LE.0) THEN
         WRITE(*,1)
         RETURN
      ENDIF
      IF (NDIVS.NE.NDIVP1-1) THEN
         WRITE(*,2)
         RETURN
      ENDIF
      IF (NEQ.NE.NEQP1-1) THEN
         WRITE(*,3)
         RETURN
      ENDIF
      IF (DABS(X0-XF).LT.ZTOL) THEN
         WRITE(*,5)
         WRITE(*,6)
         RETURN
      ENDIF
      WRITE(*,7)
C
C     BEGIN PROGRAM
C
C     INITIALIZE VARIABLES AND ARRAYS
C
      NEND=NDIVS
      DELX = (XF-X0)/DBLE(NEND)
      WRITE(*,*) ' DELX = ',DELX
      WRITE(*,*)
      RESULT(1,1) = X0
      II=1
      DO 11 L=1,NEQ
         RESULT(L+1,1) = Y(L)
         YP(L)=0.0
  11  CONTINUE
C
C     APPLICATION SPECIFIC ADDITION TO CALCULATE INTERMEDIATE VOLTAGE
C
      DO 122 I=1,8
      VC(I)=VCHARG
      VOLT(I,1)=VCHARG
      CURR(I)=Y(I)
122   CONTINUE
C
C     END APPLICATION SPECIFIC ADDITION
C
      DO 90 I=1,NEND
```

```
C
C     FIRST RUNGE-KUTTA STEP
C
          DO 20 J=1,NEQ
  20         YO(J) = Y(J)
          CALL RKSVAL(NEQ,A,X,YO,YP)
          DO 25 J=1,NEQ
             RKTEMP(1,J) = YP(J)
  25      CONTINUE
C
C         SECOND AND THIRD RUNGE-KUTTA STEPS
C
          X = XO + DELX/2.0
          DO 50 K=2,3
             DO 30 J=1,NEQ
  30            Y(J) = YO(J) + DELX*RKTEMP(K-1,J)/2.0
             CALL RKSVAL(NEQ,A,X,Y,YP)
             DO 40 J=1,NEQ
  40            RKTEMP(K,J) = YP(J)
  50      CONTINUE
C
C         FOURTH RUNGE-KUTTA STEP
C
          X = XO+DELX
          DO 60 J=1,NEQ
  60         Y(J) = YO(J) + DELX*RKTEMP(3,J)
          CALL RKSVAL(NEQ,A,X,Y,YP)
          DO 70 J=1,NEQ
             Y(J) = YO(J) + DELX*(RKTEMP(1,J)+YP(J)+2.0*
     &               (RKTEMP(2,J)+RKTEMP(3,J)))/6.0
  70      CONTINUE
C
C         APPLICATION SPECIFIC FUNCTION TO CALCULATE THE
C         VOLTAGE THROUGH A TRAPEZOIDAL INTEGRATION METHOD.
C         THIS REQUIRES STORAGE OF THE PREVIOUS VALUES OF THE
C         CURRENT IN VECTOR CURR.
C
          IF(I.NE.1) THEN
             DO 76 J=1,7
             IF (J.EQ.1) THEN
               VC(J)=VC(J)-DELX*((CURR(J)-CURR(8))+(Y(J)-Y(8)))/(2.*C)
             ELSE
               VC(J)=VC(J)-DELX*((CURR(J)-CURR(J-1))+(Y(J)-Y(J-1)))/
     &                (2.*C)
             ENDIF
  76         CONTINUE
          ENDIF
          DO 77 J=1,8
  77         CURR(J)=Y(J)
C
```

```
C        END OF THE APPLICATION SPECIFIC SECTION
C
C        FILL UP RESULT ARRAYS
C
C        THE MOD STATEMENT IS NECESSARY IF NDIVS IS NOT EQUAL TO NEND
C
         IF(MOD(I,1).EQ.0) THEN
            II=II+1
            RESULT(1,(II+1)) = X
            DO 80 L=1,NEQ
               RESULT((L+1),(II+1)) = Y(L)
               IF(L.GT.8)GOTO 80
               IF (FLAG) THEN
                  IF(L.EQ.1) THEN
                     VOLT(1,(II+1))=VC(L)+LP*(Y(L+9)-Y(18))
                  ELSE
                     VOLT(L,(II+1))=VC(L)+LP*(Y(L+9)-Y(L+8))
                  ENDIF
               ELSE
                  VOLT(L,(II+1))=VC(L)
               ENDIF
80          CONTINUE
         ENDIF
         XO = X
C
C        COUNTER TO SHOW ITERATION
C
         IF(MOD(I,100).EQ.0) THEN
            WRITE(*,8) I
         ENDIF
  90  CONTINUE
C
C     ERROR MESSAGES
C
    1  FORMAT(' *** ERROR: NUMBER OF DIVISIONS IS NOT GREATER THAN 0 ***
      & ')
    2  FORMAT(' **** ERROR: NDIVS IS NOT ONE LESS THAN NDIVP1 ****')
    3  FORMAT(' NEQ IS NOT ONE LESS THAN NEQP1')
    5  FORMAT(' **** ERROR: START AND END POINTS (XO AND XF) ARE THE SAME
      & GIVEN ****')
    6  FORMAT(' ****
      & ZTOL  ****')
    7  FORMAT('    ')
    8  FORMAT('+BE PATIENT, FORTRAN PROGRAM IS RUNNING  ',I5)
       RETURN
       END

       SUBROUTINE RKSVAL(NEQ,A,X,Y,YP)
       IMPLICIT DOUBLE PRECISION(A-H,O-Z)
       DOUBLE PRECISION L,LP,LCON,LF
```

```
      DIMENSION A(8,8),Y(16),YP(16),BVEC(8)
      COMMON/RESIST/R,RL,L,LP,C,LF
C
C     THIS SUBROUTINE CALCULATES THE VALUES OF THE DERIVATIVE MATRIX,
C     YP, IN THE MATRIX STATE EQUATION
C
C                          YP = A*Y
C
C     NEQ ----- NUMBER OF ROWS IN A AND B AND NUMBER OF COLUMNS IN A
C     A ------- COEFFICIENT MATRIX OF THE DIFFERENTIAL EQUATIONS
C     X ------- INDEPENDENT VARIABLE
C     Y ------- VECTOR OF DEPENDENT VARIABLES (LENGTH NEQ)
C     YP ------ VECTOR OF DERIVATIVES (LENGTH NEQ)
C
      LCON=L+2.*LP
      RCON=(RL+(R*(1+LF/L)))/(LF+LP)
      DO 1 I=1,8
1       YP(I)=Y(I+8)
      BVEC(1)=RCON*(YP(8)-YP(1))+(Y(2)-Y(1))/(C*(LF+L))
      BVEC(2)=((Y(1)+Y(3)-2.*Y(2))/(C*LCON))-R*YP(2)/LCON
      BVEC(3)=((Y(2)+Y(4)-2.*Y(3))/(C*LCON))-R*YP(3)/LCON
      BVEC(4)=((Y(3)-2.*Y(4))/(C*LCON))-R*YP(4)/LCON
      BVEC(5)=((Y(6)-2.*Y(5))/(C*LCON))-R*YP(5)/LCON
      BVEC(6)=((Y(5)+Y(7)-2.*Y(6))/(C*LCON))-R*YP(6)/LCON
      BVEC(7)=((Y(6)+Y(8)-2.*Y(7))/(C*LCON))-R*YP(7)/LCON
      BVEC(8)=RCON*(YP(1)-YP(8))+(Y(7)-Y(8))/(C*(LF+LP))
      DO 10 I=9,16
10       YP(I) = 0.0
      DO 30 I=1,8
      DO 20 J=1,8
         YP(8+I)=YP(8+I)+A(I,J)*BVEC(J)
20    CONTINUE
30    CONTINUE
      RETURN
      END

      SUBROUTINE MATINV(N,A,ZTOL)
      IMPLICIT DOUBLE PRECISION (A-H,O-Z)
      DIMENSION A(8,8),MR(8),MC(8)
C
C     SUBROUTINE MATINV FINDS THE MATRIX INVERSE OF A
C     NON-SINGULAR 2-D MATRIX OF X AND Y VALUES
C
C     N-------NUMBER OF ROWS OR COLUMNS IN MATRIX
C     ARRAY---MATRIX WHERE INITIAL VALUES ARE ENTERED AND ANSWER IS
C             RETURNED
C     ZTOL----TOLERANCE FOR QUANTITY ZERO
C
C     REVISED 7/26/86 BY DJH
C
```

```
      DO 100 I=1,N
         MR(I) = I
         MC(I) = I
100   CONTINUE
C
C     FIND THE FIRST PIVOT
C
      MPIVI = 1
      MPIVJ = 1
      DO 200 I=1,N
         DO 300 J=1,N
            IF (DABS(A(I,J)).GT.DABS(A(MPIVI,MPIVJ))) THEN
               MPIVI = I
               MPIVJ = J
            ENDIF
300      CONTINUE
200   CONTINUE
C
C     BEGIN MATRIX INVERSION
C
      DO 400 I=1,N
         L = MR(I)
         MR(I) = MR(MPIVI)
         MR(MPIVI) = L
         L = MC(I)
         MC(I) = MC(MPIVJ)
         MC(MPIVJ) = L
C
C     CHECK THAT THE PIVOT IS NOT ZERO
C
         IF(DABS(A(MR(I),MC(I))).LT.ZTOL)THEN
            WRITE(*,1000)
            RETURN
         ENDIF
C
         DO 500 J=N,1,-1
            IF(I.NE.J)THEN
               A(MR(I),MC(J)) = A(MR(I),MC(J))/A(MR(I),MC(I))
            ENDIF
500      CONTINUE
         PIVOT = 0.0
         A(MR(I),MC(I)) = 1.0/A(MR(I),MC(I))
         DO 600 K=1,N
            IF(I.NE.K)THEN
               DO 700 J=N,1,-1
                  IF(I.NE.J)THEN
                     A(MR(K),MC(J)) =  A(MR(K),MC(J))-A(MR(I),MC(J))*
     &                                 A(MR(K),MC(I))
                     IF (K.GT.I.AND.J.GT.I.AND.DABS(A(MR(K),MC(J)))
     &                  .GE.DABS(PIVOT)) THEN
```

```
                        MPIVI = K
                        MPIVJ = J
                        PIVOT = A(MR(K),MC(J))
                     ENDIF
                  ENDIF
700            CONTINUE
               A(MR(K),MC(I)) = -1.0*A(MR(I),MC(I))*A(MR(K),MC(I))
            ENDIF
600      CONTINUE
400   CONTINUE
C
C     REARRANGE THE ROWS THEN THE COLUMNS TO THEIR PROPER ORDER
C
      CALL PERMUT(A,MR,MC,N,1)
      CALL PERMUT(A,MC,MR,N,0)
C
C     ERROR MESSAGES
C
1000  FORMAT(' THE MATRIX IS SINGULAR, A ZERO PIVOT WAS FOUND')
      RETURN
      END

      SUBROUTINE PERMUT(ARRAY,MS,MD,N,NCHNG)
      IMPLICIT DOUBLE PRECISION(A-H,O-Z)
      DIMENSION ARRAY(N,N),MS(N),MD(N),NTAG(8),LOC(8)
C
C     SUBROUTINE PERMUT PERMUTES A MATRIX ACCORDING TO THE PERMUTATION
C     VECTORS CONTAINED IS MS AND MD
C
C     ARRAY---THE MATRIX TO BE PERMUTED, SERVES AS INPUT AND OUTPUT
C     MS------SOURCE LOCATION FOR ARRAY ELEMENT
C     MD------DESTINATION LOCATION FOR ARRAY ELEMENT
C     N-------NUMBER OF ROWS OR COLUMNS IN MATRIX
C     NCHNG---WHEN NCHNG IS 1 THE ROWS ARE REARRANGED, ELSE THE COLUMNS
C             ARE REARRANGED
C
      DO 100 I=1,N
         NTAG(I) = I
         LOC(I) = I
100   CONTINUE
      DO 200 I=1,N
         M = MS(I)
            J = LOC(M)
            K = MD(I)
            IF(J.NE.K)THEN
               DO 300 NP=1,N
                  IF(NCHNG.EQ.1)THEN
                     W = ARRAY(J,NP)
                     ARRAY(J,NP) = ARRAY(K,NP)
                     ARRAY(K,NP) = W
```

```
                ELSE
                   W = ARRAY(NP,J)
                   ARRAY(NP,J) = ARRAY(NP,K)
                   ARRAY(NP,K) = W
                ENDIF
300          CONTINUE
          NTAG(J) = NTAG(K)
          NTAG(K) = M
          LOC(M) = LOC(NTAG(J))
          LOC(NTAG(J)) = J
       ENDIF
200    CONTINUE
       RETURN
       END
```

References

1. Jahn, R.G., Physics of Electric Propulsion, McGraw Hill Book Company, New York, 1968.

2. Clark, K.E., "Quasi-Steady Plasma Acceleration", Ph.D. Dissertation, Department of Aerospace and Mechanical Sciences, Princeton University, Princeton, New Jersey, May 1969.

3. Rudolph, L.K. and Jahn, R.G., "The MPD Thruster Onset Current Performance Limitation", Ph.D. Dissertation, Department of Mechanical and Aerospace Engineering, Princeton University, Princeton, New Jersey, September 1980.

4. Turchi, P.J., Heimerdinger, D.J., "The Current Integral Approach Applied to Inlet Flow Electrical Conductivity in Self-Field MPD Arcjets", AIAA-87-1097 presented at the AIAA/DGLR/JSASS 19th International Electric Propulsion Conference, May 11-13, 1987, Colorado Springs, Colorado.

5. Heimerdinger, D.J., "Control of the Barrel Phenomenon in an MPD Discharge", Undergraduate Thesis, Department of Mechanical and Aerospace Engineering, Princeton University, Princeton, New Jersey, June 1980.

6. Merfeld, D.M. and Jahn, R.G., "MPD Thruster Performance: Propellant Injection and Species Effects", M.S.E. Thesis, Department of Mechanical and Aerospace Engineering, Princeton University, Princeton, New Jersey, October 1984.

7. Ho, D.D., Jahn, R.G., "Erosion Studies in an MPD Thruster", Masters Thesis, Princeton University, Princeton, New Jersey, MAE Report No. 1515, May 1981.

8. Kuriki, K., and Onishi, M., "Thrust Measurement of KIII MPD Arcjet", AIAA Paper 81-0683, 15th International Electric Propulsion Conference, Las Vegas, Nevada, 1981.

9. Heimerdinger, D.J., "The Barrel Phenomenon in MPD Arcjets", Junior Independent Work, Department of Mechanical and Aerospace Engineering, Princeton, New Jersey, 1979.

10. Vainberg, L.I., Lyubimov, G.A., Smolin, G.G., "High-Current Discharge Effects and Anode Damage in an End-Fire Plasma Accelerator", Sov. Phys. Tech. Phys. 23(4) April 1978, pp. 439-443.

11. Hugel, H., "Effect of Self-Magnetic Forces on the Anode Mechanism of a High Current Discharge", IEEE Transactions on Plasma Sciences, PS-8(4), December 1980, pp. 437-442.

12. Barnett, J.W. and Jahn, R.G., "Operation of the MPD Thruster with Stepped Current Input", Ph.D. Dissertation, Department of Mechanical and Aerospace Engineering, Princeton University, Princeton, New Jersey, April 1985.

13. Baksht, F.G., Moizhes, B.Ya., Rybakov, A.B., "Critical Regime of a Plasma Accelerator", Sov. Phys. Tech. Phys. 18(12), 1974, p. 1613.

14. Heimerdinger, D.J. and Martinez-Sanchez, M., "An Approximate Two-Dimensional Model of an MPD Arcjet", S.M. Thesis, Department of Aeronautics and Astronautics, Massachusetts Institute of Technology, Cambridge, Massachusetts, June 1984.

15. Martinez-Sanchez, M., Heimerdinger, D.J., Poon, T.W., "Second Annual Report", Air Force Office Of Scientific Research Grant number AFOSR-83-0035A, submitted May, 1986.

16. von Jaskowsky, W.F., in Pulsed Electromagnetic Gas Acceleration Report 634o, Department of Aeronautics and Mechanical Sciences, Princeton University, Princeton, New Jersey, July 1970, p. 76.

17. King, D.Q., Smith, W.W., Jahn, R.G., and Clark, K.E., "Effect of Thrust Chamber Configuration on MPD Arcjet Performance", AIAA Paper 79-2051 presented at Princeton/AIAA/DGLR 14th International Electric Propulsion Conference, Princeton, New Jersey, Oct. 30 - Nov. 1, 1979.

18. Malliaris, A.C., John,R.R., Garrison, R.L., Libby, D.R., "Performance of Quasi-Steady MPD Thrusters at High Powers", AIAA Journal, Volume 10, Number 2, February 1972, pp. 121-122.

19. Boyle, M.J., and Jahn, R.G., "Acceleration Processes in the Quasi-Steady MPD Discharge", Ph.D. Dissertation, Department of Aerospace and Mechanical Sciences, Princeton University, Princeton, New Jersey, July 1974.

20. Boyle, M.J., Clark, K.E., and Jahn, R.G., "Flowfield Characteristics and Performance Limitations of Quasi-Steady Magnetoplasmadynamic Accelerators", AIAA Journal 14(7), July 1976, pp. 955-962.

21. Schrade, H.O., Auweter-Kurtz, M., Kurtz, H.L., "Cathode Phenomena In Plasma Thrusters", AIAA-87-1096 presented at the AIAA/DGLR/JSASS 19th International Electric Propulsion Conference, May 11-13, 1987, Colorado Springs, Colorado.

22. Morozov, A.I., and Shubin, A.P., "Theory of Plane Flows of a Readily Conducting Plasma in a Pipe", Zh. Prikl. I Tekh. Fiz. #4, July - August 1970, pp. 9-19.

23. Shubin, A.P., "Dynamic Nature of the Critical Regime in Steady-State High-Current Plasma Accelerators", Sov. J. Plasma Phys. 2(1), Jan.-Feb. 1976, p. 18.

24. Choueiri, E.Y., Kelly, A.J., Jahn, R.G., "MPD Thruster Plasma Instability Studies", AIAA-87-1067 presented at the AIAA/DGLR/JSASS 19th International Electric Propulsion Conference, May 11-13, 1987, Colorado Springs, Colorado.

25. Kuriki, K., Iida, H., Spectrum Analysis of Instabilities in MPD Arcjet", IEPC Paper 84-28, presented at the AIAA/DGLR/JSASS 17th International Electric Propulsion Conference, Tokyo, Japan, May, 1984.

26. Poon, T.W., "Local Stability Analysis of the Magnetoplasmadynamic (MPD) Thruster", S.M. Thesis, Department of Aeronautics and Astronautics, Massachusetts Institute of Technology, Cambridge, Massachusetts, June 1984.

27. Martinez-Sanchez, M., "The Structure of Self-Field Accelerated Plasma Flows", AIAA Paper 87-1065 presented at the AIAA/DGLR/JSASS 19th International Electric Propulsion Conference, May 11-13, 1987, Colorado Springs, Colorado.

28. Sutton, G.W, and Sherman, A, Engineering Magnetohydrodynamics, McGraw-Hill Book Company, New York, 1965.

29. Mitchener, M. and Kruger, C.H. Jr., Partially Ionized Gases, John Wiley and Sons, New York City, 1973.

30. Hirsch, M.N. and Oskam, H.J., ed., Gaseous Electronics Volume 1: Electrical Discharges, Academic Press, New York City, 1978.

31. Capitelli, M., Ficocelli, E., and Molinari, E., "Equilibrium Compositions and Thermodynamic Properties of Mixed Plasmas, II: $Ar-O_2$ Plasmas at 10^{-2} - 10 atm Between 2000 and 35000 K", Centro di Studio per la Chimica dei Plasmi del Consiglio Nazionale delle Ricerche-Instituto di Chimica Generale e Inorganica, Univ. degli Studi-Bari, Italy, 1970.

32. Capitelli, M., Ficocelli, E., and Molinari, E., "Transport Properties of Mixed Plasmas: $He-N_2$, $Ar-N_2$, and $Xe-N_2$ Plasmas at One Atmosphere, Between 5000 and 35000 K", Centro di Studio per la Chimica dei Plasmi del Consiglio Nazionale delle Ricerche-Instituto di Chimica Generale e Inorganica, Univ. degli Studi-Bari, Italy, 1970.

33. Nighan, W.L., "Electrical Conductivity of Partially Ionized Noble Gases", Physics of Fluids Vol. 12, No. 1, January 1969.

34. Turchi, P.J. and Jahn, R.G., "The Cathode Region of a Quasi-Steady Magnetoplasmadynamic Arcjet", Ph.D. Dissertation, Department of Aerospace and Mechanical Sciences, Princeton University, Princeton, New Jersey, October 1970.

35. Huddlestone, R.H. and Leonard, S.L., Plasma Diagnostic Techniques, Academic Press, New York City, 1965.

36. Griem, H.R., Spectral Line Broadening By Plasmas, Academic Press, New York, 1974.

37. Turchi, P.J., "Critical Speed and Voltage-Current Characteristics in Self-Field Plasma Thrusters", Journal of Propulsion and Power, Vol. 2, Sept.-Oct. 1986, pp.398-401.

38. Wolff, M., Kelly, A.J., and Jahn, R.G., "A High Performance Magnetoplasmadynamic Thruster", IEPC Paper 84-32, presented at the AIAA/DGLR/JSASS 17th International Electric Propulsion Conference, Tokyo, Japan, May 1984.

39. Toki, K., Sumida, M., Kuriki, K., "Multi-Channel Two-Dimensional MPD Arcjet", AIAA-87-1000 presented at the AIAA/DGLR/JSASS 19th International Electric Propulsion Conference, May 11-13, 1987, Colorado Springs, Colorado.

40. Yoshikawa, T., et. al., "Performance Characteristics of Quasi-Steady MPD Thrusters", IEPC Paper 84-58, presented at the AIAA/DGLR/JSASS 17th International Electric Propulsion Conference, Tokyo, Japan, May 1984.

41. Kuriki, K., Kunii, Y., Shimizu, Y., "Current Distribution in Plasma Thruster", AIAA Paper 81-0685, presented at the AIAA/DGLR/JSASS 15th International Electric Propulsion Conference, Las Vegas, Nevada, April 21-23, 1981.

42. Uematsu, K., Mori, K., Kuninaka, H., and Kuriki, K., "Effect of Electrode Configuration on MPD Arcjet Performance", IEPC Paper 84-11, presented at the AIAA/DGLR/JSASS 17th International Electric Propulsion Conference, Tokyo, Japan, May 1984.

43. Black, N.A., "Dynamics of a Pinch Discharge Driven by a High Current Pulse Forming Network", Ph.D. Dissertation, Department of Aerospace and Mechanical Sciences, Princeton University, Princeton, New Jersey, May 1966.

44. American Institute of Physics Handbook, McGraw-Hill Book Company, New York City, New York, 1963.

45. Grover, F.W., Inductance Calculations, Working Formulas and Tables, D. Van Nostrand, New York, 1946.

46. White, F.M., Viscous Fluid Flow, McGraw-Hill Book Company, New York, 1974.